

# **Detection and Localisation**

## **Using Light**

Aubida Abdulwahab Jasim Al-Hameed

Submitted in accordance with the requirements for the  
degree of Doctor of Philosophy



**UNIVERSITY OF LEEDS**

School of Electronic and Electrical Engineering

March 2019

The candidate confirms that the work submitted is his own, except where work which has formed part of jointly authored publications has been included. The contribution of the candidate and the other authors to this work has been explicitly indicated below. The candidate confirms that appropriate credit has been given within the thesis where reference has been made to the work of others.

**The work in Chapter 3, 4, 5, 6 and 7 of the thesis has appeared in publications as follows:**

1. Aubida A. Al-Hameed, Safwan Hafeedh Younus, Ahmed Taha Hussein, Mohammed T. Alresheedi and Jaafar M. H. Elmirghani, "LiDAL: Light Detection and Localisation," *IEEE Access*, submitted March 2019.

- My contribution: literature review, developed the idea, produced results and wrote the work.
- Professor Jaafar M. H. Elmirghani suggested the paper idea, supervised and revised the work.
- Dr. Safwan Hafeedh Younus, Dr. Ahmed Taha Hussein and Dr. Mohammed T. Alresheedi helped with the revision of the work.

This copy has been supplied on the understanding that it is copyright material and that no quotation from the thesis may be published without proper acknowledgement.

*To my father*

# Acknowledgements

First and foremost, all praise to Almighty Allah, for endowing me with health, patience, and knowledge to complete this work. I would like to acknowledge my supervisor, Professor Jaafar Elmirghani for his guidance and patience through my PhD journey. I am grateful for his teachings, guidance and support. He has offered me invaluable opportunities and continuously kept faith in me.

I am very grateful and thankful to the Higher Committee for Education Development (HCED) in Iraq for fully funding my PhD.

Many thanks go to my colleagues in the Communication Systems and Networks group in the School of Electronic and Electronic Engineering at University of Leeds. Also, I send my special thanks to Dr. Ahmed T. Hussein Dr. Safwan H. Younus and Dr. Mohamed Musa. It was a privilege to have known them. I thank them for their company, reassurance and fruitful discussions.

I would like to express my appreciation to my beloved family back home, my mother, sister and brother. I don't have enough words to thank them for supporting me in all possible ways. They are the reason behind my life achievements and have always shown me by example that everything is doable. I hope I made them proud.

# Abstract

Visible light communication (VLC) systems have become promising candidates to complement conventional radio frequency (RF) systems due to the increasingly saturated RF spectrum and the potentially high data rates that can be achieved by VLC systems. Furthermore, people detection and counting in an indoor environment has become an emerging and attractive area in the past decade. Many techniques and systems have been developed for counting in public places such as subways, bus stations and supermarkets. The outcome of these techniques can be used for public security, resource allocation and marketing decisions.

This thesis presents the first indoor light-based detection and localisation system that builds on concepts from radio detection and ranging (radar) making use of the expected growth in the use and adoption of visible light communication (VLC), which can provide the infrastructure for our light detection and localisation (LiDAL) system. Our system enables active detection, counting and localisation of people, in addition to being fully compatible with existing VLC systems. In order to detect human (targets), LiDAL uses the visible light spectrum. It sends pulses using a VLC transmitter and analyses the reflected signal collected by an optical receiver. Although we examine the use of the visible spectrum here, LiDAL can be used in the infrared spectrum and other parts of the light spectrum.

We introduce LiDAL with different transmitter-receiver configurations and optimum detectors considering the fluctuation of the received reflected signal from the target in the presence of Gaussian noise. We design an efficient multiple input multiple output (MIMO) LiDAL system with wide field of view (FOV) single photodetector receiver, and also design a multiple input single output (MISO) LiDAL system with an imaging receiver to eliminate ambiguity in target detection and localisation.

We develop models for the human body and its reflections and consider the impact of the colour and texture of the cloth used as well as the impact of target mobility. A number of detection and localisation methods are developed

for our LiDAL system including cross correlation, a background subtraction method and a background estimation method. These methods are considered to distinguish a mobile target from the ambient reflections due to background obstacles (furniture) in a realistic indoor environment.

# Contents

|  |      |
|--|------|
| Acknowledgements .....   | i    |
| Abstract .....   | ii   |
| Contents .....   | iv   |
| List of Figures .....  | vii  |
| List of Tables .....   | x    |
| List of Abbreviations .....  | xi   |
| List of Symbols .....  | xiii |
| Chapter 1 Introduction .....   | 16   |
| 1.1 Research Motivation and Objectives .....                                   | 17   |
| 1.2 Research Contributions .....   | 19   |
| 1.3 Publications .....   | 20   |
| 1.4 Thesis Outline .....   | 20   |
| Chapter 2 Review of Optical Wireless, RADAR and Human Sensing<br>Systems ..... | 23   |
| 2.1 Introduction .....   | 23   |
| 2.2 Visible Light Communication System .....                                   | 24   |
| 2.2.1 VLC Transmitter .....  | 27   |
| 2.2.2 VLC Receiver .....   | 27   |
| 2.2.3 Channel Modelling of Optical Wireless System .....                       | 33   |
| 2.3 Radio Detection And Ranging (RADAR) .....                                  | 42   |
| 2.3.1 RADAR System Setup .....   | 43   |
| 2.3.2 RADAR Configurations .....   | 44   |
| 2.3.3 Continuous Waveform RADAR .....  | 46   |
| 2.3.4 Pulsed Waveform RADAR .....  | 47   |
| 2.3.5 Light Detection And Ranging (LiDAR) .....                                | 48   |
| 2.4 Human Sensing Techniques .....   | 50   |
| 2.5 Summary .....  | 53   |
| Chapter 3 LiDAL System Design .....  | 54   |
| 3.1 Introduction .....   | 54   |
| 3.2 Realistic Environment and Target Modelling .....                           | 55   |
| 3.3 LiDAL Range Analysis .....   | 58   |
| 3.4 Optical Receiver Design For LiDAL .....                                    | 63   |
| 3.4.1 Receiver Bandwidth .....   | 63   |

|  |     |
|--|-----|
| 3.4.2 Receiver Noise .....   | 68  |
| 3.5 LiDAL Resolution and Ambiguity in Target Detection Analysis .....                              | 69  |
| 3.6 Received Signal Fluctuation and Target Reflectivity Modelling .....                            | 72  |
| 3.7 Summary .....  | 77  |
| Chapter 4 LiDAL Optimum Receiver Design .....  | 78  |
| 4.1 Introduction .....   | 78  |
| 4.2 Optimum Detection Threshold Analysis (Hard Decision).....                                      | 79  |
| 4.2.1 Probability of False Detection ( $P_{FD}$ ).....   | 84  |
| 4.2.2 Probability of Detection ( $P_D$ ).....  | 84  |
| 4.3 LiDAL Optimum Detector .....   | 85  |
| 4.3.1 Case I: Single Target Detection .....  | 86  |
| 4.3.2 Case II: Multiple Targets Detection .....  | 91  |
| 4.3.3 Case III: Target Detection in Channel Dispersion .....                                       | 97  |
| 4.4 Performance Analysis of LiDAL Optimum Receivers .....  | 99  |
| 4.5 Summary .....  | 100 |
| Chapter 5 Target Distinguishing Approaches and Mobility Modelling in<br>Realistic Environment..... | 101 |
| 5.1 Introduction .....   | 101 |
| 5.2 Background Subtraction Method (BSM) .....  | 103 |
| 5.2.1 Evaluation of Background Subtraction Method .....  | 103 |
| 5.3 Cross-Correlation Method (CCM).....  | 106 |
| 5.3.1 Fast Cross-correlation .....   | 108 |
| 5.3.2 Slow Cross-correlation .....   | 116 |
| 5.4 Target Mobility Modelling .....  | 119 |
| 5.4.1 Probability of Mobility Detection ( $P_{MD}$ ).....  | 120 |
| 5.4.2 Directed Random Walk with Obstacle Avoidance .....   | 124 |
| 5.4.3 Pathways Mobility Model.....   | 126 |
| 5.5 Background Estimation Method (BEM) .....   | 127 |
| 5.6 Target Distinguishing Evaluation .....   | 129 |
| 5.7 Summary .....  | 134 |
| Chapter 6 MIMO LiDAL System .....  | 135 |
| 6.1 Introduction .....   | 135 |
| 6.2 MIMO LiDAL System Configurations.....  | 138 |
| 6.3 Collaboration of the MIMO-LiDAL Transceivers Units .....                                       | 143 |



|   |     |
|---|-----|
| 6.4 MIMO LiDAL System Receiver Operating Characteristics (ROC)..... | 145 |
| 6.5 Probability of Target Detection in MIMO LiDAL System .....      | 149 |
| 6.6 Target Localisation .....                                       | 150 |
| 6.7 MIMO LiDAL System Operating Algorithm .....                     | 152 |
| 6.7.1 MIMO LiDAL Overhead .....                                     | 154 |
| 6.8 Simulation Setup and Results Discussion .....                   | 156 |
| 6.8.1 System Setup .....  | 157 |
| 6.8.2 Key Parameters for Counting and Localisation .....            | 159 |
| 6.8.3 Simulation Flow Setup.....                                    | 160 |
| 6.8.4 Scenario 1: The Baseline .....                                | 162 |
| 6.8.5 Scenario 2: Challenging Localisation Environment .....        | 164 |
| 6.8.6 Scenario 3: Harsh Localisation Environment.....               | 166 |
| 6.9 Summary .....   | 168 |
| Chapter 7 Imaging LiDAL System .....                                | 169 |
| 7.1 Introduction .....  | 169 |
| 7.2 System Configurations .....                                     | 171 |
| 7.2.1 MISO-IMG-LiDAL Receiver Operating Characteristics.....        | 175 |
| 7.3 Target localisation .....                                       | 179 |
| 7.4 Targets Detection in MISO-IMG-LiDAL .....                       | 181 |
| 7.4.1 Challenges of Target Detection In MISO-IMG-LiDAL.....         | 184 |
| 7.5 MISO-IMG-LiDAL System Operating Algorithm .....                 | 187 |
| 7.5.1 MISO-IMG LiDAL Overhead.....                                  | 188 |
| 7.6 Simulation Setup and Results Discussion .....                   | 189 |
| 7.6.1 Systems Setup .....   | 189 |
| 7.6.2 Scenario 1: The Baseline .....                                | 192 |
| 7.6.3 Scenario 2: Challenging Localisation Environment .....        | 193 |
| 7.6.4 Scenario 3: Harsh Localisation Environment.....               | 195 |
| 7.7 Case Study Setup and Results Discussion .....                   | 197 |
| 7.7.1 Case Study Setup .....  | 197 |
| 7.7.2 Targets Following a Pathway Model .....                       | 199 |
| 7.7.3 Targets Following a Random Walk Model.....                    | 200 |
| 7.9 Summary .....   | 200 |
| Chapter 8 Conclusions and Future Work.....                          | 201 |
| References.....   | 209 |

|   |     |
|---|-----|
| Appendix A.....   | 222 |
| A.1 Simulation results of VLC system originally reported in [A1]..... | 222 |
| A.2 Simulation results of VLC system originally reported in [A2]..... | 223 |
| A.3 Simulation results of OW system originally reported in [A3].....  | 225 |
| A.4 Simulation results of OW system originally reported in [A4].....  | 228 |
| Appendix B Convolution of Gaussian random variables.....              | 231 |

## List of Figures

|  |    |
|--|----|
| Figure 2.1 Block diagram of VLC system. ....   | 26 |
| Figure 2.2: Non-directional hemispherical lens that employs a planar filter [53]. ....   | 29 |
| Figure 2.3: Compound parabolic concentrator [53]. ....   | 29 |
| Figure 2.4: Relative spectral power densities of the three common ambient light sources [53]. ....   | 30 |
| Figure 2.5: Ray tracing setup for LOS, first and second order reflections [93], [94]. ....   | 37 |
| Figure 2.6: Ray tracing for LOS [94].....  | 38 |
| Figure 2.7: Ray tracing for first order reflections [94]. ....   | 39 |
| Figure 2.8: Radar system setup. ....   | 43 |
| Figure 2.9:(a) Bistatic radar configuration and (b) Monostatic radar configuration.....  | 45 |
| Figure 2.10: Block diagram of LiDAR system with (a) incoherent detection and (b) coherent detection.....   | 49 |
| Figure 3.1: Realistic office room setup. ....  | 57 |
| Figure 3.2: Basic 3D and 2D target model. ....   | 57 |
| Figure 3.3: (a) a spaced transmitter-receiver (bistatic) placed on room ceiling with a target located near by the transmitter and distance of $R_{MaxFOV}$ from the receiver (b) a spaced transmitter-receiver placed on room ceiling with a target located away from the..... | 61 |
| Figure 3.4: (a) and (b) a collocated transmitter-receiver (monostatic) placed on room ceiling with a target at two different locations. ....   | 62 |
| Figure 3.5: Tx and Rx placed in different locations (bistatic LiDAL) with a target located in the centre of the optical footprint.....   | 64 |
| Figure 3.6:Tx and Rx placed in same location (monostatic LiDAL ) a target located in the centre of the optical footprint.....  | 64 |

|   |     |
|---|-----|
| Figure 3.7: (a) Bistatic LiDAL impulse response of target located at $x=2.5\text{m}$ , $y=5\text{m}$ , (b) Bistatic LiDAL impulse response of target located at $x=2\text{m}$ , $y=3\text{m}$ and (c) the PDF of the Bistatic LiDAL channel bandwidth. ....       | 66  |
| Figure 3.8: (a) Monostatic LiDAL impulse response of target located at $x=1.5\text{m}$ , $y=3\text{m}$ , (b) Monostatic LiDAL impulse response of target located at $x=2\text{m}$ , $y=5\text{m}$ and (c) the PDF of the monostatic LiDAL channel bandwidth. .... | 67  |
| Figure 3.9: The LiDAL resolution to distinguish two targets. ....   | 70  |
| Figure 3.10: The reflected received current signal from two targets located in empty room of monostatic LiDAL. ....   | 71  |
| Figure 3.11: The PDF of target reflection factor. ....  | 73  |
| Figure 3.12: The PDF of the effective target cross section area. ....   | 75  |
| Figure 4.1: The Optimum detection threshold with $\beta\sigma$ for different LiDAL cost factors. ....   | 83  |
| Figure 4.2: The LiDAL optimum detector block diagram, single target detection. ....   | 89  |
| Figure 4.3: The orthonormal $\phi_{jt}$ signalling diagram. ....  | 90  |
| Figure 4.4: The LiDAL sub-optimum receiver block diagram. ....  | 94  |
| Figure 4.5: The LiDAL receiver two-dimensional observation space. ....  | 95  |
| Figure 4.6: Probability of error of detecting targets for ESR and SOR. ....   | 99  |
| Figure 5.1: BSM of the received snapshots measurements. ....  | 105 |
| Figure 5.2: Receiver block diagram of LiDAL with BSM. ....  | 105 |
| Figure 5.3: LiDAL snapshots measurement cube. ....  | 107 |
| Figure 5.4: (a) received reflected signals in two snapshots measurement in Proposition I and (b) CCM of received snapshots measurement of Proposition I. ....   | 109 |
| Figure 5.5: (a) received reflected signals in two snapshots measurement in Proposition II and (b) CCM of received snapshots measurement of Proposition II. ....   | 111 |
| Figure 5.6: : (a) received reflected signals in two snapshots measurement in Proposition III and (b) CCM of received snapshots measurement of Proposition III. ....   | 113 |
| Figure 5.7: (a) received reflected signals in two snapshots measurement in Proposition IV and (b) CCM of received snapshots measurement of Proposition IV. ....   | 114 |
| Figure 5.8: LiDAL receiver block diagram with CCM. ....   | 118 |
| Figure 5.9: Target random walk model in $G(x, y)$ space. ....   | 121 |
| Figure 5.10: Probability of target mobility detection in a realistic environment. ....  | 123 |

|  |     |
|--|-----|
| Figure 5.11: Pathways Mobility Model.....  | 126 |
| Figure 5.12: LiDAL receiver block diagram with BEM. ....   | 128 |
| Figure 5.13: Simulation room setup with Monostatic LiDAL. ....   | 129 |
| Figure 5.14: False target distinguishing error in static environment. ....   | 130 |
| Figure 5.15: False target distinguishing error in dynamic environment. ....  | 132 |
| Figure 6.1: MIMO-LiDAL system setup. ....  | 139 |
| Figure 6.2: MIMO monostatic LiDAL. ....  | 140 |
| Figure 6.3: ROC of Monostatic MIMO LiDAL. ....   | 142 |
| Figure 6.4: Monostatic MIMO LiDAL false detection with optimum <b><i>DthM</i></b> .<br>.....   | 142 |
| Figure 6.5: Target detection ambiguity in MIMO-LiDAL system with<br>targets ranging .....  | 144 |
| Figure 6.6: (a) the reflected pulses from targets when Tx <sub>1</sub> -Rx <sub>1</sub> are active,<br>(b) the reflected pulses from targets when Tx <sub>2</sub> -Rx <sub>1</sub> are active and<br>(c) the reflected pulses from targets when Tx <sub>3</sub> -Rx <sub>1</sub> are active..... | 145 |
| Figure 6.7: Bistatic MIMO LiDAL system.....  | 146 |
| Figure 6.8: ROC of Bistatic MIMO LiDAL. ....   | 148 |
| Figure 6.9: Bistatic MIMO LiDAL probability of false detection with<br>optimum <b><i>DthB</i></b> . ....   | 148 |
| Figure 6.10: The receiver block diagram of MIMO-LiDAL system. ....   | 154 |
| Figure 6.11: MIMO LiDAL Room A setup in scenario 1. ....   | 157 |
| Figure 6.12 MIMO LiDAL Room B setup in scenario 2.....   | 157 |
| Figure 6.13: MAPE of MIMO LiDAL system with BSM and CCM in Room<br>A of scenario 1. ....   | 163 |
| Figure 6.14: MAPE of MIMO LiDAL system with BSM and CCM in Room<br>B of scenario 2. ....   | 164 |
| Figure 6.15: CDF of DRMSE of the proposed MIMO LiDAL system. ....  | 165 |
| Figure 6.16: CDF of counting MAPE in the MIMO LiDAL system for<br>nomadic targets with different MF. ....  | 167 |
| Figure 7.1: MISO-IMG-LiDAL system.....   | 171 |
| Figure 7.2: LiDAL imaging receiver design, lens FOV with <b><i>RMaxFOV</i></b> . ....  | 172 |
| Figure 7.3: targets optical resolution in MISO IMG LiDAL system.....   | 173 |
| Figure 7.4: Pixel's angles of IMG LiDAL system. ....   | 175 |
| Figure 7.5: Bistatic MISO-IMG-LiDAL system. ....   | 177 |
| Figure 7.6: ROC of Bistatic MISO -IMG-LiDAL system. ....   | 178 |
| Figure 7.7: Bistatic MISO-IMG-LiDAL false detection with optimum<br><b><i>DthBimg</i></b> . ....   | 178 |

|  |     |
|--|-----|
| Figure 7.8: Target localisation in MISO IMG-LiDAL. ....  | 180 |
| Figure 7.9: A top view of three targets movement on the detection floor of MISO-IMG- LiDAL system during S snapshots measurements..... | 183 |
| Figure 7.10: Eight GRPs of the imaging receiver. ....  | 186 |
| Figure 7.11: The proposed sub-optimum imaging receiver (SOIMR) for IMG LiDAL system. ....  | 186 |
| Figure 7.12: the receiver block diagram of MISO-IMG-LiDAL. ....  | 187 |
| Figure 7.13: MISO IMG LiDAL Room A setup in scenario 1.....  | 190 |
| Figure 7.14: MISO IMG LiDAL Room A setup in scenario 2.....  | 190 |
| Figure 7.15: MAPE of LiDAL systems with BSM and CCM in empty environment of scenario 1.....  | 192 |
| Figure 7.16: MAPE of LiDAL systems with BSM and CCM in realistic environment of scenario 2.....  | 193 |
| Figure 7.17: CDFs of DRMSE of the proposed LiDAL systems. ....   | 194 |
| Figure 7.18: MISO-IMG LiDAL system MAPE CDF for the nomadic targets with different MF.....   | 195 |
| Figure 7.19: CDF of counting MAPE in the MIMO LiDAL system for nomadic targets with different MF. ....                                 | 196 |
| Figure 7.20: CDF of counting MAPE of the targets, when the targets move along fixed pathways.....                                      | 199 |
| Figure 7.21: CDF of counting MAPE of the targets, when the targets move following a random walk model. ....                            | 201 |

## List of Tables

|   |     |
|---|-----|
| Table 3.1: Reflection model for a different target coating materials [152]..... | 56  |
| Table 3.2: Characteristic of LiDAL Channel. ....                                | 66  |
| Table 3.3: Popular Colours with Reflection Factor. ....                         | 73  |
| Table 4.1: Single target detection in $N$ time slots ....                       | 88  |
| Table 4.2: Multiple targets detection hypotheses ....                           | 95  |
| Table 4.3: ZFE delay spread and noise enhancement.....                          | 98  |
| Table 5.1: Target movement indicator decision.....                              | 115 |
| Table 5.2: Setup algorithm of the background estimation method ....             | 128 |
| Table 5.3: Simulation Parameters of Target Distinguishing.....                  | 133 |
| Table 6.1: LiDAL localisation compared to traditional radar localisation....    | 137 |
| Table 6.2: MIMO LiDAL simulation parameters.....                                | 158 |

|   |     |
|---|-----|
| Table 6.3: SIMULATION FLOW .....                                  | 161 |
| Table 7.1: Simulation parameters of LiDAL systems.....            | 191 |
| Table 7.2: Mobility simulation parameters of the case study ..... | 198 |

## List of Abbreviations

|                    |   |
|--------------------|---|
| ADR                | Angle Diversity Receiver                        |
| BJT                | Bipolar Junction Transistor                     |
| BEM                | Background estimation method                    |
| BP                 | Backpropagation algorithm                       |
| BSM                | Background substation method                    |
| CCM                | Cross-correlation method                        |
| CDS                | Conventional diffuse system                     |
| CDF                | Cumulative distribution function                |
| CoN <sub>TRx</sub> | Collaboration between neighbouring transceivers |
| CPC                | Compound parabolic concentrator                 |
| DRMSE              | Distance root mean square error                 |
| DSP                | Digital signal processor                        |
| ESR                | Exhaustive search receiver                      |
| FSO                | Free space optical communication                |
| FET                | Field effect transistor                         |
| FOV                | Field of View                                   |
| GRP                | Group of receiver pixels                        |
| HPBW               | Half power beam width                           |
| IR                 | Infrared  |
| IM/DD              | Intensity modulation and direct detection       |
| LD                 | Laser diodes                                    |
| LiDAL              | Light detection and localisation                |

|       |  |
|-------|--|
| LIDAR | Light detection and ranging                |
| Li-Fi | Light fidelity                             |
| LEDs  | Light emitting diodes                      |
| LMA   | Levenberg-Marquardt algorithm              |
| LSMS  | Line strip multi-spot diffusing system     |
| MIMO  | Multiple input multiple output             |
| MISO  | Multiple input single output               |
| MAPE  | Mean absolute percentage error             |
| MF    | Mobility factor                            |
| OOK   | On-off keying                              |
| OFDM  | Orthogonal frequency division multiplexing |
| OBPF  | Optical bandpass filter                    |
| OW    | Optical wireless                           |
| PCCM  | Pixels cross-correlation method            |
| PD    | Photodetector                              |
| PDF   | Probability density function               |
| PIR   | Passive infrared                           |
| PPM   | Pulse position modulation                  |
| PSM   | Pixels subtractions method                 |
| RADAR | Radio detection and ranging                |
| RMSE  | Root mean square error                     |
| TOA   | Time-of-arrival                            |
| TRx   | Transceiver unit                           |
| SNR   | Signal to noise ratio                      |
| SOR   | Suboptimum receiver                        |
| SUF   | Space utilization factor                   |
| TIA   | Transimpedance amplifier                   |
| UWB   | Ultra-wideband system                      |
| VLC   | Visible light communication                |
| ZFE   | Zero forcing equaliser                     |

# List of Symbols

|                   |  |
|-------------------|--|
| $\alpha_{11}$     | Cost of deciding that the target is absent when it is true |
| $\alpha_{22}$     | Cost of deciding the target is present when it is true     |
| $\alpha_{12}$     | Cost of deciding the target is absent when it is false     |
| $\alpha_{21}$     | Cost of deciding the target is present when it is false    |
| $A_R$             | Photodetector area   |
| $A_{eff}(\delta)$ | Effective signal-collection area                           |
| $A_e$             | Effective target cross section area                        |
| $A_Z$             | Azimuth angle  |
| $Bw_{ch}$         | LiDAL channel bandwidth                                    |
| $Bw_{Rx}$         | LiDAL bandwidth receiver                                   |
| $\beta_\sigma$    | Colour factor  |
| $c$               | Speed of light   |
| $D$               | Root mean square delay spread                              |
| $D_{th}(z)$       | LiDAL optimum detection threshold                          |
| $dA$              | Reflection surface element area                            |
| $d_o$             | Room height  |
| $\gamma_{FA}$     | Cost factor of missing target                              |
| $\gamma_{FP}$     | Cost factor of false alarm                                 |
| $\delta$          | Angle of incidence with respect to the receiver normal     |



|                          |  |
|--------------------------|--|
| $\Delta R$               | LiDAL resolution   |
| $erfc$                   | Error function complementary   |
| $El$                     | Elevation angle  |
| $G(\delta)$              | Concentrator gain  |
| $h$                      | Target height  |
| $h(t)$                   | Impulse response   |
| $h_p$                    | Planck's constant  |
| $\mu_{A_e}$              | Mean of the effective target cross section area  |
| $\mu_\rho$               | Mean of the target reflection factor   |
| $\mu$                    | Mean delay   |
| $P_{LOS}$                | Direct received power  |
| $P_r$                    | Received reflected signal  |
| $P_t$                    | Transmitted optical power of VLC light unit  |
| $P_{FD}$                 | Probability of false detection   |
| $P_D$                    | Probability of detection   |
| $\psi_c$                 | Concentrator's FOV (semi-angle)  |
| $P_{rM}^{R_{Max}^{FOV}}$ | The received reflected optical power from a target at maximum range for a monostatic LIDAL |
| $P_{rB}^{R_{Max}^{FOV}}$ | The received reflected optical power from a target at maximum range for a bistatic LIDAL   |
| $q$                      | Electronic charge  |
| $R_{Max}^{FOV}$          | Maximum range of LiDAL receiver  |
| $R_{esp}$                | Photodetector responsivity   |
| $\rho$                   | Target reflection coefficient  |
| $\sigma_{shot}$          | Background shot noise component  |

|                    |   |
|--------------------|---|
| $\sigma_{thermal}$ | Preamplifier shot noise component                             |
| $\sigma_{\rho}$    | Standard deviation of the target reflection factor            |
| $\sigma_{A_e}$     | Standard deviation of the effective target cross section area |
| $t_{trip}$         | Round trip time   |
| $\tau$             | Pulse width of LiDAL transmitted signal                       |
| $T_c(\delta)$      | Transmission factor of concentrator                           |
| $x(t)$             | Transmitted instantaneous optical power                       |

# Chapter 1

## Introduction

Visible Light Communication (VLC) systems are used to provide illumination and data communications. VLC uses light emitting diodes (LEDs) or lasers to encode data into light intensity in the visible spectrum [1]-[2]. VLC systems have many advantages such as cost-effective of existing lighting infrastructure, operate using a broad, unlicensed bandwidth, securely (light signals do not penetrate walls) and there is no interference with Radio Frequency (RF) signals [3]-[4]. VLC system applications can support indoor high data rate communication [5], [4] under-water communication [2], [6], LED to LED communication [7], [8] and indoor user localisation [9]-[10]. In [11], a light sensing system using VLC (LiSense) was proposed to track the human gesture and reconstruct the human skeleton. The LiSense system makes use of 324 array of photodetectors placed on the floor to sense the beacon signals sent from the light sources (VLC transmitters) to recover the human shadow pattern created by individual VLC transmitters. A laser radar in conjunction with VLC system was introduced in [12] to provide vehicle to vehicle ranging and VLC communication.

People counting has become an emerging and attractive area in the past decade [13], [14]. Many approaches have been developed for counting in public places such as subways, bus stations and supermarkets [14], [15]. The outcome of these techniques can be used for public security, resources allocation and marketing decisions. Passive infrared (PIR) imaging systems have been employed to detect and count people [15], [16]. Ultra-wideband (UWB) radar has been utilised to effectively detect and track outdoor pedestrians [17]. However, for the indoor environment, the effects of signal scattering and absorption by obstacles significantly impairs the performance of UWB indoor radar [16], [17]. IR Laser detection and ranging (LADAR) has been used to detect people by monitoring the reflected signal patterns of

people legs [18]. Counting systems based on computer vision and digital image processing are becoming meaningful and useful. Video cameras with image processing algorithms have been widely used to count people indoor and count pedestrians outdoor [16], [19], [20].

In this thesis, we present the first indoor light-based detection and localisation system that builds on concepts from radio detection and ranging (radar) making use of the expected growth in the use and adoption of visible light communication (VLC), which can provide the infrastructure for our LiDAL system. Our LiDAL system broadens the VLC system applications and enables active detection, counting and localisation of people, in addition to being fully compatible with existing VLC systems. The LiDAL system can be used for people detection, counting and localisation in an indoor setting. The LiDAL system focuses on human sensing to provide people with spatio-temporal indoor localisation information. LiDAL carries out presence detection, counting, localisation. In order to detect human (targets), LiDAL uses the visible light spectrum to send a pulse through a VLC transmitter and analyses the reflected signal collected by a photodetector receiver. Although we examine the use of the visible spectrum here, LiDAL can be used in the infrared spectrum and other parts of the light spectrum. It is worth mentioning that, our LiDAL system does not support target (human) tracking and identification as the reflected light signals from multiple target are similar in nature.

In addition, a low-complexity high-speed VLC system employing transmitter mapping technique and the adaptive receiver has been proposed and published to validate our modelling of the indoor optical wireless channel which is used for the light signal propagation and channel modelling of the LiDAL system.

## **1.1 Research Motivation and Objectives**

We introduced for the first time indoor light-based detection, counting and localisation of people based on the use of radar-like reflections. This can significantly expand the utility of indoor VLC systems. The key concept behind

our LiDAL system is the use of the (visible) light reflected from targets (people) where the light reflectivity is a function of the material type and colour of the target's surface. The reflected light signal is captured by a photodetector which monitors the change in the light intensity in the time domain. LiDAL can be a system embedded in the VLC system to provide additional functionality to detect, count and localise people. In addition, LiDAL reduces the complexity and cost associated with the acquisition and digital processing of images to detect the presence of people. It should be noted however that acquiring images of people poses in many cases privacy concerns, whereas our LiDAL system uses light reflections from people and therefore no images of people are acquired, stored or transmitted.

The LiDAL system can be deemed as the first step to employ an indoor optical radar for people detection and localisation. It uses the visible light spectrum of VLC systems and can potentially use other parts of the light spectrum. It is worth noting that the use of the infrared spectrum for example can eliminate issues with light dimming and switching off light sources. The concept of LiDAL has the benefits of active radio waves radar systems while avoiding, as mentioned, the issues associated with UWB (and other radio) radar signal propagation indoor. It also makes use of the existing lighting/illumination systems and potentially the existing VLC systems infrastructure.

There are however several challenges that face the development of LiDAL systems, and these challenges include:

- Ambiguity in target detection and localisation is the main challenge for the LiDAL system used in an indoor environment.
- Due to the fact that (visible) light is reflected from multiple objects, the major critical issue in LiDAL is how to distinguish people (targets) from other background objects (i.e., furniture).

The primary objectives of this work were to:

1. Design different LiDAL configurations to optimise the target detection in LiDAL systems.
2. Investigate the major attributes that influence the fluctuation of the received reflected optical signal from a target in LiDAL system.
3. Investigate the techniques needed for signal detection and estimation in order to design optimum receivers for LiDAL systems.
4. Propose and evaluate new techniques for LiDAL systems to distinguish targets (humans) from other background obstacles (furniture) in a realistic environment.
5. Investigate the benefits of using single photodetector receivers and imaging detection receivers in conjunction with single and/or multiple transmitters for target localisation accuracy in LiDAL systems.

## **1.2 Research Contributions**

The thesis has:

- 1- Proposed for the first time an indoor (visible) light pulsed radar-like system which utilises the VLC system transmitters to detect, count and localise multiple targets.
- 2- Designed, investigated and evaluated the use of monostatic and bistatic LiDAL systems in terms of maximum target range, optimum targets detection resolution and LiDAL channel propagation.
- 3- Developed a model for the human body and its reflections and the impact of the colour and texture of the clothing used, which are all important attributes of the target of interest.
- 4- Designed and optimised receivers and algorithms for the LiDAL systems to optimise target detection. An exhaustive search receiver and a sub-optimum receiver were proposed and evaluated.
- 5- Introduced and investigated a number of detection and localisation methods for our LiDAL system including cross correlation, a background subtraction method and background estimation method. These methods are considered to distinguish a mobile target from the

ambient reflections due to background obstacles (furniture) in a realistic indoor environment.

- 6- Investigated a range of different mobility models for humans and used these as an important input to our LiDAL human detection and localisation system.
- 7- Designed and evaluated an efficient multiple input multiple output (MIMO) LiDAL system with wide field of view (FOV) single photodetector receiver, and also designed a multiple input single output (MISO) LiDAL system with an imaging receiver to eliminate the ambiguity in target detection and localisation. In addition investigated MIMO-LiDAL and MISO-Imaging-LiDAL systems which are compatible with VLC and light fidelity (Li-Fi) systems.

### 1.3 Publications

The original contributions are supported by the following publications:

#### Journals

2. Aubida A. Al-Hameed, Safwan Hafeedh Younus, Ahmed Taha Hussein, Mohammed T. Alresheedi and Jaafar M. H. Elmirghani, "LiDAL: Light Detection and Localisation," *IEEE Access*, submitted March 2019.

The work in Chapter 3, 4, 5, 6, 7 of this thesis has appeared in publication (1).

### 1.4 Thesis Outline

**Chapter 2** provides an overview of indoor visible light communication systems. It also describes the structure of the VLC system, including transmitters and receivers. In addition, the chapter presents the modelling of the optical wireless channel which is used in our LiDAL system. Furthermore, the chapter provides a general review of radio and light detection and ranging systems. The advantages of human sensing techniques and systems are outlined in the chapter as well.

**Chapter 3** presents for the first time the concepts of a light detection and localisation (LiDAL) system. It also provides an analysis of LiDAL system configurations, maximum detection range, resolution and the fluctuation of the received signal. In addition, the chapter describes the modelling of a realistic environment and presents a model for reflections from the human body. This mode is used in our LiDAL system.

**Chapter 4** introduces an optimum receiver design for the LiDAL system. It also presents an analysis to determine the optimum detection threshold and the receiver operating characteristics for the LiDAL system. Furthermore, the chapter describes the structures of the optimum and sub-optimum receivers to optimise the targets detection in the LiDAL systems.

**Chapter 5** introduces approaches for target (human) distinguishing from background obstacles in an indoor realistic environment. The chapter presents an analysis of the three main approaches we introduced for target distinguishing including a background subtraction method (BSM), a cross-correlation method (CCM) and background estimation method (BEM). In addition, the chapter describes human indoor mobility models considering directed random walks with obstacle avoidance; and pathways for pedestrian and nomadic indoor human motion.

**Chapter 6** presents a new multiple-input multiple-output (MIMO) LiDAL system for targets counting and localisation. The MIMO LiDAL system employs multiple transmitters in conjunction with multiple wide field of view optical receivers. The results of the chapter show that MIMO LiDAL has an accuracy of 84% to 96% when detecting and counting up to 15 pedestrian targets located in a realistic indoor environment. It also shows that our MIMO LiDAL system has a maximum target localisation error of 0.5m, which is acceptable given the typical minimum human-to-human separation indoor.

**Chapter 7** introduces a new multiple-input single-output (MISO) imaging LiDAL system for targets counting and localisation. The MISO Imaging LiDAL system uses multiple transmitters in conjunction with an imaging detection receiver consisting of 128 pixels. The results show that the MISO Imaging LiDAL system has an accuracy of 88% to 98% when detecting and counting



up to 15 pedestrian targets located in a realistic indoor environment. Furthermore, the results show that our MISO-IMG-MIMO system has a maximum target localisation error of 0.19m.

**Chapter 8** summarises the contributions of the work and outlines possible directions of future work.

# Chapter 2

## Review of Optical Wireless, RADAR and Human Sensing Systems

### 2.1 Introduction

Visible light communication (VLC) is a part of optical wireless communication (OWC) that uses light as a carrier to modulate the information signal in the visible spectrum (380nm to 780nm) [21], [24]-[22]. VLC systems are becoming more popular everyday due to their inherent advantages over radio frequency (RF) systems. The advantages include a large unregulated spectrum, low complexity of transceiver unit, freedom from fading, confidentiality and immunity against interference from electrical devices [23], [5], [3], [4].

People detection and counting in an indoor environment (such as offices, exhibition halls, shopping malls etc.) can provide useful information for different applications [24]-[25]. For example, human presence detection is valuable for security purposes. Also knowing the number of people in a supermarket may have an important practical use in terms of marketing, management, optimisation and maintaining high quality of service. The RADAR concept (send a signal then listen to the reflection) can be used to obtain human range information [26]-[27].

Following this introduction, this chapter is organised as follows. The visible light communication system is discussed in Section 2.2. The principle of radio frequency detection and ranging (RADAR) and the light detection and ranging (LiDAR) system are reviewed in Section 2.3. Next, human sensing, detection and counting are presented in Section 2.4. A summary is given in Section 2.5

## 2.2 Visible Light Communication System

The concept of VLC systems revolves around the use of light emitting diodes (LEDs) for both lighting and communications. The main drives for this new technology include the recent development of solid state lighting, longer lifetime of high brightness LEDs compared to other artificial light sources, high data rate, low power consumption and green communications [2], [28]. The dual functionality of a VLC system, i.e., illumination and communication, makes it a very attractive technology for many indoor and outdoor applications, such as car-to-car communication via LEDs, lighting infrastructures in buildings for high speed data communication and high data rate communication in airplane cabins [29], [30]. White-LEDs can be classified into two types according to the technology used to emit the white colour. The first type is a combination of a blue LED with a yellow phosphor layer. The blue colour excites the phosphor and gives a white illumination. Blue LEDs are low cost, but have a small modulation bandwidth, and only one stream of data can be modulated over the blue wavelength [31], [32]. The second type is a multi-coloured technique using an LED with three colours (red, green, blue: RGB) embedded in a one chip, and the combination of the trichromatic signals generates white illumination [31], [33]. However, the bottleneck of White LEDs is the limited electrical bandwidth and non-linearity issue [33], [34]. There are two major limitations in VLC systems. The first is the low modulation bandwidth of the LEDs, which limits the achievable data rates. The second is the spread of the received pulse due to the reflections from walls and ceiling in an indoor environment which causes multipath dispersion that leads to inter symbol interference (ISI). Many techniques in the transmitter and receiver side have been proposed in order to improve the modulation bandwidth of LED and to mitigate the effect of ISI. A blue filter has been used to increase the modulation bandwidth of LED up to 20 MHz [35]. A transmitter LED equalization method with a resonant driving circuit was proposed with bandwidth of 25 MHz [32]. A simple pre-equalisation circuit in the transmitter has been shown to achieve a bandwidth of 45 MHz [34]. On other hand, post equalisation at the receiver improved the bandwidth up to 65 MHz [35]. However, recently a high modulation bandwidth VLC transmitter architecture

involving laser diodes (RGB-LD) with combiner and diffuser has been proposed in [36]. Orthogonal frequency division multiplexing (OFDM), has been used in VLC systems in order to minimise the ISI. A DC-biased Optical DCO-OFDM was proposed with a data rate of 513 Mbps [37]. An adaptive receiver using rake reception with equalisation has been proposed in [38]. It achieved 200 Mbps with a bit error rate (BER) of  $10^{-5}$ . An adaptive equaliser with DFE was developed to combat ISI, which showed that a simple equaliser with multiple taps can improve the data rates up to 1 Gbps [39]. A RGB-LED VLC transmitter with an adaptive DCO-OFDM was introduced with data rate up to a 3.4 Gbps [40]. An indoor VLC system with very complex RGB-LD transceiver was proposed that can achieve 4 Gbps data rates [41]. A high data rate, up to 6.5 Gbps, was achieved using a LD with OFDM and an adaptive loading method [42]. A number of scenarios have been used with wavelength division multiplexing (WDM) and parallel streams to examine the abilities of LDs in terms of potentially achieving data rates of 100 Gbps [43].

Costly and highly complex receivers, such as an angle diversity receiver (ADR) and an imaging receiver, have been proposed to combat ISI and improve the performance of the OW system to provide multi-gigabit data rates [44], [45]. The ADR consists of multiple photodetectors elements with a narrow field of view (FOV) that are aimed in different directions, each light signal received by the elements is amplified independently, and then they can be combined to increase the signal to noise ratio (SNR) [46]. The imaging receiver includes an array of pixels covered by a concentrator. Each pixel is a photo diode (PD) with small FOV to limit the range of optical rays [47], [48]. A delay adaptation technique with imaging receiver has been demonstrated to provide high data rates [36]. VLC systems have the potential to play a major part in next generation communication networks and future smart homes. There is significant on-going work to realise high data rate VLC systems [49]. However, an increase in the system complexity and receiver cost is incurred.

A block diagram of an indoor VLC system is shown in Figure 2.1. The VLC system consists of (i) a transmitter that uses white LEDs or visible LD, (ii) a VLC channel (VLC links design) and (iii) a receiver that employs a photodetector (PD). In VLC system, on the transmitter (Tx) side the intensity

light of LED is used to convey the data after DSP processing (modulation, coding) through an optical wireless channel where the light signal suffers reflections. At the receiver (Rx) a lens is used as light collector and as an optical amplifier to focus the light to a Photodetector (PD) which converts the light into a current. Also, an optical filter is used to reduce the noise from ambient lights or to filter a specific colour of light in some cases. The Trans-impedance Amplifier (TIA) amplifies signal before DSP processing at the receiver (demodulation, decoding).

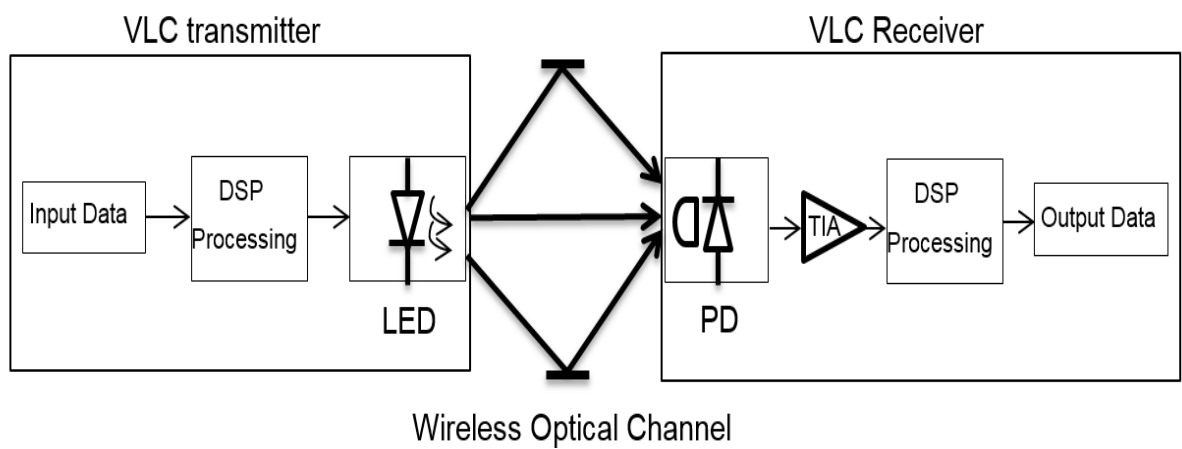


Figure 2.1 Block diagram of VLC system.

### **2.2.1 VLC Transmitter**

The main function of the VLC transmitter is to transform an electrical signal into an optical signal that propagates into the free space medium. LEDs and LDs are used for VLC communication [50]. Commercial white LEDs are available at low cost and they can be made eye-safe. The LEDs have large surface area emitting light over a relatively wide spectral range [50]. White LEDs produce light into semi-angles in the range of  $12^\circ$  to  $70^\circ$  [51]. On the other hand, the LEDs have some drawbacks, including; (i) Low modulation bandwidth (typically tens of MHz) (ii) Low electro-optic power conversion efficiency and (iii) Non linearity [52]. White LDs may be considered in VLC systems due to their various advantages, which are (i) high modulation bandwidth (ii) high electro-optic power conversion efficiency and (iii) linear electrical to optical signal conversion characteristics [48]. However, LD are more expensive than LEDs as well as requiring a more complex drive circuit.

### **2.2.2 VLC Receiver**

A VLC receiver transforms the received optical signal into an electrical current signal. Typically, it includes a photodetector, concentrator, optical filter and a preamplifier circuit (trans-impedance amplifier TIA). The concentrator increases the amount of signal power at the receiver [53]-[54]. The optical filter reduces the amount of ambient light collected by eliminating the collected light outside the signal optical spectral band [55]-[56]. A key component in a VLC receiver is the photodetector where the optical signal (analogue or digital) is converted directly into an electric current. The next process is the amplification of the electrical current. Therefore, the photodetector is followed by a preamplifier. The main components of a VLC receiver are discussed next.

#### **2.2.2.1 Concentrators**

Increasing the active area of the photodiode leads to an improvement in the received optical power. This would increase the capacitance, thus reducing the receiver bandwidth [57]-[58]. An optical concentrator can be used to increase the collected signal power by increasing the effective collecting area [53].

There are two types of concentrators: imaging and non-imaging. Imaging concentrators can be found in long range systems such as FSO. In general, most indoor OW links, typically consider the use of non-imaging concentrators. The effective signal-collection area can be written as [48]:

$$A_{eff}(\delta) = \begin{cases} A \cos(\delta), & 0 \leq \delta \leq \pi/2 \\ 0 & \delta > \pi/2 \end{cases} \quad (2.1)$$

where  $\delta$  is the angle of incidence with respect to the receiver normal and  $A$  is the physical area of the detector. An idealised non-imaging concentrator has a relationship between the FOV and gain. The maximum achievable concentrator gain is as follows [48], [59], [60]:

$$g(\delta) = \begin{cases} \frac{N^2}{\sin^2 \psi_c}, & 0 \leq \delta \leq \psi_c \\ 0 & \delta > \psi_c \end{cases} \quad (2.2)$$

where  $N$  is the internal refractive index and  $\psi_c$  is the semi-angle FOV of the concentrator (usually  $\psi_c \leq 90^\circ$ ). Equation (2.2) shows an inverse relation between the gain and FOV of the receiver. If the receiver's FOV is reduced, the gain is increased.

In this section, two types of optical concentrators (imaging and non-imaging) are reviewed. A hemispherical lens and compound parabolic concentrator (CPC). The hemispherical lens has an acceptance semi-angle of  $90^\circ$ , therefore  $g(\delta) = N^2$ . A hemisphere-based receiver has an effective area of:

$$A_{eff}(\delta) = AN^2 \cos(\delta) \quad (2.3)$$

Figure 2.2 shows a non-directional hemispherical lens that employs a planar filter.

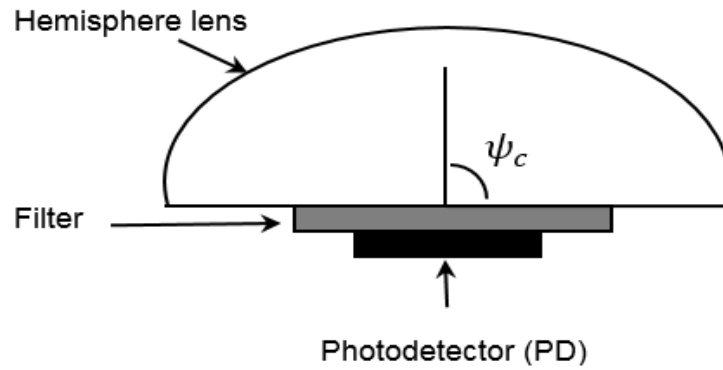


Figure 2.2: Non-directional hemispherical lens that employs a planar filter [53].

A CPC can achieve a higher gain than a hemispherical lens, however, this is at the cost of a narrow FOV. This makes a CPC more suitable for LOS OW links. A multiple elements of CPC can be employed with an ADR to reduce the multipath dispersion [61], [62]. A CPC can be coupled with an optical filter on the front surface, as shown in Figure 2.3.

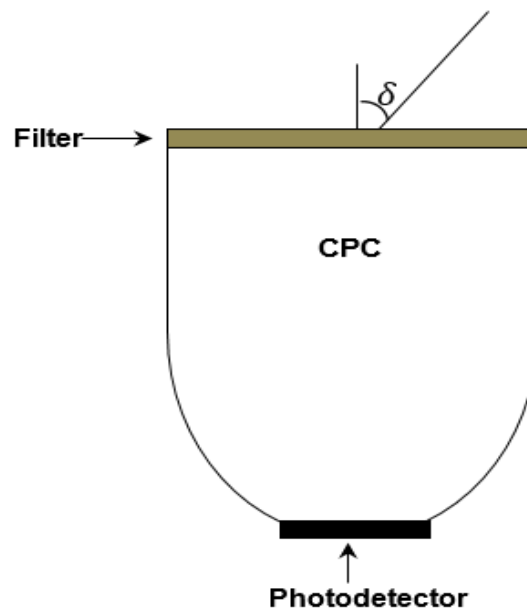


Figure 2.3: Compound parabolic concentrator [53].



### 2.2.2.2 Optical filters

OW systems including VLC are exposed to ambient light and sunlight. Thus, to minimise the effect of undesirable noise in the received signal, an optical filter can be implemented before detection by the photodetector [63]. Figure 2.4 illustrates the relative spectral power densities of the three ambient light sources (Sun light, Incandescent and florescent). A high pass filter (HPF) and a band pass filter (BPF) are used in OW systems. A HPF passes light at wavelengths higher than the cut off wavelength, and they are typically made of colour glass or plastic [48]. A BPF can be used to reduce the ambient light in optical receivers. A BPF can have very narrow bandwidths (typically 1 nm), and can be fabricated using multiple thin dielectrics with varying indices of refraction and relies upon optical interference in the created Fabry-Perot cavities [64]. The transmission characteristics of such BPFs vary greatly depending on the angle of incidence. Therefore, they should be used with an adequate concentrator to be suitable for diffuse systems, such as a hemispherical concentrator [48]. In VLC system, A blue optical filter at the receiver is employed to filter the slow response yellowish component of the visible light, and this method is considered to be the simplest and most cost effective approach to increase data rates [65]-[66].

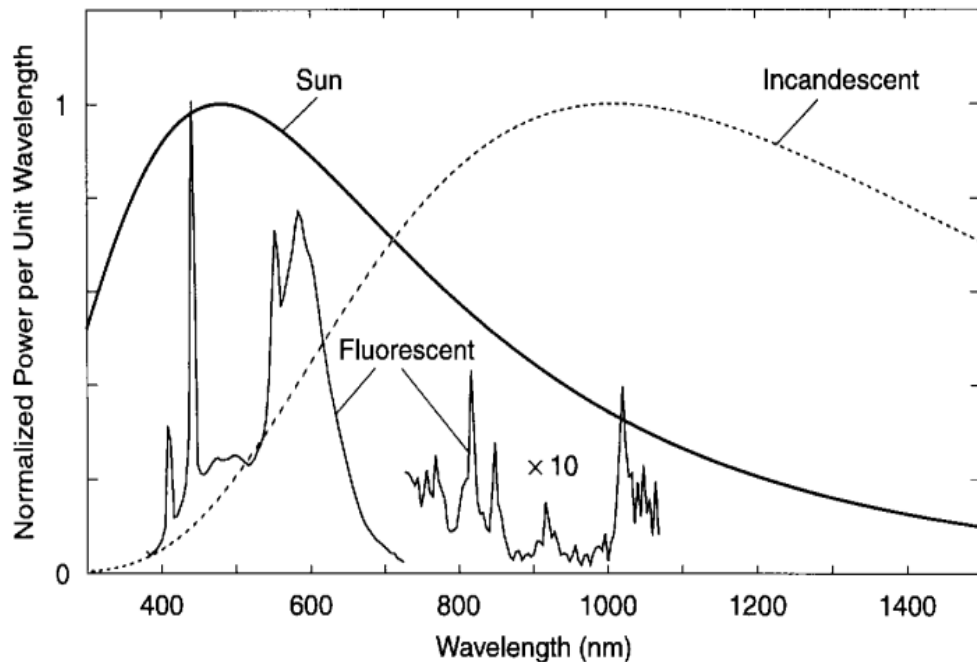


Figure 2.4: Relative spectral power densities of the three common ambient light sources [53].

### 2.2.2.3 Photodetectors

A photodetector is an optoelectronic transducer that generates an electrical signal that is proportional to the incident light. Since, the received light in an OW system is generally weak, the photodetector must therefore meet important performance specifications, such as: (1) high sensitivity at the operating frequency, (2) high conversion efficiency within its operational range of wavelengths, (3) High response speed and (4) high reliability, low cost and small size.

Two photodetector types are commonly used in OW systems: PIN photodiodes and avalanche photodiodes (APDs). PIN photodiodes require less complex biasing than APDs and are cheaper and simpler to manufacture. However, PIN photodiodes are less sensitive than APDs. APDs are usually 10 to 15 dB more sensitive than PINs [48]. APDs provide an inherent current gain through an ionisation process, hence improving the SNR and reducing the effect of front-end noise [67]. APDs are the preferred choice when the ambient induced shot noise is weak and the pre-amplifier noise is the major source of noise. Shot noise due to the ambient light is present in OW systems, and therefore a PIN photodiode is considered to be the better option [68]. A photodiode should have a large bandwidth and a high responsivity (PIN photodiodes are capable of operating at high bit rates [69]. The bandwidth of the photodiode is limited by the transit time of the carriers through the PN junction. Responsivity is a key parameter in photodiodes and is measured at the central optical frequency of operation. Responsivities of silicon photodiodes operating in the 430nm-655nm wavelength bands, are in the range of 0.21 A/W to 0.46 A/W [50].

The responsivity of the photodiode can be expressed as [64]:

$$R_{es} = \frac{\eta q \lambda}{h_p c} \quad (2.4)$$

where  $q$  is the electronic charge,  $\eta$  is the quantum efficiency of the device,  $\lambda$  and  $c$  are the wavelength and the speed of light respectively and  $h_p$  is the Planck constant. The internal quantum efficiency ( $\eta$ ) is the probability of the

incident photon producing an electron-hole pair (typically in range of 0.7 to 0.9).

To collect an adequate optical signal, the photodetector active area must be large, but the capacitance of the photodetector is directly proportional to its area. Therefore, a large photodetector area implies a large capacitance, which results in a restriction in the attainable bandwidth. The large capacitance at the input of the amplifier operates as a low pass filter (LPF), which means that the received high frequency components will be attenuated. Although, a large capacitance acts as a LPF, it does not eliminate the dominant white thermal noise that is observed after the input stage. This noise may negatively affect the SNR at higher signal frequencies. When a white noise process following a LPF is fed back into the input of the filter, its power spectral density becomes quadratic in frequency and is often called  $f^2$  noise [70]. Due to the  $f^2$  noise variance being proportional to the square of the capacitance, an array of photodetectors can be used instead of a single photodetector (hence avoiding the photodetector's high capacitance) to reduce the effect of  $f^2$  noise [71].

The authors in [72] proposed the use of an array of photodetectors instead of a single photo detector to mitigate the effects of the large capacitance and to maximise the collected power at the same time. The photodetector's effective area can be enhanced by using a hemispherical lens, as proposed in [48]. Bootstrapping was proposed by the authors in [73] to minimise the effective capacitance of a large area photodetector.

#### **2.2.2.4 Preamplifiers**

The preamplifiers that are used in the photo-receivers can be categorised into three types: low impedance, high impedance and trans-impedance preamplifiers. The low impedance preamplifier offers a large bandwidth but has high noise and hence low receiver sensitivity. On the other hand, the high impedance preamplifier provides high sensitivity but an equaliser must be used to mitigate the limitations imposed on the frequency response by the front end RC time constant. In addition, due to their high input load resistance they also have a limited dynamic range [68], [74]. In contrast, a trans-impedance preamplifier provides a large dynamic range and avoids the need

for an equaliser. Therefore, it is suitable in most OW link applications. However, it has lower sensitivity (high noise level) compared to a high impedance amplifier. Sensitivity can be improved when a field-effect transistor (FET) is used as a front-end device instead of a bipolar junction transistor (BJT). However, in terms of power consumption, a BJT can provide better performance [68], [44].

### **2.2.3 Channel Modelling of Optical Wireless System**

To examine the performance of a LiDAL system design in terms of signal integrity, light ray tracing in optical wireless channel is fundamental. The characterisation of LiDAL channel is essential to address and evaluate the performance of the system and design issues. The use and the expected growth in the implementation and adoption of visible light communication (VLC), can provide an infrastructure for our LiDAL system. Hence, we consider modelling the wireless optical channel in an indoor environment. This section describes the tools that were used to model the optical wireless channel, through the use of simulation based on geometrical modelling of indoor environment with an iterative method for multiple reflections calculation.

We compared the results of our simulator in the case of the traditional VLC system with the theoretical results detailed in [33], [75]. In addition, the author has verified his simulator against the results of the basic optical wireless systems in the literature such as a conventional diffuse system (CDS) and line strip multi-beam system (LSMS) [76], [77]. A very good match was observed between the results of the author's simulator and other researchers' work (see Appendix A). Furthermore, the author's proposed and published a low-complexity high-speed VLC system employing transmitter mapping technique and adaptive receiver [78], [79]. This gives confidence in the capability of the author's simulator to simulate indoor light propagation and LiDAL channel modelling. The simulations and calculations reported in this thesis were carried out using MATLAB.

### 2.2.3.1 Indoor Optical Wireless Channel

In optical wireless links, IM/DD is the preferred choice [38], [48] due to its low complexity and cost. At the transmitter side, IM can be simply used to modulate the desired signal into the instantaneous power of the optical carrier by varying the intensity of the optical source. At the receiver side, DD is used to generate the electrical current  $I(t)$  so that it is proportional to the instantaneous received optical power. The typical detector size is larger than the wavelengths of the received optical signal, and hence allows spatial diversity and prevents fading [48]. An indoor OW channel that uses IM/DD can be fully characterised by the impulse response ( $h(t)$ ) of the channel as given in [77]:

$$I(t, Az, El) = \sum_{m=1}^{M_t} R x(t) \otimes h_m(t, Az, El) + \sum_{m=1}^{M_t} R n_m(t, Az, El) \quad (2.5)$$

where  $I(t, Az, El)$  is the received instantaneous photocurrent in the photo-detector with photo-detector responsivity ( $R$ ) using  $M$  elements to receive a transmitted signal  $x(t)$  through channel  $h$  in the presence of AWGN ( $n_m$ ).  $Az$  and  $El$  are the direction of arrival in the azimuth and elevation angles, respectively,  $t$  is the absolute time and  $\otimes$  denotes convolution. It should be noted that  $x(t)$  represents power and not amplitude. This implies that the visible light signal is non-negative. In addition, the total average transmitted optical power in (2.5) is provided by the mean value of  $x(t)$  and not an integral of  $|x(t)|^2$  as is the case with RF systems.

The visible light signal emitted by the LED or LDs reaches the receiver through various paths of different lengths. These propagation paths change with the receiver movement, and/or the movement of the surrounding objects. However, the paths are fixed for a given fixed configuration. The channel impulse response can be represented approximately as the sum of scaled and delayed Dirac delta functions [48]. In this thesis a simulation package based on a ray tracing algorithm was developed to compute the impulse response on the entire communication plane. The channel impulse response can be given as:

$$h(t) = \sum_{k=0}^{\infty} h^{(k)}(t) \quad (2.6)$$

where  $h^{(k)}$  is the impulse response due to the LOS and reflection components.

### 2.2.3.2 Transmitted Optical Power

The indoor channel propagation characteristics depend on the relative positions of the transmitter, receiver and reflectors, as well as their patterns (i.e., FOV for transmitter and receiver). These characteristics are also affected by the movement of the surrounding objects and people (targets), but these changes are slow compared with the transmission rate. Hence, the channel can be considered stationary for a given fixed configuration.

Multipath propagation causes the transmitted pulses to spread and may lead to ISI. Multipath dispersion increases when the dimensions of the room increase, and this is due to the increase in the difference in paths lengths. Gfeller and Bapst studied the reflection coefficients for a number of materials normally used in indoor settings [80]. They showed that the reflection coefficients ranged from 0.4 to 0.9. They also found that the power reflected by elements either on the walls or the ceiling was well approximated by an ideal Lambertian pattern. Thus, in their work and in this thesis the reflection elements on the ceiling and walls are treated as a small transmitter that transmits an attenuated version of the received signals from its centre in a Lambertian pattern. The power radiated into a solid-angle element  $d\Omega$  can be modelled as [81]:

$$dP = \frac{n+1}{2\pi} \times P_s \times \cos^n(\alpha) \times d\Omega \quad (2.7)$$

where the coefficient  $(n + 1)/2\pi$  ensures that integrating  $dP$  over the surface of a hemisphere results in the total average transmitted optical power  $P_s$  being radiated by the light source:

$$P_s = \int_{Hemisphere} dP \quad (2.8)$$

$\alpha$  is the angle of incidence with respect to the transmitter's surface normal and the parameter  $n$  represents the mode number that determines the shape of the reflected beam, which is related to the half-power semi-angle ( $hps$ ) and can be defined as [48]:

$$n = \frac{-\ln(2)}{\ln(\cos(hps))} \quad (2.9)$$

It is suitable to use  $n = 1$  as all surfaces are presumed to be rough, and this is in agreement with experimental measurements in [80].

### 2.2.3.3 Calculations of received optical power

More than one path may be present between the transmitter and the receiver as a result of multipath propagation. Temporal dispersion in the optical signal occurs as a result of multiple paths. A ray tracing algorithm can be used to compute the received optical power. The reflected optical rays from different reflectors are traced for all potential paths to the other reflectors or the receiver. Therefore, to implement ray tracing, the reflecting surfaces were divided into a number of equal-sized (square shaped) reflection elements [82]. The optical rays reflected from these elements were in the shape of a Lambertian pattern ( $n = 1$ ). The small size of these elements enhances the accuracy of the impulse response. However, the computation time increases dramatically when the surface element size is decreased.

The total received optical power ( $P_r$ ) at the receiver, considering the LOS component ( $P_{LOS}$ ), first order reflections ( $P_{FST}$ ) and second order reflections ( $P_{SEC}$ ) can be expressed as [83]:

$$P_r = \sum_{i=1}^S P_{LOS} + \sum_{i=1}^M P_{FST} + \sum_{i=1}^F P_{SEC} \quad (2.10)$$

where  $S$  is the number of transmitter units,  $M$  is the number of reflecting elements in the first order reflection and  $F$  is the number of reflecting elements in the second order reflection.

Figure 2.5 shows the ray tracing setup for LOS as well as first and second order reflections. The impulse response of the channel can be computed by tracing all potential light rays between the transmitter and the receiver [94].

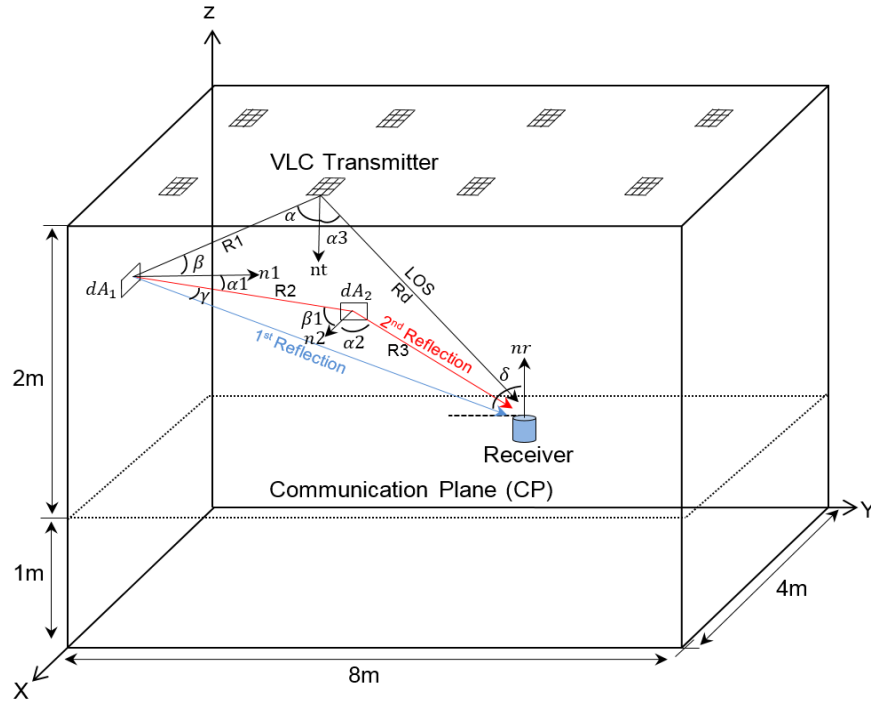


Figure 2.5: Ray tracing setup for LOS, first and second order reflections [82], [83].

#### 2.2.3.4 Line-of-Sight (LOS) analysis

A LOS component is available when a direct path connects the transmitter and the receiver. For example, in the VLC system, when the transmitter is placed on the ceiling and has an elevation angle of  $-90^\circ$  (facing downwards) and the receiver is on the communication plane with an elevation angle of  $90^\circ$  (facing upwards), as shown in Figure 2.6, the  $P_{LOS}$  component can be written as [82], [83]:

$$P_{LOS} = \begin{cases} \frac{n+1}{2\pi R_d^2} \times P_s \times \cos^n(\alpha) \times \cos(\delta) \times A & 0 \leq \delta \leq \psi_c \\ 0 & \delta > \psi_c \end{cases} \quad (2.11)$$

where  $P_s$  represents the total average transmitted optical power radiated by the light source (LED or LD).  $A$  is the detector area.  $\delta$  is the angle between the normal of the photodetector and the incident ray.  $\alpha$  is the angle between the normal of the transmitter and the irradiance ray.  $R_d$  is the distance between the transmitter and the receiver. If the received angle ( $\delta$ ) is larger than the acceptance semi-angle ( $\psi_c$ ), then the direct LOS received power approaches zero. Since, the signal must lie within the FOV of the receiver to be received,



changing the receiver's FOV can be used to minimise noise (background light) or unwanted reflections.

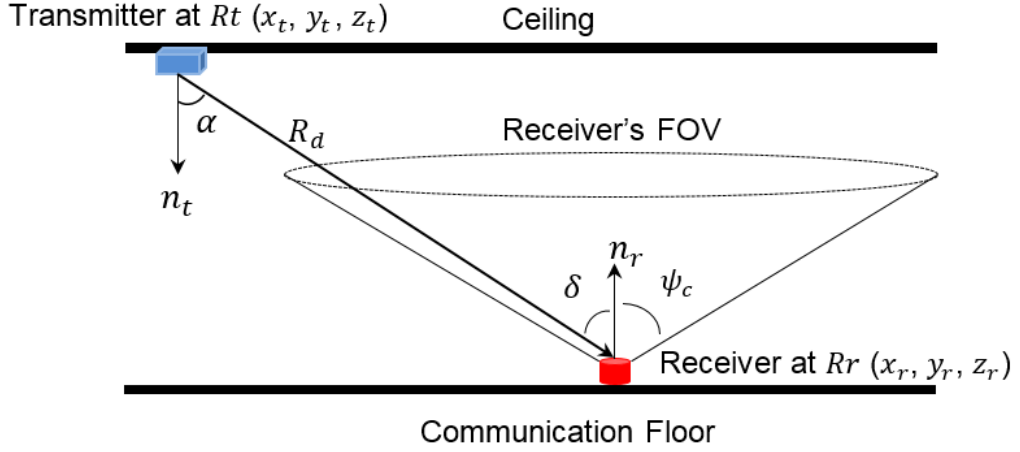


Figure 2.6: Ray tracing for LOS [83].

The transmitting and receiving angles  $(\alpha, \delta)$  are calculated as follows [82], [94]:

$$\cos(\alpha) = \frac{\hat{n}_t \cdot (R_r - R_t)}{R_d} \quad \text{and} \quad \cos(\delta) = \frac{\hat{n}_r \cdot (R_t - R_r)}{R_d} \quad (2.12)$$

where  $\hat{n}_t$  is the normal of the transmitter at location  $R_t$  and  $\hat{n}_r$  is the normal of the receiver at location  $R_r$ . It should be noted that both angles in (2.12) are equal if the transmitter and the receiver are placed in parallel planes, like the case in Figure 2.6. However, if the  $\hat{n}_t$  is perpendicular to the  $\hat{n}_r$ , or vice versa, then the transmitting and receiving angles are different. Both situations were considered when computing these angles. The direct distance between the transmitter and the receiver,  $R_d$ , can be calculated as [82], [94]:

$$R_d = \|R_r - R_t\| = \sqrt{(x_r - x_t)^2 + (y_r - y_t)^2 + (z_r - z_t)^2} \quad (2.13)$$

where  $x_t, y_t, z_t$  and  $x_r, y_r, z_r$  are the transmitter and the receiver coordinates respectively.

### 2.2.3.5 First order reflection analysis

Figure 2.7 shows a ray incident from the transmitter on a square reflecting element and then from the reflective element to the receiver. Plaster walls can be considered as Lambertian reflectors with  $ne = 1$  [80]. By using the Lambertian model, the received optical power of the first order reflections  $P_{FST}$  can be computed as [83]:

$$P_{FST} = \begin{cases} \frac{(n+1)(ne+1)}{4\pi^2 R_1^2 R_2^2} \times P_s \times \rho_1 \times dA1 \times \cos^n(\alpha) \times \cos(\beta) \times \cos^m(\gamma) \times \cos(\delta) \times A & 0 \leq \delta \leq \psi_c \\ 0 & \delta > \psi_c \end{cases} \quad (2.14)$$

where  $R_1$  is the distance between the transmitter and the reflective element,  $R_2$  is the distance between the reflective element and the receiver and  $\alpha$  is the angle between the normal of the transmitter and the irradiance ray.

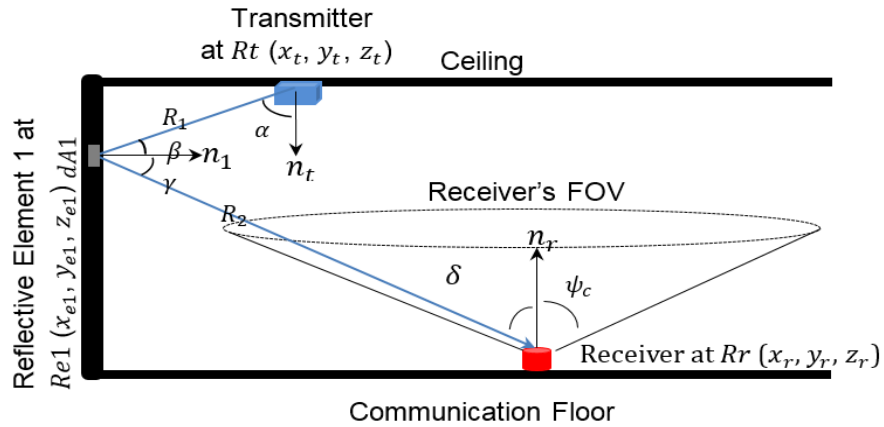


Figure 2.7: Ray tracing for first order reflections [83].

In Figure 2.7,  $\beta$  is the angle between the irradiance ray from the transmitter and the reflective element's normal,  $\gamma$  is the angle between the reflective element's normal and the reflected ray toward the receiver and  $\delta$  is the angle between the normal of the receiver and the incident ray,  $dA1$  is the area of the reflective element and  $\rho_1$  is the reflection coefficient of the reflective surface.

The reflective elements are treated as secondary small transmitters where the retransmitted power is determined by the received optical power from the transmitter and its reflection coefficient  $\rho_1$ . The four angles in Equation 3.10 can be computed as [82], [83]:

$$\begin{cases} \cos(\alpha) = \frac{\hat{n}_t \cdot (Re1 - Rt)}{R_1} & \cos(\beta) = \frac{\hat{n}_1 \cdot (Rt - Re1)}{R_1} \\ \cos(\gamma) = \frac{\hat{n}_1 \cdot (Rr - Re1)}{R_2} & \cos(\delta) = \frac{\hat{n}_r \cdot (Re1 - Rr)}{R_2} \end{cases} \quad (2.15)$$

where  $\hat{n}_1$  is the normal of the reflective element 1 at location  $Re1$ .

### 2.2.3.6 Second order reflection analysis

Figure 2.7 shows the tracing of the reflected rays for the second order reflection. The second order reflection,  $P_{SEC}$ , can be calculated as [93], [83]:

$$P_{SEC} = \begin{cases} \frac{(n+1)(ne+1)^2}{8\pi^3 R_1^2 R_2^2 R_3^2} \times P_s \times \rho_1 \times \rho_2 \times dA1 \times dA2 \times \cos^n(\alpha) \times \cos(\beta) \times \\ \cos^m(\alpha1) \times \cos(\beta1) \times \cos^m(\alpha2) \times \cos(\delta) \times A & 0 \leq \delta \leq \psi_c \\ 0 & \delta > \psi_c \end{cases} \quad (2.16)$$

where  $R_1$  is the distance between the transmitter and the reflective element 1.  $R_2$  is the distance between the reflective element 1 and the reflective element 2.  $R_3$  is the distance between reflective element 2 and the receiver,  $dA1$  and  $dA2$  are the areas of the reflective elements 1 and 2, respectively,  $\alpha$  is the angle between the normal of the transmitter and the irradiance ray,  $\beta$  is the angle between the irradiance ray from the transmitter and the normal of reflective element 1 and  $\gamma$  is the angle between the normal of reflective element 1 and the reflected ray towards reflective element 2;  $\beta1$  is the angle between the incident light from the reflective element 1 and the normal of the reflective element 2;  $\alpha2$  is the angle between the normal of the reflective element 2 and the second reflected ray and  $\delta$  is the angle between the second reflected ray and the normal of the receiver;  $\rho_1$  and  $\rho_2$  are the reflection coefficients of the first and second reflective elements, respectively.

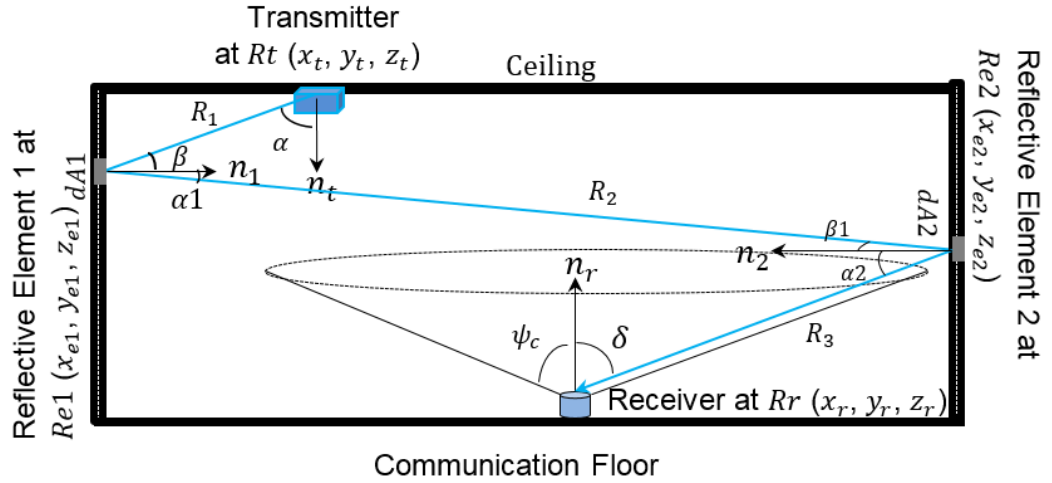


Figure 2.7: Ray tracing for second order reflections [83].

In the second order reflection, six angles are required and can be computed in a similar way to the direct power and first order reflection by tracing the ray from the transmitter to the receiver as [82], [94]:

$$\left\{ \begin{array}{ll} \cos(\alpha) = \frac{\hat{n}_t \cdot (R_{e1} - R_t)}{R_1} & \cos(\beta) = \frac{\hat{n}_1 \cdot (R_t - R_{e1})}{R_1} \\ \cos(\alpha_1) = \frac{\hat{n}_1 \cdot (R_{e2} - R_{e1})}{R_2} & \cos(\beta_1) = \frac{\hat{n}_2 \cdot (R_{e1} - R_{e2})}{R_2} \\ \cos(\alpha_2) = \frac{\hat{n}_2 \cdot (R_r - R_{e2})}{R_3} & \cos(\delta) = \frac{\hat{n}_r \cdot (R_{e2} - R_r)}{R_3} \end{array} \right. \quad (2.17)$$

where  $\hat{n}_2$  is the normal of the reflecting element 2 at location  $Re2$ .

### 2.2.3.7 Impulse Response

In optical wireless, the impulse response is continuous, but the simulator subdivides the reflecting surfaces into discrete elements (reflecting elements on the walls, ceiling and floor). Thus, the received optical power is recorded at the receiver within time intervals (time bins). Each time bin duration should be roughly of a duration comparable to the time light takes to travel between neighbouring elements [81]. A good choice of time bin width is provided by [81], [84]:

$$time\ bin = \sqrt{dA}/c \quad (2.18)$$

where  $c$  is the speed of light and  $dA$  is the reflection element area. Rays arriving within similar time intervals are assembled and stored for a particular

receiver-transmitter location on the CP. An identical histogram of the practical impulse response is achieved as  $dA$  approaches zero. It should be noted that the reflective element size  $dA$  has to be selected to keep the computation requirements within a reasonable time (the computation time increases dramatically when the surface element size is decreased) [44], [85]-[86].

### 2.2.3.8 Delay Spread

The root mean square (rms) delay spread is a good measure of the signal pulse spread due to the diffuse transmission of the indoor VLC channel, which can cause ISI. The delay spread of an impulse response is given by [51], [99]:

$$D = \sqrt{\frac{\sum_{i=1}^I (t_i - \mu)^2 P_{ri}^2}{\sum P_{ri}^2}} \quad (2.19)$$

where  $t_i$  is the delay time associated with optical power received  $P_{ri}$ ,  $I$  is the number of collected rays at the receiver, and  $\mu$  is the mean delay given by [46], [87], [88]:

$$\mu = \frac{\sum_{i=1}^I t_i p_{ri}^2}{\sum_{i=1}^I p_{ri}^2} \quad (2.20)$$

## 2.3 Radio Detection And Ranging (RADAR)

RADAR refers to 'RADio Detection And Ranging' where the electromagnetic spectrum is used to detect and range objects of interest (targets) [89]-[90]. RADAR operates by sending a radio frequency signal and listening to the echo signal returned from the target [90]-[91]. The received echo signal has different amplitude, frequency and time delay as compared the transmitted signal. This information can be employed to detect the target and its range. The received echo signal suffers attenuation because the signal propagation is in free space, while the signal is delayed due to the round trip time needed from the transmitter and back to the receiver. Also, the frequency of the received signal may be shifted due to Doppler effect for a target with high velocity [92], [93], [94].

### 2.3.1 RADAR System Setup

A radar system sends a radio-frequency signal towards an area of the interest and receives the reflected signal from the targets located within the radar detection area. A typical radar system consists of a transmitter, antenna, receiver and signal detection and processing as presented in Figure 2.8 [90], [94], [95]. In the transmitter, an electromagnetic (EM) wave is generated then a switch or circulator conveys the EM wave to an antenna to be introduced to the propagation medium (free-space). The circulator has a function of connecting both transmitter and receiver to the same antenna simultaneously using two connection points to provide isolation between the high power generated signal and the sensitive receiver components [90], [96]. The propagated EM wave induces currents on the target which reradiates these currents back to the propagation medium, then received by the radar antenna. The received signal is amplified then signal processing is applied to detect the reflected signal from the target of interest and determine its range.

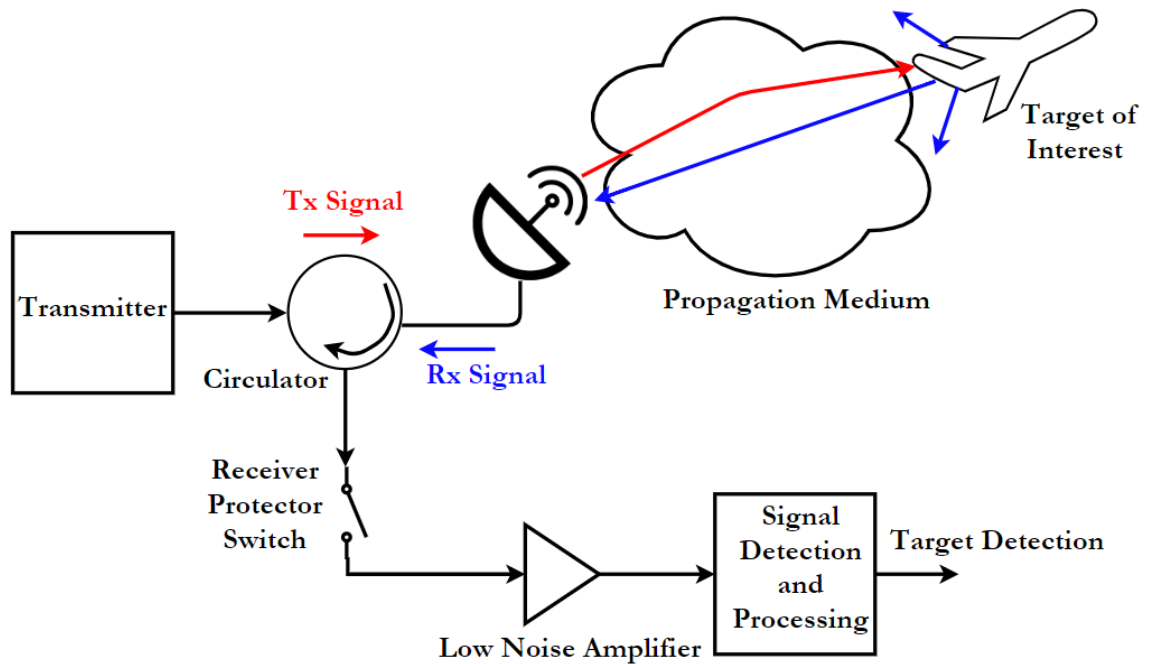


Figure 2.8: Radar system setup.

### 2.3.2 RADAR Configurations

There are two common radar configurations; bistatic and monostatic radar systems. The bistatic radar system includes two separated antenna, (dedicated antenna for transmitter and receiver) and both transmitter and receiver antenna have sufficient separation distance where the angles or ranges to the target are different [90], [97], [98]. In the monostatic radar system, one antenna is shared between the transmitter and the receiver. Also, the monostatic radar can have a dedicated antenna for transmitter and receiver however, both antennas have to be located very close on the same radar system [90], [99], [100]. Figures 2.9a and b illustrate the concepts of bistatic and monostatic radar systems.

The bistatic radar system can be used to enhance the radar's ability to detect targets more efficiently. The signal reflected from the target is very low when the target has small cross section area, ie small radar cross section (RCS). This is also the case for stealthy targets which are designed to have low RCS. Thus, using bistatic radar (separating the transmitter and receiver) can reduce the distance at which the target can be seen [90], [101], [94]. The monostatic radar is widely used as it has more practical and less complex design since one antenna is shared between the transmitter and receiver. The monostatic radar can have poor performance in case the stealthy target is designed to scatter most of the radiated signal away from the direction of the signal arrival [90]. Hence, the bistatic radar may have better RCS in this case. It worth mentioning that, if the stealthy target shape is built to scatter completely the radiated signal away (almost zero reflected signal towards radar antenna) the target cannot be detected by the monostatic and bistatic radar systems.

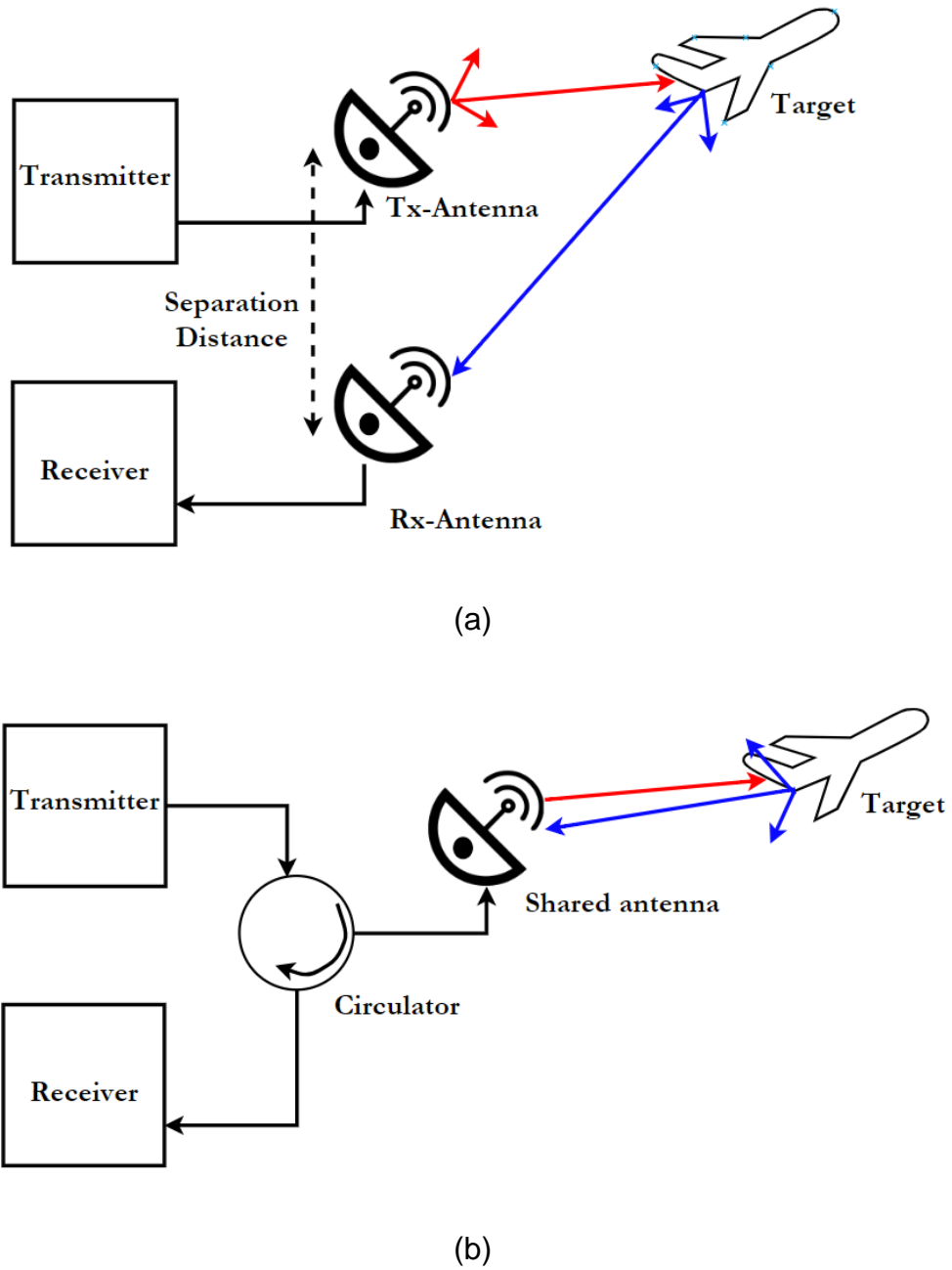


Figure 2.9:(a) Bistatic radar configuration and (b) Monostatic radar configuration.



### 2.3.3 Continuous Waveform RADAR

The radar transmitter generates a continuous wave (CW) waveform and sends the signal continuously without any interruption as all the time the transmitter is switched on [90], [94]. CW radar usually implements the radar configuration with two dedicated antennas for transmitter and receiver in order to maintain the isolation between the transmitter (always on) and receiver operations. Short-range applications are considered for the CW radar as it has relatively low transmitted power [94], [102]. Since the CW radar transmitter is always on, sending a signal, target detection is accomplished by monitoring the change in the characteristics of the wave's frequency over the time. Where, the received waveform frequency is shifted from the original transmitted waveform frequency, the target is in motion with a velocity relative to the radar system (i.e. Doppler effect). Doppler effect is the key principle of the CW radar operation. The Doppler frequency shift  $f_d$  can be calculated as [90], [107]:

$$f_d = \frac{2V_r f_o}{c} \quad (2.21)$$

where,  $V_r$  is the target velocity relative to the radar system,  $f_o$  is the transmitted signal frequency and  $c$  is the velocity of EM waveform. For stationary radar, the  $V_r$  is given as:

$$V_r = V_t \cos \omega \quad (2.22)$$

where,  $V_t$  is the target speed and  $\omega$  is the incident angle (angle of the trajectory between the radar receiver and target velocity vector),  $f_d$  is a positive value when the target is moving towards the radar system (approaching target); while,  $f_d$  is a negative value when the target is moving away from the radar system (receding target) [108], [103] [94]. It worth mentioning that,  $f_d$  is equal to zero when the target is perpendicular to radar line of sight (i.e.  $\omega = 90^\circ$ ).

### 2.3.4 Pulsed Waveform RADAR

The pulsed radar transmits a single pulse (or a sequence of multiple pulses) of a short duration time. During the pulse transmission time, the receiver is isolated from the radar antenna and no received signal can be monitored during this time [90], [104]. The receiver is connected to the radar antenna to collect (listen) to echo pulse signals reflected from targets and other surrounding objects (i.e. clutter). The transmitted pulse duration plus the receiver listening time represent one radar cycle time, called pulse repetition interval (PRI) [90], [105]. In monostatic pulsed radar, the target range is determined based on the round trip time which is defined as the time it takes the transmitted waveform to propagate from the transmitter to the target and back to the receiver at the speed of light. The target range is given as [90]:

$$R = \frac{c \Delta T}{2} \quad (2.23)$$

where,  $R$  is target range in meters and  $\Delta T$  is the round trip time.

In pulsed radar, a radar ambiguous range occurs when the target round trip time  $\Delta T$  is greater than the transmitted interpulse period (IPP). In other words, the reflected pulse from the target will not return within the given receiver listening time before the next cycle of the transmitted pulse resulting in a time ambiguity lead to incorrect target ranging. Range ambiguity can be mitigated by increase the radar pulse repetition interval such that all the reflected signals are received within the listening time before the next pulse is transmitted. Hence, the maximum target range  $R_{Max}$  that can be supported by monostatic pulsed radar is given as [90], [94]:

$$R_{Max} = \frac{c PRI}{2} \quad (2.24)$$

### 2.3.5 Light Detection And Ranging (LiDAR)

The LiDAR, short for 'Light Detection And Ranging' system was introduced for the first time in 1938 to measure the heights of clouds [106]. LiDAR uses optical sources to transmit a pulsed signal and optical detectors are used to collect the reflected signal. In the LiDAR system, a Laser diode is employed as a transmitter. Laser diodes have higher bandwidth compared to LEDs and can transmit the pulse in a very narrow beam which is more robust to propagation losses and less sensitive to ambient noises in the receiver [89], [107], [108]. There are two types of detection methods in LiDAR systems; incoherent detection, which relies on the intensity of the received signal and coherent detection which uses the information of the both amplitude and phase of the received reflected signal [109]-[110]. Figures 2.10a and b present the LiDAR system with coherent and incoherent receivers. In the coherent detection case, a part of the laser pulse generated is split off and redirected to the receiver combiner as can be seen in Figure 2.5b while the other part of the signal is transmitted through laser optics. Coherent LiDAR can work with low SNR (i.e. weak received reflected signal), however, an optical coherent detection receiver is costly and is complicated as compared to an incoherent detection receiver [111], [112]. In the coherent optical receiver, the received signal is mixed with a local oscillator in order to obtain the phase information of the received signal. The optical coherent detection can be implemented using heterodyne and homodyne receiver's techniques [125].

LiDAR systems are used in many applications such as range-finders, 3D Imaging landscapes and autonomous vehicles [108], [113], [114]. In the LiDAR system, time of flight (ToF) is one of the most used methods to measure the target range. Where a short and high energy optical pulse is sent by the laser diode and the time is measured until the received reflected signal from the target is received. This time equals to the round trip distance from the transmitter to target then to receiver divided by the speed of light [115]. The ToF can be used in incoherent LiDAR system with high power laser and single photo-detector receiver. A phase-shift range finder is another method used in LiDAR systems where a generated continuous sinewave signal of frequency  $f_0$  is generated by a local oscillator then modulated by the laser

diode. By calculating the phase difference between the received reflected signal from the target and the generated signal from the local oscillator, the target distance can be determined [115].

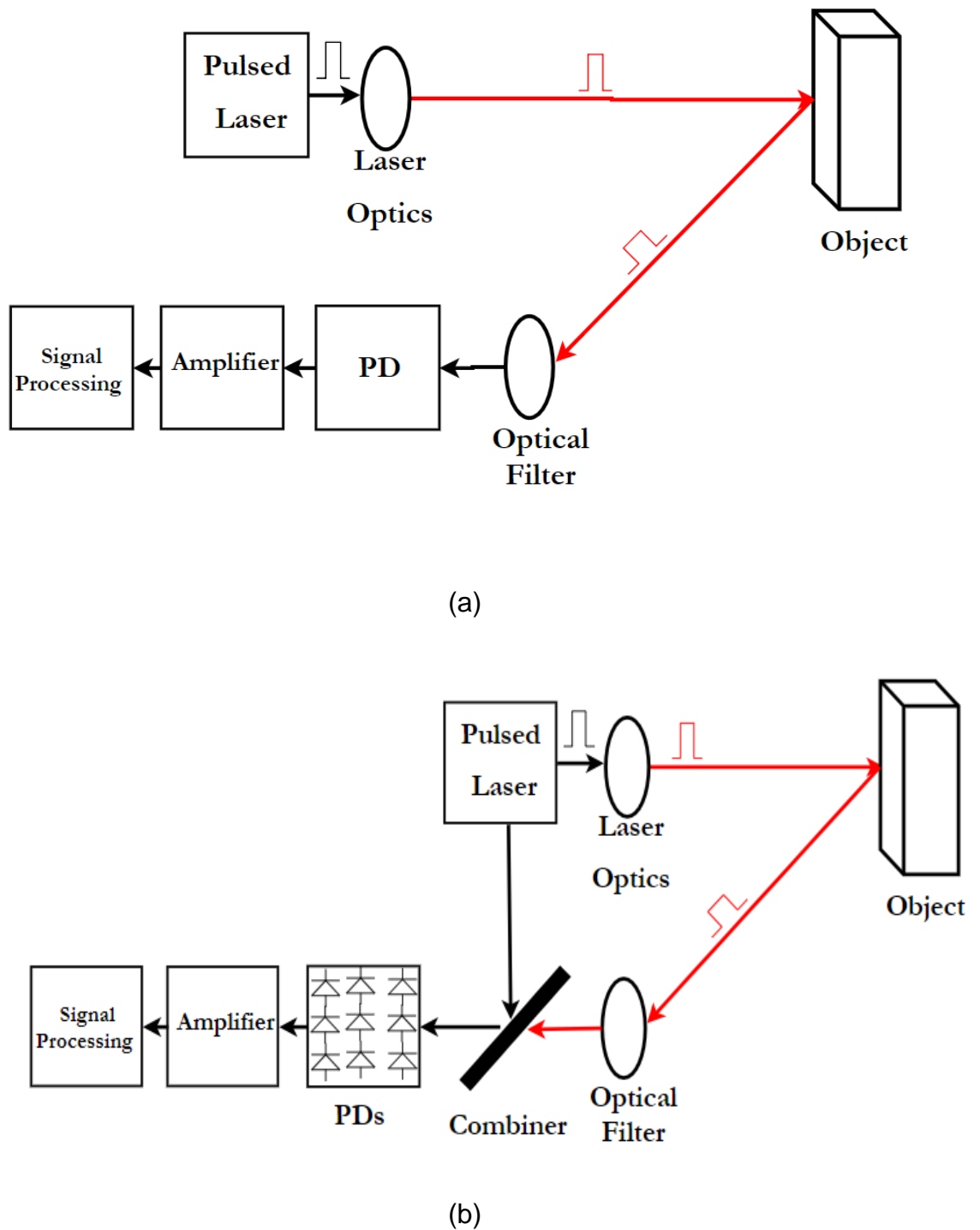


Figure 2.10: Block diagram of LiDAR system with (a) incoherent detection and (b) coherent detection.

## 2.4 Human Sensing Techniques

Human sensing can provide information about people spatio-temporal, behavioural and physical properties. Human sensing has vast variety of applications such as; detecting the presence of a person, counting the number of people, opening a door as people pass, switching on/off light units for an occupied/unoccupied environment and person identification and tracking [16], [116]-[117]. In addition, human sensing can be used for medical applications to identify people and measure their vital signs such as body temperature, blood pressure and heart rate for instance [118], [119]. Going further, human sensing in conjunction with computer applications can be employed to analyse people's mood through their speech, posture and behaviour in order to execute a better decision/action [16]. Many contributions have been proposed to meet the human sensing application by RADAR, computer vision, robotics and sensor network researchers.

Human sensing is a very challenging endeavour for many reasons; (i) sudden changes may occur in the environment conditions. For instance in an outdoor environment, RADAR signals can be effected by the rain or fog while for an indoor environment the passive infrared (PIR) sensors can be activated wrongly by heat currents from heating and air conditions [16], [17], [120]; (ii) the reflected signal from the background is very similar to the one reflected by a person, thus separating a person from the background is an essential requirement for human sensing in a realistic environment. Also, for RADAR and LADAR sensing systems, the reflected received signal suffers from multipath propagation leading to fooling the sensing system and to false person detection (phantom detection) [16]; and (iii) people behaviour is unpredictable with a high degree randomness that may change suddenly resulting in a serious challenge to localise and track individuals correctly [16].

Our LiDAL system aims to focus on human sensing to provide people spatio-temporal indoor application. It carries out presence detection, counting, localisation and tracking. In this application, people can be distinguished from the background due to their dynamic characteristics that arise from their

activity (sitting/standing) and motion (walking), while stationary people are undetectable.

Ultra-wideband (UWB) RADAR systems with a transmitted signal bandwidth greater than 500 MHz have been introduced to detect, localise and tracking humans in the indoor environment [17], [121], [122]. The UWB carrier signal with a typical frequency range of 3.1GHz to 5.3 GHz can penetrate the walls, furniture and human body [123]. This enables UWB RADAR systems to support various applications such as human movement detection through-walls for security applications and biomedical applications (i.e. monitoring human vital signs) [124]-[125]. In UWB RADAR, detection of the target (human) depends on the target motion where the human movement causes changes in frequency, phase and time of arrival. The advantages of using UWB RADAR can be summarised as [17], [122], [126] :

1. Large UWB bandwidth allows increase in the RADAR detection resolution where multiple targets detection can be achieved.
2. UWB signals have low transmitted power over a wide frequency band and thus do not contribute high interference to communication systems.
3. Due to its wide bandwidth, UWB RADAR is immune to narrowband jamming.
4. UWB Radar can identify the target features as the reflected signal carries information not only about the target presence but also about its separated elements.

However for UWB radar employed in an indoor environment, the effects of signal scattering and absorption by obstacles significantly impairs the performance of UWB indoor radar [16], [17].

Binary sensors such as Passive Infrared (PIR) sensors, break beam and binary Doppler sensors have been used to detect human presence and rely on human motion [16, 127], [128]. The main drawback of binary sensors is their large false detection. Doppler shift sensors use the concept that signals reflected from a mobile object suffer a frequency shift depending on the

object's speed. The Doppler shift sensor can provide a speed measurement of the detected human unlike the PIR sensor. In [129] a one dimensional Doppler radar has been proposed to detect stationary humans relying on the motion of human breathing lungs. A laser radar (LADAR) has been used to detect people based on their shape through extracting high resolution two and/or three dimensional snapshots of the environment [130]-[131]. In [132] a single 360-degree LADAR system was introduced to detect and track people in an indoor environment. However, the main disadvantage is the system complexity, eye safety due to the laser beam and the relative long time needed to scan the environment with high resolution which may lead to miss detecting humans walking at fast pace. Compared to other approaches, video cameras with image processing are inexpensive and support high spatial resolution for targets located in an environment. The video cameras provide an information about target's size, shape and colour which can be used to distinguish the target from the surrounding background scene [19]. The major challenge in human sensing using video cameras lies on the target detection and may contain vast number of false detection [19] [143]. The background subtraction is one of the most popular approaches has been used to detect the target presence by video camera for security applications [19] [142]. In [133], a video camera system in conjunction with background subtraction method has been proposed to detect human based on the assumption of the background obstacles scene is static. The main advantage of the background subtraction method is enable fast target detection (i.e. less processing time which important factor in imaging process) [134]. In [135], an object (target) segmentation method has been introduced to extract the target's shape from the camera image directly without need to use the background subtraction. In other hand, a pattern matching method has been proposed in [136] to convolve the camera images taken with the sampling stored images in order to detect the target. Thermal video camera has been used to recognise the target through their body temperature [137].

The Wi-Fi device free approach has been proposed for the first time in [138] [139] to detect the target. This approach take advantage of the vast numbers of deployed Wi-Fi access points to enable target detection through monitoring

the pattern changes of the received Wi-Fi signals due to target presence [140]. In [141], a target detection method using WLAN network based on the received signal strength indicator (RSSI) has been introduced to observe the RSSI changes then identify the target. In other hand, in [142] an approach using a radio frequency identification (RFID) technology with a mobile robot has been proposed to detect and track the targets. In this approach, a mobile robot with a stereo camera vision and RFID reader is used to recognise the target where the information of the target can be easily stored in an RFID tag [143].

## **2.5 Summary**

This chapter provided an overview of VLC, RADAR and human sensing systems. It introduced the structure of VLC transmitters and receivers. It also introduced the modelling of the optical wireless channel. A ray tracing model and calculations of received optical power were explained. The simulations and calculations of the system reported in this thesis were carried out using the MATLAB program. The author proposed and published a low-complexity high-speed VLC system employing transmitter mapping and an adaptive receiver. This gave confidence in the capability of the author's simulator to simulate light propagation and model the LiDAL channel. This chapter has also addressed the configuration and setups of traditional radio frequency RADAR and light radar systems. Furthermore, this chapter highlighted the advantages of human sensing techniques and their challenges.



# Chapter 3

## LiDAL System Design

### 3.1 Introduction

In this chapter, we analyse the LiDAL system maximum range which is related to the receiver's field of view. We also pay attention to the received reflected signal in two LiDAL configurations that relate to the colocation or separation of transmitter and receiver in space. Furthermore, we analyse the resolution and the ambiguity of target detection which are related to the transmitted pulse width. In addition, we examine the optical receiver design for LiDAL and consider the receiver bandwidth and thermal and ambient noises. In our LiDAL system, the sources of randomness are attributed to the target colour of cloth, the target orientation and the receiver noise. Note that in terms of indoor optical wireless channel, we consider the channel at the target's maximum range dictated by the receiver field of view (and the receiver sensitivity). The fluctuation of the received reflected signal attributed to the different colours worn by the target is modelled leading to a PDF of the target reflection factor. The target (human) random orientation and its impact on reflections was determined through extensive simulations, leading a PDF of the effective target cross-section.

The remainder of this chapter is divided into sections as follows: Section 3.2 presents the modelling of the target (human) and the realistic indoor environment. An analysis of LiDAL system configurations and maximum detection range is given in Section 3.3. The design of an optical receiver in terms of receiver bandwidth and noise for LiDAL systems is investigated in Section 3.4. Section 3.5 provides an analysis of LiDAL resolution and ambiguity in target detection. The analysis of the recovered reflected signal

from the target is presented in Section 3.6. A summary is then provided at the end of the chapter.

### 3.2 Realistic Environment and Target Modelling

To study the performance of the proposed LiDAL system, simulations were performed in a typical office consisting of a furnished room, with dimensions of 4 m (width) × 8 m (length) × 3 m (height) as shown in Figure 3.1. The walls, furniture and floor were segmented into small reflective elements. The reflective elements were represented as small secondary emitters that diffuse the received signal in the shape of a Lambertian pattern, with a reflectivity of 0.8 for the walls and ceiling and 0.3 for the floor [80] [77]. In addition, the reflection elements can be treated as small secondary transmitters that diffuse the incident rays back into space from their centre. The accuracy of the received impulse response profile was controlled by the size of the reflective elements, which were 5 cm × 5 cm and 20 cm × 20 cm for the first and second order reflections, respectively [36], [80], [144], [145]. Eight light units were placed at a height of 3m above the floor and were used to satisfy ISO and European illumination standards. Each unit had 9 RGB laser diodes (LDs), and the total transmitted power from each RGB-LDs light unit was 18 W [36], [144]. It is worth mentioning that, each light unit consists of red, green and blue laser diodes which are driven by different modulation currents to meet the illumination standards [36].

The average target (person) dimensions considered were 15 cm × 48 cm × 170 cm (depth × width × height) [146] as shown in Figure 3.2 and coloured polyester fabric was considered as the target coating material. The fabric reflection model used was based on the work in [147], which analysed the reflections from different types of fabric including silk, cotton, polyester, acetate and glass fibre. We also made use of the work in [148] which examined the combination of fabric colour and material and their impact on light reflection. The resulting reflections in [147] were observed to be a combination of diffuse (Lambertian) and specular reflections. In [147], the distribution of the reflected visible light of several cloth materials was experimentally studied. In particular, cotton reflectance was about 9%

specular and 91% diffuse, while polyester reflectance was 10% specular, 26% diffuse and 63% internal multiple reflections which are treated as diffuse reflections as can be seen in Table 3.1. It should be noted that 1% of the polyester reflections are internal reflections which occur inside the fabric layers [147]. Therefore, in our simulation, we only considered a Lambertian pattern (ie diffuse) as the model for the target's surface material. The reflectivity factor of different dyed polyester fabric ranges between 0.25-0.72 [148]. Moreover, the reflectivity of dark and white human skins in the range of 0.04-0.35 and 0.16-0.86 respectively [149]. Regarding furniture, office desks (1.54 m (width) × 0.76 m (length) × 0.75 m (height)) and a bookshelf (3 m × 0.8 m × 2 m) are considered, and are located in the room as shown in Figure 3.1, where the office desks and bookshelf materials were finished-wood with a reflectivity factor of 0.55 and diffuse reflections [150]. The Lambertian diffuse reflection order for the furniture and target is assumed to be 1.

Table 3.1: Reflection model for a different target coating materials [147].

|                  | <b>Specular reflector (%)</b> | <b>Diffuse reflector (%)</b> |
|------------------|-------------------------------|------------------------------|
| <b>Cotton</b>    | 9%                            | 91%                          |
| <b>Polyester</b> | 10%                           | 89%                          |

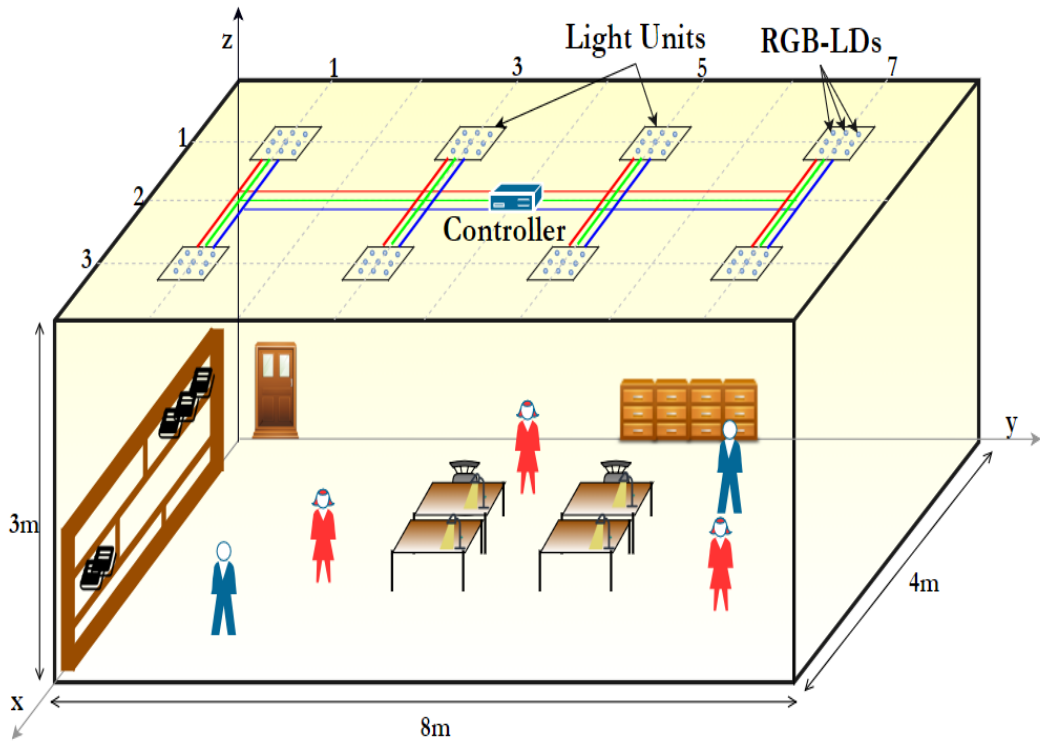


Figure 3.1: Realistic office room setup.

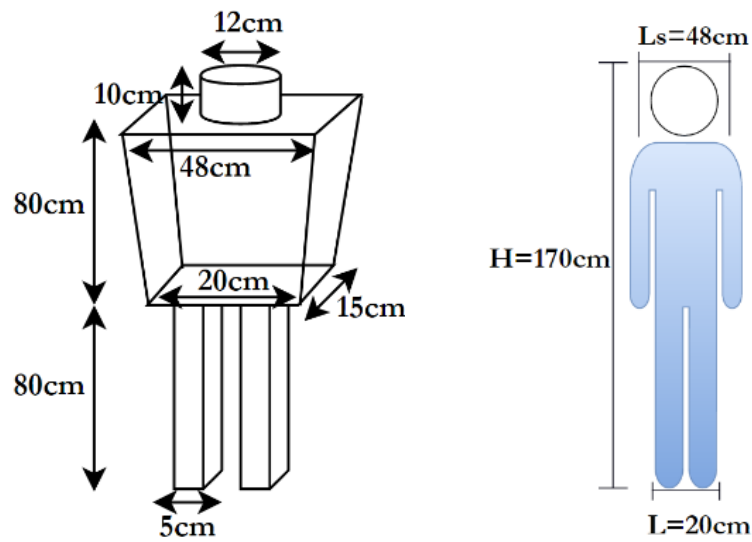


Figure 3.2: Basic 3D and 2D target model.

### 3.3 LiDAL Range Analysis

The light unit emits a narrow pulse in a wide optical beam (Lambertian radiation pattern) directed towards the floor. An optical receiver, collocated or separated from the transmitter, collects the received reflected pulses. The received signal is a superposition of the reflected pulses from the target(s), static environment obstacles (furniture) and noise. Note that, in this section we assumed the target(s) are located in an ideal environment (i.e. an empty room with zero reflectivity from walls, ceiling and floor). Therefore, the received reflected signal randomness is only due to target(s) colours and effective cross-section and is corrupted by noise.

The maximum range of LiDAL can be determined depending on the receiver's photodetector FOV. The maximum range  $R_{Max}^{FOV}$  for a certain receiver concentrator FOV ( $\Psi_c$ ) is given as (see Figure 3.3):

$$R_{Max}^{FOV} = \tan(\Psi_c) (d_o - h) \quad (3.1)$$

where  $\Psi_c$  is the semi-angle of photodetector's concentrator,  $d_o$  is the perpendicular distance between the  $i^{th}$  receiver location  $L_{Rx}^i(x_{Rx}^i, y_{Rx}^i, z_{Rx}^i)$  and the ground reference point  $L_o^i(x_o^i, y_o^i, 0)$  as shown in Figure 3.3 and  $h$  is the target height.

Figures 3.3 and 3.4 present two arrangements of different possible transmitter and receiver configurations with a target located inside the receiver optical footprint (i.e. receiver FOV). We refer to collocated transmitter-receiver configuration as 'monostatic LiDAL' and refer to the spaced transmitter-receiver configuration as 'bistatic LiDAL'.

The received reflected optical power ( $P_{r_B}^{R_{Max}^{FOV}}$ ) from a target at maximum range, ie located in the receiver optical footprint at a radius of  $R_{Max}^{FOV}$ , for a bistatic LIDAL (see Figure 3.3a and b) is derived as:

$$P_{r_B}^{R_{Max}^{FOV}} = \frac{(n+1)(n_{ele}+1)}{4\pi^2 R_1^2 R_2^2} T_f(\Psi_c) G_c(\Psi_c) P_t d_A \rho A_R \cos^n(\theta) \cos(\varphi) \cos^{n_{ele}}(\varphi_1) \cos(\Psi_c) \quad (3.2)$$

and for monostatic LIDAL (see Figure 3.4a and d), the  $P_{r_M}^{R_{Max}^{FOV}}$  is written as:

$$P_{r_M}^{R_{Max}^{FOV}} = \frac{(n+1)(n_{ele}+1)}{4\pi^2 \left( (d_o - h)^2 + R_{Max}^{FOV^2} \right)^2} T_f(\Psi_c) G_c(\Psi_c) P_t d_A \rho A_R \cos^{n+3}(\Psi_c) \quad (3.3)$$

where  $R_1$  is the distance between the transmitter and target,  $R_2$  is the distance between the target and receiver,  $R_2 = \left( (d_o - h)^2 + R_{Max}^{FOV^2} \right)^{\frac{1}{2}}$ ,  $T_f(\Psi_c)$  is the optical filter transmission factor,  $G_c(\Psi_c)$  is the gain of the concentrator,  $P_t$  is the transmitted power,  $d_A$  is target cross section area (top and/or the sides),  $A_R$  is the photodetector physical area,  $\rho$  is the target reflection coefficient,  $\theta$  and  $\varphi$  are the angles of irradiance and incidence respectively,  $n_{ele}$  is Lambertian order for the target diffuse reflector and  $n$  is the Lambertian emission factor of LD defined as [48]:

$$n = -\frac{\ln(2)}{\ln(\cos(\Phi))} \quad (3.4)$$

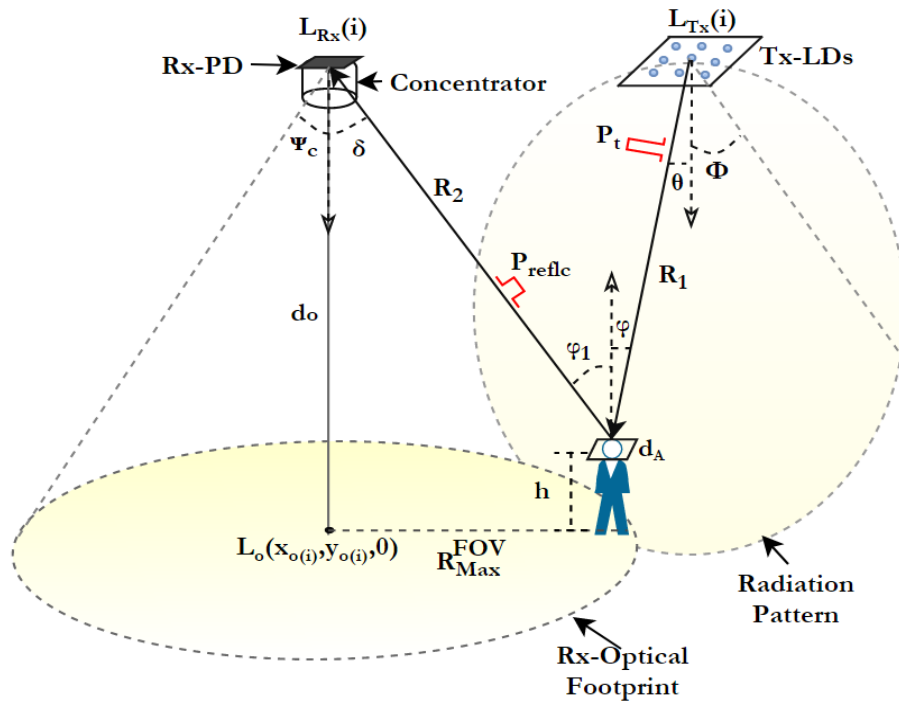
The gain of the concentrator  $G_c(\Psi_c)$  is given as [48]:

$$G_c(\Psi) = \frac{N_c^2}{\sin^2(\Psi_c)} \quad (3.5)$$

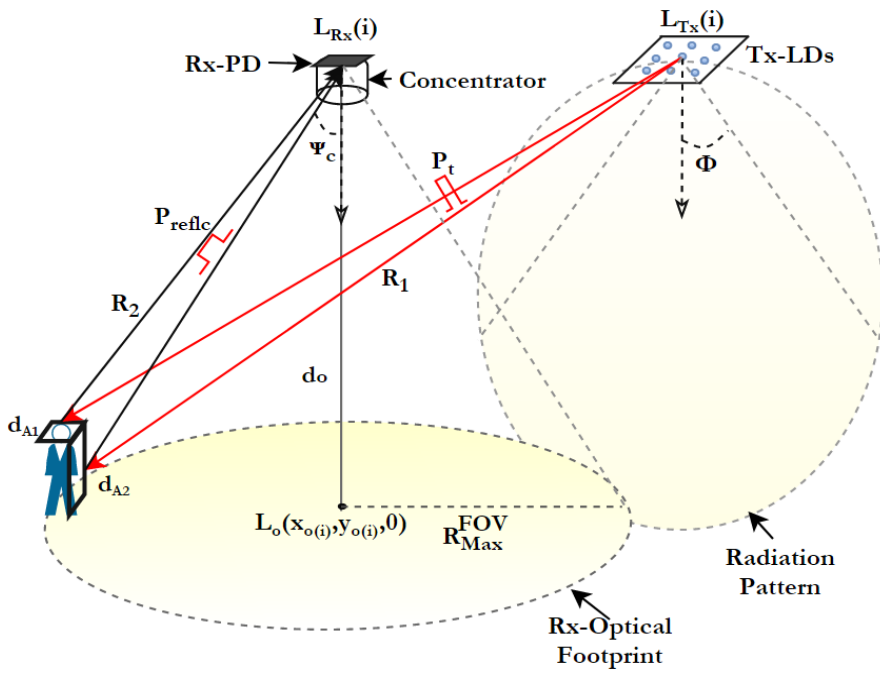
where  $\Phi$  is the semi-angle at half power of LD ( $\Phi > \Psi_c$ ) and  $N_c$  is the concentrator refractive index.

It should be noted that the transmitter has a broad radiation pattern ( $n=0.52$  for illumination purposes [144]) and the target assumed has a diffuse emission factor of  $n_{ele}=1$ . Therefore, the target has a narrow radiation pattern compared to the transmitter's radiation pattern. With such narrow radiation pattern, the target delivers maximum power to the receiver if it is directly under or near the receiver. As such, the weakest received reflected signal from a target occurs when the target is at the edge of the receiver FOV (i.e. target located at  $R_{Max}^{FOV}$ ).

The photodetector area ( $A_R$ ) and the concentrator's FOV and gain are among the receiver's key parameters that determine the LiDAL detection performance. The values of these parameters have to satisfy the LiDAL (radar) design requirements. We analyse their impacts later in this chapter. In addition, the transmitted power  $P_t$  is set at the maximum power needed for normal illumination in the room. (i.e.  $P_t=18W$  according to the design in [36]). We therefore do not consider in this thesis the impact of dimming on our LiDAL system, and in cases where dimming is an issue, infrared sources and detectors can be used for LiDAL. In addition, a VLC LD-transmitter with beam steering and computer generated hologram (CGH) [150] can be employed for VLC RADAR system (with wide-FOV receiver) to obtain very narrow optical beam width. However, we have not included in this work and will be considered in future work.



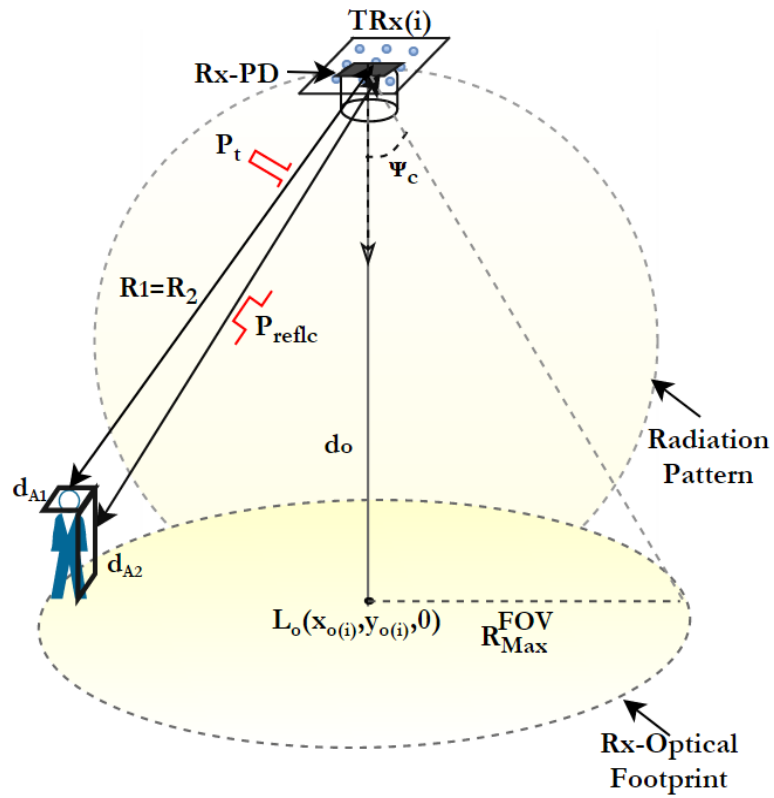
(a)



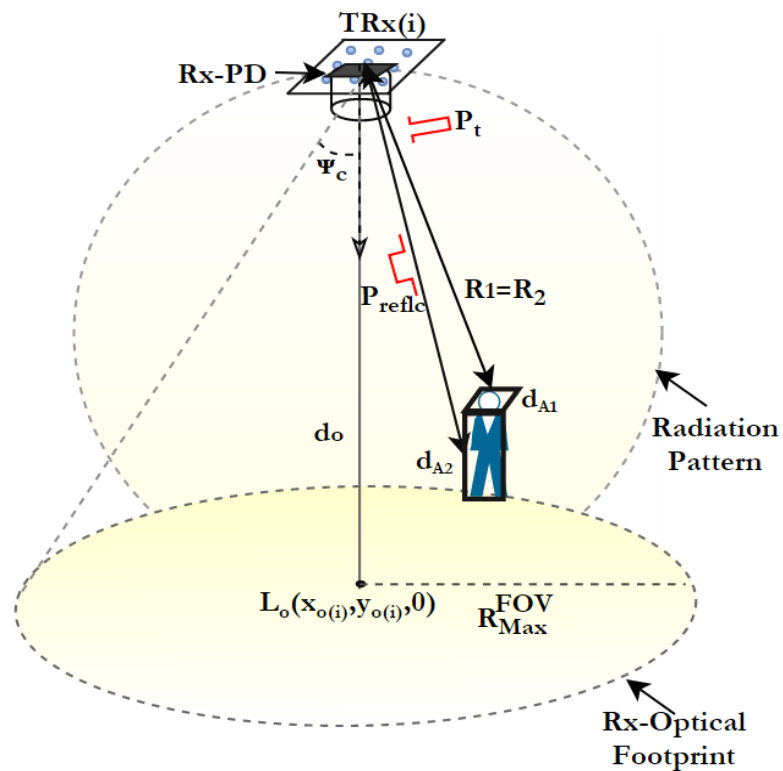
(b)

Figure 3.3: (a) a spaced transmitter-receiver (bistatic) placed on room ceiling with a target located near by the transmitter and distance of  $R_{Max}^{FOV}$  from the receiver (b) a spaced transmitter-receiver placed on room ceiling with a target located away from the





(a)



(b)

Figure 3.4: (a) and (b) a collocated transmitter-receiver (monostatic) placed on room ceiling with a target at two different locations.

### 3.4 Optical Receiver Design For LiDAL

In this section we analyse the design parameters of the optical receiver for LiDAL monostatic and bistatic LiDAL systems corresponding to required bandwidth and induced optical noises.

#### 3.4.1 Receiver Bandwidth

To determine the maximum receiver bandwidth needed, we selected the LiDAL configurations that result in the largest channel bandwidths which the receiver has to deal with. The largest channel bandwidths occur when the target is under the receiver. We have also evaluated the channel bandwidths at a large number of target locations. Figures 3.5 and 3.6 show a target located underneath the receiver for the LiDAL bistatic and monostatic scenarios respectively. We have simulated the pulse dispersion associated with the bistatic and monostatic LiDAL channels due to target presence at different target locations. The target's locations have been generated uniformly inside the receiver optical footprint (see Figures 3.5 and 3.6) to calculate the channel impulse response and then to obtain the 3dB channel bandwidth for each location. It should be noted that we considered an ideal indoor environment without furniture or background obstacles, and we treated the room's floor as a non-reflective surface (i.e. zero reflection factor). In addition, the simulation and calculations of the received reflected signal were carried out using MATLAB. Our simulation tool is similar to the one developed by Barry [81] in terms of the indoor channel impulse response calculation method. Figures 3.7 and 3.8 depict the probability distribution of the channel bandwidth ( $B_{w_{ch}}$ ) for the bistatic and monostatic LiDALs respectively. As can be seen in Figures 3.7 and 3.8, the bistatic LiDAL channel is more dispersive than the monostatic LiDAL channel due to the large distance between the transmitter, target and receiver. Thus, the channel bandwidth is the bottleneck for the LiDAL system performance. Table 3.2 summarises the bistatic and monostatic LiDAL channels characteristics.

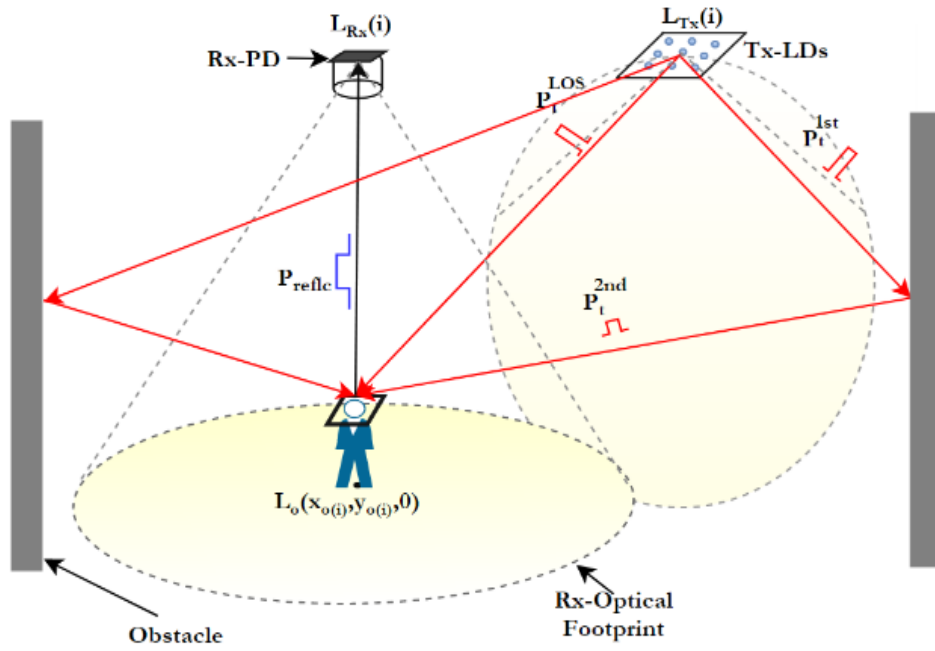


Figure 3.5: Tx and Rx placed in different locations (bistatic LiDAL) with a target located in the centre of the optical footprint.

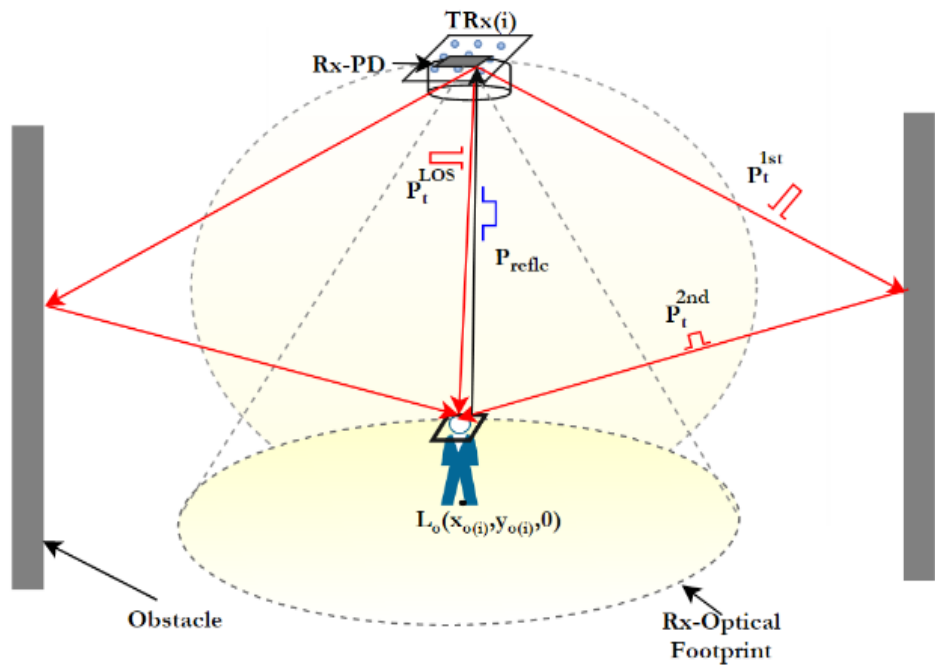


Figure 3.6: Tx and Rx placed in same location (monostatic LiDAL ) a target located in the centre of the optical footprint.

We calculated the channel bandwidth for the monostatic and bistatic LiDAL as follows:

- 1) An input pulse  $x(\tau)$  with time duration  $\tau$  of 0.01ns (equal to the time bin duration used in simulation [36], [144]) is presented to the input of a transmitter unit, RGB-LDs, with impulse response  $h_{tx}(t)$  followed by calculation of:

$$H_{tx}(f) = \mathcal{F}(h_{tx}(t)) \mathcal{F}(x(\tau)) \quad (3.6)$$

It is worth mentioning that, the RGB-LDs have a large bandwidth (few GHz) [144] and therefore, given a channel with few hundred MHz bandwidth, we ignored the laser transfer function.

- 2) We set the following simulation parameters for the monostatic and bistatic LiDAL system: The room has dimensions of 8m × 4m × 3m and the illumination requirements were met using 8 light units distributed as shown in Figure 3.1. These light units also represent the LiDAL receiver locations. To provide overlapping LiDAL coverage zones, the receiver FOV was set to 43°. The transmitter beamwidth was set 75° for illumination purposes [36], [144] and the impulse response was calculated with a time bin of 0.01ns. The bistatic transmitter was located at (2m, 5m, 3m) and the receiver was located at (2m, 4m, 3m) at the centre of the room in Figure 3.1. Figures 3.7a and b show the impulse responses of bistatic LiDAL for a target placed in two different locations. The monostatic transmitter-receiver pair was located at (2m, 4m, 3m). Figures 3.8a and b show the impulse responses of monostatic LiDAL for a target located in two different locations.
- 3) We calculated the LiDAL channel impulse response  $h_{ch}(t)$  (i.e. the LiDAL system configuration with the target present) using the ray tracing propagation model in [81]. In this work, we considered the first and second order reflection components in the simulation of the impulse response of the LiDAL channel. We then determined the 3dB channel bandwidth,  $Bw_{ch}$ , using  $h_{ch}(t)$ .
- 4) The required 3dB receiver bandwidth is determined as:

$$Bw_{Rx} = \max(H_{tx}(f) \times H_{ch}(f))|_{3dB} \quad (3.7)$$

Table 3.2: Characteristic of LiDAL Channel.

|                  | Min. $Bw_{ch}$<br>(MHz) | Max. $Bw_{ch}$<br>(MHz) | Mean. $Bw_{ch}$<br>(MHz) |
|------------------|-------------------------|-------------------------|--------------------------|
| Bistatic LiDAL   | 65                      | 260                     | 125                      |
| Monostatic LiDAL | 140                     | 315                     | 230                      |

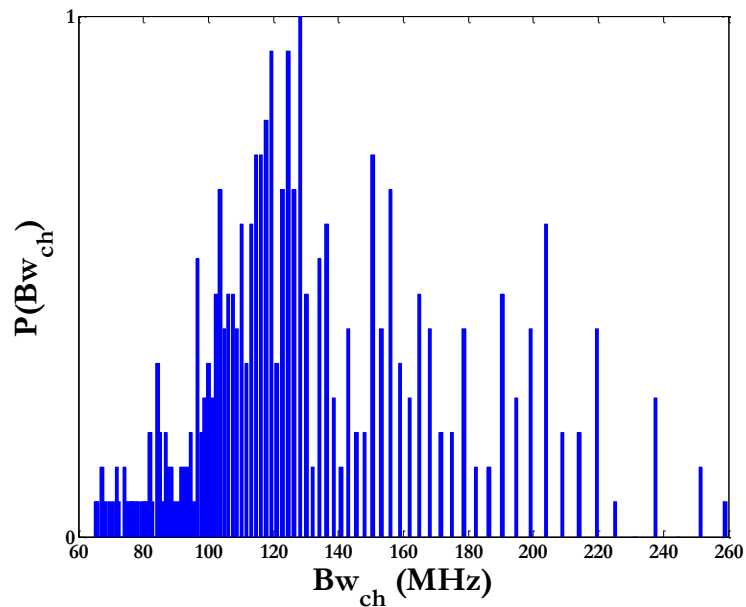
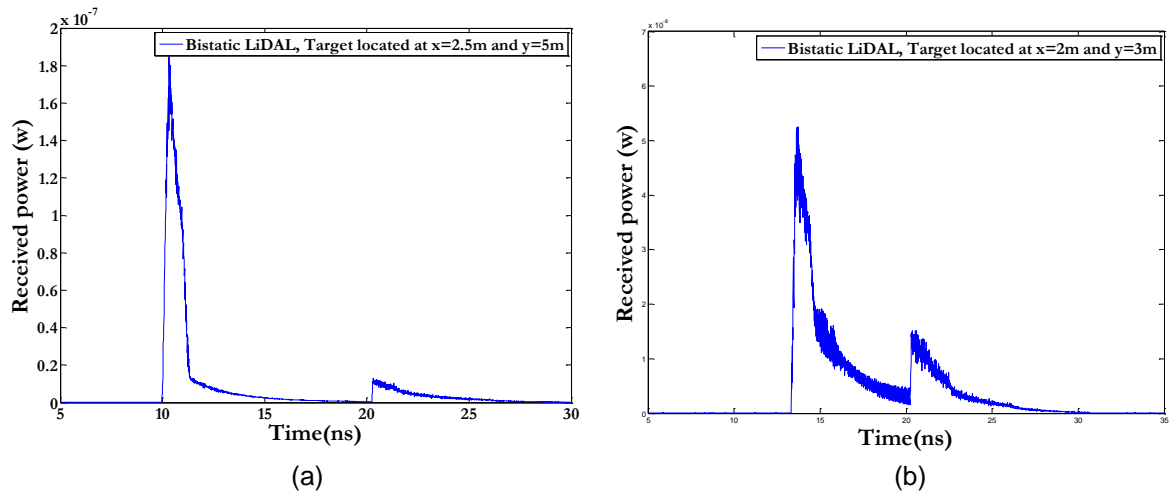
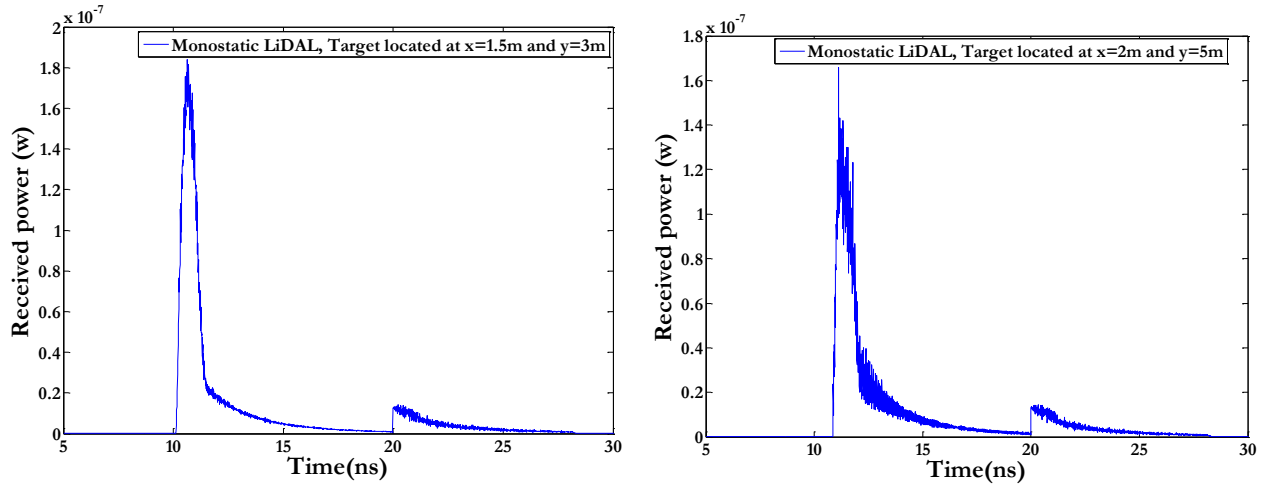
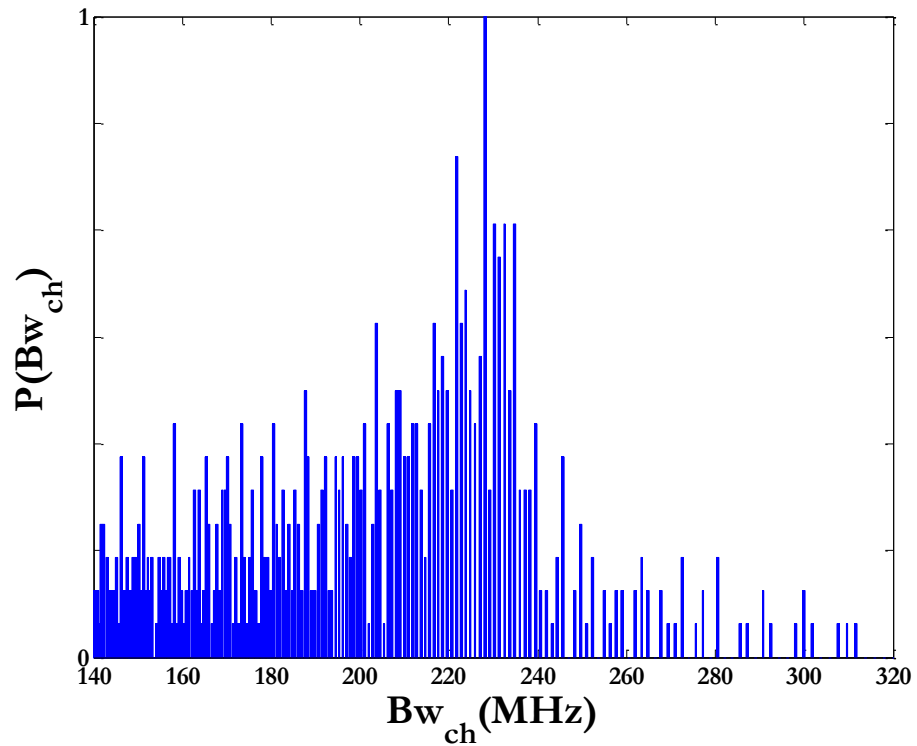


Figure 3.7: (a) Bistatic LiDAL impulse response of target located at  $x=2.5m$ ,  $y=5m$ , (b) Bistatic LiDAL impulse response of target located at  $x=2m$ ,  $y=3m$  and (c) the PDF of the Bistatic LiDAL channel bandwidth.



(a)

(b)



(c)

Figure 3.8: (a) Monostatic LiDAL impulse response of target located at  $x=1.5m$ ,  $y=3m$ , (b) Monostatic LiDAL impulse response of target located at  $x=2m$ ,  $y=5m$  and (c) the PDF of the monostatic LiDAL channel bandwidth.

### 3.4.2 Receiver Noise

In optical wireless (OW) systems, the noise can be divided into two components, a shot noise ( $\sigma_{shot}^2$ ) component and a thermal noise component ( $\sigma_{thermal}^2$ ). The total noise variance  $\sigma_t^2$  is given by [48], [77]:

$$\sigma_t^2 = \sigma_{thermal}^2 + \sigma_{shot}^2 \quad (3.8)$$

The shot noise variance is defined as the sum of contributions from the ambient lights (direct sunlight, desk lamps etc.) and the noise from the received signal. The shot noise,  $\sigma_{shot}^2$ , is written as [10]:

$$\sigma_{shot}^2 = 2qBw_{Rx}(I_b + R_{esp}P_r) \quad (3.9)$$

where  $q$  is the electronic charge,  $Bw_{Rx}$  is the receiver bandwidth,  $R_{esp}$  is the photodiode responsivity and  $I_b$  is the background current due to ambient lights. We considered the effects of shot noise due to desk-lamps. For the four office desk-lamps shown in Figure 3.1, we considered Philips light bulbs where each light bulb has an optical power of 13w [55]. The background current measured in [55] was  $I_b = 8.8\mu\text{A}$  (without optical filter) and corresponded to a typical setup with a  $0.85\text{ cm}^2$  photodetector area at a distance of 2.2m from the light source with a line of sight path (worst case induced shot noise) between the light source and receiver. The setup in [55] is comparable to the realistic environmental setup used in LiDAL in terms of the distance between the desk-lamp and LiDAL receiver (distance of 2.25m in LiDAL). The background current was scaled by a factor that accounts for the difference in area of the photodetector we used, where our photodetector had an area of  $20\text{ mm}^2$  to provide sufficient bandwidth. An optical bandpass filter (OBPF) can be used to suppress the effect of the ambient noise. For example the background current in [55] was reduced from  $8.8\mu\text{A}$  to  $0.48\mu\text{A}$  when an OBPF used. It is worth mentioning that the measurements in [55] included the infrared part of the optical spectrum, while this work focuses on the visible spectrum, however, an optical bandpass filter within the visible spectrum can be used to reduce the background noise to comparable levels. In addition, an electrical high pass filter can be implemented to reduce the DC component of the ambient noise. However, these solutions may increase the cost and the complexity of the LiDAL receiver.

In this work, the optical receiver was a silicon *p-i-n* photodetector with a transimpedance amplifier (TIA) to achieve high sensitivity and a good dynamic range [151], [152]. The receiver considered in this work had high speed and low input noise, designed by Texas Instruments® [153] The TIA had a  $BW_{Rx}$  of 300 MHz and a thermal input noise current of about  $2.5 \text{ pA}/\sqrt{\text{Hz}}$  [153].

### 3.5 LiDAL Resolution and Ambiguity in Target Detection Analysis

The distance ( $R_1$ ) between the monostatic LiDAL transceiver unit ( $T_{Rx}$ ) and the target is calculated based on the round trip time (time taken by the pulse from the transmitter to the target plus the time taken by the reflected pulse back from the target to the receiver),  $t_{trip}$ , and the speed of light,  $c$ , as:

$$R_1 = \frac{c t_{trip}}{2} \quad (3.10)$$

The range resolution of LiDAL is defined as the minimum separation distance ( $\Delta R$ ) at which two or more targets can be reliably detected as illustrated in Figure 3.9. The range resolution is related to the pulse width of the transmitted signal. The LiDAL resolution ( $\Delta R$ ) is given as:

$$\Delta R = R_{1,1} - R_{1,2} = \frac{c \tau}{2} \quad (3.11)$$

where  $\tau$  is the transmitted pulse width. The separation distance  $\Delta xy$  between two targets as can be seen in Figure 3.9 is given as:

$$\Delta xy = R_{1,1} \sin \theta_{1,1} - R_{1,2} \sin \theta_{1,2} \quad (3.12)$$

and if  $\theta_{1,1} \cong \theta_{1,2} = \theta$ , then

$$\Delta xy = (R_{1,1} - R_{1,2}) \sin \theta = \Delta R \sin \theta. \quad (3.13)$$

Therefore,  $\Delta xy \leq \Delta R$ , and in a typical room such as that in Figure 3.1, we determined that  $\theta = 43^\circ$ , hence here  $\Delta xy \leq 0.68\Delta R$ .

Figure 3.10 shows an example of the received pulse response attributed to the reflected signal, as received by a transceiver ( $T_{Rx}$ ) unit which covers an optical footprint that includes two targets in the presence of noise. In this work, we considered typical room layouts, where for example in a meeting room



(closest separation between people in a business setting), the designers recommend an inter-chair-distance more than 60cm as in [154] and 75cm as in [155], and the typical justifiable distance between two people having a conversation is 30 cm. Therefore, we selected a minimum LiDAL resolution of  $\Delta R=30\text{cm}$  and therefore given (3.13),  $\Delta xy \leq 30\text{cm}$  which is the required minimum separation between two targets (i.e. the required  $\tau$  is 2ns from (3.11)). Optical transmitters and optical receivers that support this bandwidth are readily available, and the optical wireless channel is able to provide such bandwidth [59], [144]. The analysis of the channel bandwidth for the bistatic and monostatic LiDAL systems (Figures 3.7 and 3.8) showed high channel dispersion and low channel bandwidth which can't accommodate a transmitted pulse of 2ns without pulse spreading in the receiver. Thus, an equaliser is required to mitigate the imperfections of the LiDAL channel.

Let us first assume an ideal indoor environment (i.e. no reflected signal from the room's background). Here ambiguity in multiple targets detection occurs when the distance between targets is less than the LiDAL (radar) resolution  $\Delta R$ . In other words, when the difference of the targets' round trip times is less than the transmitted pulse width ( $|t_{trip}(1) - t_{trip}(2)| < \tau$ ), this leads to ambiguity. Furthermore, the ambiguity in target detection is affected by the configurations of the LiDAL system.

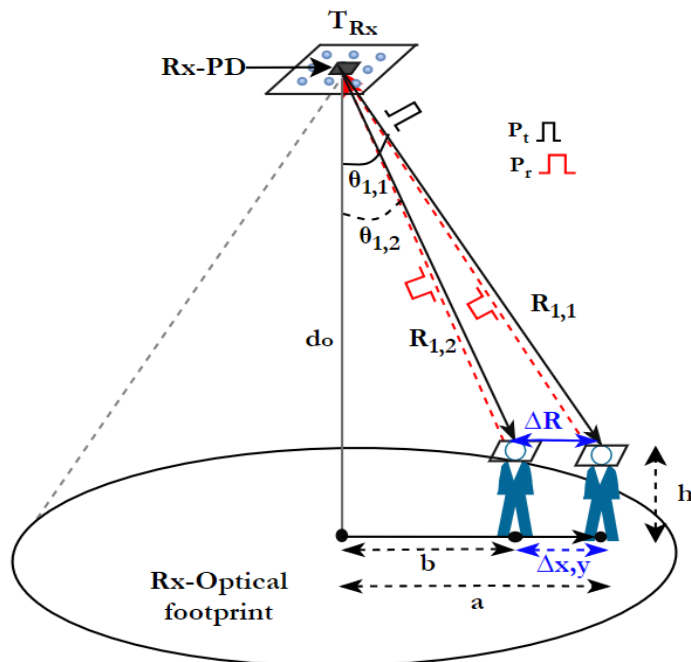


Figure 3.9: The LiDAL resolution to distinguish two targets.

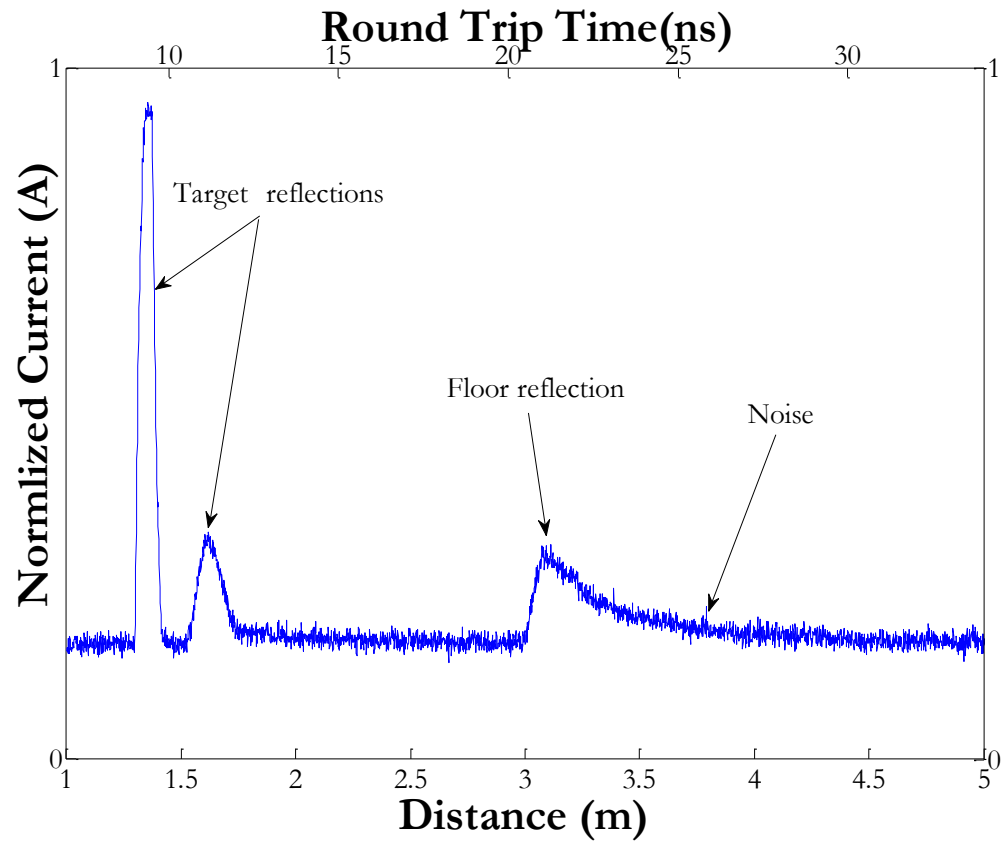


Figure 3.10: The reflected received current signal from two targets located in empty room of monostatic LiDAL.

### 3.6 Received Signal Fluctuation and Target Reflectivity Modelling

The fluctuation of the received optical power reflected from a target is related to the target coating reflection factor ( $\rho$ ) (i.e. colour, material type and reflection type) and the target effective cross section area ( $A_e$ ). The target effective cross section area is the size of the target surface area illuminated by the transmitted pulse (which reflects light) and depends on the target position, LiDAL transmitter and receiver configuration and LiDAL field of view. It should be noted that, the fluctuation of the received signal due to target reflection factor (colour of clothing and type of clothing worn) is independent of the target position and the target orientation (i.e independent of the target effective cross section area).

Table 3.3 presents a range of popular colours with their weights and reflection factors for dyed cotton coating material [156], [157]. The colours popularity show features of a Gaussian distribution as can be seen in Figure 3.11, where, the target reflection factor is the random variable of the distribution. The survey data of favourite colours [156], [157] was fitted to minimise the root mean square error (RMSE), and the minimum RMSE obtained was about 15%. It should be noted that in the curve fitting, we ignored the impact of the black colour with has a very low popularity of 7%.

The probability distribution function (PDF) of the target reflection factor  $p(\rho)$  is given as:

$$p(\rho) = \frac{1}{\sigma_\rho \sqrt{2\pi}} e^{-\left(\frac{(\rho - \mu_\rho)^2}{2\sigma_\rho^2}\right)} \quad (3.14)$$

where,  $\mu_\rho$  and  $\sigma_\rho$  are the mean and standard deviation of the target reflection factor respectively.

Table 3.3: Popular Colours with Reflection Factor.

| Popular Colours [156] | Popularity [156] | Target coating reflectance ( $\rho$ ) [157] |
|-----------------------|------------------|---|
| Black                 | 7%               | 0   |
| Yellow                | 3%               | 0.5   |
| White                 | 4%               | 1   |
| Red                   | 8%               | 0.9   |
| Purple                | 14%              | 0.78  |
| Orange                | 5%               | 0.4   |
| Green                 | 14%              | 0.6   |
| Brown                 | 3%               | 0.45  |
| Blue                  | 42%              | 0.75  |

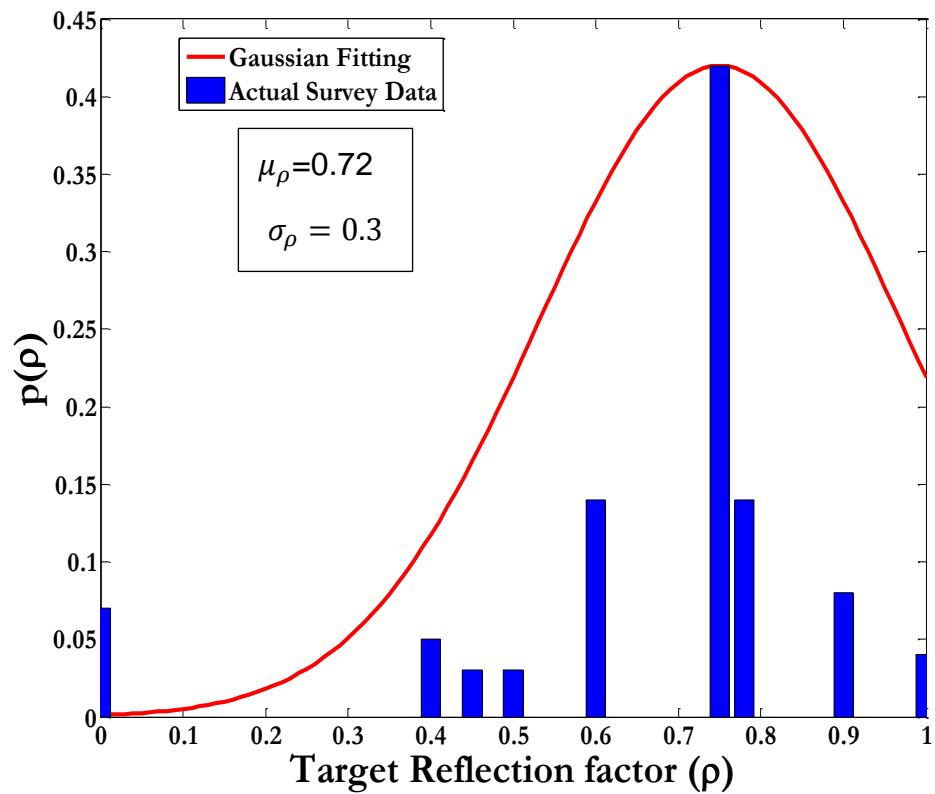


Figure 3.11: The PDF of target reflection factor.

We determined the PDF of the effective target cross section area through simulation. The target shown in Figure 3.2 (human body model) was placed at a large number of locations in the room and the ray tracing indoor propagation method was used to determine the power reflected by all the target surface area elements for the given target location and orientation and the given LiDAL transmitter and receiver configurations. We then fitted the simulated data to a normalised Gaussian distribution as can be seen in Figure 3.12 where the target is placed randomly in the receiver optical footprint edge with different locations and orientations. At each location, the target is rotated to eight directions randomly. The minimum RMSE of the effective target cross section area fitting obtained was 5%. The PDF of the effective target cross section area  $p(A_e)$  is written as:

$$p(A_e) = \frac{1}{\sigma_{A_e} \sqrt{2\pi}} e^{-\left(\frac{(A_e - \mu_{A_e})^2}{2\sigma_{A_e}^2}\right)} \quad (3.15)$$

where,  $\mu_{A_e}$  and  $\sigma_{A_e}$  are the mean and standard deviation of the target effective cross section area respectively. Observing the results in Figure 3.12, it can be seen that the effective target cross section area variation is small with a  $\sigma_{A_e}=4$  and a large mean  $\mu_{A_e}=50$ . Thus, the average value of target cross section area is used. In other words, the target effective cross section area is modelled as a random viable with mean ( $\mu_{A_e}$ ) and very small variance, which is ignored.

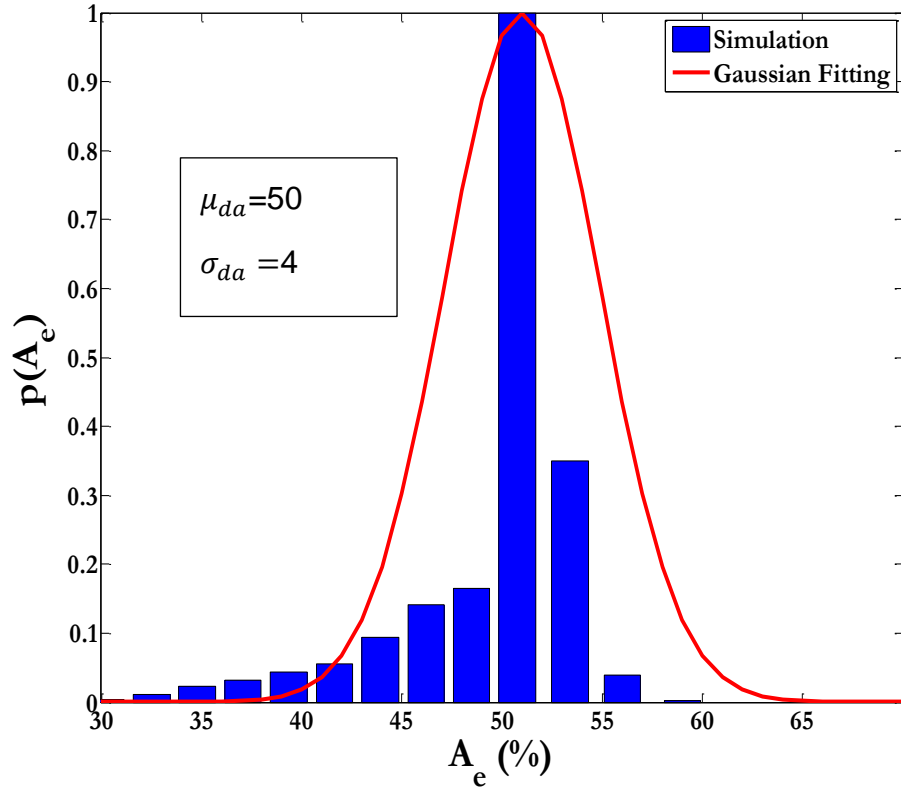


Figure 3.12: The PDF of the effective target cross section area.

The received reflected signal from target is given as:

$$P_r = A_o \rho \quad (3.16)$$

where,  $A_o$  is the LiDAL channel gain for a target located at  $R_{\text{Max}}^{\text{FOV}}$  as in equations (3.2) and (3.3) of bistatic and monostatic LiDAL systems respectively; and  $\rho$  is a Gaussian random variable described in equation (3.14). Thus, the PDF of the received reflected signal  $p(P_r)$  without noise can be defined as:

$$p(P_r) = \frac{1}{\sigma_s \sqrt{2\pi}} e^{-\left(\frac{(P_r - \mu)^2}{2\sigma_s^2}\right)} \quad (3.17)$$

where,  $(\mu = A_o \sigma_\rho)$  and  $(\sigma_s = A_o \sigma_\rho)$  are the mean and standard deviation of the received reflected signal. Equation (3.17) represents a Gaussian random variable scaled by a positive constant representing the LiDAL channel gain for a target located at  $R_{\text{Max}}^{\text{FOV}}$ .

In the OW channel, ambient light induces shot noise in the photodetector receiver in addition to the thermal noise of the receiver amplifier. This noise is modelled as white Gaussian noise [48] with zero mean and variance of  $\sigma_t^2$  (see equation 3.7). The noise probability density is given as:

$$p(n) = \frac{1}{\sqrt{2\pi}\sigma_t} e^{-\left(\frac{n^2}{2\sigma_t^2}\right)} \quad (3.18)$$

where  $n$  is the total detected noise current in the receiver and  $\sigma_t$  is the noise current standard deviation.

The noise is statistically independent and additive to the received reflected signal from the target. The shot noise due to the signal presence may be neglected compared to the thermal and shot ambient noises. Therefore, the joint probability density of the received signal in the presence of noise  $p(p_{r_n})$  is written as:

$$p(p_{r_n}) = \frac{1}{\sqrt{(\sigma_s^2 + \sigma_t^2)}\sqrt{2\pi}} e^{-\left(\frac{(P_r - \mu)^2}{2(\sigma_s^2 + \sigma_t^2)}\right)} \quad (3.19)$$

where,  $\mu$  and  $\sqrt{(\sigma_s^2 + \sigma_t^2)}$  are the mean and standard deviation of the received reflected random signal in noise. Note that the convolution of the received signal PDF (3.17) and noise PDF (3.18) resulting in (3.19) has been proven mathematically in Appendix B.

### 3.7 Summary

In this chapter, we introduced for the first time monostatic and bistatic optical indoor ‘radar’ configurations. Our resulting LiDAL systems provide coverage of the indoor environment through the use of multiple transmitters. The transmitters have broad beams for illumination, however we use relatively narrow FOV receivers to define optical target detection zones on the floor. This is very compatible with VLC systems where multiple light engines are used to illuminate the indoor environment. These light VLC sources can also act as our LiDAL transmitters. This chapter introduced models for the sources of randomness in our LiDAL environment considering randomness due to the random nature of the reflection factor of humans (random colour and texture of clothing), the variable cross section of the target (human) which depends on human orientation with respect to the light source; and finally randomness due to receiver noise and background noise. The monostatic LiDAL has better channel characteristics, received reflected signal from a target and less dispersion compared to the bistatic LiDAL due to the distance between the transmitter-receiver configurations. On the other hand, the bistatic LiDAL has better performance in terms of reducing the ambiguity of multiple target detection.

Chapter 4 will address the design of an optimum receiver for LiDAL systems accounting for the fluctuation of the received signal discussed in this chapter.



# Chapter 4

## LiDAL Optimum Receiver Design

### 4.1 Introduction

In this chapter, we used Bayes receivers and signal space theory to design an optimum receiver structure for LiDAL taking into account the minimisation of the average cost of making decisions and the error in target detection. Bayes criterion takes into account the impact of the cost of making a wrong decision in different LiDAL applications by setting an optimum detection threshold. For instance, in a people counting application the cost of mis-detecting people may be low, however, for a LiDAL security application the cost of mis-detecting a target may be very high. We employed signal space techniques with a maximum posterior probability (MAP) decision rule to design an optimum LiDAL receiver based on minimum probability of error to detect target(s) for multiple cases as we discuss later in this chapter. In addition, we evaluated the performance of the optimum detection threshold  $D_{th}(z)$  where the random variable  $z$  represents the received power in Chapter 4. This was used to produce the receiver operating characteristics (ROC) in terms of the probability of false detection ( $P_{FD}$ ) and the probability of detection ( $P_D$ ).

Following this introduction, this chapter is divided into sections as follows: Section 4.2 describes the analysis of the optimum detection threshold considering the fluctuation of the received signal discussed in Chapter 3. Section 4.3 presents the proposed structures of the optimum and sub-optimum receivers to optimise targets detection in our LiDAL system. Section 4.4 summarises the performance evaluation of the LiDAL receivers. At the end of the chapter a summary is provided.

## 4.2 Optimum Detection Threshold Analysis (Hard Decision)

We analysed the optimum detection threshold for the LiDAL receiver considering the fluctuation of the received reflected signal and the cost of making a decision on LiDAL given the application considered. In LiDAL, the goal is to decide the presence or absence of a received reflected signal from a target in the presence of noise. This situation can be cast into two hypotheses. Let  $H_1$  represent the hypothesis where noise is present and the reflected signal (from the target) is absent. Let  $H_2$  represent the hypothesis where both the received signal (from target) and noise are present. The PDF of  $H_1$  can be written as:

$$F_z(z|H_1) = \frac{1}{\sqrt{2\pi}\sigma_t} e^{-\left(\frac{z^2}{2\sigma_t^2}\right)} \quad (4.1)$$

and the PDF of  $H_2$  is given as:

$$F_z(z|H_2) = \frac{1}{\sqrt{2\pi}\sigma} e^{-\left(\frac{(z-\mu)^2}{2\sigma^2}\right)} \quad (4.2)$$

where,  $\sigma^2$  and  $\mu$  are the variance and the mean of the received signal in  $H_2$  with  $\sigma^2 = (\sigma_s^2 + \sigma_t^2)$ , see equation (3.19) in Chapter 3.

The Bayesian average cost of making decision  $C(D)$  is given as [158], [159]:

$$\begin{aligned} C(D) = & (p_o\alpha_{21} + q_o\alpha_{22}) \\ & + \int (q_o(\alpha_{12} - \alpha_{22})F_z(z|H_2) - (p_o(\alpha_{21} - \alpha_{11}))F_z(z|H_1))d_z \end{aligned} \quad (4.3)$$

where,  $p_o$  and  $q_o$  are the prior probabilities of  $H_1$  and  $H_2$  respectively. For LiDAL, we define the four prior costs as:  $\alpha_{11}$  which is the cost of deciding that the target is absent when it is true,  $\alpha_{22}$  is the cost of deciding the target is present when it is true,  $\alpha_{12}$  is the cost of deciding the target is absent when it is false and  $\alpha_{21}$  is the cost of deciding the target is present when it is false. It should be observed that  $p_o$  and  $q_o$  were set to 0.5 which is a general case where it is equally likely to have a target or no target (for example in an indoor environment). In particular dense (user wise) indoor environments  $q_o$  may be higher than  $p_o$  and the converse is true in sparse indoor environments.

Therefore, the parameters can be determined accordingly. We are interested in the costs of wrong decisions ( $\alpha_{12}$  and  $\alpha_{21}$ ), hence we assumed  $\alpha_{11}$  and  $\alpha_{22}$  (costs of correct decisions) are equal to zero. To clarify this,  $\alpha_{12}$  is defined as the cost of missing a target, while  $\alpha_{21}$  is defined as the cost of a false alarm. Note that,  $\alpha_{12}$  should be set higher than  $\alpha_{21}$ , for security applications where missing a target is worse than a false alarm. However we are interested here in target counting applications, and therefore  $\alpha_{12}$  was set equal to  $\alpha_{21}$  where both wrong decisions equally contribute to wrong counting. Thus, the LiDAL average cost of making decision  $C(D)_{LiDAL}$  can be written as:

$$C(D)_{LiDAL} = p_o \alpha_{21} + \left( q_o \alpha_{12} \int_{H_2} F_z(z|H_2) d_z - p_o \alpha_{21} \int F_z(z|H_1) d_z \right). \quad (4.4)$$

The first term of (4.4) represents the fixed cost while the second term represents the variable cost. We wish to minimise the second term of (4.4) by choosing the value of  $z$ . Mathematically (4.4) can be summarised by a pair of inequalities, and can thus be rewritten as:

$$q_o \alpha_{12} \int_{H_2} F_z(z|H_2) d_z \leq p_o \alpha_{21} \int_{H_1} F_z(z|H_1) d_z \quad (4.5)$$

For LiDAL, we define  $\gamma_{FA}$  and  $\gamma_{FP}$  as the cost factors of missing the target and false alarm respectively. Therefore,  $\gamma_{FA}$  (FA is False Absence) is given as:

$$\gamma_{FA} = q_o \alpha_{12} \quad (4.6)$$

and the  $\gamma_{FP}$  (FA is False Presence) is given as:

$$\gamma_{FP} = p_o \alpha_{21}. \quad (4.7)$$

Thus, we get:

$$\frac{F_z(z|H_2)}{F_z(z|H_1)} \leq \frac{\gamma_{FP}}{\gamma_{FA}} \quad (4.8)$$

where  $\eta = \frac{\gamma_{FP}}{\gamma_{FA}}$  is the LiDAL likelihood test threshold, and  $\frac{F_z(z|H_2)}{F_z(z|H_1)}$  is the LiDAL likelihood test ratio.

Substituting equations (4.1) and (4.2) into equation (4.8) and let  $B = \frac{\sigma_t}{\sigma}$  then we get:

$$e^{\left(\frac{-(z-\mu)^2}{2\sigma^2} + \frac{z^2}{2\sigma_t^2}\right)} B \underset{H_2}{\overset{H_1}{\leq}} \eta \quad (4.9)$$

By taking the natural logarithm of both sides of (4.9)

$$\left(\frac{-(z-\mu)^2}{2\sigma^2}\right) + \left(\frac{z^2}{2\sigma_t^2}\right) + \ln(B_1) \underset{H_2}{\overset{H_1}{\leq}} \ln(\eta) \quad (4.10)$$

$$\left(\frac{\sigma_t^2((-z^2 + 2\mu z - \mu^2) + \sigma^2 z^2)}{2\sigma^2\sigma_t^2}\right) \underset{H_2}{\overset{H_1}{\leq}} \ln(\eta) - \ln(B) \quad (4.11)$$

$$\left(\frac{\left(\frac{\sigma^2}{\sigma_t^2} - 1\right)z^2 + 2\mu z - \mu^2}{2\sigma^2}\right) \underset{H_2}{\overset{H_1}{\leq}} \ln(\eta) - \ln(B_1) \quad (4.12)$$

Let  $\gamma_\sigma = \left(\frac{\sigma^2}{\sigma_t^2} - 1\right)$  and by dividing the numerator and denominator of the left term of (4.12) by  $\gamma_\sigma$ , we get:

$$\left(\frac{z^2 + \frac{2\mu}{\gamma_\sigma}z - \frac{\mu^2}{\gamma_\sigma}}{\frac{2\sigma^2}{\gamma_\sigma}}\right) \underset{H_2}{\overset{H_1}{\leq}} \ln(\eta) - \ln(B) \quad (4.13)$$

We add and subtract  $\frac{\mu^2}{\gamma_\sigma^2}$  to the numerator of the left term of (4.13), we get:

$$\left(\frac{\left(z^2 + \frac{2\mu}{\gamma_\sigma}z + \frac{\mu^2}{\gamma_\sigma^2}\right) - \frac{\mu^2}{\gamma_\sigma^2} - \frac{\mu^2}{\gamma_\sigma}}{\frac{2\sigma^2}{\gamma_\sigma}}\right) \underset{H_2}{\overset{H_1}{\leq}} \ln(\eta) - \ln(B) \quad (4.14)$$

$$\left(\frac{\left(z + \frac{\mu}{\gamma_\sigma}\right)^2 - \frac{\mu^2}{\gamma_\sigma^2} - \frac{\mu^2}{\gamma_\sigma}}{\frac{2\sigma^2}{\gamma_\sigma}}\right) \underset{H_2}{\overset{H_1}{\leq}} \ln(\eta) - \ln(B) \quad (4.14)$$

By multiplying both sides of (4.14) by  $\frac{2\sigma^2}{\gamma_\sigma}$ , we get :

$$\left(z + \frac{\mu}{\gamma_\sigma}\right)^2 \frac{H_1}{H_2} \leq \frac{\mu^2}{\gamma_\sigma^2} + \frac{\mu^2}{\gamma_\sigma} + \left(\frac{2\sigma^2}{\gamma_\sigma} (\ln(\eta) - \ln(B))\right) \quad (4.15)$$

By substituting  $\eta = \frac{\sigma_t}{\sigma}$ ,  $\gamma_\sigma = \left(\frac{\sigma^2}{\sigma_t^2} - 1\right)$ ,  $\sigma^2 = \sigma_s^2 + \sigma_t^2$  and  $\eta = \frac{\gamma_{FP}}{\gamma_{FA}}$  into (4.15) then solving (4.15) in terms of  $z$ , the optimum detection threshold  $D_{th}(z)$  can be derived as:

$$D_{th}(z) \frac{H_1}{H_2} \leq \left( \sqrt{\frac{\mu^2}{(\beta_\sigma - 1)^2} + \frac{\mu^2}{\beta_\sigma - 1} + \frac{2(\sigma_s^2 + \sigma_t^2)}{\beta_\sigma - 1} \left( \ln \frac{\gamma_{FP}}{\gamma_{FA}} - \ln \frac{\sigma_t}{\sqrt{\sigma_s^2 + \sigma_t^2}} \right)} \right) - \left( \frac{\mu}{\beta_\sigma - 1} \right) \quad (4.16)$$

where, we define  $\beta_\sigma = \left(\frac{\sigma_s^2 + \sigma_t^2}{\sigma_t^2}\right)$  as a colour factor where  $\beta_\sigma \geq 1$ . The colour factor  $\beta_\sigma$  is a measure of the variation in the received reflected signal due to the colour worn by the target, versus the variation in the received signal due to noise. For example, if all the targets wore the same colour, then  $\sigma_s^2 = 0$  and  $\beta_\sigma = 1$ . At the other extreme, if the colours worn by the targets are very different and the receiver noise is very small,  $\beta_\sigma \rightarrow \infty$ . It is worth observing that in addition to colour, other optical properties of the target coating affect  $\beta_\sigma$ , such as the material used in the clothing (i.e. cotton verses polyester).

As can be noted in Figure 4.1, when the weights of cost factors are equal ( $\frac{\gamma_{FP}}{\gamma_{FA}} = 1$ ) and  $\beta_\sigma \approx 1$  (i.e. the value of signal variance is very small  $\sigma_s \approx 0$ ), the optimum  $D_{th} \approx \frac{\mu}{2}$ . This case is the classical scenario [159], which acts to validate our derivation of equation (4.16). Figure 4.1 shows the main operating region for the LiDAL detection system. Firstly, the LiDAL system can be used for counting purposes only. Here the cost of missing a target and the cost of a false alarm are identical as they result in equal counting errors. This is represented by  $\gamma_{FP} = \gamma_{FA}$ . Secondly, if the application is such as that there is high cost associated with falsely identifying the presence of a target in the indoor environment, then the detection threshold is set high, represented for example by  $\gamma_{FP} = 10$  and  $\gamma_{FA} = 1$  in Figure 4.1. Finally, if the cost of missing a human pedestrian target is very high (security or safety application), then

the threshold should be set very low as shown in Figure 4.1 where for example  $\gamma_{FP} = 1$  and  $\gamma_{FA} = 10$  and  $\gamma_{FA} = 100$ .

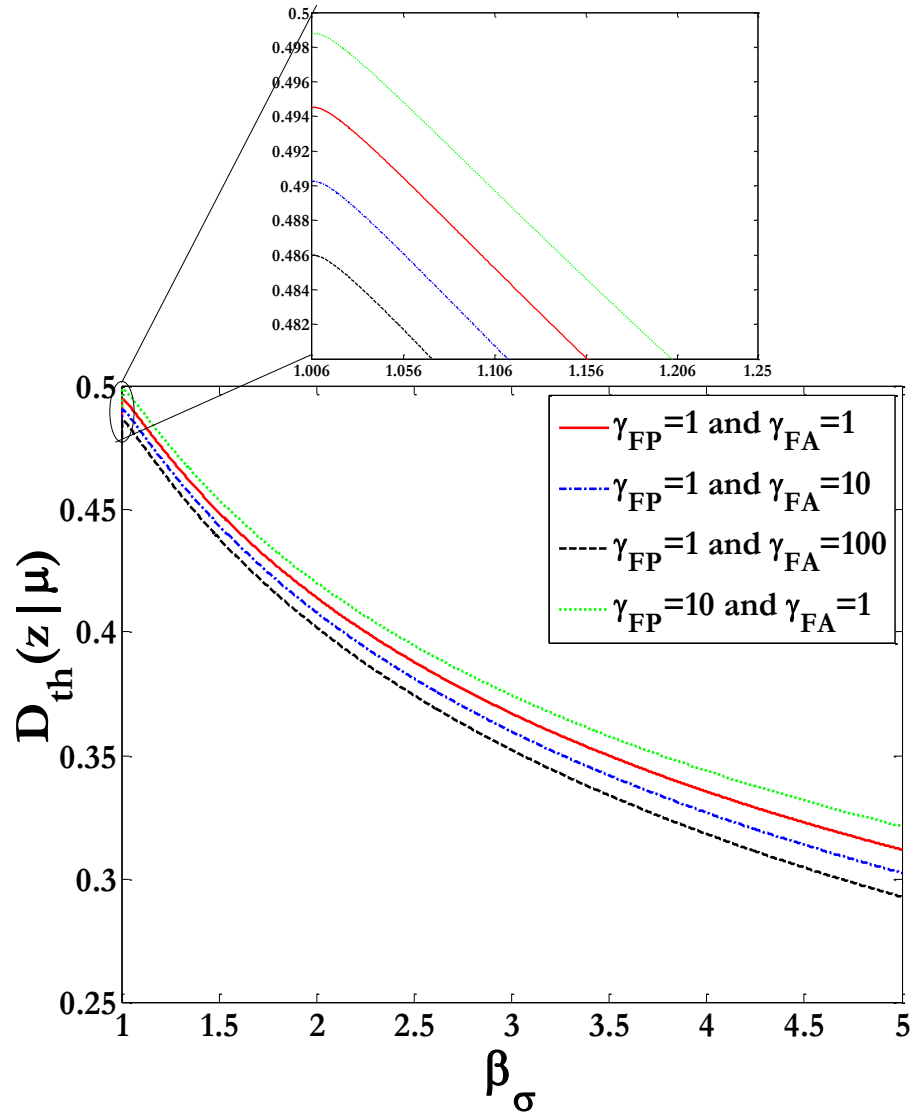


Figure 4.1: The Optimum detection threshold with  $\beta_\sigma$  for different LiDAL cost factors.

### 4.2.1 Probability of False Detection ( $P_{FD}$ )

In the absence of a target there is a chance that a noise signal from any ambient light source can exceed the detection threshold. This noise signal can thus be interpreted as a reflected signal from a target which causes a false detection (earlier referred to as false presence or false alarm). The probability of false detection ( $P_{FD}$ ) is defined as the integral of the Gaussian noise probability density function from the detection threshold to the positive infinity which is given as [90], [159]:

$$P_{FD} = \int_{D_{th}}^{\infty} F_z(z|H_1) dz \quad (4.17)$$

By solving (4.17),  $P_{FD}$  can be written as:

$$P_{FD} = \frac{1}{2} \operatorname{erfc} \left( \frac{\left( \left( \sqrt{\frac{\mu^2}{(\beta\sigma-1)^2} + \frac{\mu^2}{\beta\sigma-1} + \frac{2\sigma^2}{\beta\sigma-1} \left( \ln \frac{\gamma_{FP}}{\gamma_{FA}} - \ln \frac{\sigma_t}{\sigma} \right)} \right) - \left( \frac{\mu}{\beta\sigma-1} \right) \right)}{\sqrt{2}\sigma_t} \right) \quad (4.18)$$

where  $\operatorname{erfc}$  is the error function complementary.

### 4.2.2 Probability of Detection ( $P_D$ )

The probability of detecting a target relies on the received signal reflected by the target in the presence of noise. The probability of detection ( $P_D$ ) is defined as the integral of the reflected received signal PDF from detection threshold ( $D_{th}$ ) to positive infinity. The  $P_D$  can be given as [90], [159] :

$$P_D = \int_{D_{th}}^{\infty} F_z(z|H_2) dz \quad (4.19)$$

Solving equation (4.19) we get:

$$P_D = \frac{1}{2} \operatorname{erfc} \left( \frac{\left( \left( \left( \sqrt{\frac{\mu^2}{(\beta\sigma-1)^2} + \frac{\mu^2}{\beta\sigma-1} + \frac{2\sigma^2}{\beta\sigma-1} \left( \ln \frac{\gamma_{FP}}{\gamma_{FA}} - \ln \frac{\sigma_t}{\sigma} \right)} \right) - \left( \frac{\mu}{\beta\sigma-1} \right) \right) - \mu \right)}{\sqrt{2}\sigma} \right) \quad (4.20)$$

The ROC can now be evaluated for the proposed MIMO and Imaging LiDAL systems. This will be reported Chapter 6 and Chapter 7, after considering the environments and systems of interest, hence the optimum threshold  $D_{th}$  which in turn relies on the statistical characteristics of the reflected signal and noise in each LiDAL system.

### 4.3 LiDAL Optimum Detector

We use the term detector here to imply and include the initial signal detection by the optical receiver, followed by its optimum processing and finally decision making. We implemented a MAP detection approach in LiDAL to design an optimum receiver based on observation of the received reflected signal(s); and hence calculation of the posterior probability to minimise the probability of decision errors [158]. In LiDAL, a single transmitted pulse is sent and is reflected from the target(s) to the receiver where the receiver uses a finite listening time. The LiDAL receiver listening time ( $T_s$ ) is divided into  $N$  time slots. Two cases arise, the single target case and the multiple target case. In the single target case, (i) if the target presence in all spatial locations is equally likely, then the time slots have equal prior probabilities for target reception; (ii) in the single target case, however, the reception of a pulse in a time slot implies that the remaining time slots (if any) will contain no pulses, hence the independence of the time slots does not hold. In the multiple target case, condition (i) holds, and further in (ii) the reception of a pulse does not exclude the remaining time slots from having targets / pulses. Therefore, independence of the time slots can be assumed (ignoring instances where targets may walk in pairs for example). Therefore, we assume here equal prior probabilities for the time slots and assume the independence of the time slots, which is a general common case. The LiDAL receiver has to optimally determine (i) target presence, (ii) number of targets (number of time slots containing pulses) and (iii) identify the time slot (target's range).



The time slot width ( $T_s$ ) is related to the desired LiDAL resolution and target ranging accuracy. Therefore, we select a time slot width equal to the transmitted pulse width ( $T_s = \tau$ ) in order to obtain a  $\Delta R = 30\text{cm}$  resolution. This 30cm resolution corresponds to the minimum typical separation of interest between humans in an indoor environment. Selecting narrower pulse can improve the resolution, however this is not needed and can lead to higher dispersion in the channel. Here we analyse three cases of interest: Single target case, multiple targets case and multiple targets with channel dispersion.

### 4.3.1 Case I: Single Target Detection

We assume a single target, noise present, no channel dispersion, the receiver's  $N$  time slots are orthogonal (i.e. only one received reflected pulse), the received reflected pulse may fit into one time slot or overlap with a neighbour time slot (i.e. the received pulse is shifted in the listening frame depending on target location and may occur at the boundary of the time slot), and independent time slots. For the purpose of this case, the objectives of the designed receiver are detecting the target presence and its range.

Case I is similar to M-ary orthogonal signals (pulse position modulation (PPM)) [159], where a single transmitted pulse is reflected from one target and received by a time slot  $T_{s_j}$ . The MAP rule for minimum probability of error is given as [158] [159]:

$$P(H_i | z_1, \dots, z_N) = \frac{f_Z(z_1, \dots, z_N | H_i) P(H_i)}{f_Z(z_1, \dots, z_N)} \quad (4.21)$$

where,  $Z \in [z_1, \dots, z_N]$  is the observed received signal vector in  $N$  time slots and  $P(H_i)$  is the probability of receiving  $H_i$ , with  $P(H_i) = \left(\frac{1}{N+1}\right)$   $i \in \{1, \dots, N+1\}$ ;  $P(H_i)$  takes this values since the received reflected signal from a target can be present (equi-probably) in any of  $N$  time slots depending on the target location. Note that,  $P(H_i)$  and  $f_Z(z_1, \dots, z_N)$  do not depend on  $H_i$  [159]. Therefore, we require a receiver to calculate  $f_Z(z_1, \dots, z_N | H_i)$  and choose the  $H_i$  associated with the largest probability.

The orthonormal expansion  $Z$  of the received signal can be written as [159]:

$$Z_j = \int_0^{T_s} (p_r(t) + n(t))\phi_j(t) dt \quad j$$

$$\in \{1, \dots, N\} \text{Error! Bookmark not defined. (4.22)}$$

where,  $p_r(t)$  is the received signal,  $n(t)$  is the noise and  $\phi_j(t)$  is the orthonormal basis function chosen as:

$$\int_0^{T_s} \phi_u(t) \phi_j(t) dt = \begin{cases} 1, & u = j \\ 0, & u \neq j \end{cases} \quad (4.23)$$

where,  $\phi_j(t) = \Pi(t - jT_s)$ . It should be noted that  $z_1, \dots, z_N$  are uncorrelated and statistically independent, therefore their joint probability is given as:

$$f_Z(z_1, \dots, z_N | H_i) = \prod_{j=1}^N F_z(z_j | H_i) \quad i \in \{1, \dots, N + 1\} \quad (4.24)$$

The mean and variance of hypothesis  $H_i$  are given as:

$$E\{Z_j | H_i\} = A_{ij} \quad (4.25)$$

$$\text{var}\{Z_j | H_i\} = \sigma^2 \quad (4.26)$$

where  $A_{ij}$  is the orthonormal coefficient given as [159]:

$$A_{ij} = \int_0^{T_s} p_r(t)\phi_j(t)dt \quad (4.27)$$

Equation (4.24) can be rewritten as:

$$f_Z(z_1, \dots, z_N | H_i) = \prod_{j=1}^N \frac{e^{-\frac{(z_j - A_{ij})^2}{2\sigma^2}}}{\sigma\sqrt{2\pi}} \quad (4.28)$$

$$f_Z(z_1, \dots, z_N | H_i) = \frac{e^{-\left(\sum_{j=1}^N \frac{(z_j - A_{ij})^2}{2\sigma^2}\right)}}{(\sigma 2\pi)^{N/2}} \quad (4.29)$$

Thus,

$$f_Z(z_1, \dots, z_N | H_i) = \frac{e^{-\left(\frac{\|z_j - s_i\|^2}{2\sigma^2}\right)}}{(\sigma^2\pi)^{N/2}} \quad (4.30)$$

where:

$$s_i(t) = \sum_{j=1}^N A_{ij} \phi_j(t) \quad (4.31)$$

Therefore, as equation (4.30) shows the optimum receiver that maximises the likelihood is one that minimises the distance between  $z$  and  $s_i$ . In other words, it is a receiver that chooses the minimum distance to the orthonormal coefficient coordinates.

For instance when  $N = 2$ , we have three hypotheses: (i)  $H_0$  no target and both time slots contain only noise (note equation 19 for  $F_z(z)$ ), (ii)  $H_1$  time slot  $T_{s_1}$  contains the received reflected signal from a target with noise and  $T_{s_2}$  contains only noise and (iii)  $H_2$  time slot  $T_{s_1}$  contains only noise and  $T_{s_2}$  contains the received reflected signal with noise. The receiver decision rule for  $H_1$  and  $H_2$  will be to compare the values of  $z_j$  to the orthonormal coefficient values and select the minimum distance to the orthonormal coefficients as illustrated in Table 4.1. However, for  $H_0$  all time slots (i.e.  $z_j$  values) have comparable energy.

Table 4.1: Single target detection in  $N$  time slots

| Observation  | Decision |
|--|----------|
| $f_Z(z_1, z_2   H_1) > f_Z(z_1, z_2   H_2) \Rightarrow z_1 > z_2$                          | $H_1$    |
| $f_Z(z_1, z_2   H_2) > f_Z(z_1, z_2   H_1) \Rightarrow z_2 > z_1$                          | $H_2$    |
| $f_Z(z_1, \dots, z_N   H_j) > f_Z(z_1, z_N   H_m) \forall m \in \{1, \dots, N\}, m \neq j$ | $H_j$    |

Figure 4.2 shows the optimum LiDAL receiver structure to be used to detect a single target (see Case I) based on the analysis of Table 4.1 and equation (4.22). Each branch uses one of the orthonormal functions (see shift register) and an integrator to determine the  $N$  dimensional expansion point collectively between the branches. Therefore, after observing the received signal in  $N$  time slots during the listening time ( $T = NT_s$ ), the receiver decides the target presence and range (related to  $T_{s_j}$ ) through the decision circuit. Figure 4.3 presents an example of the orthonormal functions  $\phi_j(t)$  for  $N=4$  time slots with  $T_s=2ns$  for three radar (LiDAL) scans during the  $T$  listening time.

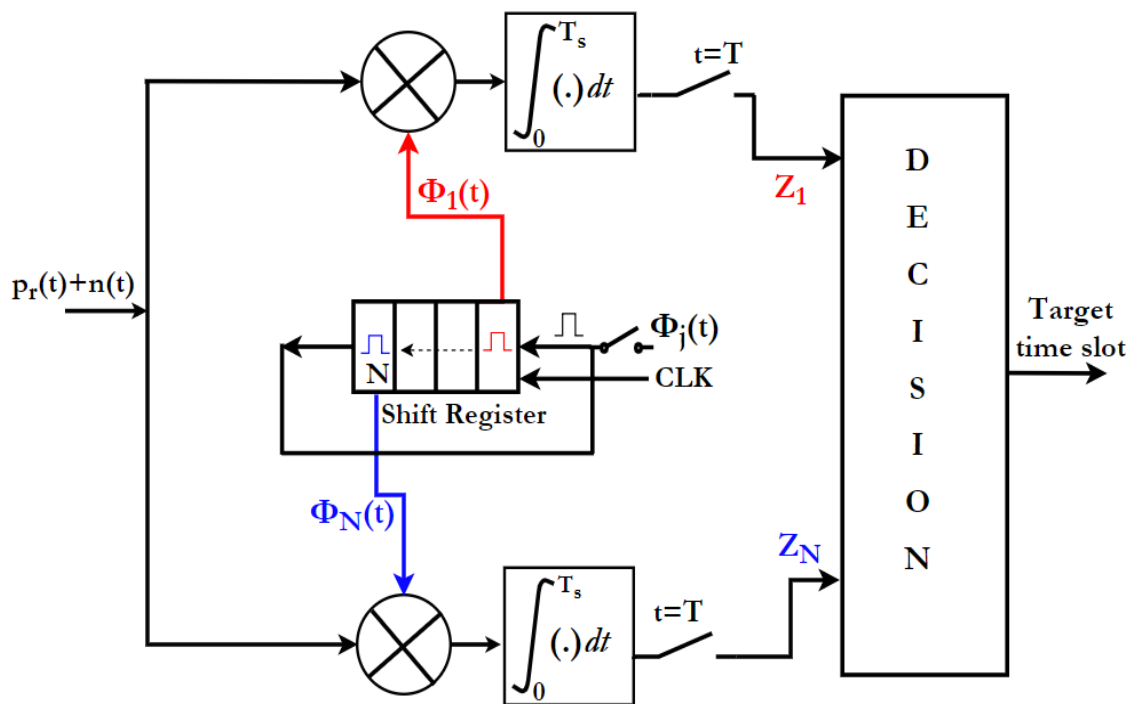


Figure 4.2: The LiDAL optimum detector block diagram, single target detection.

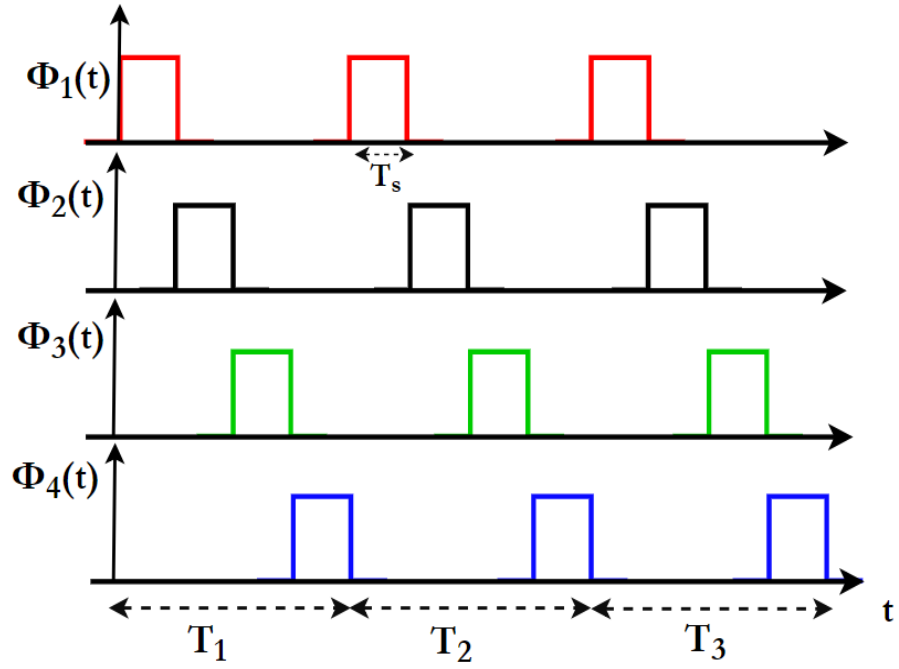


Figure 4.3: The orthonormal  $\phi_j(t)$  signalling diagram.

We evaluated the performance of the LiDAL receiver (Case I) through the probability of making a correct decision  $P_c$  on  $H_i$ , where the reflected signal from the target is received as  $z_i$ ;  $P_c$  can be derived as:

$$P_c = P(z_i | H_j) = P(z_j > z_m) \text{ where } \forall m \in \{1, \dots, N\}, m \neq j \quad (4.32)$$

Substituting equations (4.22) and (3.18) in equation (4.32), we get:

$$P_c = \left( \int_{-\infty}^{z_j} \frac{e^{-\left(\frac{n_j^2}{2\sigma_t^2}\right)}}{\sqrt{2\pi} \sigma_t} dn_j \right)^{N-1} \quad (4.33)$$

### 4.3.2 Case II: Multiple Target Detection

We assume multiple targets, targets locations are spaced by  $\Delta R$  or more, noise is present, there is no channel dispersion, the receiver  $N$  time slots are orthogonal, but the received multiple reflected pulses from  $M$  targets ( $M \leq N$ ) may be shifted depending on the target locations and hence the received pulses are not orthogonal. We do not consider the case where there are more targets than time slots, which is an extension that warrants further investigation. We consider this situation however in the imaging receiver case in Chapter 7.

#### 4.3.2.1 Exhaustive Search Receiver (ESR)

In this section, we propose and analyse an optimum receiver for Case II based on an exhaustive search algorithm as follows:

1. The receiver observes the reflected signal  $p_r$  and produces the orthonormal expansion  $Z$  for the  $N$  time slots in the presence of noise.
2. First, the receiver's decision block (as can be seen in Figure 4.2) compares these  $N$  orthonormal coefficients coordinates to the no target hypothesis as all  $N$  time slots contain only noise, where the observed  $N$  orthonormal coordinates are  $(z_1, z_2, \dots, z_N)$  and the orthonormal coefficient are  $(A_{v_1}, A_{v_2}, \dots, A_{v_N})$ . For the no target case,  $A_{i_j} = 0, \forall j$  and the error  $e_v$  can be defined as:

$$e_v = \sum_{j=1}^N ||z_j - A_{v_j}||^2 \quad (4.34)$$

3. The decision block then compares the observed  $N$  orthonormal coefficients coordinates to the coefficients associated with the presence of a single target hypothesis. There are  $N$  time slots which may contain the received reflected signal from a single target thus  $N$  possible candidate answers are generated. Then the errors of the candidate answers are calculated as in equation (4.34).

4. Next, the decision block calculates the errors assuming the presence of two targets, where there are  $\binom{N(N-1)}{2}$  candidate answers. Thus, the total candidate answers ( $C_A$ ) for  $N$  time slots and  $k$  targets can be defined as:

$$C_A = 1 + \sum_{k=1}^N \frac{N!}{(N-k)! k!} \quad N \geq k \quad (4.35)$$

5. Finally the decision block continues to find the errors for all cases and chooses the  $v^{th}$  case (number of targets and their time slots) which has the minimum error:

$$v = \arg \min_v \left( \sum_{v=1}^{C_A} e_v \right) \quad v \in \{1, \dots, C_A\} \quad (4.36)$$

In the exhaustive research receiver, the probability of making a correct decision  $P_c^{ESR}$  to detect  $k$  targets in  $N$  time slots can be written as:

$$P_c^{ESR} = \left( \int_{-\infty}^{z_j} \frac{e^{-\left(\frac{n_j^2}{2\sigma_t^2}\right)}}{\sqrt{2\pi} \sigma_t} dn_j \right)^{N-k} \quad N > k \quad (4.37)$$

For example, a LiDAL system with listening time divided into  $N = 14$  time slots and maximum counted targets of  $k = 10$ , the total candidate answers are  $C_A = 15914$ . Therefore, the exhaustive search receiver may be very complex to implement for the LiDAL system.

### 4.3.2.2 Sub-Optimum Receiver (SOR)

In this section, we introduce a sub-optimum receiver with lower complexity compared to the exhaustive search receiver. Following the analysis of the MAP rules, Figure 4.4 presents the sub-optimum receiver for Case II. For the sake of simplifying the analysis of Case II, let us assume two targets,  $k=2$ , detection in  $N=2$  time slots. Hence, we have four hypotheses: (i)  $H_0$  noise present only targets are absent (ii)  $H_1$  a single target is present at  $T_{s_1}$  with noise, (iii)  $H_2$  a single target is present at  $T_{s_2}$  with noise and (iv)  $H_3$  two targets present at  $T_{s_1}$  and  $T_{s_2}$  with noise. Table 4.2 illustrates the four possible hypotheses and receiver observation with the optimum decision. To determine  $H_0$  with minimum error, a comparator is connected at the output of each correlator to determine the presence/absence of the received reflected signal at each time slot compared to a lower optimum detection threshold  $D_{thL}$  as can be seen in Figure 4.4. In addition, the receiver has to determine whether there is a single reflected pulse located between two neighbouring time slots (i.e. the correct decision is  $H_1$  or  $H_2$ ) or there are two reflected pulses from two targets received in the two time slots (i.e. the correct decision is  $H_3$ ). Consequently, we set up a second comparator at the output of each correlator with a high detection threshold  $D_{thH} = \frac{\mu}{2}$  as can be seen in Figure 4.4. Therefore, the final receiver decision block decides as follows:

1. If the observed received signal  $z_j$  is below  $D_{thL}$ , then the target is absent in  $T_{s_j}$ .
2. If the observed received signal  $z_j$  is above  $D_{thH}$ , then the target is present in  $T_{s_j}$ .
3. If the observed received signal  $z_j$  is above  $D_{thL}$  and below  $D_{thH}$ , then it is a pulse received in two neighbouring time slots  $T_{s_j}, T_{s_{j+1}}$ . Thus the decision circuit compares  $z_j$  with  $z_{j+1}$  and selects the largest.



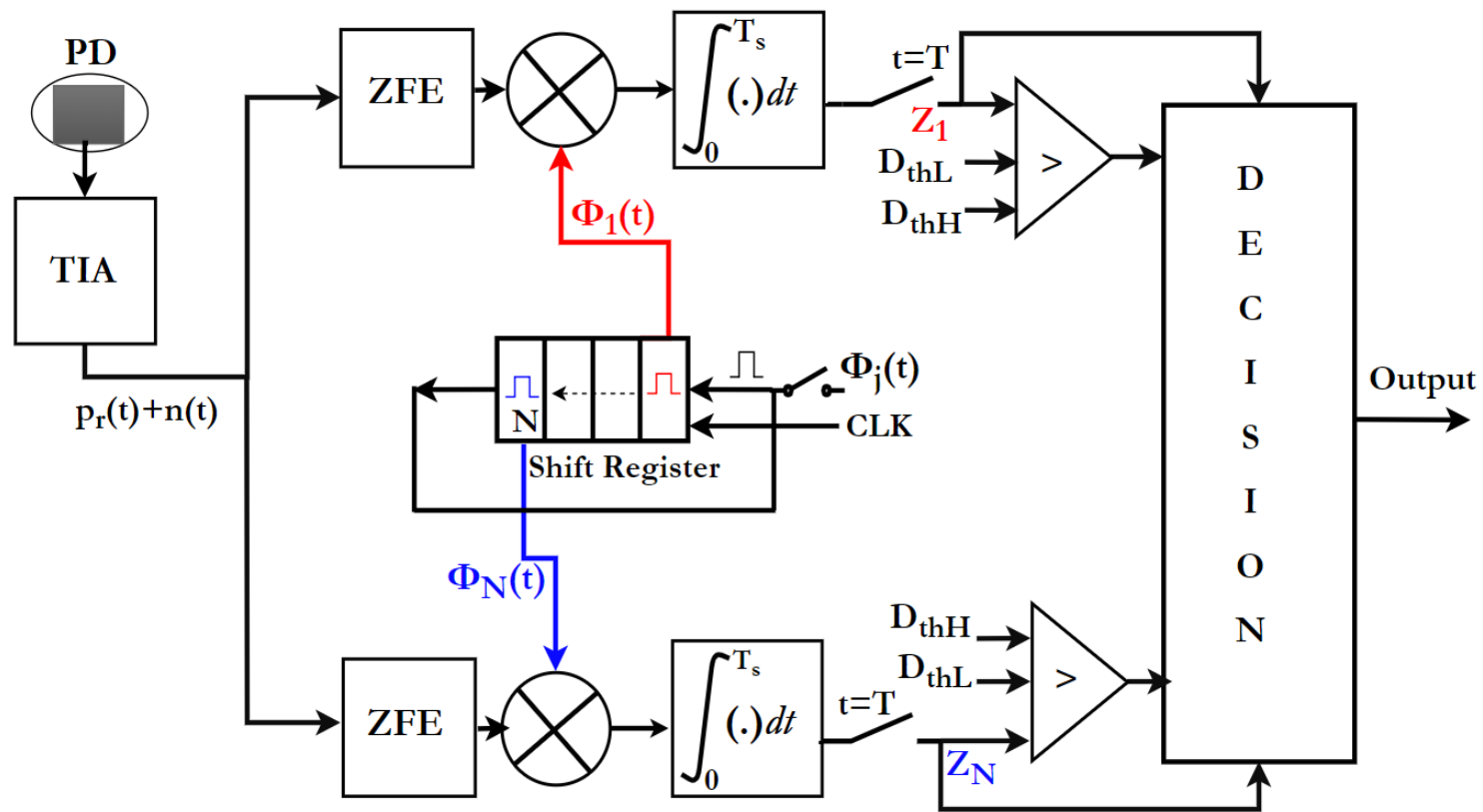


Figure 4.4: The LiDAL sub-optimum receiver block diagram.

Table 4.2: Multiple targets detection hypotheses

| Hypothesis                                     | Observation   | Decision |
|--|---|----------|
| No target ( $T_{s_1}$ ) and ( $T_{s_2}$ )      | $z_1, z_2 < D_{thL}$  | $H_0$    |
| One target ( $T_{s_1}$ )                       | $f_z(z_1, z_2 H_1) > f_z(z_1, z_2 H_i) \quad \forall i, i \neq 1$ | $H_1$    |
| One target ( $T_{s_2}$ )                       | $f_z(z_1, z_2 H_2) > f_z(z_1, z_2 H_i) \quad \forall i, i \neq 2$ | $H_2$    |
| Two targets at ( $T_{s_1}$ ) and ( $T_{s_2}$ ) | $z_1, z_2 > D_{thH}$  | $H_3$    |

Figure 4.5 shows the LiDAL observation space diagram for multiple (two) target detection in two time slots. Each plane of the observation space is divided into four decision regions. Wherever, (region) the coordinates of the observed received signal fall, the receiver decision is based.

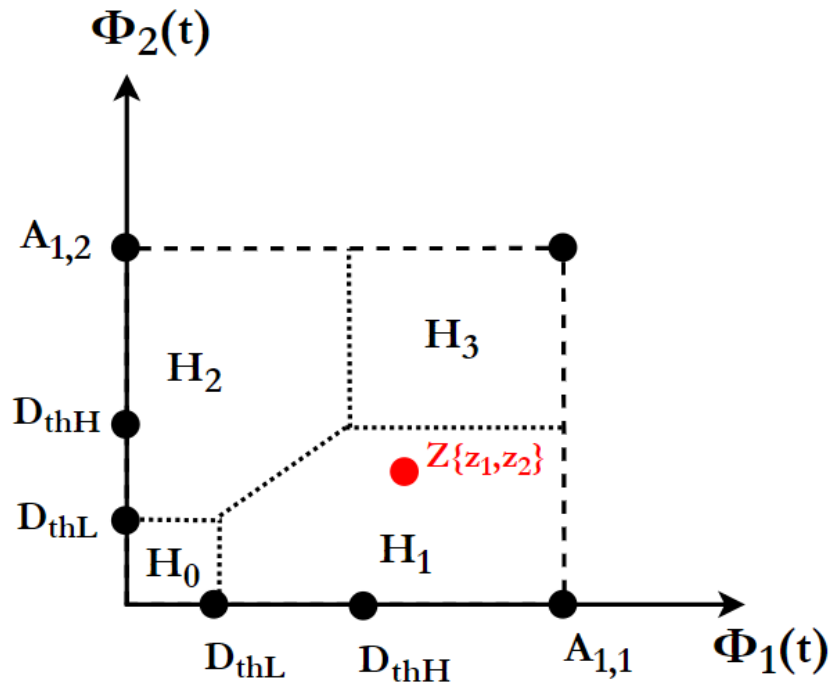


Figure 4.5: The LiDAL receiver two-dimensional observation space.

The probability of a correct decision on target detection in a time slot  $P_{c_T}^{SOR}$  for the SOR can be given as:

$$P_{c_T}^{SOR} \geq \int_{D_{th_H}}^{\infty} \frac{e^{-\left(\frac{(z_j - \mu)^2}{2\sigma^2}\right)}}{\sigma\sqrt{2\pi}} dz_j \quad (4.38)$$

where the use of the high detection threshold ( $D_{th_H}$ ) establishes an upper bound on the detection errors and hence a lower bound on the probability of correct detection. This is therefore conservative.

The total probability of correct decisions,  $P_c^{SOR}$ , when detecting  $k$  targets in  $N$  time slots for the SOR can be derived as:

$$P_c^{SOR} = P(H_0)P_{c_Z}^{SOR} + P(H_1)P_{c_T}^{SOR} + \dots + P(H_k)P_{c_T}^{SOR} \quad (4.39)$$

where,  $P(H_k)$  is the prior probability of having  $k$  targets in  $N$  time slots,  $P(H_k) = \frac{1}{N}$  and  $P_{c_Z}$  is the probability of correct decision of detecting zero targets which is written as:

$$P_{c_Z}^{SOR} = \int_{-\infty}^{D_{th_L}} \frac{e^{-\left(\frac{(z_j)^2}{2\sigma_t^2}\right)}}{\sigma_t\sqrt{2\pi}} dz_j. \quad (4.40)$$

The probability  $P_c^{SOR}$  can therefore be given as:

$$P_c^{SOR} = \frac{1}{N+1} \left( P_{c_Z}^{SOR} + \sum_{k=1}^N \frac{N!}{(N-k)!k!} (P_{c_T}^{SOR})^k (P_{c_Z}^{SOR})^{N-k} \right) \quad (4.41)$$

### 4.3.3 Case III: Target Detection with Channel Dispersion

Case III assumptions are the same as Case II but now we consider the effects of the optical channel propagation. The LiDAL channel can be heavily dispersive as discussed in Chapter 3 (see Figures 3.7 and 3.8). The narrow-transmitted pulse and receiver time slot widths cause; (i) pulse spreading (over two or more neighbouring time slots) of the received pulse reflected from a single target. This leads to a decrease in the probability of correct decision for the proposed LiDAL optimum receivers (ESR and SOR); (ii) ambiguity in target location due to the pulse spread over multiple time slots.

To eliminate the effect of the inter-time slots interference (ITI), the receiver time slot width must be selected according to the minimum LiDAL channel bandwidth where the optimum time slot width  $T_{sOp}$  for ITI free operation can be chosen as  $T_{sOp} = \frac{1}{BW_{chmin}}$ . The optimum time slot width for ITI free operation is  $T_{sOp}=12\text{ns}$  in the room in Chapter 3 using the system parameters in that section. However, for  $T_s=12\text{ns}$ , the radar (LiDAL) detection resolution  $\Delta R$  will decrease significantly by a factor of 6 (from  $\Delta R =0.3\text{m}$  to  $\Delta R =1.8\text{m}$ ). Thus, the time slot width was chosen in Chapter 3 to maintain the desired radar detection resolution of  $\Delta R =0.3\text{m}$  with  $T_s=2\text{ns}$ . Therefore, we implemented a zero forcing equaliser (ZFE) in the LiDAL receiver to equalise the channel [160]-[161]. In other words, to minimize the inter-time slots interference, while maintaining the selected time slot width ( $T_s =2\text{ns}$ ) for optimum radar detection resolution.

We designed the ZFE to equalise the LiDAL channel at the worst target location. Table 4.3 illustrates the noise enhancement and LiDAL channel delay spread with number of ZFE taps.

Table 4.3: ZFE delay spread and noise enhancement

| Number of ZFE taps | Delay Spread (ns) | Noise Variance                     |
|--------------------|-------------------|------------------------------------|
| 0                  | 4.5               | $\sigma_{ZF}^2 = 1 \sigma_t^2$     |
| 1                  | 4.41              | $\sigma_{ZF}^2 \approx \sigma_t^2$ |
| 3                  | 3.13              | $\sigma_{ZF}^2 = 1.15 \sigma_t^2$  |
| 5                  | 1.43              | $\sigma_{ZF}^2 = 1.17 \sigma_t^2$  |
| 7                  | 1.02              | $\sigma_{ZF}^2 = 1.2 \sigma_t^2$   |
| 9                  | 1.01              | $\sigma_{ZF}^2 = 1.22 \sigma_t^2$  |

The ZFE consists of 7-taps weighted finite impulse response filter (FIR). The weights  $c[-l, \dots, l]$  were optimised according to [160]. The ZFE output signal is written as:

$$y_{ZFE}(t) = \sum_{n=-l}^l c_n P_r(t - nT) \quad (4.42)$$

The noise variance after ZFE can be given as [161]:

$$\sigma_{ZF}^2 = \sigma_t^2 \sum_{n=1}^l c_n^2 \quad (4.43)$$

Note that, for the ZFE design  $\sum_{n=1}^K c_n^2$  is 1.2 and therefore the new variance  $\sigma_{ZF}^2 = 1.2 \sigma_t^2$ .

#### 4.4 Performance Analysis of LiDAL Optimum Receivers

Figure 4.6 depicts the probability of error ( $P_E = 1 - P_c^{SOR}$ , or  $P_E = 1 - P_c^{ESR}$ ) of detecting single and multiple targets for ESR and SOR after employing the ZFE. The receiver listening time is divided into  $N = 4$  time slots (which is the number of time slots needed to cover one optical footprint whose radius is 1.2m, and with  $\Delta R = 0.3m$ ). As can be seen in Figure 4.6, the ESR has better performance compared to SOR. For  $k = 3$  with 15dB SNR, the  $P_E$  was 0.1 and 0.21 for ESR and SOR respectively.

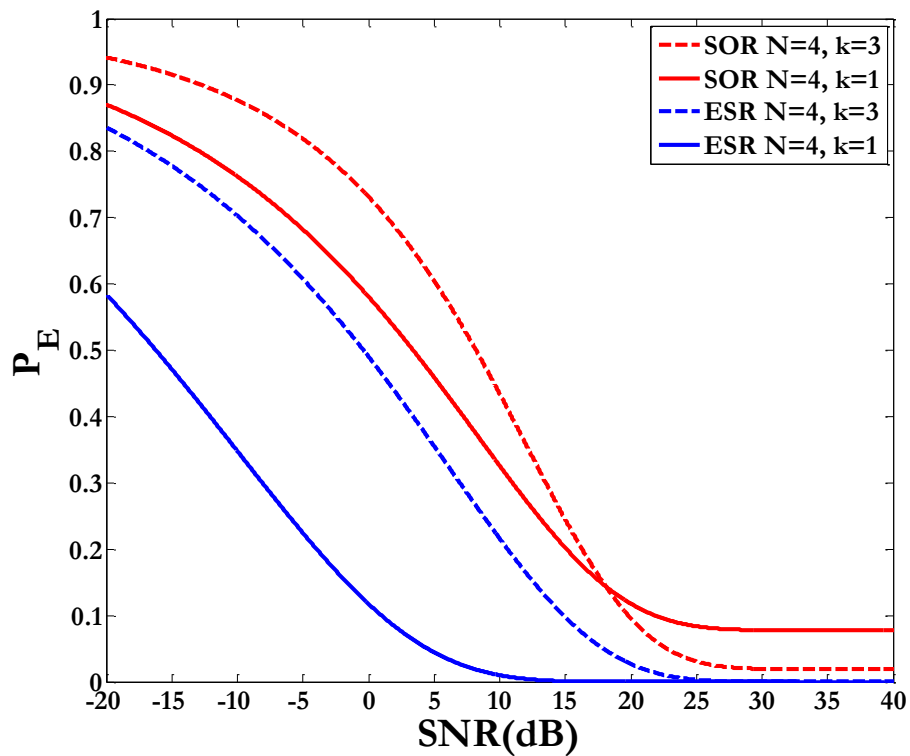


Figure 4.6: Probability of error of detecting targets for ESR and SOR.

## 4.5 Summary

In this chapter, we introduced optimum Bayes receiver structures based on the signal and noise models, considering and interpreting the priors associated with target presence and absence and the costs associated with correct decisions and the costs associated with wrong decisions together with the forms of decision errors. This chapter derived an optimum detection threshold for the LiDAL system accounting for the cost of missing a target and the cost of false alarms. The optimum LiDAL receiver is then formulated using Bayes structures and signal space theory for single and multiple targets in the presence of the impairments outlined above. The LiDAL optimum receiver implemented a MAP detection approach based on observation of the received reflected signal(s); and hence calculation of the posterior probability to minimise the probability of decision errors. To simplify the receiver design, we derived a sub-optimum receiver structure that uses two thresholds for detection thus eliminating the need for exhaustive search and quantified the complexity reduction and the sacrifice in performance.

Chapter 5 will address approaches to distinguish a target from the background obstacles (furniture) based on target motion.

# Chapter 5

## Target Distinguishing Approaches and Mobility Modelling in Realistic Environment

### 5.1 Introduction

To detect the desired targets (humans in our case) using LiDAL, first the unwanted reflected signals from the environment obstacles must be eliminated through signal processing then detection and localisation of the target follows using an optimum receiver in conjunction with an operating algorithm. Hence, the most important task in LiDAL is to distinguish the target reflected signal from the background obstacles reflections in a realistic indoor environment. We considered an active target located in a realistic environment (office room in Figure 3.1). We define an ‘active target’ as a target that has the ability to be mobile, standing and sitting which are considered a unique signature that can be used to identify the target from the static obstacles in the realistic environment. In other words, the received reflected signal from the target is time-variant due to target activity while the background obstacles reflections are time-invariant (here we ignore for example the potential slow OW channel variations due to oscillations of indoor fans and the fast variations due to fan blades rotation for example). Thus, by monitoring multiple received signals for a duration of time, it is possible to eliminate the time-invariant signals and detect the changes in the signals reflected from the target movement.



In this chapter, we considered and analysed three main approaches for target detection in a realistic environment. Firstly, a background subtraction method was developed to distinguish the target from background obstacles under the assumption that the realistic environment obstacles are static. Here, the target is detected by distinguishing the background reflections in multiple LiDAR measurements / scans. Secondly, a cross-correlation method is used to identify the changes in the LiDAR received signal scans in order to establish the target mobility. Thirdly, a background estimation method is introduced to distinguish the target by eliminating the background reflections. Furthermore, we have considered two types of target movement which describe pedestrian and nomadic targets. The target behaviour is modelled as; (i) a random walk using a model that avoids obstacles employing Markov chains. This may suit a small environment where a target may move randomly if the environment is mostly empty; (ii) a pathway model where the target chooses to walk on certain fixed paths due to the layout of the indoor environment.

The remainder of this chapter is divided into sections as follows: Section 5.2 presents the analysis of the background subtraction method. Section 5.3 investigates the proposed cross-correlation method. Section 5.4 describes the target mobility models with analysis of probability of target mobility detection. Section 5.5 introduces the background estimation method. Section 5.6 presents the simulation setup and performance evaluation of the target distinguishing approaches. At the end of the chapter a summary is provided.

## 5.2 Background Subtraction Method (BSM)

The background subtraction method was investigated and implemented practically in [162]-[163] for UWB radar and camera surveillance systems. This method has poor performance only in cases where a target is moving (i.e. horizontal movement) and its signal reflections arrive at the same time during radar scans leading to ambiguity in single mobile target detection [164]-[165]. In LiDAL systems we introduce and make use of collaboration between monostatic and bistatic LiDAL configurations to eliminate the ambiguity in mobile target detection.

### 5.2.1 Evaluation of Background Subtraction Method

To develop the BSM concept in LiDAL we first considered a BSM example under two assumptions (which we remove later) (a) single mobile target with a single stationary background obstacle and zero reflections from the room's floor and walls; (b) there is no ambiguity between the target and the background obstacle (i.e. the target and the obstacle are separated by a minimum distance of  $\Delta R$  or more). The received signal is  $p_{r_i}(t)$  representing the  $i^{\text{th}}$  snapshot measurement taken during a time frame of duration  $T$  in the presence of noise. The received signal is a superposition of the signals reflected from the target, background object and noise, thus  $p_{r_i}(t)$  can be expressed as:

$$p_{r_i}(t) = \alpha_i m(t - t_{m_i}) + \beta_i b(t - t_{b_i}) + n_i(t) \quad (5.1)$$

where  $m(t)$  is the reflected signal from the target,  $b(t)$  is the reflected signal from the background obstacle,  $n_i(t)$  is the noise during the  $i^{\text{th}}$  snapshot,  $\alpha$  and  $\beta$  are the attenuation factors due to signal propagation and  $t_{m_i}$ ,  $t_{b_i}$  are the time delays for target and background signals respectively. It should be noted that  $(|t_{m_i} - t_{b_i}| \geq \tau)$  according to assumption (b). The BSM requires at least two snapshots to distinguish a pedestrian target and eliminate the background reflections. Thus, the received signal for the next snapshot ( $i + 1$ ) is given as:

$$p_{r_{i+1}}(t) = \alpha_{i+1}m(t - t_{m_{i+1}}) + \beta_{i+1}b(t - t_{b_{i+1}}) + n_{i+1}(t). \quad (5.2)$$

The subtraction of equations (5.1) and (5.2) yields:

$$y_s(t) = \alpha_{i+1}m(t - t_{m_{i+1}}) - \alpha_i m(t - t_{m_i}) + (n_{i+1}(t) - n_i(t)) \quad (5.3)$$

where  $t_{m_{i+1}} \neq t_{m_i}$  as the target is assumed to move while  $t_{b_{i+1}} = t_{b_i}$  due to the stationary obstacle. Equation (5.3) results in perfect elimination of the reflected signal from the background obstacle only if  $(\beta_{i+1} = \beta_i)$ . However, part of the signal reflected from the target (due to multiple reflections) may contribute to the reflected signal from the obstacle. This is attributed to the presence of the target and its movement which may also block partially the signal reflected by the obstacle. This leads to  $\beta_{i+1} \neq \beta_i \rightarrow \beta_{i+1} = \omega_i \beta_i$ , where  $\omega_i$  is the target impact factor on background reflections due to target presence and/or movement. Thus  $y_s(t)$  is written as:

$$y_s(t) = \alpha_{i+1}m(t - t_{m_{i+1}}) + \alpha_i m(t - t_{m_i}) + \beta_i(\omega_i - 1)b(t - t_{b_i}) + (n_{i+1}(t) - n_i(t)) \quad (5.4)$$

The subtracted signal term  $\beta_i(\omega_i - 1)b(t - t_{b_i})$  of equation (5.4) may be interpreted as a reflected signal from a target if  $\beta_i(\omega_i - 1)b(t - t_{b_i}) \geq D_{th_L}$  and this can lead to false target distinguishing. Furthermore, the subtracted noise term  $(n_{i+1}(t) - n_i(t))$  has a variance  $\sigma_{t_s}^2$  equals to  $2\sigma_t^2$ . Note that, the lower optimum detection threshold  $D_{th_L}$  introduced in this work is based on two hypotheses  $H_0$  only noise is present and  $H_1$  noise and target are present. Thus, this leads to a new hypothesis which we have not included and will be considered in future work. It is however typically not an issue for the imaging receivers in Chapter 7 due to their narrow FOV.

Figure 5.1 shows an example of two snapshot measurements for a mobile target and a stationary obstacle. As can be seen in Figure 5.1 the BSM of the snapshots may lead to false target distinguishing due to target movement which affects the signal reflected by the stationary obstacle. The simulation in

Figure 5.1 was carried out in a room (4m × 8m × 3m) in the presence of a single target and background obstacle located at ranges of 2m and 3m receptivity. A monastic LiDAL setup was used where the transmitter and receiver are located at the centre of the room's ceiling. Figure 5.2 illustrates the proposed LiDAL receiver for target detection and distinguishing using BSM with the sub-optimum receiver.

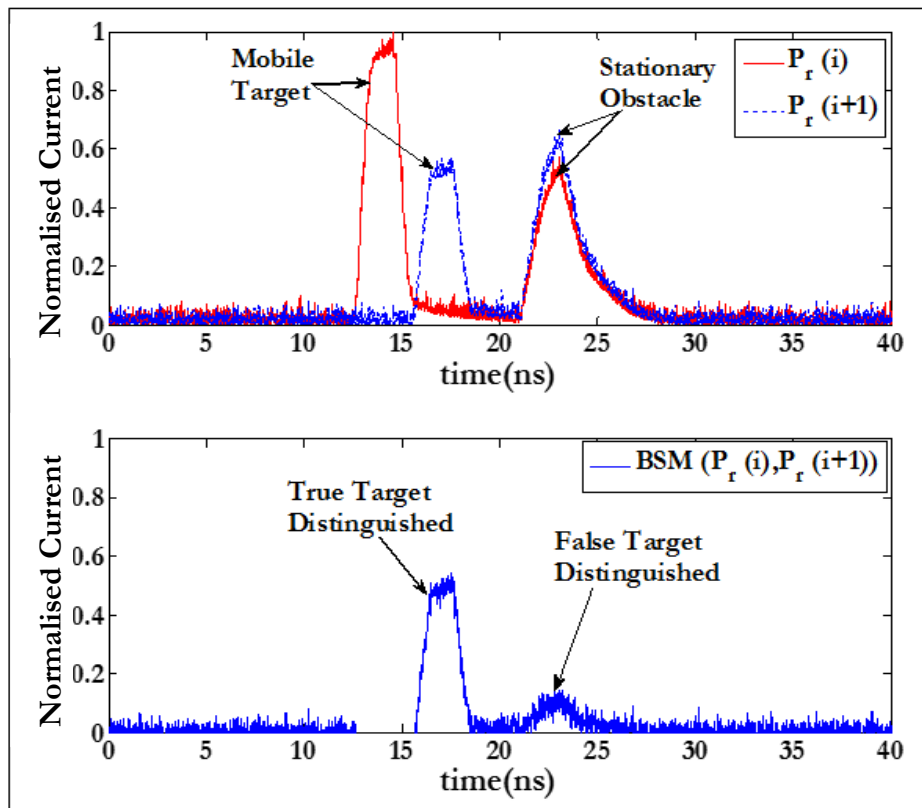


Figure 5.1: BSM of the received snapshots measurements.

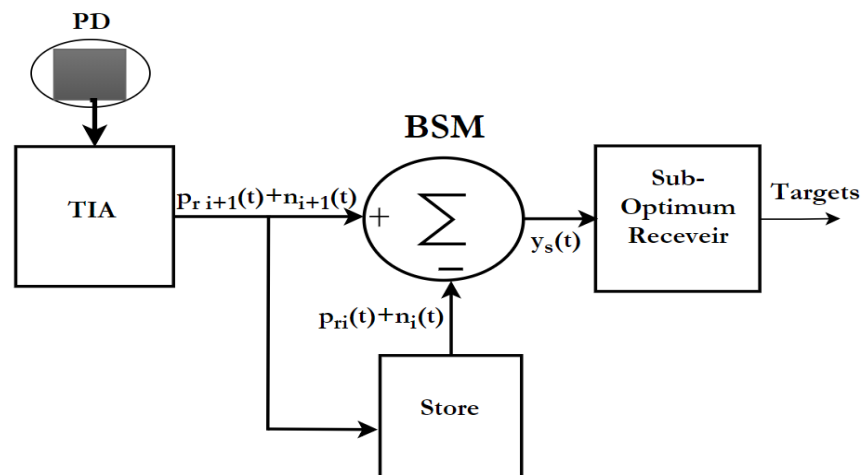


Figure 5.2: Receiver block diagram of LiDAL with BSM.

### 5.3 Cross-Correlation Method (CCM)

If there is target motion with continuous velocity (mobile) or discrete velocity (nomadic) in an indoor environment, the target can then be distinguished relative to the stationary background furniture by monitoring the changes in the received reflected signals through the use of multiple snapshots. We employed cross-correlation to identify the correlation between the snapshot measurements of the received reflected signals. Although there is relative motion between the target and  $T_{RX}$  unit, Doppler techniques cannot be used in LiDAL systems due to the limited target speed. Furthermore, cross-correlation is better than Doppler methods at low speeds, for example to estimate low velocity dispersion using ultrasound signals [166]. Also, cross-correlation has the advantage of detecting weak signals [167]. The peak displacement resulting from the cross-correlation between the two snapshots indicates target movement as the background obstacles are stationary and can also be used to determine target range.

In using cross-correlation we firstly look at coarse time scales to determine if there is a mobile target. We refer to this as fast cross-correlation. Here two snapshots are correlated over the full observation time window  $T$ . If target movement is detected, then a finer time scale cross-correlation is carried out at the slot level comparing two or more time slots, and carrying out each time a cross-correlation of up to  $S$  snapshots. We refer to this finer cross-correlation as slow cross-correlation. We furthermore define a binary Target Movement Indicator (TMI) whose value is equal to one if the fast or the slow cross-correlations show a change, TMI is equal to zero otherwise. Figure 5.3 presents the proposed LiDAL snapshot measurements cube for target movement and shows the values of TMI. In Figure 5.3, the  $y$  axis represents time and shows one time frame of duration  $T$  subdivided into  $N$  time slots. The  $z$  axis of Figure 5.3 represents the TMI values associated with fast cross-correlation when two snapshots are cross-correlated. Finally, the  $x$  axis represent TMI values for each time slot when the slow cross-correlation is evaluated. Note that the values of  $S$  indicate the number of snapshots cross-correlated. As can be seen in Figure 5.3, the first snapshot measurement ( $i=1$ ) is stored until the next measurement ( $i=2$ ) is collected.

Then a cross-correlation between the two snapshots for the whole time duration  $T$  is carried out to determine the TMI ('0' and '1') i.e to determine the 'fast cross-correlation'. In this case, cross-correlating the ( $i=1$ ) and ( $i=2$ ) snapshots yields  $TMI=0$ . If TMI is equal to zero, the fast cross-correlation is continued, to carry out cross-correlation between the current snapshot ( $i=2$ ) and the next snapshot ( $i=3$ ). However, if TMI is equal to one, multiple cross-correlations are implemented between the identical time slots of the consecutive snapshots yielding the slow cross-correlation. The slow cross-correlation determines the TMI values associated with each time slots. The value of the TMI associated with slot  $j$  is referred to as a weight ( $w_j$ ) which represents change / no change in each time slot. For example,  $S=4$  represents cross-correlation between snapshots ( $i=1$ ), ( $i=2$ ), ( $i=3$ ) and ( $i=2$ ) and yields a TMI value for each time slot where the TMI values ( $w_j$ ) are ( $w_1, w_2$  and  $w_3=1, w_4, w_5$  and  $w_6=0$ ). The values of the TMI weights are integrated in the proposed LiDAL sub-optimum receiver to detect and localise the targets as will be discussed in conjunction with Figure 5.8.

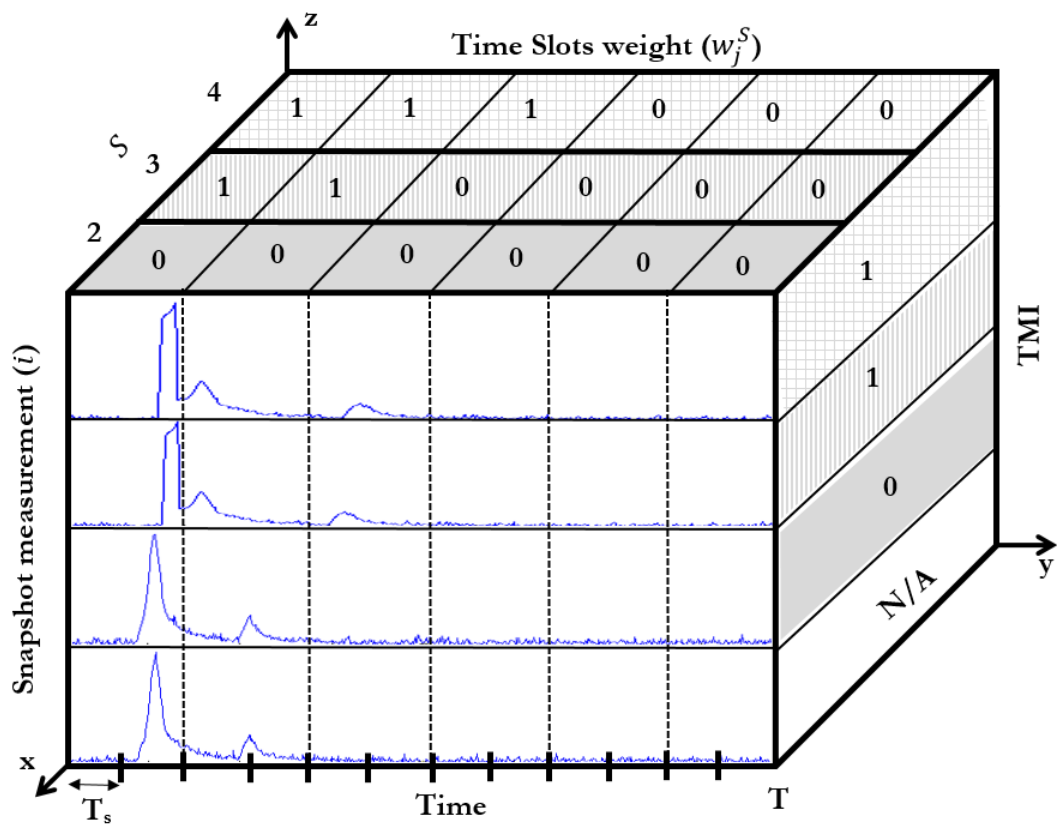


Figure 5.3: LiDAL snapshots measurement cube.

### 5.3.1 Fast Cross-correlation

To investigate the performance of the proposed cross-correlation method let us consider (i) a single mobile target with a stationary background obstacle, (ii) no ambiguity (i.e. the minimum distance between the mobile target and the background obstacle is  $\Delta R$  or more) and (iii) white Gaussian noise due to the receiver and ambient noise as discussed in Chapter 3. Here, we analyse the key scenarios of interest and in particular we consider five propositions / scenarios to test the fast cross-correlation method to decide the TMI.

**Proposition I:** we assume that there is no target in the environment, only (background) obstacle in the two snapshot measurements ( $i, i + 1$ ) as can be seen in Figure 5.4a. The received signal reflected from the obstacle in the presence of noise in the  $i^{th}$  snapshot,  $p_{r_i}(t)$ , can be expressed as:

$$p_{r_i}(t) = \beta_i b(t - t_{b_i}) + n_i(t) \quad (5.5)$$

and the received signal  $p_{r_{i+1}}(t)$  is given as:

$$p_{r_{i+1}}(t) = \beta_{i+1} b(t - t_{b_{i+1}}) + n_{i+1}(t) \quad (5.6)$$

The fast cross-correlation function ( $\mathcal{R}_{p_{r_i} p_{r_{i+1}}}$ ) of equations (5.5) and (5.6) over the listening time  $T$  is:

$$\mathcal{R}_{p_{r_i} p_{r_{i+1}}}(\tau) = \mathcal{R}_{bb}(\tau) + \mathcal{R}_{bn}(\tau) + \mathcal{R}_{nn}(\tau) \quad (5.7)$$

where the term  $\mathcal{R}_{bb}$  is an auto-correlation function of the received signal from the obstacle which is defined as:

$$\mathcal{R}_{bb}(\tau) \triangleq \int_{-T}^T \beta_i b(t - t_{b_i}) \beta_{i+1} b(t - t_{b_{i+1}} + \tau) dt \quad (5.8)$$

and  $\mathcal{R}_{sn}$  is the cross-correlation of the received signal (from the obstacle) with noise; and  $\mathcal{R}_{nn}$  is the noise auto-correlation. These two correlations are given as:

$$\mathcal{R}_{bn}(\tau) \triangleq \int_{-T}^T \beta_i b(t - t_{b_i}) n_{i+1}(t + \tau) dt + \int_{-T}^T \beta_{i+1} b(t - t_{b_{i+1}}) n_i(t + \tau) dt \quad (5.9)$$

and

$$\mathcal{R}_{nn}(\tau) \triangleq \int_{-T}^T n_i(t) n_{i+1}(t + \tau) dt \quad (5.10)$$

The correlation factor  $\hat{t}$  (i.e. displacement factor which represents the time delay) can be calculated by determining  $\tau = \hat{t}$  for which  $\mathcal{R}_{bb}$  is maximised. Therefore,  $\hat{t}_{bb}$  is defined as:

$$\hat{t}_{bb} = \arg \max_{\tau} (\mathcal{R}_{bb}(\tau)) \quad (5.11)$$

It should be noted that the noises in the snapshot measurements are assumed uncorrelated and orthogonal, thus  $\mathcal{R}_{nn} \approx 0$  [168], [169]. Also, the value of  $\mathcal{R}_{bn}$  can be assumed very small and can thus be neglected [168], [169]. Hence,  $\mathcal{R}_{bb}(\hat{t}_{bb})$  identifies whether there is a change or not between the snapshot measurements. For proposition I, the obstacle is stationary ( $t_{b_i} = t_{b_{i+1}} \forall i$ ). Therefore  $\hat{t}_{bb} = 0$ , see Figure 5.4b, indicates that no change took place in the “target” location (TMI=0). Note that the received signal is sampled with  $T_{sa} = 0.01\text{ns}$  which yields the x axis scale of Figure 5.4b.

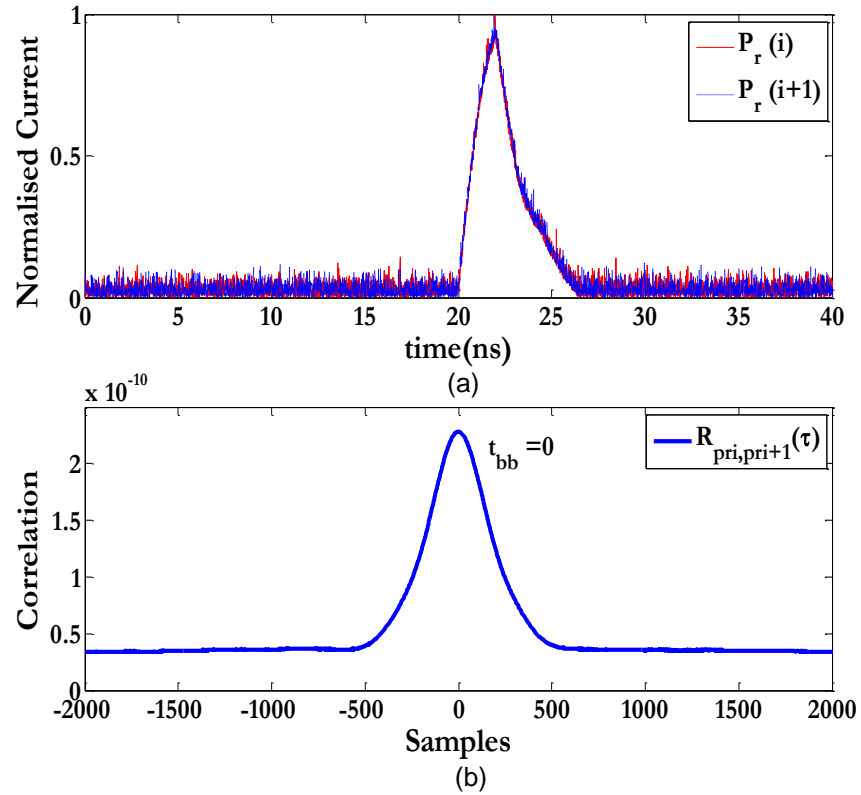


Figure 5.4: (a) received reflected signals in two snapshots measurement in Proposition I and (b) CCM of received snapshots measurement of Proposition I.



**Proposition II:** We assumed that the target appears in the environment in the  $i^{th} + 1$  snapshot measurement while the  $i^{th}$  snapshot includes only the stationary obstacle as depicted in Figure 5.5a. The received signal reflected from the target and the obstacle in noise,  $p_{r_{i+1}}(t)$ , is given as:

$$p_{r_{i+1}}(t) = \alpha_{i+1}m(t - t_{m_{i+1}}) + \beta_{i+1}b(t - t_{b_{i+1}}) + n_{i+1}(t) \quad (5.12)$$

while  $p_{r_i}(t)$  is as given in (5.1). Thus using (5.1) and (5.12)  $\mathcal{R}_{p_{r_i}p_{r_{i+1}}}(\tau)$  is given by:

$$\mathcal{R}_{p_{r_i}p_{r_{i+1}}}(\tau) = \mathcal{R}_{bm}(\tau) + \mathcal{R}_{bb}(\tau) + \mathcal{R}_{bn}(\tau) + \mathcal{R}_{mn}(\tau) + \mathcal{R}_{nn}(\tau) \quad (5.13)$$

where  $\mathcal{R}_{bm}(\tau)$  is the cross-correlation function between the signal received from the target and that received from the obstacle, while  $\mathcal{R}_{mn}(\tau)$  is the cross-correlation between the signal reflected from the target and noise. Thus  $\mathcal{R}_{bm}(\tau)$  is written as:

$$\mathcal{R}_{bm}(\tau) \triangleq \int_{-T}^T \beta_i b(t - t_{b_i}) \alpha_{i+1} m(t - t_{m_{i+1}} + \tau) dt \quad (5.14)$$

and the  $\mathcal{R}_{mn}(\tau)$  is:

$$\mathcal{R}_{mn}(\tau) \triangleq \int_{-T}^T \alpha_{i+1} m(t - t_{m_{i+1}}) n_i(t + \tau) dt \quad (5.15)$$

It should be noted that,  $\mathcal{R}_{mn}(\tau)$  can be neglected in a similar fashion to the decision to neglect  $\mathcal{R}_{bn}$ . The peak in the target-obstacle cross-correlation occurs at  $\hat{t}_{bm}$  which can be calculated as  $\hat{t}_{bm} = \arg \max_{\tau} (\mathcal{R}_{bm}(\tau))$ . For proposition II,  $\hat{t}_{bm} \neq 0$  and  $\hat{t}_{bb} = 0$ . Thus,  $\hat{t}_{bm}$  indicates the change that occurred due to the target presence (TMI=1) as can be seen in Figure 5.5b.

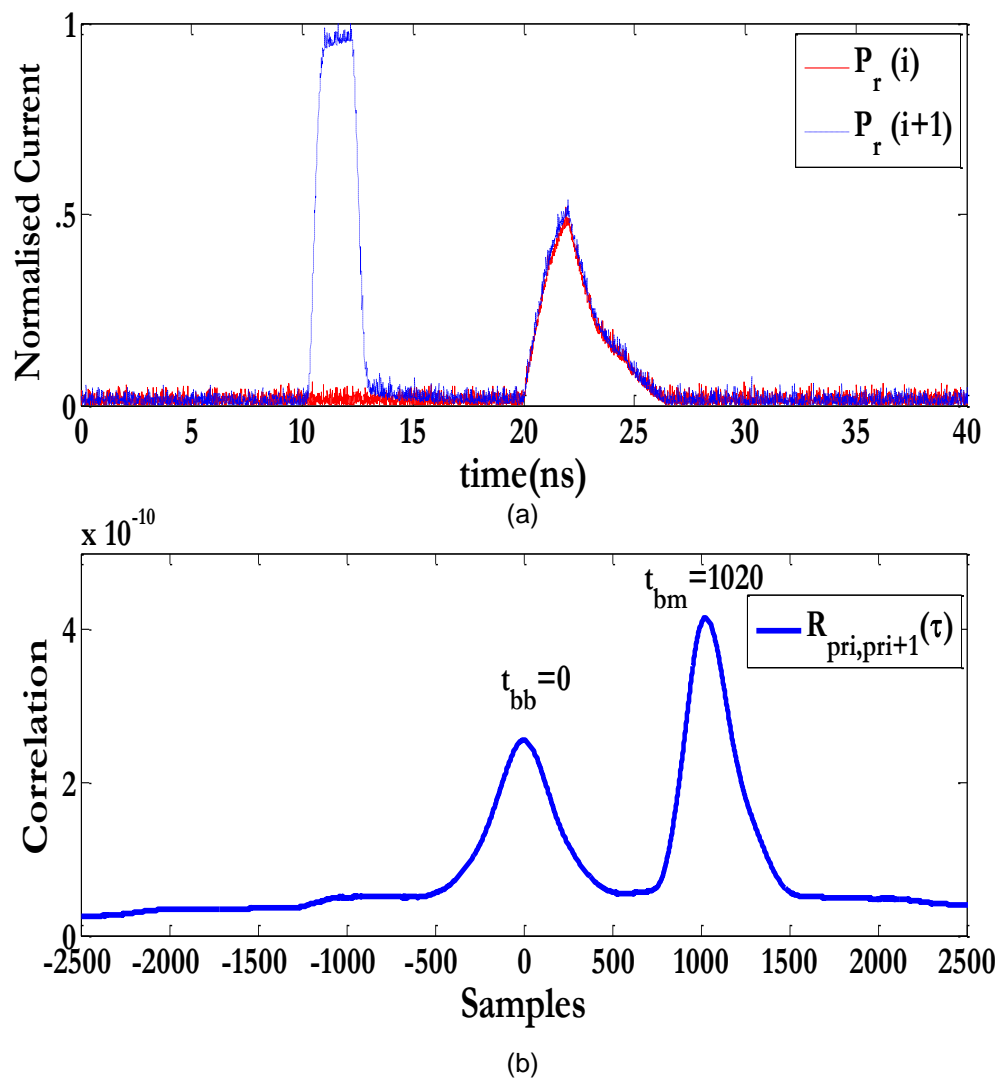


Figure 5.5: (a) received reflected signals in two snapshots measurement in Proposition II and (b) CCM of received snapshots measurement of Proposition II.

**Proposition III:** Here we assumed the presence of a mobile target in two successive snapshot measurements with a stationary obstacle as shown in Figure 5.6a. The received reflected signals are:

$$p_{r_i}(t) = \alpha_i m(t - t_{m_i}) + \beta_i b(t - t_{b_i}) + n_i(t) \quad (5.16)$$

and:

$$p_{r_{i+1}}(t) = \alpha_{i+1} m(t - t_{m_{i+1}}) + \beta_{i+1} b(t - t_{b_{i+1}}) + n_{i+1}(t) \quad (5.17)$$

The cross-correlation ( $\mathcal{R}_{p_{r_i}, p_{r_{i+1}}}$ ) of equations (5.16) and (5.17), gives:

$$\mathcal{R}_{p_{r_i}, p_{r_{i+1}}}(\tau) = \mathcal{R}_{mm}(\tau) + \mathcal{R}_{mb}(\tau) + \mathcal{R}_{bm}(\tau) + \mathcal{R}_{bb}(\tau) + \mathcal{R}_{bn}(\tau) + \hat{\mathcal{R}}_{mn}(\tau) + \mathcal{R}_{nn}(\tau) \quad (5.18)$$

where  $\mathcal{R}_{mm}$  is the auto-correlation function of the received reflected signal from the target given as:

$$\mathcal{R}_{mm}(\tau) \triangleq \int_{-T}^T \alpha_i m(t - t_{m_i}) \alpha_{i+1} m(t - t_{m_{i+1}} + \tau) dt \quad (5.19)$$

The cross-correlation  $\mathcal{R}_{mb}(\tau)$  is given as:

$$\mathcal{R}_{mb}(\tau) \triangleq \int_{-T}^T \alpha_i m(t - t_{m_i}) \beta_{i+1} b(t - t_{b_{i+1}} + \tau) dt. \quad (5.20)$$

The cross-correlation  $\hat{\mathcal{R}}_{mn}(\tau)$  is given by:

$$\begin{aligned} \hat{\mathcal{R}}_{mn}(\tau) \triangleq & \int_{-T}^T \alpha_{i+1} m(t - t_{m_{i+1}}) n_i(t + \tau) dt \\ & + \int_{-T}^T \alpha_i m(t - t_{m_i}) n_{i+1}(t + \tau) dt. \end{aligned} \quad (5.21)$$

The time  $\hat{t}_{mm}$  is defined as  $\hat{t}_{mm} = \arg \max_{\tau} (\mathcal{R}_{mm}(\tau))$  while  $\hat{t}_{mb} = \arg \max_{\tau} (\mathcal{R}_{mb}(\tau))$ . In proposition III, we are interested in observing the values of  $\hat{t}_{mm}$ ,  $\hat{t}_{mb}$ ,  $\hat{t}_{bm}$  and  $\hat{t}_{bb}$ , as seen in Figure 5.6b, to determine whether a change has occurred or not between the snapshot measurements.

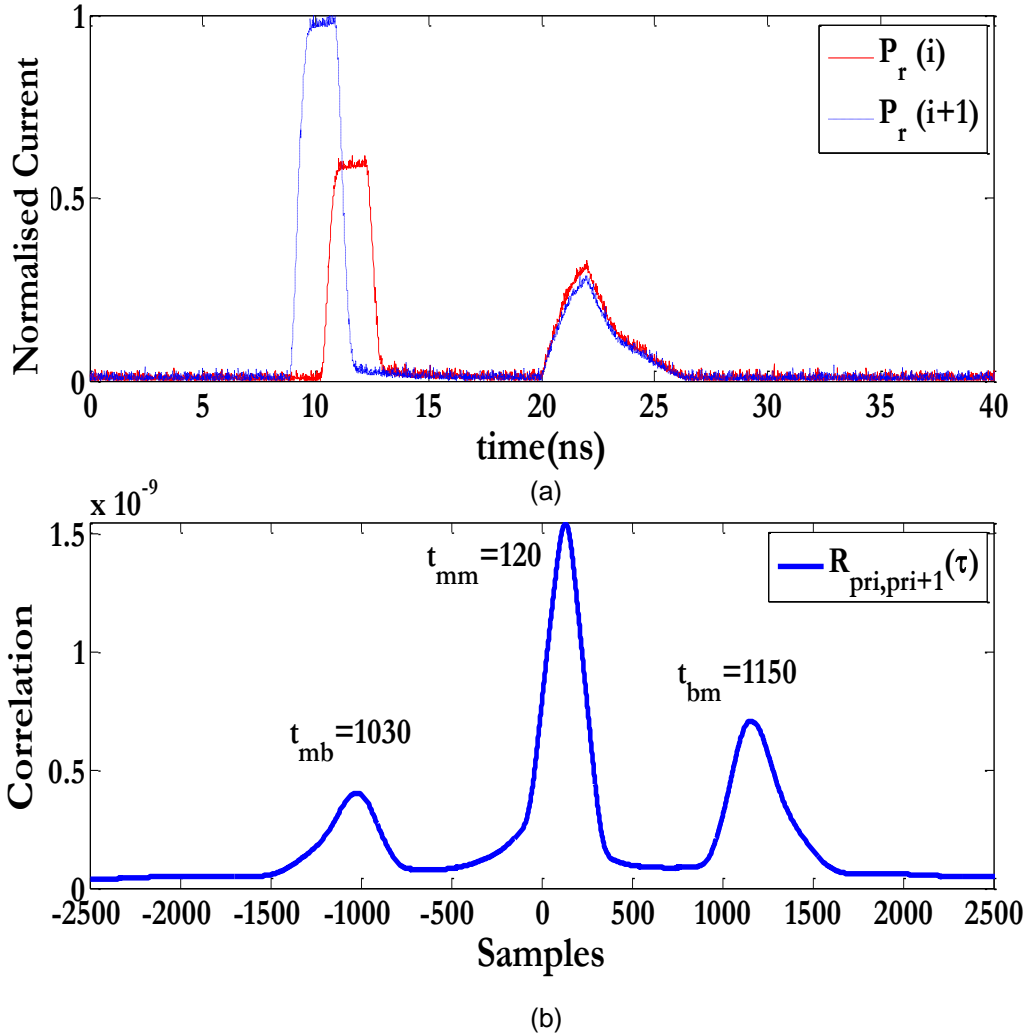


Figure 5.6: : (a) received reflected signals in two snapshots measurement in Proposition III and (b) CCM of received snapshots measurement of Proposition III.

**Proposition IV:** In this proposition, we assume that the target and the obstacle are stationary during the snapshot measurements as presented in Figure 5.7a. Here the cross-correlations will have the same definitions as in proposition III, however,  $t_{m_i} = t_{m_{i+1}}$  (ie a stationary target). Therefore, as can be seen in Figure 5.7b  $\hat{t}_{mb} = \hat{t}_{bm}$  and the corresponding (side) peaks have the same magnitude.

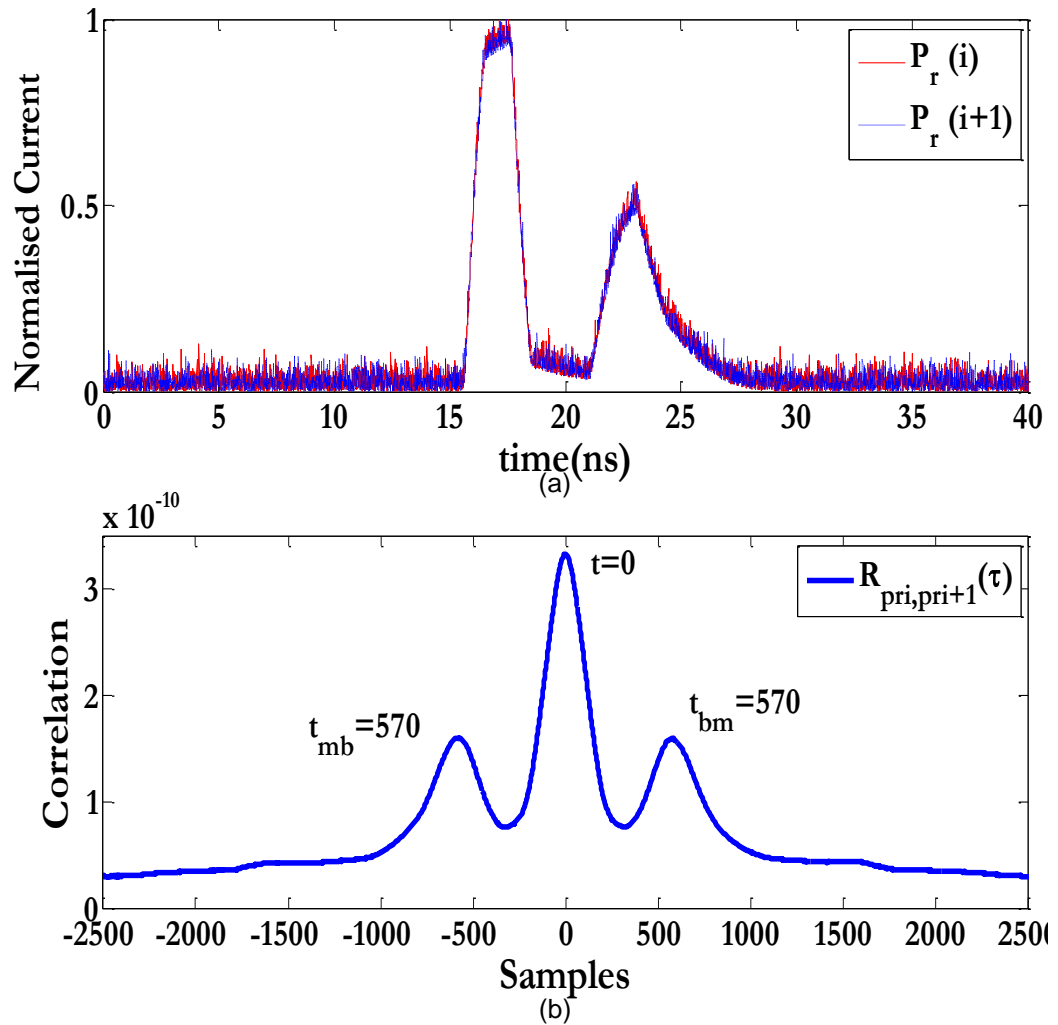


Figure 5.7: (a) received reflected signals in two snapshots measurement in Proposition IV and (b) CCM of received snapshots measurement of Proposition IV.

**Proposition V:** We assumed in this case that in the  $i^{th}$  snapshot the target and the obstacle are present, while in the  $i^{th} + 1$  snapshot, only the obstacle is present (i.e. the target left the environment). This is similar to Proposition II, the case shown in Figure 5.5a, but with the  $p_{r_i}(t)$  and  $p_{r_{i+1}}(t)$  exchanging their roles. Here  $\hat{t}_{mb} \neq 0$  and  $\hat{t}_{bb} = 0$ . The cross-correlation will be similar to that shown in Figure 5.5b.

Table 5.1 summarises the fast correlation outcomes and the value of TMI associated with two consecutive snapshot measurements in LiDAL.

Table 5.1: Target movement indicator decision

| Proposition | Arrival times<br>$t_i, t_{i+1}$                       | Correlation factor $\hat{t}$   | Decision<br>TMI |
|-------------|---|--|-----------------|
| I           | $t_{b_i} = t_{b_{i+1}}$                               | $\hat{t}_{bb} = 0$   | 0               |
| II          | $t_{b_i} = t_{b_{i+1}}, t_{m_{i+1}} \neq t_{b_i}$     | $\hat{t}_{bb} = 0, \hat{t}_{bm} \neq 0$  | 1               |
| III         | $t_{b_i} = t_{b_{i+1}}, t_{m_i} \neq t_{m_{i+1}}$     | $\hat{t}_{bb} = 0, \hat{t}_{mm} \neq 0,$<br>$ \hat{t}_{mb}  \neq  \hat{t}_{bm} $ | 1               |
| IV          | $t_{b_i} = t_{b_{i+1}}, t_{m_i} = t_{m_{i+1}}$        | $\hat{t}_{bb} = 0, \hat{t}_{mm} = 0,$<br>$ \hat{t}_{mb}  =  \hat{t}_{bm} $       | 0               |
| V           | $t_{b_i} = t_{b_{i+1}},  t_{m_i}  \neq  t_{b_{i+1}} $ | $\hat{t}_{bb} = 0, \hat{t}_{mb} \neq 0$  | 1               |

### 5.3.2 Slow Cross-correlation

The slow cross-correlation is employed over the duration of the time slot  $T_{s_j}$  where the same time slot in the frame is considered over several ( $S$ ) consecutive snapshots measurements. The cross-correlation  $\mathcal{R}_{xy}(\tau, T_{s_j})$  can be given as:

$$\mathcal{R}_{p_{r_i}, p_{r_{i+1}}}(\tau, T_{s_j}) \triangleq \int_{-T_s}^{T_s} p_{r_{i+1}}(t - T_{s_j} + \tau) \sum_{i=1}^S p_{r_i}(t - T_{s_j}) dt \quad (5.22)$$

where,  $i \in [1, \dots, S]$  and  $S$  is the total number of snapshots. The time slot correlation factor  $\hat{t}_{T_{s_j}}$  is calculated as:

$$\hat{t}_{T_{s_j}}^S = \arg \max_{\tau} \left( \mathcal{R}_{p_{r_i}, p_{r_{i+1}}}(T_{s_j}, \tau) \right) \quad (5.23)$$

It should be noted that, if the value of  $\hat{t}_{T_{s_j}}^S$  changes for different values of  $S$  (i.e. when, more snapshots measurements are considered), then this indicates the presence of the target in a time slot  $T_{s_j}$ . Thus, when  $\hat{t}_{T_{s_j}}^S$  equals to zero, this indicates no change between the received reflected pulses in  $T_{s_j}$  in  $S$  consecutive snapshots.

We define a time slot weight  $w_j^S$  in CCM to be used in the operation of the LiDAL sub-optimum receiver. The weight  $w_j^S$  is defined as:

$$w_j^S = \begin{cases} 0 & \text{if } \hat{t}_{T_{s_j}}^S = 0 \\ 1 & \text{otherwise} \end{cases} \quad (5.24)$$

Equation (5.24) can be understood by observing that  $\hat{t}_{T_{s_j}}^S$  is the time slot at which the peak of the correlation occurs. If there is no target and hence no motion, then the correlation (5.22) is an auto-correlation whose peak occurs at  $\hat{t}_{T_{s_j}}^S = 0$  and therefore, the  $w_j^S$  is equal to zero in this case indicating the absence of the target.

The time of arrival (TOA) of the received reflected pulse from the target in  $T_{s_j}$  can be determined as:

$$TOA_j = \arg \max_{\tau} \left( \int_{-T_s}^{T_s} w_j^S p_{ri} (t - T_{s_j} + \tau) x(t) dt \right) \quad (5.25)$$

Equation (5.25) can only have a meaningful use if the receiver time slot of interest is large and the received pulse is much narrower than the time slot. In which case equations (5.22) and (5.24) identify the time slot in which the reflected pulse from target occurs (i.e. time slot number); while equation (5.25) can identify the target pulse location within a time slot.

Figure 5.8 presents the LiDAL optimum receiver for target distinguishing and detection using CCM. As can be noted in Figure 5.8, The output of CCM is represent by time slot weights  $w_j^S$  which are multiplied by the orthonormal expansion coefficient,  $\Phi_j(t)$ , of each time slot. The target indicator block has to be allowed to operate and accumulate  $S$  snapshots (see second term of equation (5.22)) and hence produce  $w_j^S$  values for the  $j^{th}$  slot and for  $N$  time slots before the sub-optimum receiver starts operating. This is only an initialization phase. Furthermore, the  $w_j^S$  weights cause the  $j^{th}$  slot to produce zero energy in the SOR if there is no target motion, hence stopping the SOR from reporting the reflected pulse from an obstacle as a target.



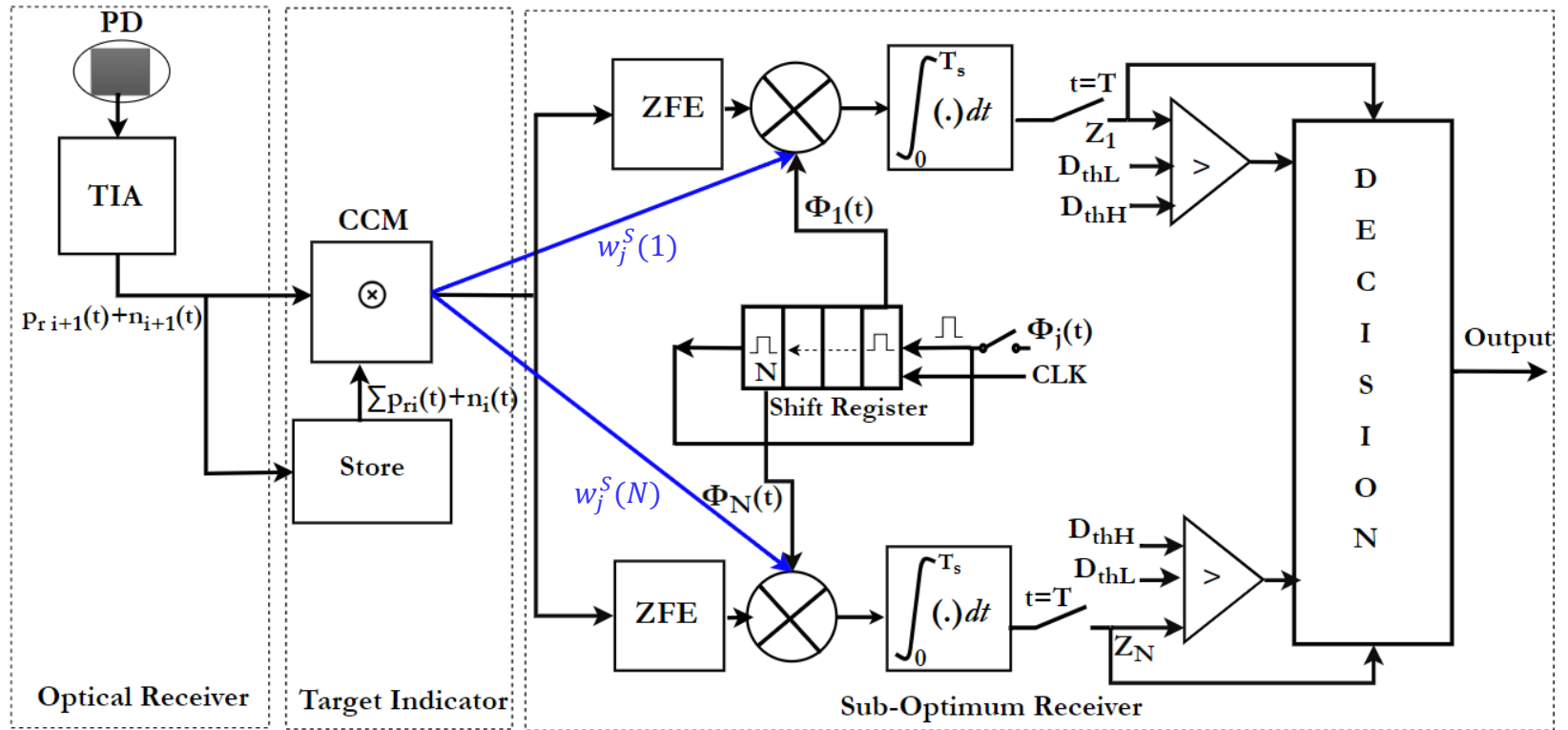


Figure 5.8: LiDAL receiver block diagram with CCM.

## 5.4 Target Mobility Modelling

Target distinguishing relies on the target movement in the indoor environment in conjunction with the use of the BSM and CCM distinguishing approaches in our study. Target movement leads to a change in the observed signals received by LiDAL. Therefore, modelling the target mobility behaviour is essential to examine the performance of the proposed LiDAL systems. A random walk approach that avoids obstacles is considered for pedestrian and nomadic targets in the realistic indoor environment. For pedestrian targets, we assumed continuous movement at a speed of 1m/s, while for the nomadic targets, discrete movement is assumed.

Three distinct additional studies can be conducted in this area. We address two of these and leave the third for future work. Firstly, mobility helps distinguish targets, however not all locations may be allowed in the room or indoor environment, due to obstacles and furniture. To account for this, we define a space utilization factor (SUF) that effectively reflects the reduction in the allowed target mobility. Secondly, some spaces may be more popular than others, for example a working desk surface in a room. We account for this in simulations by using different transition probabilities from location to another. This is also used to reflect possible target nomadic behaviour. Thirdly, the probability of correct decisions at the output of the receiver, such as that given in Chapter 4 equation (4.41) can be combined with the probability of detecting target movement as derived in this section to give a combined performance analysis of the receiver and the human mobility pattern and indoor space configuration. In this third study target motion through a number of steps in a given time window (for example a one second time window) provides more repeated opportunities for the receiver to detect the moving target. This can be analysed within the framework of repetition coding. This third study area warrants further research and is not reported here. We consider the first two studies in this section.

### 5.4.1 Probability of Mobility Detection ( $P_{MD}$ )

The BSM and CCM employ snapshot measurements to distinguish the target. This relies on the target's motion where a minimum step distance of  $\Delta R$  (LiDAL resolution) is assumed. The calculation of the probability of detection is related to: (i) the probability that the target moves from location ( $L_1$ ) to location ( $L_2$ ) and (ii) the number of target steps required to achieve a  $\Delta R$  distance. In order to determine the probability of detection, the following setting was considered:

- 1) A Markov chain is considered as a representation of the random walk process on a graph. This models the target mobility behaviour in the indoor environment in two dimensions. Markov chain models allow the target walking behaviour to be represented either on directed or on undirected paths [170], [171]. The presence of obstacles was accounted for through the elimination of certain transitions in the Markov chain.
- 2) The indoor environment floor of the interest  $G(x, y)$  is divided into a 2D grid with size  $j \times i$  and  $L$  locations where  $L = \frac{x \times y}{\Delta_l^2}$ ,  $i = \frac{x}{\Delta_l}$  and  $j = \frac{y}{\Delta_l}$ ; here  $\Delta_l$  is the inter-locations distance as shown in Figure 5.9.
- 3) The target can move in space to one of  $N_D$  neighbour destinations ( $N_D \in [l_1, \dots, l_{N_D}]$ ) or can stay at the current location ( $l_c$ ) as shown in Figure 5.9. The Markov chain considered is a stochastic process on states defined in terms of a transition matrix ( $P$ ) ( $N_D + 1$  rows and  $N_D + 1$  columns). The transition matrix of the graph in Figure 5.9 is given as:

$$P = \begin{bmatrix} p_{s(1)} & p_{m(1,2)} & p_{m(1,N_D)} \\ p_{m(2,1)} & p_{s(2)} & p_{m(2,N_D)} \\ \vdots & \ddots & \vdots \\ p_{m(L,1)} & \cdots & p_{s(L)} \end{bmatrix} \quad (5.26)$$

where  $p_{s(i)}$  is the probability of the target staying in the current state (location  $i$ ) which is related to the target's behaviour,  $p_{m(i,j)}$  is the probability of the target moving from current location ( $i$ ) to one of the neighbour locations ( $j$ ).

- 4) We have considered an undirected target motion pattern. Typically, the target walks to one of  $L$  random locations inside an indoor environment where at each location the probability of the target staying at the current location ( $i$ ),  $p_{s(i)}$ , can be written as:

$$p_{s(i)} = 1 - \sum_{j=1}^{N_D} p_{m(i,j)} \quad j \neq i \quad (5.27)$$

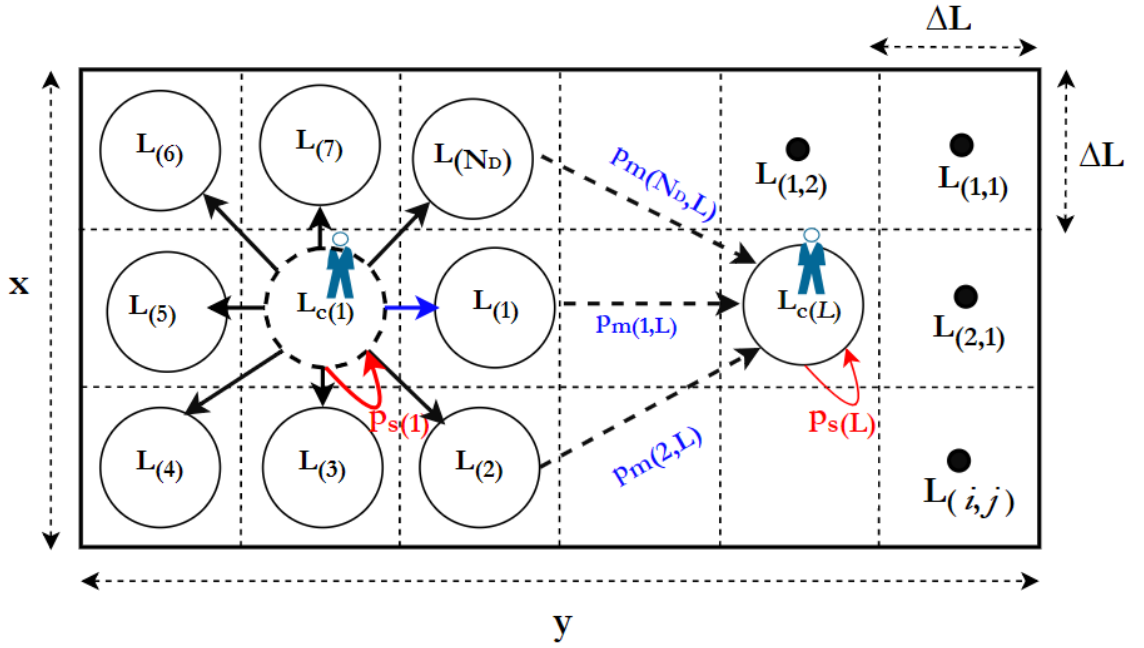


Figure 5.9: Target random walk model in  $G(x, y)$  space.

To simplify the setup of modelling the indoor environment, let the inter-locations distance equal to the LiDAL resolution (i.e.  $\Delta_l = \Delta R$ ). Thus the grid size considered is  $\left(\frac{x}{\Delta R} \times \frac{y}{\Delta R}\right)$ . This is reasonable as  $\Delta R$  is typically about 30 cm where we set this design parameter for LiDAL resolution and it is the minimum typical expected distance between people in an indoor environment. Also, we will assume that pedestrians move at a speed that is an integer multiple of  $\Delta R$  m/s to simplify the analysis. Therefore, if the pedestrian speed is  $v$  m/s, then in one second the pedestrian visits  $\frac{v}{\Delta R}$  locations at most. At each location the target can be distinguished since it has moved at least  $\Delta R$  which is a change that can be captured in the snapshot measurements. Therefore, the probability of target movement detection taking into account the target speed in an empty indoor environment,  $G_E(x, y)$ ,  $P_{MDT}^E$  can be expressed as:

$$P_{MD}^E = \left( \frac{\Delta R^2}{xy} \right) \sum_{j=1}^L \sum_{i=1}^{N_D} p_{(i,j)}. \quad (5.28)$$

Equation (5.28) describes the probability of target movement in an empty environment that has  $L$  possible locations with  $N_D$  neighbour destination to each current location. The probability  $p_{(i,j)}$  depends on target activity behaviour (nomadic, continuous motion etc). It is worth mentioning that, we assumed for all  $L$  possible locations an equal probability of being in that location, given by  $\left( \frac{\Delta R^2}{xy} = \frac{1}{L} \right)$ .

For a realistic indoor environment  $G_R(x, y)$ , free flow in the space is hindered by obstacles (i.e. furniture and walls) where the target movement is restricted and mobility detection can be harder. Therefore, we introduce a 'space utilization factor' in realistic environments to determine the target probability of detection.

The space utilisation factor  $SUF$  can be written as:

$$SUF = 1 - \left( \frac{\Delta R^2}{xy} \right) \left( \frac{1}{N_D} \right) \sum_{j=1}^L \left( N_D - \frac{1}{p_{(j)}} \right) \quad (5.29)$$

where,  $p_{(j)}$  is a property of the current location  $j$  and is given as  $p_{(j)} = \frac{1}{N_A}$ . Note that  $N_A$  is the number of neighbour locations of location  $j$  allowed for the target to move to; with  $N_A \leq N_D$ . The space utilization factor,  $SUF$ , has a unity value for a room that has no obstacles ( $N_A = N_D$ ), while for a room with obstacles ( $N_A < N_D$ ),  $SUF$  is less than one.

The probability of target mobility detection in a realistic environment  $P_{MD_T}^R$  can be given as:

$$P_{MD_T}^R = SUF [P_{MD}^E] \quad (5.30)$$

Figure 5.10 presents the probability of target mobility detection in a realistic environment for different values of LiDAL resolutions and space utilised by background obstacles (furniture). The results are obtained for a pedestrian target walking randomly with a speed of  $v=1$  m/s in space of  $G_E(4\text{m}, 8\text{m})$ . The Markov transition matrix for the pedestrian behaviour selected has  $p_s=0.02$ ,  $\sum_i^{N_D} p_m=0.98$  and  $N_D=8$ . As can be seen in Figure 5.10, the space utilization  $SUF$  significantly affects the  $P_{MDT}^R$  due to variation in the space allowed for the target to be mobile.

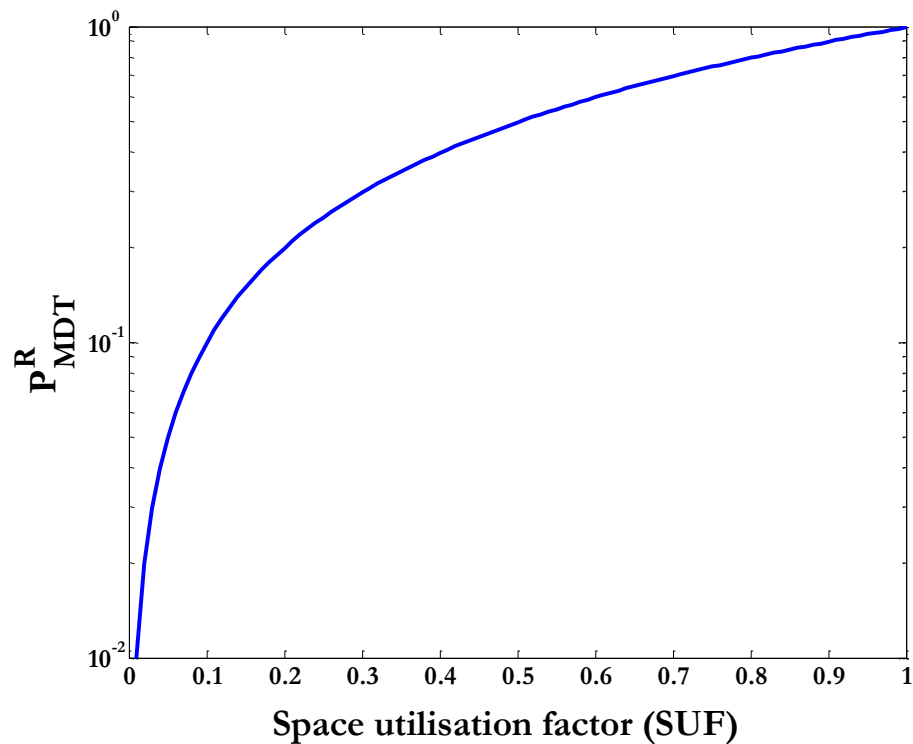


Figure 5.10: Probability of target mobility detection in a realistic environment.

### 5.4.2 Directed Random Walk with Obstacle Avoidance

In this model, we assume that the pedestrian and nomadic targets walk freely inside the room in all the directions except directions that lead to obstacles. In addition, we considered a common scenario where the targets arrival into the room follows a Poisson distribution [172], [173] and the time spent in the room follows a negative exponential distribution [174], [175].

Initially, targets reach the room's entrance at different arrival times  $t_a$  with an arrival rate of  $\lambda$  and mean time spent in the environment of  $1/\gamma$  and therefore in a simulation, the leaving times  $t_d$  can be determined. Targets spend times  $t_{sp}$  in the environment.

For nomadic behaviour in an indoor environment such as an office room, the nomadic target continuously walks inside the room until it reaches one of the interesting destinations (for instance an office desk). For each nomadic target,  $L_D$  interesting destinations are generated randomly where  $L_D \in [1, \dots, L]$ . It is assumed that the nomadic target has a speed of (0.5-2 m/s). A Markov transition matrix is then created for the current location to describe the probability of transition to its neighbours. We considered  $N_D=8$  neighbours that are equi-probable if no obstacle is present. In the presence of obstacles, some of the  $N_D$  directions have zero transition probabilities, while the rest are equi-probable. The decision of staying in the current location or moving to the next destination relies on the allocated probabilities in the transition matrix. Let us assume that the nomadic target has the same behaviour in terms of staying at the interesting destinations (i.e... the staying probability is equal among the locations of interest  $L_D$ ). Thus the probability of staying at a location  $l_D$  of interest ( $l_D \in [1, \dots, L_D]$ ) for a nomadic target is  $p_{s(l_D)}^{no} = \frac{1}{L_D}$  and the probability of moving is  $p_{m(l_D,j)}^{no} = \frac{1-p_{s(l_D)}^{no}}{N_D}$ . For the locations other than the  $L_D$  locations of high interest, ie for the  $l(i)$  general locations where ( $i \neq l_D$ ), the nomadic target moves with a speed  $v$ , thus the probability of staying at  $l(i)$  should be very small due to lack of interest. We thus set the  $p_{s(i)}^{no} = 0$  and  $p_{m(i)}^{no} = \frac{1-p_{s(i)}^{no}}{N_D}$ .

During the simulation the nomadic target follows the path with the highest probabilities. Note that, the neighbour destinations to the location of interest have equal probabilities, therefore, the next neighbour destination is decided on equi-probable basis.

The simulation starts with the arrival of targets into the environment following a Poisson distribution and proceeds by determining the time each target spends in the environment where this time follows a negative exponential distribution. The motion of the targets with the environment is then governed by the transition matrix probabilities.

Let the arrival rate to be  $\lambda$  per hour and let the average dwell time be  $1/\gamma$  in hours. Let  $T_{ob}$  be the observation window, ie the simulation time. The probability of having  $k$  arrivals in  $T_{ob}$  is given as:

$$p_a(k) = \frac{(\lambda T_{ob})^k}{k!} e^{-\lambda T_{ob}} \quad (5.31)$$

The probability of a target leaving after  $t_d$  is:

$$p_d(t_d) = \gamma e^{-\gamma t_d} \quad t_d < T_{ob} \quad (5.32)$$

The room is considered a form of  $M/M/1$  queue and therefore the maximum number of targets  $K$ , given  $\lambda$  and  $\gamma$ , can be written as:

$$K = \frac{\lambda/\gamma}{1 - \lambda/\gamma} \quad (5.33)$$

Note that, the European standards for the minimum workplace space required per person is  $3.7\text{m}^2$  for an office environment and  $2\text{m}^2$  for a meeting room [176]. Thus, in this work we set  $K=6$  for the office room presented in Figure 3.1 (with an area of  $8\text{m} \times 4\text{m}$ ) where the space left unoccupied by obstacles is  $24\text{m}^2$ . We have used  $\lambda = 12$  arrivals per hour and  $\gamma = 14$ , giving the average time spent in the room as  $\frac{K}{\lambda} = 30$  minutes.



### 5.4.3 Pathways Mobility Model

In this model, the targets move on pre-determined indoor pathways as shown in Figure 5.11. Note that, the targets' behaviour in terms of arrival rate, departure rates and number of destination of interest are similar to the setup discussed in the 'random walk with obstacle avoidance' model. However, in this model, there is no random target motion, the targets follow the pre-determined paths.

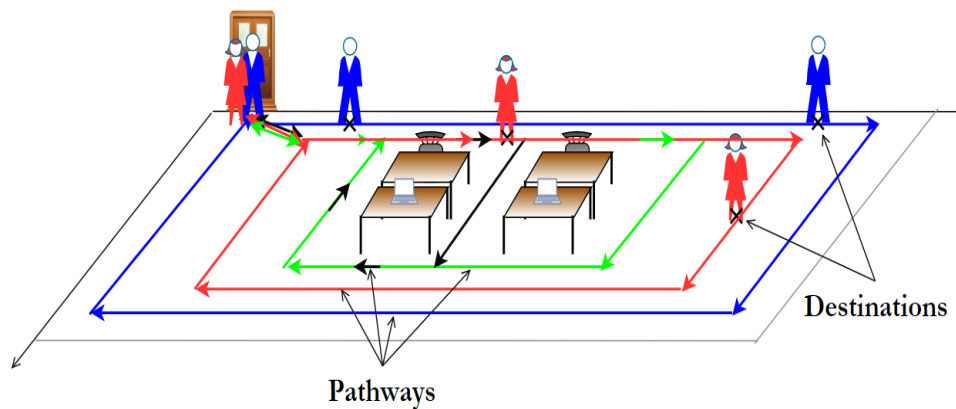


Figure 5.11: Pathways Mobility Model.

## 5.5 Background Estimation Method (BEM)

We introduce a reference signal pulse-response to estimate the background reflections. In this method, the target is distinguished based on eliminating the background reflections. Here, the target activity is not essential for distinguishing through multiple snapshots measurements as in BSM and CCM. Note that, we considered BEM to distinguish the target from background obstacles under the assumption that the environment obstacles are static. The BEM approach can be summarised as:

1. In absence of targets, the LiDAL system sends a reference pulse to observe the received reflected signals from the obstacles of an environment in each time slot  $w_j$  as can be seen in Figure 5.12. Table 5.2 illustrates the setup algorithm of LiDAL system use BEM.
2. Set the value of the observed time slots  $w_j$  of the received reference signal  $R_s(\tau)$  according to  $w_j = \begin{cases} 0, & \text{if } T_{s_j}^{RS} = 1 \\ 1, & \text{otherwise} \end{cases} \quad j \in [1, 2..N]$ , where,  $T_{s_j}^{RS}$  is the received reflected reference signal the  $j^{th}$  time slot.
3. When a target enters the environment, then a new peak (pulse) is observed in a time slot other than those pre-set to zero (i.e. occupied by obstacles).
4. The proposed receiver in Figure 5.12 is used with the BEM to force the background reflections to zero by multiplying the received reflected signal by the weights computed in (2) above. The  $w_j$  values are applied in the final decision block to distinguish the targets from the background obstacles once the sub-optimum receiver has determined the time slots that contain reflected pulses.

In contrast to the CCM, the values of the receiver time slots weights are fixed and pre-selected in the targets absence. However, any dramatic changes in the environment configurations require a re-measurement of the reference signal pulse response and calculation of  $w_j$ . Thus, the main limitation of the BEM approach is its need to constantly and continuously perform calibration.

Table 5.2: Setup algorithm of the background estimation method

| SETUP ALGORITHM OF BACKGROUND ESTIMATION METHOD |  |
|---|--|
| <b>Inputs:</b> $i_{max}$                        | Number of LiDAL transmitters                       |
| $j_{max}$                                       | Number of LiDAL receivers                          |
| $Rs(\tau)$                                      | Transmitted reference pulse signal.                |
| $P_r^{RS}$                                      | Received reflected reference pulse signal.         |
| 1.  | <b>for</b> $i = 1: i_{max};$                       |
| 2.  | <b>for</b> $j = 1: j_{max};$                       |
| 3.  | Send $Rs(\tau)$ from $T_x(i)$                      |
| 4.  | Listen $P_r^{RS}(i, j)$ and apply optimum detector |
| 5.  | Determine and save $w_j(i, j)$                     |
| 6.  | $j == j_{max}$                                     |
| 7.  | <b>end for</b>                                     |
| 8.  | $i == i_{max}$                                     |
| 9.  | <b>end for</b>                                     |

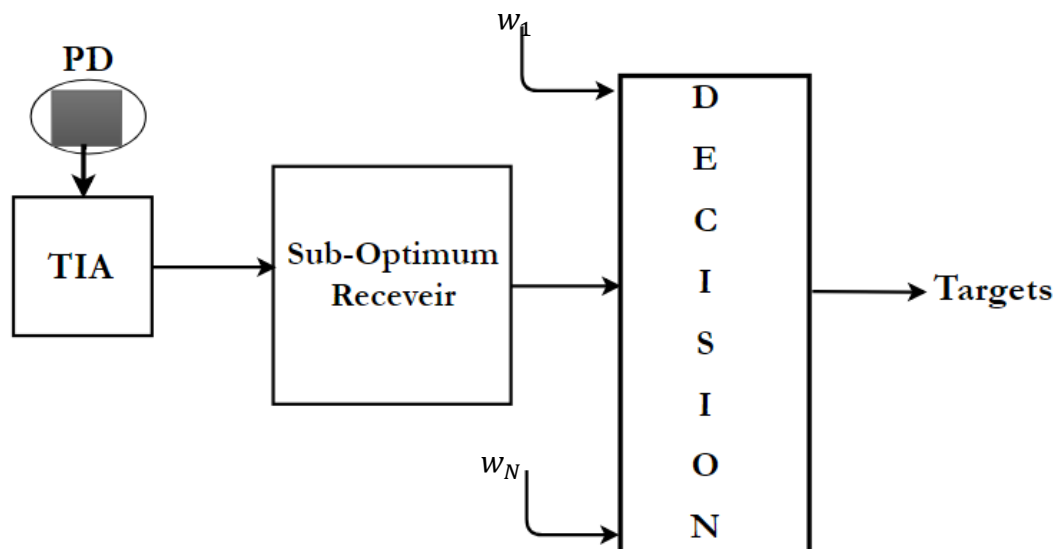


Figure 5.12: LiDAL receiver block diagram with BEM.

## 5.6 Target Distinguishing Evaluation

We have evaluated the performance of the three methods to distinguish a target in a realistic environment as shown in Figure 5.13. The evaluation is conducted in two scenarios, the first scenario included a static realistic environment where the background obstacles (furniture) are fixed over the simulation time with a single nomadic target that moves at a speed of 0.5m/s. The second scenario considered a dynamic realistic environment where the positions of some of the background obstacles (furniture) change over the simulation time in the presence of a nomadic target. A monostatic LiDAL system (collocated transmitter and receiver) was used in the room setup as shown in Figure 5.13. In addition, the pathway model was considered for target mobility with eight interesting locations ( $L_D=8$ ) in the room in Figure 5.13. Five snapshots measurements per second were collected to capture the target movement during the 5 minutes of simulation time. The total number of recorded snapshot measurements were 1500. Table 5.3 illustrates the simulation parameters of the Monostatic LiDAL system used in this experiment.

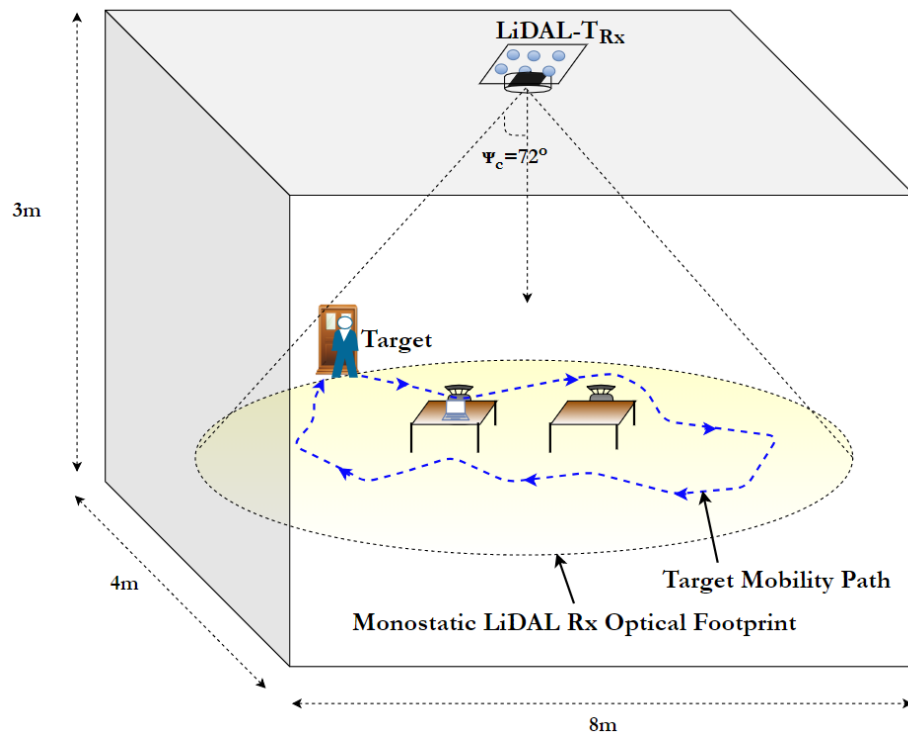


Figure 5.13: Simulation room setup with Monostatic LiDAL.

Figure 5.14 presents MAPE results, referred to here as the average (over the 1500 snapshot experiment) false distinguishing error for the first scenario, ie the static environment. The BEM is pre-calibrated in target absence and optimised for the room shown in Figure 5.13. The BEM reports target results for each snapshot. The BSM and CCM used two consecutive snapshots. As can be noted in Figure 5.14, the BEM has slightly better performance with 10% error as compared CCM and BSM with 11.3% and 19% respectively.

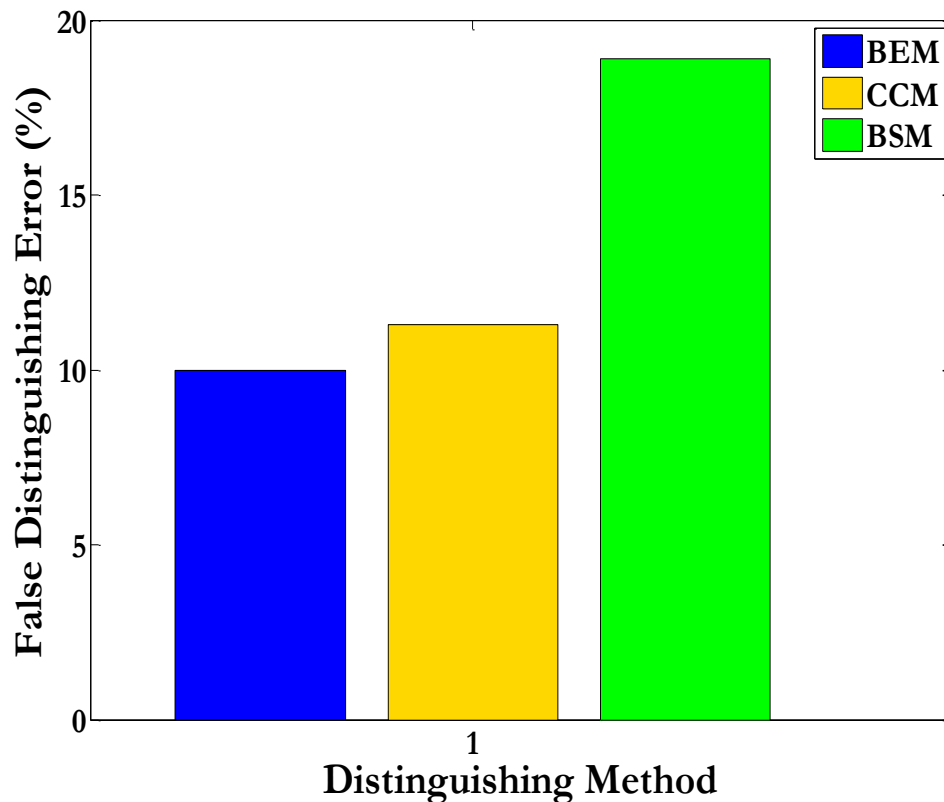


Figure 5.14: False target distinguishing error in static environment.

Note that in this experiment, there is a single moving target, the furniture is stationary and the percentage error reflects the ability of the methods to distinguish a moving target from furniture over the large number of snapshots considered. The BSM has the worst performance due to the impact of target presence and movement on the reflections of the background furniture and the particular sensitivity of subtraction to such changes. The CCM perform better, however they fail to distinguish the target only when target-furniture ambiguity occurred. In other words, when the distance between the target and furniture is less than the LiDAL resolution of 0.3m and at the same time, the target remained stationary, (nomadic), for more than 5 snapshots in our experiment. The CCM performance can be improved if the number of processed snapshots is increased to accommodate target mobility behaviour, however, this may slow the target detection process in LiDAL systems.

Figure 5.15 shows the average false target distinguishing error percentage for the second scenario, ie a dynamic environment. We simulated the impact of change in the environment, ie change in furniture configurations as can be seen in Figure 5.13 where the furniture positons were changed in each simulation. Note that, the BEM was calibrated and optimised before and after the target presence, but the furniture locations remained fixed throughout the training phase. As can be noted in Figure 5.15, the performance of BEM has significantly decreased with an error of 100% when we started changing the environment configurations without recalibrating the BEM. This 100% change in our case means that the two tables move from their initial positions at the centre of the room where they are each separated by 0.5m from the centre, to new locations next to the walls, a 2m movement for the 1.5m × 0.9m table. The BSM and CCM performed better than the BEM at 100% change in the environment, with a maximum error of 27% and 13% for BSM and CCM respectively.

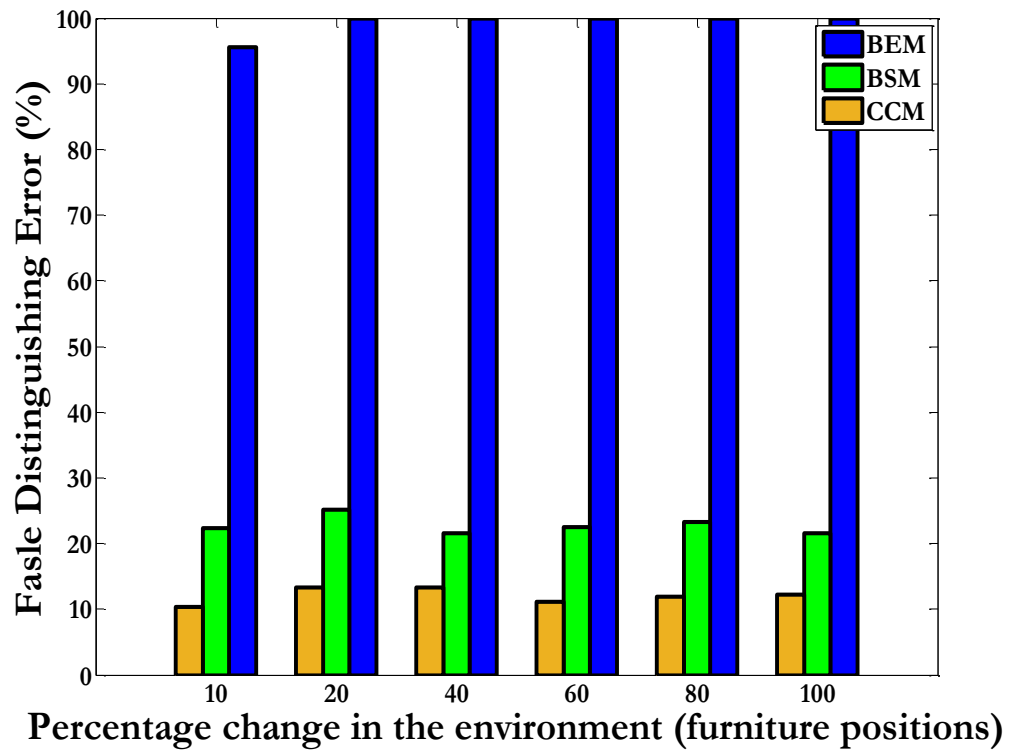


Figure 5.15: False target distinguishing error in dynamic environment.

Table 5.3: Simulation Parameters of Target Distinguishing

| Parameters  | Configurations             |
|---|----------------------------|
| Room  |                            |
| Length  | 8m                         |
| Width   | 4m                         |
| Height  | 3m                         |
| $\rho$ - wood (furniture)                         | 0.55                       |
| $\rho$ - floor                                    | 0.3                        |
| $\rho$ - walls                                    | 0.8                        |
| Bistatic LIDAL                                    |                            |
| location (x , y, z)                               | (2, 4, 3)                  |
| Elevation   | 90°                        |
| Azimuth   | 0°                         |
| Number of RGB-LDs in each unit                    | 9 (3 X 3)                  |
| Transmitted optical power of RGB-LD               | 2 W (Red , Green , Blue )  |
| LD semi-angle at half power beam width ( $\Phi$ ) | 75°                        |
| Photodetector Area                                | 20 mm <sup>2</sup>         |
| Photodetector Responsivity                        | 0.4 A/W                    |
| Acceptance Semi-angle                             | 72°                        |
| Concentrator Reflective Index ( $M$ )             | 1.7                        |
| TIA noise current                                 | 2.5 pA/ $\sqrt{\text{Hz}}$ |
| Receiver Bandwidth                                | 300 MHz                    |
| Time Bin Duration                                 | 0.01 ns                    |
| Transmitted Pulse width $\tau$                    | 2ns                        |
| Sampling Time $T_{sa}$                            | 0.1ns                      |
| Resolution $\Delta R$                             | 0.30m                      |
| Receiver Time slot $T_s$                          | 2ns                        |



## 5.7 Summary

In this chapter, we introduced three methods that use human motion to distinguish human targets from furniture; namely the background subtraction method (BSM), the cross correlation method (CCM) and background estimation method (BEM). We integrated both methods in the receiver designs developed. To distinguish reflections due to furniture from reflections attributed to the human targets, we used human mobility as the discriminator. To enable the evaluation of our LiDAL systems in a realistic environment, we furthermore developed models for human motion in the indoor environment of interest. In particular, we developed a directed random walk with obstacle avoidance mobility model and a pathway mobility model. Both models are based on Markov chains.

Chapter 6 will address the design of MIMO LiDAL system for targets detection, counting and localisation.

# Chapter 6

## MIMO LiDAL System

### 6.1 Introduction

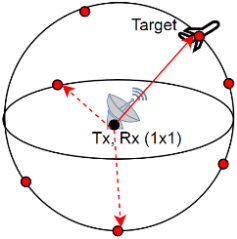
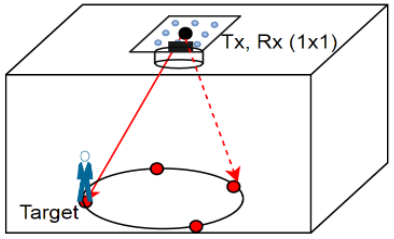
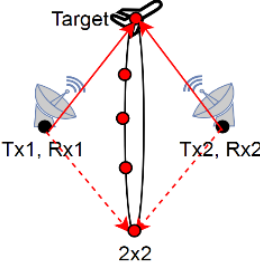
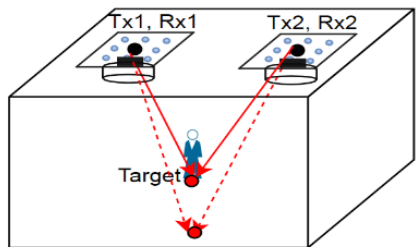
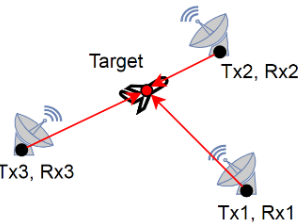
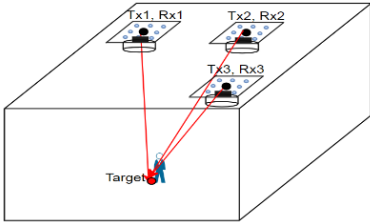
Target ambiguity is the main challenge when using monostatic or bistatic LiDAL systems in an indoor environment. Whenever, the distance between targets or between a target and a background obstacle is less than the LiDAL resolution, target detection ambiguity occurs. Increasing the LiDAL resolution by decreasing the transmitted pulse width improves the target detection resolution, however this requires a higher transmitter and receiver bandwidth and calls for a more complex optical receiver (for example in terms of equalisation). Target localisation requires determination of the target range and/or the direction (angle) of the received reflected pulse from the target. Unlike the work reported in the literature, our localisation approaches in this work are passive in the sense that the target does not have to carry an optical (VLC) receiver. In the literature [28], [177], [178] many techniques have been proposed for VLC mobile user localisation such as triangulation, scene analysis and proximity using angle of arrival, time difference of arrival and received signal strength from multiple transmitters. Our passive approach in LiDAL relies on detecting signals reflected from the target, and therefore received signal strength indicator (RSSI) is not a good detection strategy. In this passive localisation approach the reflected signals experience heavy fluctuations when the signal is reflected from the target owing to the environment, target cloth colours and the potential loss of the line of sight component. Table 6.1 provides a comparison between conventional radar and LiDAL when the only available information is range. Note that the angle of arrival in LiDAL can be determined through coherent optical detection, but this is too complex, and is not considered here. As Table 6.1 shows, complete

localisation is only achieved when three or more anchor points are available to provide range estimations.

In this chapter, a new multiple-input multiple-output LiDAL system (MIMO-LiDAL) is introduced for target detection, counting and localisation. The proposed system is designed to mitigate the ambiguity of multi-target detection to distinguish the targets correctly from the background obstacles in a realistic indoor environment. To tackle the ambiguity of target detection, collaboration of multiple transmitters and receivers is employed. The detection floor is divided into multiple optical footprints using multiple single-photodetector receivers which provide spatial selection for target detection. In addition, we integrated the MIMO-LiDAL system with the proposed target distinguishing approaches and the sub-optimum receiver to optimise the targets detection, counting and localisation supported by an algorithm executed in a connected controller. Furthermore, time-of-arrival (TOA) is employed in the MIMO-LiDAL system for target localisation. A simulation is reported in this chapter for the MIMO-LiDAL system in order to identify the accuracy of detecting, counting and localising multiple targets in a realistic environment.

Following this introduction, this chapter is divided into section: Section 6.2 introduces the system setup used in MIMO LiDAL. Section 6.3 analyses the collaboration of the MIMO LiDAL transceiver units to eliminate the ambiguity of target detection and localisation. Section 6.4 evaluates the MIMO LiDAL receivers operating characteristics. Section 6.5 analyses the probability of target detection in MIMO LiDAL systems. Section 6.6 presents the target localisation approach used in our MIMO LiDAL systems. Section 6.7 introduces the operating algorithm used in the MIMO LiDAL system. Simulation setups and performance evaluation of the MIMO LiDAL system are presented in Section 6.8.

Table 6.1: LiDAL localisation compared to traditional radar localisation

| Radar localisation in literature  | Localisation in LiDAL  | LiDAL Design Comments  |
|---|--|--|
| <b>Single Transmitter Single receiver (SISO) 1x1</b>  |  |  |
| <p>- Only range is known, hence the target can be located on the surface of a sphere.</p>  | <p>- Only range is known, hence the target can be located on a circle.</p>                     | <ul style="list-style-type: none"> <li>• 1x monostatic LiDAL (a transmitter receiver pair are monostatic if they are collocated and the target is within the FOV of the receiver)</li> <li>• Can only detect target presence.</li> <li>• Cannot determine number of targets at same range.</li> <li>• Cannot determine the exact target location.</li> <li>• Therefore target ambiguity is very high.</li> </ul>   |
| <b>Multiple Transmitters Multiple receivers (MIMO) 2x2</b>  |  |  |
| <p>- Only two ranges are known, hence the target can be located on a circle.</p>          | <p>- Only two ranges are known, hence the target can be located in one of two locations.</p>  | <ul style="list-style-type: none"> <li>• 1x Bistatic and 1x monostatic LiDAL, (a transmitter receiver pair are bistatic if they are not collocated and the target is within the FOV of the receiver).</li> <li>• Ambiguity in target detection is less due to use of both monostatic and bistatic LiDAL systems together.</li> <li>• Scene localisation can be implemented, but exact location is not known.</li> <li>• Cannot determine the exact target location.</li> </ul> |
| <b>Multiple Transmitters Multiple receivers (MIMO) 3x3</b>  |  |  |
| <p>-Exact target location can be determined.</p>   | <p>-Exact target location can be determined.</p>   | <ul style="list-style-type: none"> <li>• 2x Bistatic and 1x monostatic LiDAL; the target is within the FOV of one receiver only, and that receiver – transmitter pair act as monostatic LiDAL.</li> <li>• Can detect, count and exact localisation of multiple targets.</li> <li>• The mean and standard deviation of the received signal can be different.</li> </ul>   |

## 6.2 MIMO LiDAL System Configurations

We introduce the MIMO-LiDAL system, to detect, count and localise multiple targets. We implemented multiple narrow-FOV receivers collocated with the light units. The system is designed to tackle the ambiguity of target detection, maximise the number of counted targets and minimise false target distinguishing by employing both monostatic and bistatic LiDAL systems. Figure 6.1 presents the setup of the MIMO LiDAL system with the controller. The MIMO-LiDAL system includes eight receivers that are collocated with the eight VLC transmitter units on the room ceiling. The room setup and transmitters' configuration is similar to that in [144], [145] which is a versatile setup used to realise a multi-gigabit/s VLC system. In this work, we assumed that the LiDAL system has access and can use all the VLC transmitters. The room detection floor is divided into eight optical footprints as shown in Figure 6.1. The transmitters and their FOV have to be selected to comply with the illumination levels recommended by the standards. Therefore we have created the LiDAL optical detection zones through design and selection of the LiDAL receivers FOVs. Each receiver is chosen as a single narrow-FOV photodetector with  $\Psi_c=43.8^\circ$  which is the acceptance semi-angle of the compound parabolic concentrator (CPC). This FOV is determined based on the required maximum LiDAL range,  $R_{Max}^{FOV}$ , and is equal to 1.25m in our system. The collocated transmitter-receiver (i.e. transceiver) unit covers an optical footprint area of 4.91 m<sup>2</sup>. It is worth mentioning that the VLC transmitters designed in [36] are spaced by a distance of 2m. Therefore, the maximum spatial overlap between two neighbouring optical footprints,  $\Delta x$ , is 0.5m as can be seen in Figure 6.1.

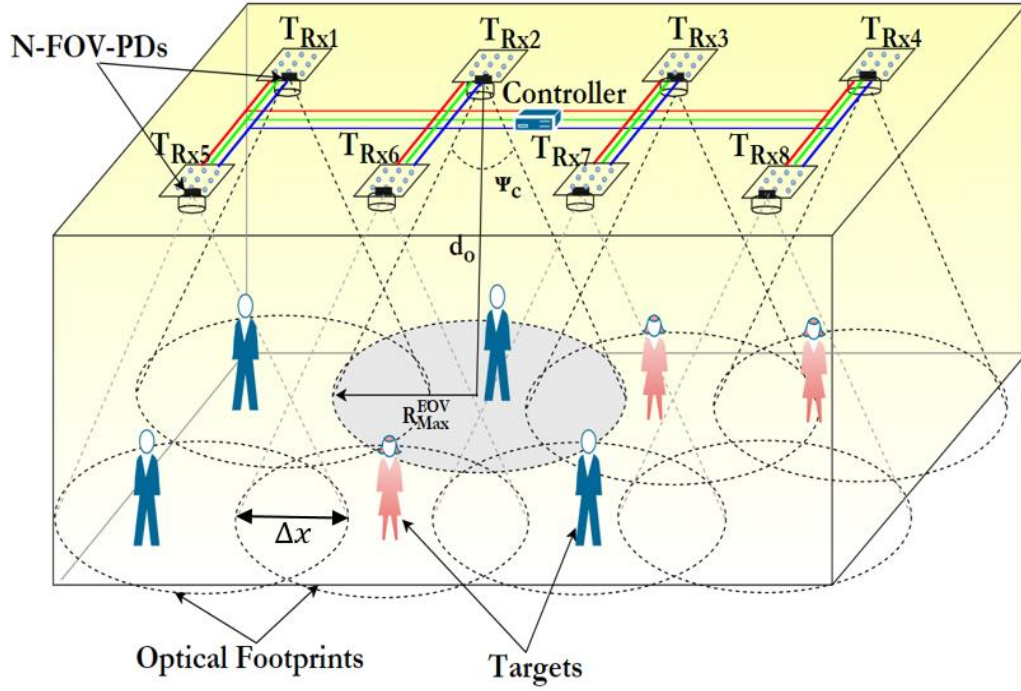


Figure 6.1: MIMO-LiDAL system setup.

In MIMO LiDAL, each transceiver unit (collocated  $T_x$  and  $R_x$ ) represents a monostatic configuration. The reflected received signal ( $P_{r_B}^{R_{Max}^{FOV}}$ ) from the target is located on the edge of the optical footprint at a distance of  $R_{Max}^{FOV}$  can be expressed as:

$$\begin{aligned}
 P_{r_M}^{R_{Max}^{FOV}} &= \frac{(n+1)(n_{ele}+1)}{4\pi^2 R_1^2 R_2^2} T_f(\Psi_c) G_c(\Psi_c) P_t d_A \rho A_R \cos^n(\theta) \cos(\varphi) \cos^{n_{ele}}(\varphi_1) \cos(\delta)
 \end{aligned} \tag{6.1}$$

For monostatic as can be seen in Figure 6.2, the range distance  $R_1$  is equal to  $R_2$ . The transmitter irradiance angle  $\theta$  and target incidence angle are alternate angles  $\varphi$ . And also the target irradiance angle  $\varphi_1$  is equal to receiver incidence angle  $\delta$  thus :

$$\cos^n(\theta) = \left( \frac{d_o - h}{R_1} \right) \tag{6.2}$$

and

$$\cos^{n_{ele}}(\varphi_1) = \left( \frac{d_o - h}{R_1} \right) \tag{6.3}$$

for  $(\theta = \varphi)$ , we get:

$$\cos^n(\theta) \cos(\varphi) = \left(\frac{d_o - h}{R_1}\right)^{n+1} \quad (6.4)$$

and  $(\delta = \varphi_1)$ , we get:

$$\cos^{n_{ele}}(\varphi_1) \cos(\delta) = \left(\frac{d_o - h}{R_1}\right)^{n_{ele}+1} \quad (6.5)$$

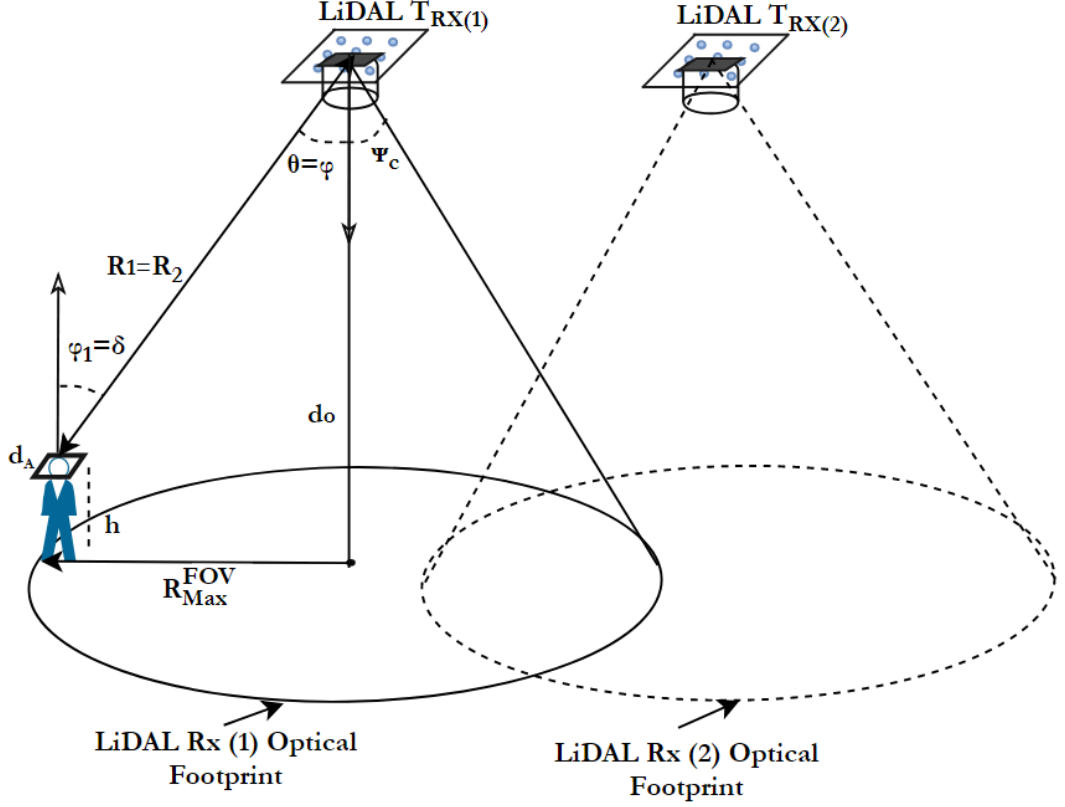


Figure 6.2: MIMO monostatic LiDAL.

For a target located at the edge of the receiver FOV,  $= \Psi_c$ ,  $n_{ele} = 1$  and

$R_1 = R_2 = \sqrt{R_{Max}^{FOV^2} + (d_o - h)^2}$ . Thus, the mean reflected received signal power ( $\bar{P}_{rM}^{FOV}$ ) from a target located at the edge of the optical footprint at a distance of  $R_{Max}^{FOV}$  can be derived as:

$$\bar{P}_{rM}^{FOV} = \frac{C \mu_\rho (d_o - h)^{n+3}}{4\pi^2 \left(R_{Max}^{FOV^2} + (d_o - h)^2\right)^{\frac{n+7}{2}}} \quad (6.6)$$

where,  $C = (n + 1)(n_{ele} + 1)P_t d_A A_R T_f(\Psi_c) G_c(\Psi_c)$ .

The standard deviation of the received signal,  $\hat{P}_{rR_{\text{Max}}}^M$ , is given as:

$$\hat{P}_{rM}^{R_{\text{Max}}^{\text{FOV}}} = \frac{C \sigma_{\rho} (d_o - h)^{n+3}}{4\pi^2 \left( R_{\text{Max}}^{\text{FOV}^2} + (d_o - h)^2 \right)^{\frac{n+7}{2}}}. \quad (6.7)$$

In this work, for the MIMO-LiDAL design we set the LD beamwidth for illumination purpose [36] as  $n=0.5$ ; and set the power transmitted by each light unit as  $P_t=18\text{W}$  (as discussed in Chapter 3). The PD area is  $A_R=20\text{mm}^2$ ,  $T_f(\Psi_c)=1$  (a lossless optical filter was assumed),  $G_c(\Psi_c)=6$  obtained using the concentrator gain equation (3.5) with  $N_c=1.7$  and  $\Psi_c=43.8^\circ$ . The target effective cross section area was set as  $d_A=0.29\text{m}^2$ , which is the minimum target cross section area. This minimum area occurs when the target orientation is such that the human (left or right) side faces the transceiver unit (a larger target cross section area results if the person faces or gives their back to the transceiver). The target height selected was  $h=1.7\text{m}$  and  $d_o=3\text{m}$  (room height [36]). The receiver bandwidth is 315 MHz which corresponds to the maximum channel bandwidth according to the monostatic LiDAL system analysis in Chapter 3. Thus the TIA thermal input noise current  $\sigma_{\text{thermal}}$  is about 2.6 pA/ $\sqrt{\text{Hz}}$  [153].

Figure 6.3, shows the ROC depicting the trade-off between  $P_D^M$  and  $P_{FD}^M$  of the monostatic LiDAL system for two locations where the targets are located at ranges of  $R_{\text{Max}}^{\text{FOV}}$  and  $\frac{1}{2}R_{\text{Max}}^{\text{FOV}}$  respectively. The impact of selecting the detection threshold  $D_{th}^M$  on the target false detection as can be seen in Figure 6.4. In this work, we consider MIMO-LiDAL for people detection, counting and localisation applications. Therefore, we adjusted the  $D_{th}^M$  to maximise the value of  $P_D^M$  which implies that high false alarms are accepted to ensure that every target is counted and localised. We chose  $P_{FD}^M=0.1$  which leads to  $P_D^M=0.92$  and therefore the optimum detection threshold for the monostatic LiDAL is  $D_{th}^M=0.32 \bar{P}_{rM}^{R_{\text{Max}}^{\text{FOV}}}$  in this case.



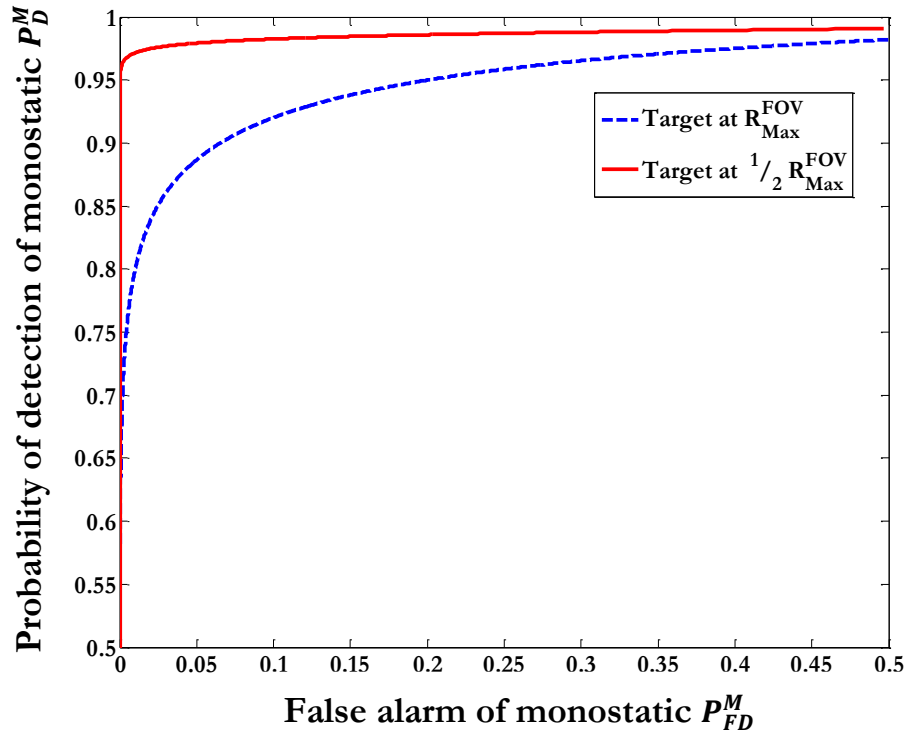
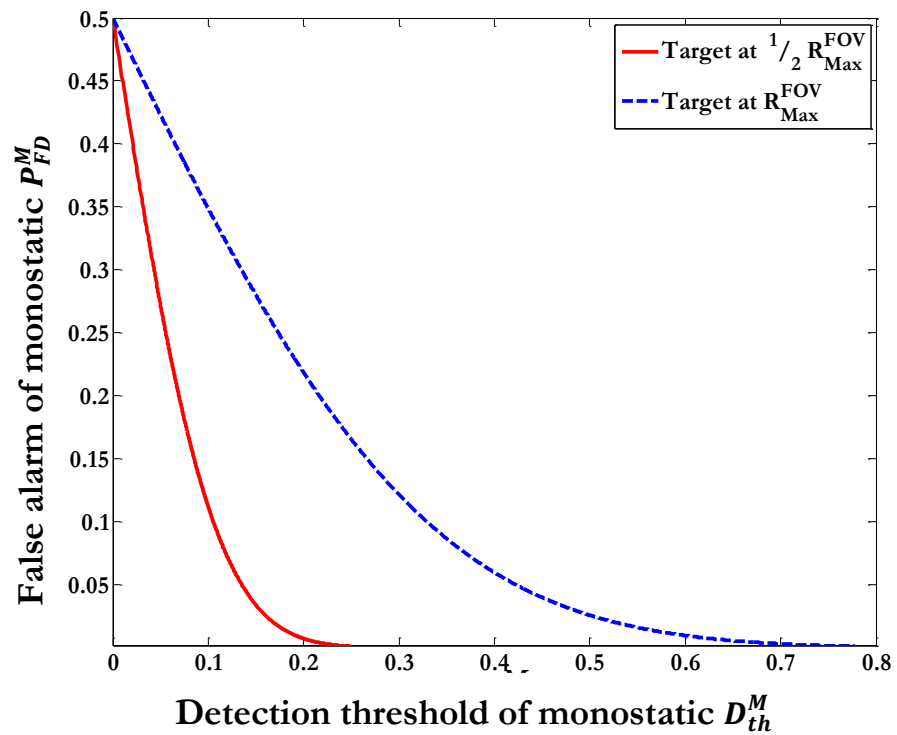


Figure 6.3: ROC of Monostatic MIMO LiDAL.

Figure 6.4: Monostatic MIMO LiDAL false detection with optimum  $D_{th}^M$ .

### 6.3 Collaboration of the MIMO-LiDAL Transceivers Units

In a realistic environment, the ambiguity of target detection can be divided into two types. Firstly, when a single target moves along a circle centred at the centre of the receiver optical footprint, the reflected pulses from the target arrive at the same time. Therefore, the exact location of a target on this circle (where on the circle) beneath the receiver cannot be established. Secondly, two or more stationary targets cannot be distinguished if they are located at different locations but their distances to a monostatic transceiver ( $T_{RX1}$  in Figure 6.5) are the same as can be seen in Figure 6.5 (targets 1 and 2).

These forms of target ambiguity can be resolved if bistatic transceivers are used. In this case, the target position has to be covered by multiple transmitters (at least three transmitters, for spatial localisation) that act as anchors, and by at least one receiver.

The footprint coverage radius of each VLC transmitter unit is 4.8m (transmitter beamwidth was set as  $75^\circ$  for illumination purposes [36]) which results in a minimum coverage overlap of 3.8m between the neighbouring transmitters (ie between the circular optical zones covered by each transmitter). Consider target 2 in Figure 6.5 located at the maximum range of  $R_{X1}$ , i.e located at  $R_{Max}^{FOV}$  of  $R_{X1}$ . This target is illuminated by LiDAL  $T_{X2}$ . Therefore, this collaboration between neighbouring transceivers ( $CoN_{TRX}$ ) has established the second anchor in a bistatic configuration where  $T_{X2}$  is now an anchor. The first anchor is  $T_{X1}$ , where  $T_{X1}$  and  $R_{X1}$  act as a monostatic LiDAL sub-system. The third anchor is established in the example in Figure 6.5 through a bistatic LiDAL subsystem formed by  $T_{X3}$  and  $R_{X1}$ . Therefore, the MIMO LiDAL system in Figure 6.5 acts to establish the target location by removing the location ambiguity.

To illustrate the removal of target ambiguity through the joint use of the three anchors, consider Figure 6.5 which depicts a worse case scenario with two targets located at positions  $P_1$  (target 1) and  $P_2$  (target 2). Observed through the field of view of the MIMO LiDAL sub-system  $T_{X1}-R_{X1}$  (i.e. monostatic LiDAL) and  $T_{X3}-R_{X1}$  MIMO LiDAL sub-system (i.e. bistatic LiDAL) both targets are at same distance to  $R_{X1}$  and therefore ambiguity occurs. Considering  $T_{X1}-R_{X1}$ , the round trip time of the reflected pulse from target 1 ( $2R_{1(1)}$ ) is equal to the round trip time associated with the pulse reflected from target 2,  $2R_{1(2)}$ , resulting in the pulse seen in Figure 6.6a. Similarly, considering  $T_{X3}-R_{X1}$  and the trip distances  $(R_{3(1)} + R_{1(1)})$  and  $(R_{3(1)} + R_{1(2)})$  results in the pulses seen Figure 6.6c. Thus, ambiguity exists. However, if  $T_{X2}-R_{X1}$  are used, the distinct trip distances  $(R_{2(1)} + R_{1(1)})$  and  $(R_{2(2)} + R_{1(2)})$  result in ambiguity resolution as seen in Figure 6.6b.

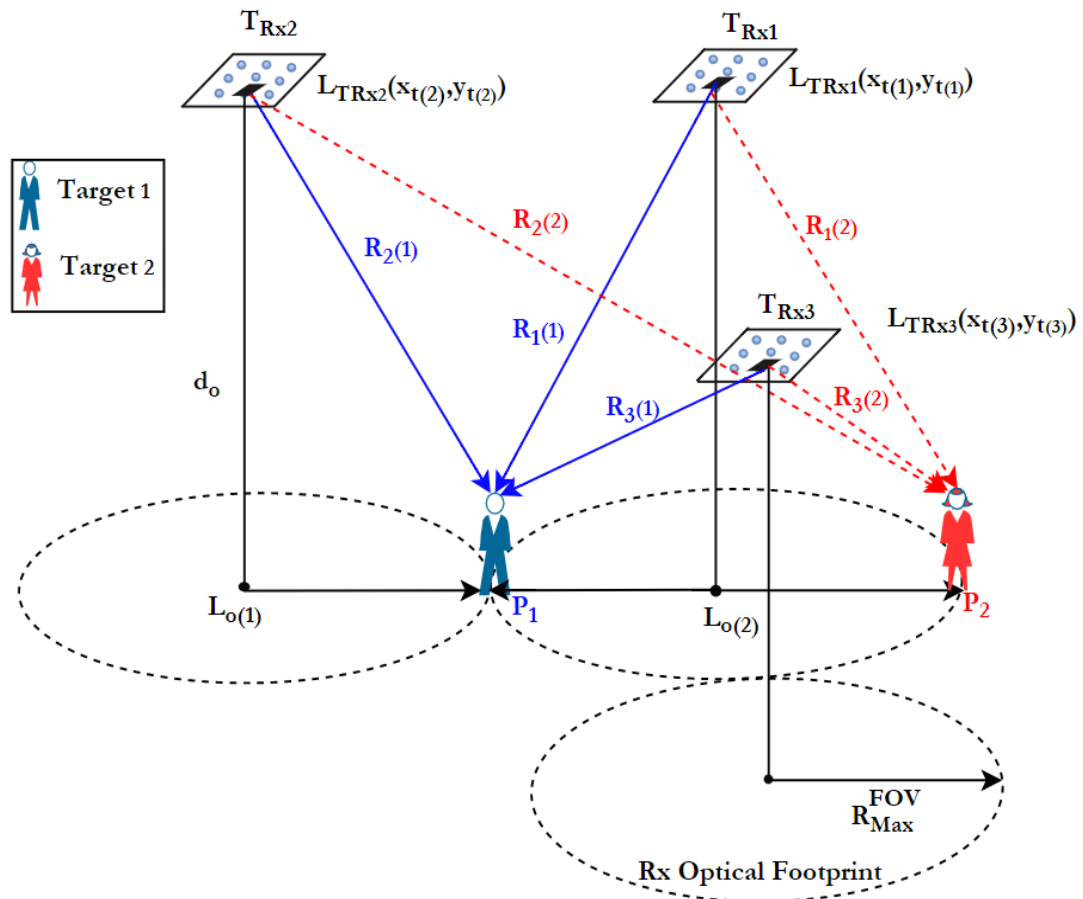


Figure 6.5: Target detection ambiguity in MIMO-LiDAL system with targets ranging

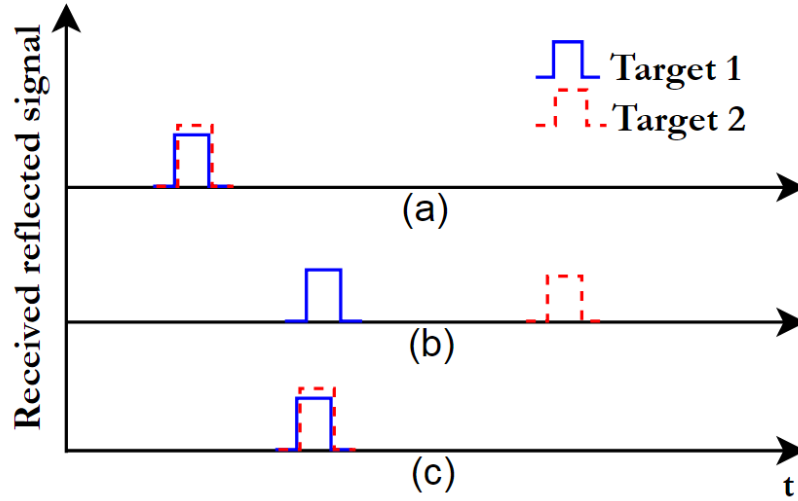


Figure 6.6: (a) the reflected pulses from targets when Tx<sub>1</sub>-Rx<sub>1</sub> are active, (b) the reflected pulses from targets when Tx<sub>2</sub>-Rx<sub>1</sub> are active and (c) the reflected pulses from targets when Tx<sub>3</sub>-Rx<sub>1</sub> are active.

## 6.4 MIMO LiDAL System Receiver Operating Characteristics (ROC)

For the bistatic LiDAL as shown in Figure 6.7, the received reflected signal

$P_{rB}^{R_{Max}^{FOV}}$  from the target is located on the edge of the detection area at a distance of  $R_{Max}^{FOV}$  can be derived as:

$$P_{rB}^{R_{Max}^{FOV}} = \frac{(n+1)(n_{ele}+1)}{4\pi^2 R_1^2 R_2^2} T_f(\Psi_c) G_c(\Psi_c) P_t d_A \rho A_R \cos^n(\theta) \cos(\varphi) \cos^{n_{ele}}(\varphi_1) \cos(\delta) \quad (6.8)$$

It can be noted from bistatic LiDAL in Figure 6.7 that the  $R_1 \neq R_2$ ,  $\theta \neq \varphi$ , and  $\delta = \varphi_1$ , thus:

$$\cos^n(\theta) = \left( \frac{d_o - h}{R_2} \right)^n \quad (6.9)$$

$$\cos(\varphi) = \left( \frac{d_o - h}{R_2} \right) \quad (6.10)$$

and

$$\cos^{n_{ele}}(\varphi_1) \cos(\delta) = \left(\frac{d_o - h}{R_1}\right)^{n_{ele}+1} \quad (6.11)$$

where:

$$R_1 = \sqrt{R_{Max}^{FOV^2} + (d_o - h)^2} \quad (6.12)$$

And:

$$R_2 = \sqrt{(3 R_{Max}^{FOV})^2 + (d_o - h)^2} \quad (6.13)$$

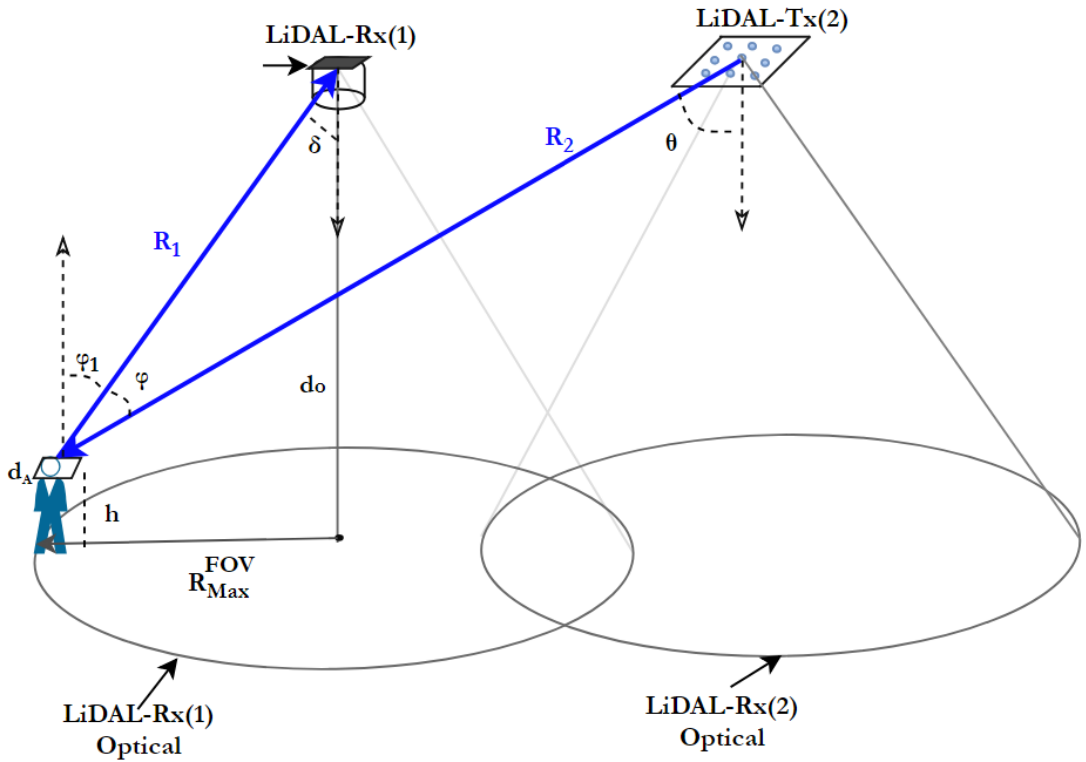


Figure 6.7: Bistatic MIMO LiDAL system.

The mean received reflected signal power,  $\bar{P}_{rB}^{R_{Max}^{FOV}}$ , from a target located at the detection edge, ie at a distance of  $R_{Max}^{FOV}$  can be derived as:

$$\bar{P}_{rB}^{R_{Max}^{FOV}} = \frac{C \mu_{\rho} (d_o - h)^{n+3}}{4\pi^2 ((3 R_{Max}^{FOV})^2 + (d_o - h)^2)^{\frac{n+3}{2}} (R_{Max}^{FOV^2} + (d_o - h)^2)^2}. \quad (6.14)$$

The standard deviation of the received signal,  $\hat{P}_{r_B}^{R_{Max}^{FOV}}$ , is given as:

$$\hat{P}_{r_B}^{R_{Max}^{FOV}} = \frac{C \sigma_\rho (d_o - h)^{n+3}}{4\pi^2 \left( (3 R_{Max}^{FOV})^2 + (d_o - h)^2 \right)^{\frac{n+3}{2}} \left( R_{Max}^{FOV^2} + (d_o - h)^2 \right)^2}. \quad (6.15)$$

Figure 6.8 presents the ROC of the bistatic MIMO-LiDAL. Note that unlike the monostatic LiDAL system, the bistatic LiDAL system makes use of distant anchor points, to help resolve the localisation ambiguity. Therefore, the mean received signal is low when a distant anchor point is used. To maintain high detection probability in this case, a higher false detection probability,  $P_{FD}^B$ , is used,  $P_{FD}^B=0.25$ . Here higher false alarms are accepted to ensure that the probability of people detection is high. This results in an optimum threshold  $D_{th}^B$  of  $(0.35 \bar{P}_{r_B}^{R_{Max}^{FOV}})$  as can be noted in Figure 6.9, with  $P_D^B=0.7$  from Figure 6.8. To improve the performance of MIMO-LiDAL system, we (i) implemented different optimum detection thresholds  $D_{th}^B$  which are adjusted adaptively in the sub-optimum detector for the both the monostatic and the bistatic LiDAL systems; (ii), optimised the ZFE for the monostatic and the bistatic LiDAL systems.

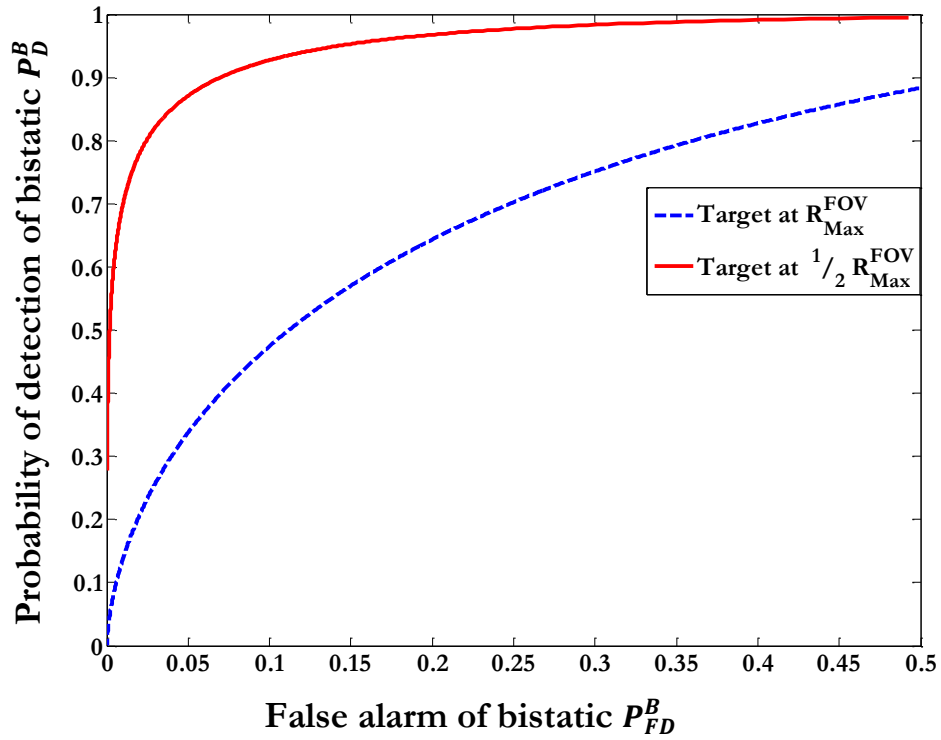
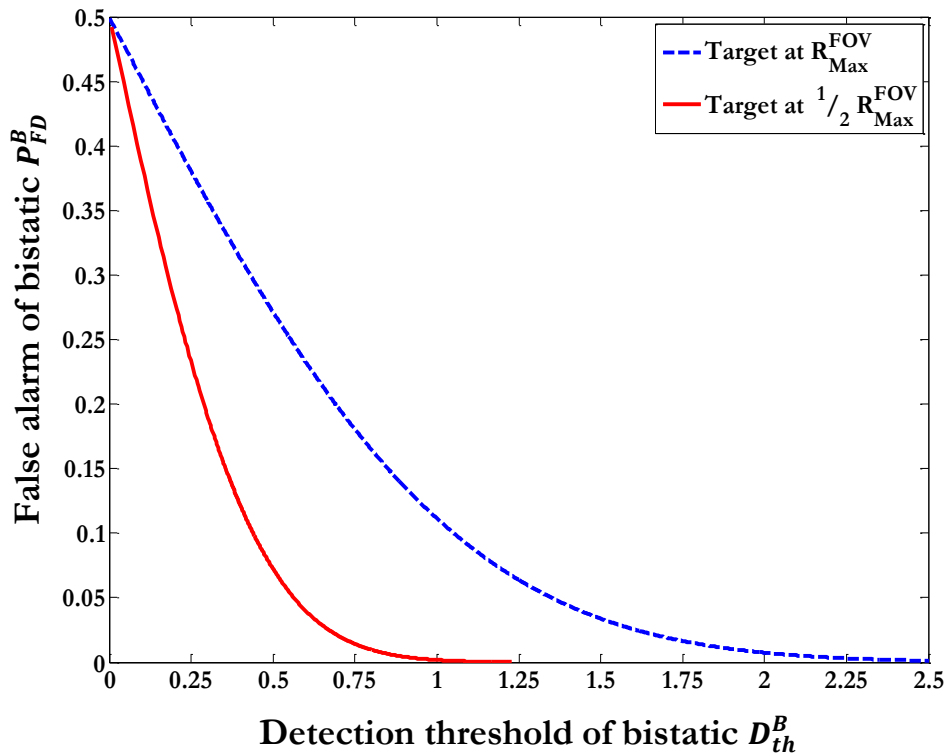


Figure 6.8: ROC of Bistatic MIMO LiDAL.

Figure 6.9: Bistatic MIMO LiDAL probability of false detection with optimum  $D_{th}^B$ .

## 6.5 Probability of Target Detection in MIMO LiDAL System

There is a finite probability that a target is present, but is missed. This probability of miss-detecting a target located at  $R_{Max}^{FOV}$  (see for example the target at  $P_2$  in Figure 6.5 which is located at the maximum range,  $R_{Max}^{FOV}$ ) of MIMO-LiDAL ( $P_{MD}^{R_{Max}^{FOV}(MIMO)}$ ) can be derived as:

$$P_{MD}^{R_{Max}^{FOV}(MIMO)} = \left(\frac{1}{2}\right)^{K_n+1} \left( 1 + \operatorname{erf} \left( \frac{D_{th}^M - \bar{P}_{r_{R_{Max}^{FOV}}}^M}{\hat{P}_{r_{R_{Max}^{FOV}}}^M \sqrt{2}} \right) \prod_{k=1}^{K_n} \left( 1 + \operatorname{erf} \left( \frac{D_{th}^B(k) - \bar{P}_{r_{R_{Max}^{FOV}}}^B}{\hat{P}_{r_{R_{Max}^{FOV}}}^B \sqrt{2}} \right) \right) \right) \quad (6.16)$$

where  $\operatorname{erf}$  is the error function and  $K_n$  is the number of neighbour transceiver units (bistatic LiDAL). The term  $\left(1 - P_{MD}^{R_{Max}^{FOV}(MIMO)}\right)$  represents the probability of the target detected by at least one transceiver unit (for example (T<sub>X2</sub>-R<sub>X1</sub>) as in the case shown in Figure 6.5).

Let  $T_{c_M}$  be the maximum number of targets that can be counted successfully when the targets are located at different distances from the LiDAL transceiver with minimum separation distance of  $\Delta R$ . This number,  $T_{c_M}$ , for the MIMO LiDAL system is given as:

$$T_{c_M(MIMO)} = \frac{T_w(MIMO)}{\tau} N_{OF} \quad (6.17)$$

where  $N_{OF}$  is the number of optical footprint zones and  $T_w$  is the LiDAL channel time window which corresponds to the difference in the round-trip times of a target placed at  $R_{Max}^{FOV}$  and a target placed underneath the transceiver, ie at the centre of the LiDAL transceiver optical detection zone. Thus  $T_w(MIMO)$  of the MIMO-LiDAL is determined as:

$$T_w(MIMO) = \frac{\left( \left( \left( \sqrt{(3 R_{Max}^{FOV})^2 + (d_o - h)^2} \right) + \left( \frac{R_{Max}^{FOV}}{\sin(\Psi_c)} \right) \right) - 2(d_o - h) \right)}{c} \quad (6.18)$$



where  $d_0$  is the perpendicular distance between of the  $i$ th transceiver unit coordinates  $L_{TRx(i)}$  and the centre of the transceiver illumination  $L_{o(i)}$  (see Figure 6.5).

## 6.6 Target Localisation

To localise a target, the time of arrival of the reflected pulse and its direction are required. However, in the MIMO-LiDAL system considered, the direction of the reflected pulse from the target cannot be determined due to the wide-FOV of the receiver. An angle diversity receiver can be used which can help determine a coarse direction of arrival based on the receiver face that detects the signal. The angular resolution is however typically coarse as the number of faces in the angle diversity receiver are typically limited and small. An even coarser localisation can be achieved with a single wide FOV LiDAL receiver which can provide an estimated range, thus placing the target (human) on a circle on the floor in an indoor environment.

For accurate target localisation, collaboration of neighbouring MIMO-LiDAL transceiver units can be utilised with a time of arrival (TOA) approach to localise the target. To determine the exact target location, ranges to at least three transmitters (anchors) must be obtained. In Figure 6.5  $R_1(j)$ ,  $R_2(j)$  and  $R_3(j)$  are the ranges of target  $j$  to the three transceivers. The location of the target is calculated as the intersection of the three (circles) ranges. Any target in the indoor environment will lie in the coverage area of at least one monostatic receiver (LiDAL system), see Figure 6.1. Therefore, this localisation technique relies on the success of target detection by at least  $K \geq 2$  neighbouring bistatic LiDAL sub-systems. The monostatic MIMO-LiDAL range can be written as:

$$R_1(j) = \frac{t_{trip}^j(T_{x1}, R_{x1}) c}{2}. \quad (6.19)$$

The bistatic MIMO-LiDAL range is given as:

$$R_k(j) = \left( t_{trip}^j(T_{xk}, R_{x1}) \right) c - R_1(j) \quad \forall k \in K, k \neq 1 \quad (6.20)$$

where  $R_1(j)$  is the range in metre of the  $j$ th target from the monostatic LiDAL subsystem (subsystem number 1),  $R_k(j)$  are the ranges in metres of the  $j$ th target from LiDAL bistatic subsystem  $k$ ,  $t_{trip}^j(T_{x1}, R_{x1})$  and  $t_{trip}^j(T_{xk}, R_{x1})$  are the trip times between the identified transmitter and receiver units, which are monostatic and bistatic respectively in this case.

Consider a target  $j$  whose position is  $P_j(x_j, y_j)$ , and consider the  $k$ th transmitter anchor located at  $(x_{t(k)}, y_{t(k)})$ , we have:

$$(x_{t(k)} - x_j)^2 + (y_{t(k)} - y_j)^2 = R_k^2(j). \quad (6.21)$$

A least squares approach [179], [180] can be used to solve (6.21) to provide an approximate location of the  $j$ th target at the intersection of  $K + 1$  circles is given as:

$$\begin{aligned} x_j(x_{t(k)} - x_{t(1)}) - y_j(y_{t(k)} - y_{t(1)}) \\ = \frac{1}{2} (R_1^2(j) - R_k^2(j) + x_{t(k)}^2 + y_{t(k)}^2 - x_{t(1)}^2 - y_{t(1)}^2). \end{aligned} \quad (6.22)$$

Equation (6.22) can be written in matrix form where  $A$  and  $B$  are location matrices [181]:

$$A = \begin{pmatrix} x_{t(k)} - x_{t(1)} & y_{t(k)} - y_{t(1)} \\ x_{t(K)} - x_{t(1)} & y_{t(K)} - y_{t(1)} \end{pmatrix} \quad (6.23)$$

$$B = \frac{1}{2} \begin{pmatrix} (R_1^2(j) - R_k^2(j)) + (x_{t(k)}^2 + y_{t(k)}^2) - (x_{t(1)}^2 + y_{t(1)}^2) \\ (R_1^2(j) - R_K^2(j)) + (x_{t(K)}^2 + y_{t(K)}^2) - (x_{t(1)}^2 + y_{t(1)}^2) \end{pmatrix} \quad (6.24)$$

and  $X$  is:

$$X = [x_j \ y_j]^T. \quad (6.25)$$

The target position  $P_j(x_j, y_j)$  can be determined as [179]:

$$X = P_j(x_j, y_j) = (A^T A)^{-1} A^T B. \quad (6.26)$$

In MIMO LiDAL, target localisation depends on collaboration of neighbouring transceivers. Thus, to localise target 2, located at  $P_2$ , in Figure 6.5,  $T_{X1}$ ,  $T_{X2}$  and  $T_{X3}$  work *separately* with  $R_{X1}$  to localise target 2. This requires three *separate* LiDAL scans. Hence, the probability of detection of target 2 by  $T_{X1}$ - $R_{X1}$  (Monostatic LiDAL sub-system) is independent of the probabilities of detection of the same target by  $T_{X2}$ - $R_{X1}$  and  $T_{X3}$ - $R_{X1}$  (both are Bistatic LiDAL sub-systems). Consequently, the probability of localizing a target located at the maximum range,  $R_{Max}^{FOV}$ ,  $P_{L(MIMO)}^{R_{Max}^{FOV}}$  can be written as:

$$P_{L(MIMO)}^{R_{Max}^{FOV}} = P_D^M \prod_{k=1}^K P_D^B(k) \quad (6.27)$$

$$P_{L(MIMO)}^{R_{Max}^{FOV}} = \left(\frac{1}{2}\right)^{K+1} \operatorname{erfc}\left(\frac{D_{th}^M - \bar{P}_{r_{R_{Max}^{FOV}}}^M}{\hat{P}_{r_{R_{Max}^{FOV}}}^M \sqrt{2}}\right) \prod_{k=1}^K \left(\operatorname{erfc}\left(\frac{D_{th}^B(k) - \bar{P}_{r_{R_{Max}^{FOV}}}^B(k)}{\hat{P}_{r_{R_{Max}^{FOV}}}^B(k) \sqrt{2}}\right)\right) \quad (6.28)$$

## 6.7 MIMO LiDAL System Operating Algorithm

To distinguish human targets from other objects (obstacles) and to localise human targets in MIMO-LiDAL, pulses are transmitted from the transmitters in a sequence through  $M$  frames (single pulse per frame) which are managed by the controller. The receiver collects the reflected signal from the targets and ambient obstacles including walls, floor and furniture during the receiver listening time  $T$ . Figure 6.10 shows the proposed receiver block diagram in each transceiver unit of the MIMO LiDAL system.

In Figure 6.10 the controller instructs transmitter (anchor)  $k$  to emit a pulse while the other anchors are silent. This action as well as the received reflected pulse (from the target) form the input to the receiver in Figure 6.10. The received signal is fed in Figure 6.10 firstly to a “distinguishing method” block, this having been discussed in Chapter 5, where humans are distinguished from obstacles using for example human motion. The output of the distinguishing method block forms the input to the optimum detector block. The optimum detector output identifies the time slots that contain targets. This

information is used to determine the TOA. Furthermore, the slots that contain targets are counted to determine the number of human targets in the environment. Given that a number of LiDAL subsystems collaborate (three or more anchors), the target location is estimated. Finally, duplicate targets are eliminated. These are targets that lie in the overlap areas of the optical zones covered by the LiDAL receivers.

The controller conducts the detection, counting and localisation process as follows:

- 1) The first pulse of the control signal  $c(t)$  activates the transceiver monostatic LiDAL sub-system to (i) send an optical pulse  $x(\tau)$  from the transmitter  $Tx(k)$ , and (ii) initiate the receiver  $Rx(k)$  to listen to the reflected signal.
- 2) The receiver  $Rx(k)$  collects the reflected optical signal in an observation window of duration  $T$ . A distinguishing method (in this work we considered BSM and CCM methods) in conjunction with the designed sub-optimum LiDAL receiver are then used to detect the targets' presence and their ranges and update the counter  $V_c(i)$  as can be seen in Figure 6.10.
- 3) For target localisation, the controller identifies the  $K$  neighbouring bistatic LiDAL sub-systems. In this work we considered  $K=2$ . The second and third control pulses activate the neighbouring transmitters  $Tx(k+1)$ , and  $Tx(k+2)$  with the receiver  $Rx(k)$ . Each control pulse generates a LiDAL pulse from one of the LiDAL bistatic sub-systems and results in reflections being observed during a time duration  $T$ . The second pulse is generated at the end of the observation time  $T$ . The three trip times (one monostatic and two neighbouring bistatic LiDAL sub-systems) are then used to determine the targets' locations using TOA.
- 4) Target elimination follows where the targets located in the overlap zones are counted only once. Due to position errors, duplicated targets are eliminated if the Euclidean distance between any two such target locations is less than  $\Delta R$ . The counter  $V_c(i)$  is updated accordingly.

- 5) For the remaining  $I - 1$  optical zones, steps (1) to (4) are repeated. The  $I$  optical zones in the room are shown in Figure 6.1.
- 6) The number of targets,  $N_E$ , is calculated as  $N_E = \sum_{i=1}^I V_C(i)$ .

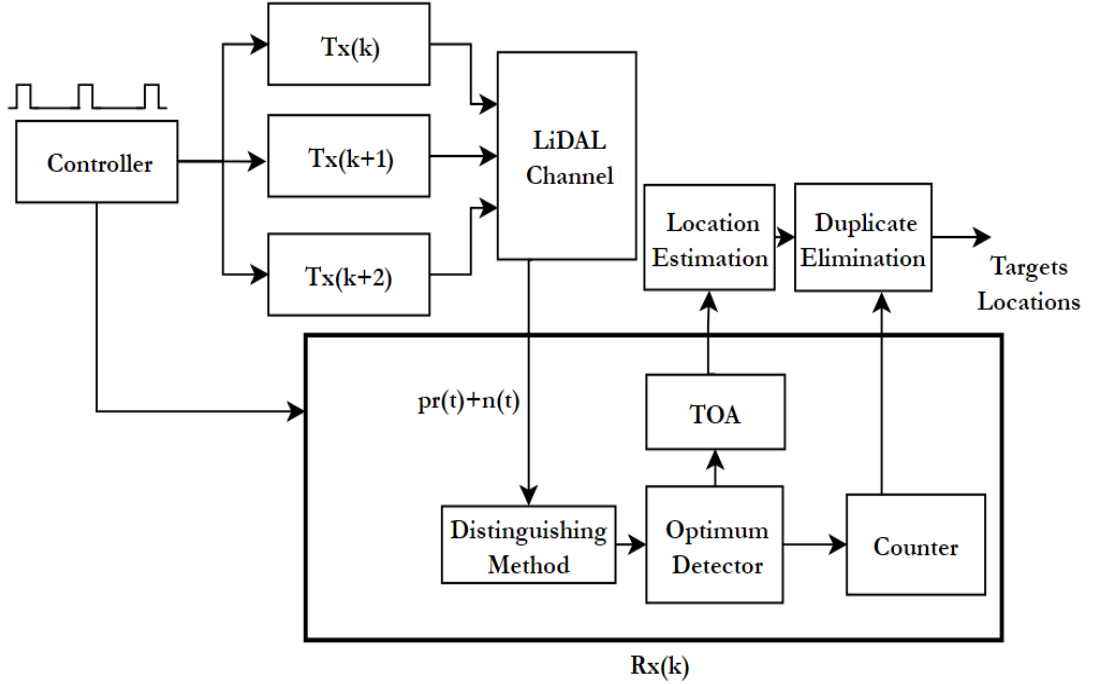


Figure 6.10: The receiver block diagram of MIMO-LiDAL system.

### 6.7.1 MIMO LiDAL Overhead

In terms of complexity, the number of scans (time frames of duration  $T$ ) needed to cover all the optical zones in the room is key. For the MIMO-LiDAL system, the number of frames,  $M$ , required to complete one monitoring cycle (i.e. detection, counting and localisation of a full room that has  $I$  optical zones) is determined as  $M = I(k + 1)$ . Therefore, the VLC MAC overhead,  $OH_{ML}$ , required to use the same VLC system for communication and MIMO-LiDAL localisation is:

$$OH_{ML} = \frac{T M}{T_{MACVLC}} \quad (6.29)$$

where  $T_{MACVLC}$  is the VLC MAC frame duration. For instance, if the MIMO-LiDAL system is used for pedestrian (more demanding than nomadic) target monitoring, then target location evaluation every 100 ms is sufficient given a maximum pedestrian speed of 3 m/s, where the 100ms results in motion by

$\Delta R = 30\text{cm}$ , which is the minimum distance of interest in this work. Therefore, a combined MIMO-LiDAL – VLC frame duration of 100ms can be considered. Considering one optical zone in Figure 6.1, its dimensions and considering the more demanding (distributed transmitters and receivers) bistatic LiDAL subsystem observation window duration, equation (6.18) gives this duration,  $T$ , for our system parameters as 44ns. If there are  $l=8$  optical zones as in Figure 6.1, then the number of frames needed is  $M=24$  frames leading to an observation time of  $5.2\ \mu\text{s}$ . The other key, non-real time blocks in Figure 6.10 are the location estimation which solves the matrix operations in (6.26) and the duplicate target elimination block which carries out a simple Euclidian distance comparison is in step 4 of the algorithm above. These non-real time operations can be carried out in the remaining part of the 100ms frame duration and may last for few milliseconds depending on the processor used. The key point is that visible light communication can resume after the  $5.2\ \mu\text{s}$ . The communications interruption overhead needed is thus negligible, however a localisation result may require 10 snapshots, which are collected in 10 frames and thus a localisation result may take one second, which is acceptable for pedestrian movement.

## 6.8 Simulation Setup and Results Discussion

In this section, we describe the simulation settings, describe three scenarios and a case study which are used in this chapter to evaluate the proposed MIMO LiDAL system in terms of targets detection and localisation. The MIMO LiDAL system is evaluated through computer simulation using MATLAB. The three scenarios as follows: (i) the first scenario establishes *the baseline*, ie the best performance expected in our MIMO LiDAL system. It evaluates the performance of our MIMO LiDAL system in an ideal environment where obstacles (furniture) are absent hence reducing interference from the environment, and reduces the likelihood of confusing a target (human) with furniture (obstacles). It also considers continuous motion, where pedestrians move continuously hence helping the target distinguishing methods; (ii) the second scenario represents a *challenging localisation* setting, which is a realistic but also favourable localisation environment. It introduces the first major impairment to localisation in LiDAL, ie the presence of obstacles. Therefore, this scenario considers a realistic room with furniture, partitions, bookshelves, doors and windows, unlike the empty room of scenario (i). Scenario (ii) however continues to consider continuous pedestrian motion to support the target distinguishing methods, thus allowing the impact of obstacles to be studied in isolation, and in this sense it is a favourable environment; (iii) the third scenario represents a *harsh localisation* environment. It adds nomadic motion to the second scenario and therefore considers the two main impairments in LiDAL localisation jointly; namely the presence of obstacles and lack of motion (sometimes) which makes target distinguishing harder. In all three scenarios we evaluate the results while using BSM and CCM for target distinguishing where mobility is the input to these methods. We also evaluate results in the three scenarios for the system of interest: MIMO-LiDAL.

### 6.8.1 System Setup

In this section we introduce the systems setup and the parameters used. The LiDAL systems were evaluated in two types of environments. Room A is an empty environment (i.e. free from furniture) as in Figure 6.11. Room B is a realistic environment, a furnished office, as shown in Figure 6.12. Table 6.2 illustrates the simulation parameters used in LiDAL systems.

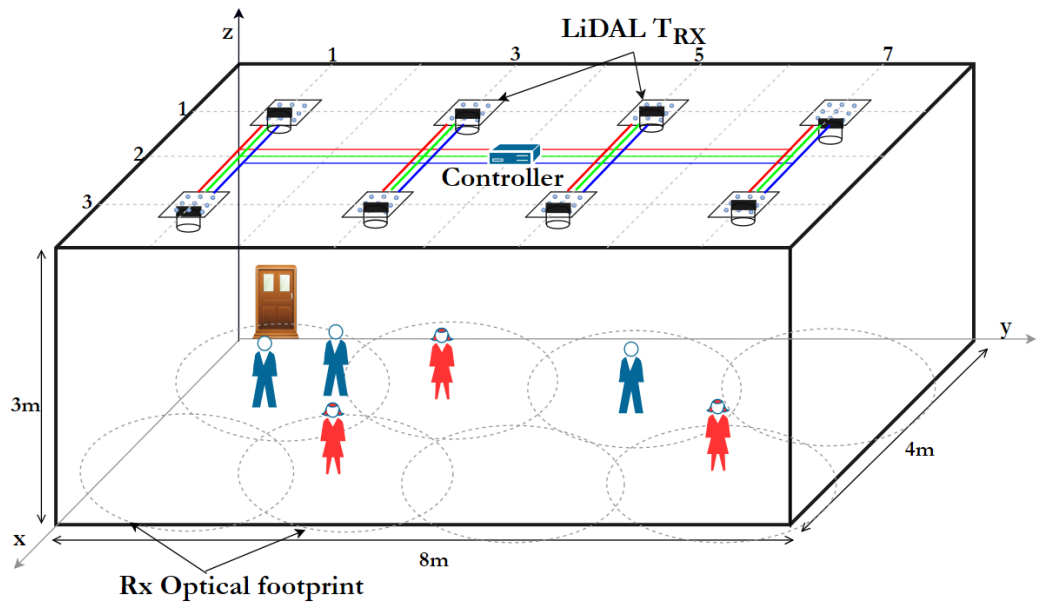


Figure 6.11: MIMO LiDAL Room A setup in scenario 1.

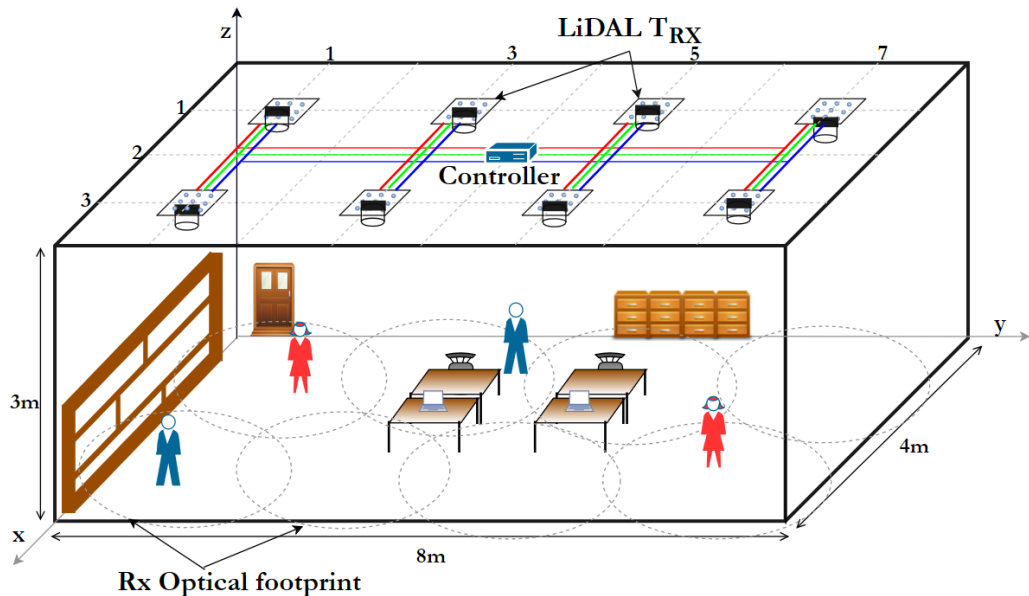


Figure 6.12 MIMO LiDAL Room B setup in scenario 2.



Table 6.2: MIMO LiDAL simulation parameters

| Parameters  | Configurations  |
|---|---|
| Room A and B  |   |
| Length  | 8m  |
| Width   | 4m  |
| Height  | 3m  |
| $\rho$ - ceiling                                      | 0.8   |
| $\rho$ - floor  | 0.3   |
| $\rho$ - walls  | 0.8   |
| LiDAL Transmitter Units                               |   |
| locations ( $x, y, z$ )                               | (1,1,3), (1,3,3), (1,5,3), (1,7,3)<br>(3,1,3), (3,3,3), (3,5,3), (3,7,3)m |
| Elevation   | 90°   |
| Azimuth   | 0°  |
| RGB-LDs in each unit                                  | 9 (3×3)   |
| Transmitted optical power per unit                    | 18 W  |
| Transmitted Pulse width $\tau$                        | 2ns   |
| RGB-LD semi-angle at half power beam width ( $\Phi$ ) | 75°   |
| MIMO LiDAL Receiver                                   |   |
| Photodetector Area                                    | 20 mm <sup>2</sup>  |
| Receivers locations                                   | Attached with Tx units  |
| Photodetector Responsivity                            | 0.4 A/W   |
| Receiver Acceptance Semi-angle                        | 43.8°   |
| CPC Reflective Index ( $N$ )                          | 1.7   |
| TIA Noise Current                                     | 2.5 pA/ $\sqrt{\text{Hz}}$  |
| Time Bin Duration                                     | 0.01 ns   |
| Time Slot Width $T_s$                                 | 2ns   |
| Listening Time $T$                                    | 1ms   |

### 6.8.2 Key Parameters for Counting and Localisation

To evaluate the counting and localisation performance of the MIMO LiDAL system two key metrics are defined: (i) The mean absolute percentage error (MAPE) which is used to quantify the counting accuracy, and (ii) the distance root means square error (DRMSE) which is used to quantify the localisation accuracy. The counting performance of the LiDAL systems is measured in terms of MAPE which is given as [182]-[183]:

$$MAPE = \frac{1}{J} \sum_{j=1}^J \left| \frac{A(j) - N_E(j)}{A(j)} \right| \times 100\% \quad (6.30)$$

where  $J$  is the number of times the experiment is repeated (iterations),  $A(j)$  and  $N_E(j)$  are the targets' actual and estimated (by MIMO LiDAL system) numbers, respectively. In order to evaluate the localisation performance of the MIMO LiDAL system, DRMSE is used to measure the location accuracy, where DRMSE is given as [184], [185]:

$$DRMSE = \sqrt{\sigma_x^2 + \sigma_y^2}. \quad (6.31)$$

Here  $\sigma_x$  and  $\sigma_y$  are the error standard deviations associated with the estimated  $(x_e, y_e)$  and the actual  $(x_a, y_a)$  coordinates of the target, respectively.

### 6.8.3 Simulation Flow Setup

The three scenarios were evaluated using the simulation flow shown in Table 6.3 . The simulation starts by considering an indoor environment that has  $i$  targets where the maximum number of targets is  $i_{max}=K$ . It then considers a number of iterations where each iteration contains the same number of targets, however the targets are located at different random locations in each iteration. The iterations continue to  $j_{max} = Itr$ . For a given number of targets, each iteration then generates random target locations, noise and reflection coefficients for each target (cloth colour and texture). The reflection coefficient associated with each target remains fixed for the number of iterations considered. The MIMO LiDAL system detection algorithm is then invoked resulting in estimated number of targets,  $N_E(j)$ , and estimated target locations,  $E_l(k,j)$ . This is finally used at the end of the  $j_{max}$  iterations to calculate MAPE and DRMSE. The simulation then continues by considering more targets in the environment (with new reflection coefficients (clothing) for the targets) and full number of  $j_{max}$  iterations.

The human target dimensions in Figure 3.1 (Chapter 3) are 48cm × 15cm. If a 50cm spacing is considered between targets, then the area needed per human target is 98cm × 65cm = 0.63m<sup>2</sup>. This leads to a maximum number of targets in an 8m×4m room of 51 targets. This represents a very dense reception type event. As discussed in this Chapter 5 (Section 5.4), the European standards for the minimum workplace space required per person is 3.7m<sup>2</sup> for an office environment and 2m<sup>2</sup> for a meeting room [176] . Therefore, we considered a 2m<sup>2</sup> space requirement per person, leading to a maximum of 16 targets in an 8m×4m room. Therefore, different number of targets, up to 15 targets, were considered in our simulations.

Table 6.3: SIMULATION FLOW

| <b>SIMULATION FLOW OF SCENARIO 1,2 AND 3</b> |   |
|--|---|
| <b>Inputs:</b>                               | $i_{max} = K;$ (Maximum number of targets)  |
|  | $j_{max} = Itr ;$ (Number of iterations )   |
|  | $N_E(j)$ is the estimated number of targets at iteration $j$ .                          |
|  | $E_l(k, j)$ is the estimated location of target $k$ at iteration $j$ .                  |
|  | $\rho(k, i)$ is target $k$ reflection factor when an environment with $i$ is considered |
| 1.   | <b>for</b> $i = 1: i_{max};$  |
| 2.   | <b>for</b> $j = 1: j_{max};$  |
| 3.   | Generate a random location(s) $l(k, j)$ and $\rho(k, i)$ for target(s) $k \in$          |
| 4.   | Generate additive white Gaussian noise $n_j(t)$   |
| 5.   | Apply LiDAL system detection algorithm  |
| 6.   | Hence determine $N_E(j)$ and $E_l(k, j)$  |
| 7.   | $j == j_{max}$  |
| 8.   | <b>end for</b>  |
| 9.   | Calculate MAPE  |
| 10.  | Calculate DRMSE   |
| 11.  | save MAPE and DRMSE at given value of $i$   |
| 12.  | $i == i_{max}$  |
| 13.  | <b>end for</b>  |

### 6.8.4 Scenario 1: The Baseline

In this scenario we considered a room that has no obstacles, ie the room is empty and no furniture is considered. We also assumed perfect mobility conditions for the mobile targets (i.e. pedestrian targets with a speed of 1 m/s). These targets were randomly and uniformly distributed on the detection floor with minimum inter-target-distance of 0.5 m. We considered a normal random distribution for the target reflection factor based on the proposed model in Chapter 3.

Figure 6.13 depicts the counting error, MAPE, of the MIMO LiDAL systems tested in scenario 1. As can be seen in Figure 6.13 the MAPE of the MIMO-LiDAL system with BSM for a single target is about 0.5% which is comparable to the probability of miss-detection of a single target in equation (6.16) with  $P_{M(MIMO)}=0.016$ . This agreement is a useful verification of our analytic results and simulations, where the single target case can experience errors due to the randomness associated with the target reflection coefficient and the noise in the receiver and environment. The MIMO-LiDAL system MAPE reaches 7% in the presence of 15 targets with BSM. Figure 6.13 shows an increase in MAPE with increase in the number of targets. This increase in MAPE can be attributed to a number of factors: (i) with increase in the number of targets, the room clutter increases with more objects (targets) acting as reflectors. Signals from LiDAL are reflected by the desired target and by other targets as well as secondary subsequent reflections from the walls. This increases the probability of error in counting the targets; (ii) with a larger number of targets, there is a higher potential for targets to occur either at the optical footprint overlap zones of MIMO LiDAL (see Figure 6.1). These locations are the most challenging for the LiDAL localisation systems.

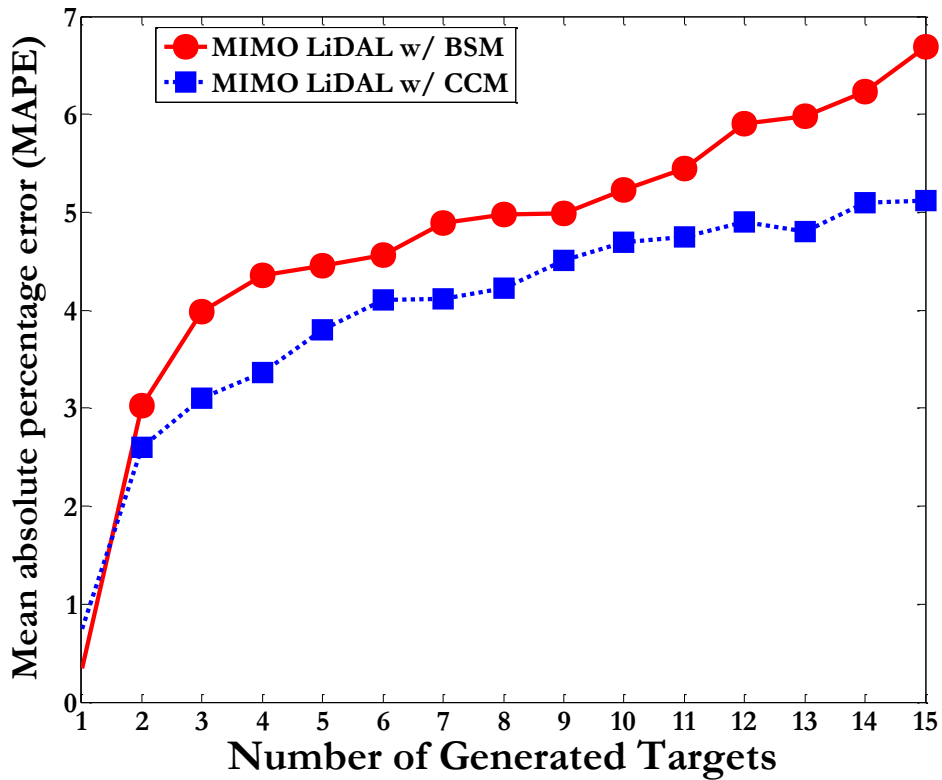


Figure 6.13: MAPE of MIMO LiDAL system with BSM and CCM in Room A of scenario 1.

In addition, the MIMO LiDAL system performance when the BSM is used for target distinguishing (ie using mobility to distinguish human targets from obstacles) is worse than the performance when the CCM is used. This is due to the increase in the inter-targets-interference (due to increased reflections) in the presence of more targets. Note that BSM and CCM perform comparably at lower number of targets, with the performance gap increasing with increase in the number of targets. As can be noted in Figure 6.13, the MAPE range for the MIMO-LiDAL system with CCM was from 0.3% to 5%. It is clear that the CCM has better performance than BSM as the inter-targets-interference does not affect the performance of CCM to the same extent.

### 6.8.5 Scenario 2: Challenging Localisation Environment

This scenario represents a challenging environment where obstacles (furniture and other objects) are present as seen in Figure 6.12, where the obstacles can reflect the MIMO LiDAL signals in a fashion similar to human targets. Continuous pedestrian motion is however considered, and therefore the environment is favourable from the point of view of being able to distinguish human targets from stationary obstacles. Figure 6.14 presents the MAPE associated with the MIMO LiDAL system for targets in scenario 2. One can observe that the MAPE increased significantly for MIMO-LiDAL with BSM from its range of 0.5% to 7% in scenario 1 to a new range of 6% to 35% in scenario 2. This is due to the presence of obstacles (furniture) in scenario 2 and due to the poor performance of BSM in a furnished environment due to the interference from the reflections attributed to background obstacles and furniture. Furthermore, in the presence of furniture, the residual space available for human motion is reduced, even when targets move continuously. This leads to impaired performance of BSM and CCM. In the MIMO-LiDAL system with the CCM, the MAPE was 1% to 5% in scenario 1, and increased to 4% to 16% in scenario 2.

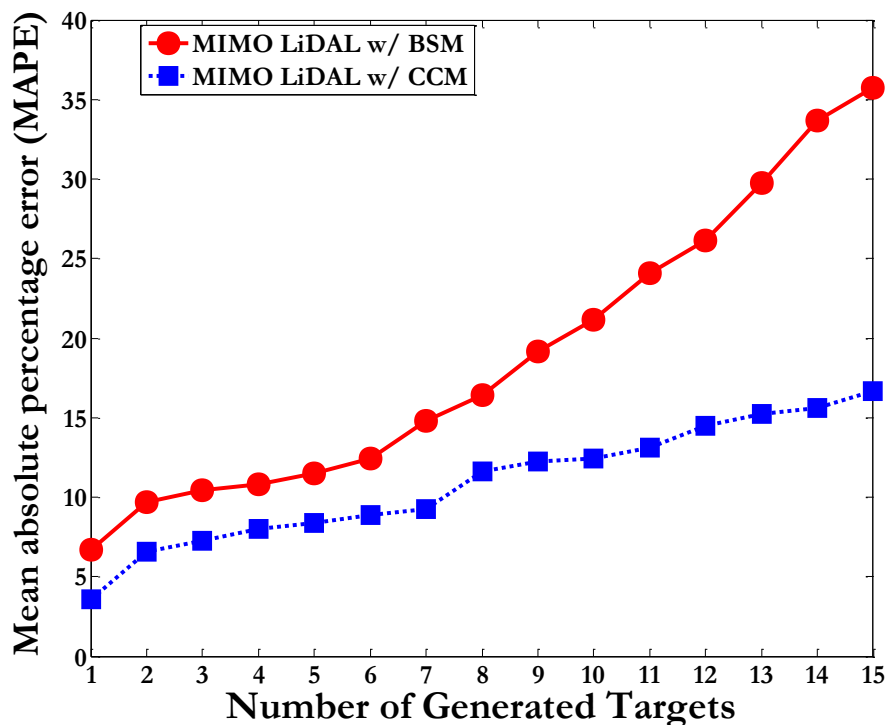


Figure 6.14: MAPE of MIMO LiDAL system with BSM and CCM in Room B of scenario 2.

Figure 6.15 shows the cumulative distribution function of the DRMSE positioning error for the MIMO-LiDAL system. Figure 6.15 presents the CDF of targets successfully detected in scenario 1 and scenario 2. As can be noted, the 95% CDF confidence interval is at 0.45m and 0.5m positioning error for scenarios 1 and 2 respectively, while the average DRMSE is 0.28m and 0.38m respectively. The results in Figure 6.15 clearly show that the DRMSE is larger in scenario 2 due to the presence of obstacles and hence the potential for such obstacles to be confused with human targets. The positioning error in MIMO-LiDAL occurs due to wrong decisions in the sub-optimum detector when it identifies the time slot that contains the signal reflected from the target. One wrong time slot leads to a 0.3m ( $\Delta R = 0.3m$ ) change in the error associated with the range to the anchor.

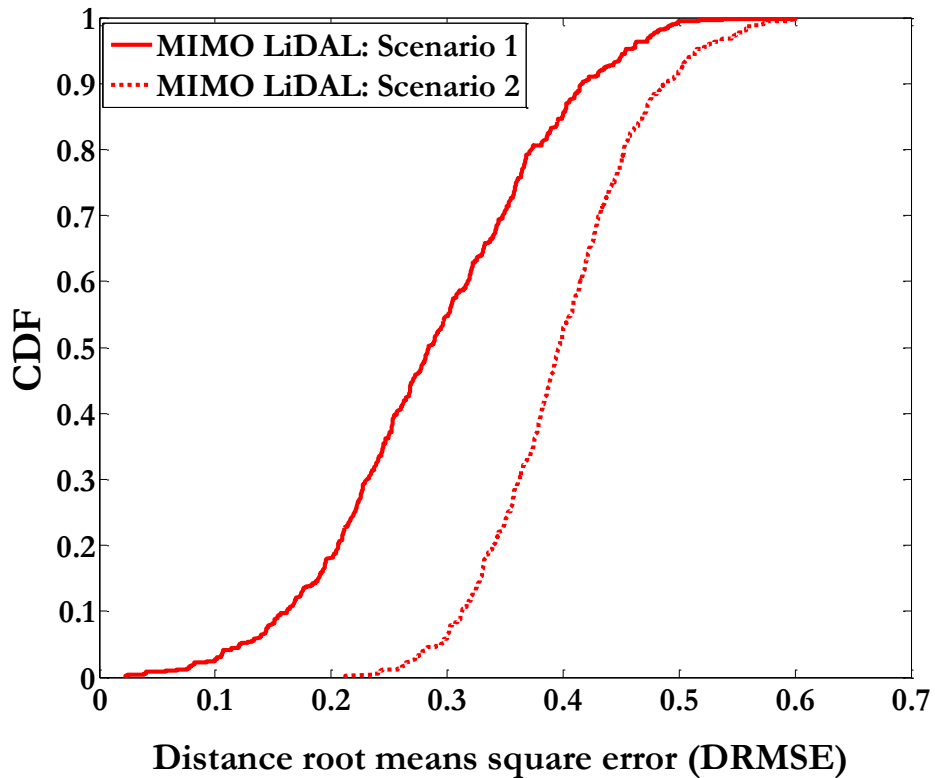


Figure 6.15: CDF of DRMSE of the proposed MIMO LiDAL system.



### 6.8.6 Scenario 3: Harsh Localisation Environment

In this scenario, the MIMO LiDAL system experience both impairments, namely the presence of obstacles (as in scenario 2) and nomadic mobility. Therefore, unlike scenario 2, the users can be stationary for periods of time and therefore the MIMO LiDAL system are not able to distinguish such stationary targets from obstacles, in furniture. To quantify the extent of nomadic behaviour, we define a mobility factor (MF) given by

$$MF = \frac{T_{ob} - \sum_{d=1}^{L_D} t_d}{T_{ob}} \quad (6.32)$$

where  $t_d$  is the time spent by the nomadic target in location  $d$ , which is a location of interest among the  $L_D$  locations of interest. Therefore, a MF=1 indicates a pedestrian target, ie a target that is in continuous motion as in scenarios 1 and 2. A MF that approaches zero, indicates a target that is fully nomadic, ie a target that spends most of the time stationary in a number of locations.

Figure 6.16 shows the MAPE for a MIMO LiDAL system where obstacles (furniture) are present as well as nomadic target behaviour. The MAPE decreases with increase in the MF as it becomes easier for the target distinguishing methods to distinguish targets from stationary obstacles. The results in Figure 6.16 used the CCM for target distinguishing. For a given value of MF, ie for a given level of nomadic behaviour, the MAPE decreases with decrease in the number of targets as was observed in scenario 2. It is worth observing that a MPAGE of 20% or less is only achieved in the MIMO LiDAL system for mobility levels that correspond to MF approaching one.

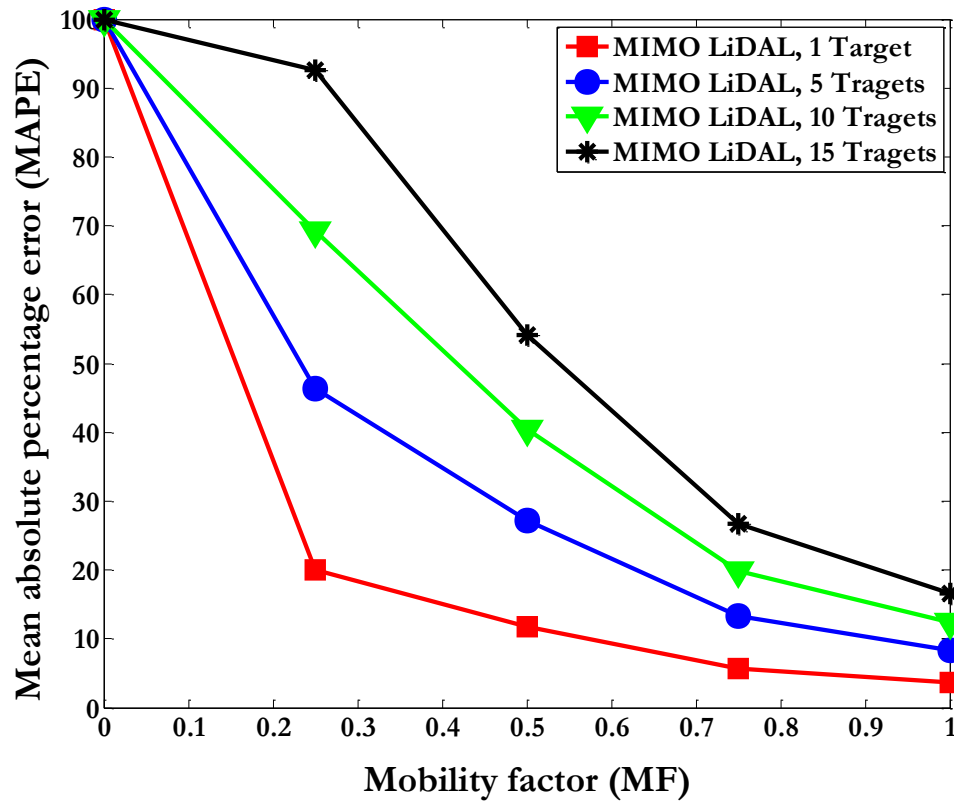


Figure 6.16: CDF of counting MAPE in the MIMO LiDAL system for nomadic targets with different MF.

## 6.9 Summary

In this chapter, we introduced MIMO LiDAL system configurations for target localisation, a MIMO LiDAL system which has multiple transmitters (can be the same transmitters as the VLC transmitters, with MAC which we outlined) and multiple collocated receivers, with each receiver having a single photodiode. We studied the performance of our system in three scenarios which progressively test our MIMO LiDAL system. The first scenario is a baseline system that produces the best performance possible. This scenario has an empty room with no obstacles (furniture) which reduces the localisation errors and has continuous human (pedestrian) motion which helps distinguish humans. When the better target distinguishing method, ie CCM, is used, the maximum target counting MAPE was 5.5% to 3.5% for MIMO LiDAL system. The maximum MAPE occurs at maximum number of targets, which was 15 human targets in our 8m × 4m × 3m room.

In the second scenario, obstacles (furniture) are introduced, however the environment has continuous pedestrian motion. Here the maximum target counting MAPE was 12% to 16% for the MIMO LiDAL system. In terms of localisation errors, the average DRMSE was 0.28m and 0.38m for scenario 1 and scenario 2 respectively for the MIMO LiDAL system.

The third scenario is more challenging, with obstacles (furniture) present in the room and with targets moving in a nomadic fashion rendering the target distinguishing task harder. We defined a target mobility factor (MF), with MF=1 representing a fully mobile target and MF=0 being the extreme end of nomadic behaviour (fully stationary target). It is worth observing that a MAPE of 20% or less is only achieved in the MIMO LiDAL system for mobility levels that correspond to MF approaching one.

# Chapter 7

## Imaging LiDAL System

### 7.1 Introduction

In LiDAL, the elimination of target ambiguity is important to detect, count and localise targets correctly. Traditional bistatic RF radar eliminates target ambiguity by using the estimated target range (round trip time) with the angle of arrival of the received signal reflected from the target, where the angle of arrival is estimated using beam steering based on mechanical rotated RF receivers or phased antenna arrays. In our optical imaging radar, the receiver consists of a photodiode array with an imaging lens that forms an image of the observed region on the receiver detectors. To determine the direction of the received reflected signal from the target, the imaging receiver pixels that observe the target are used together with their FOV. Hence, in this work we introduce an imaging LiDAL system that employs an imaging detection receiver with multiple VLC transmitters (light sources / engines). We refer to this system as multiple-input (multiple LiDAL transmitters) single-output (single LiDAL receiver) imaging LiDAL. The MISO-IMG-LIDAL system can provide; (i) target ambiguity elimination where the targets are separated in the optical imaging domain, (ii) target localisation where the imaging receiver forms an image of the floor and hence each imaging receiver pixel observes a small and finite region on the floor. Most importantly, localisation is achieved in this case using one time frame (no need for three anchors) (iii) interference minimisation, (the interference results from reflections from the background obstacles) which can lead to improvement in the performance of the distinguishing methods such as the BSM method; (iv) LiDAL channel bandwidth enhancement due to the narrow FOV of the pixels which reduces the complexity of the optimum receiver without implementing an equaliser to tackle the channel dispersion, (v) simplified system design where the

localisation accuracy / resolution is no longer a function of the pulse width. Instead the localisation accuracy can be increased by increasing the number of receiver pixels (and hence also reducing the per pixel FOV). The pulse used for localisation can thus have a longer duration compared to the pulse duration used in the MIMO LiDAL system. This leads to simplified pulsed transmitter design, which is welcome given that commercial high resolution imaging receivers are available with several million pixels (here we use hundreds of pixels). (vi) overhead reduction, where the imaging LiDAL overheads are reduced compared to MIMO LiDAL due to the lower number of radar scans required to detect and localise targets.

The remainder of this chapter is divided as follows: Section 7.2 presents the configuration of MISO IMG LiDAL. Section 7.3 introduces target localisation in MISO imaging LiDAL. Section 7.4 discusses the challenges of target detection and the solutions for MISO IMG LiDAL. Section 7.5 analyses the receiver operating characteristics of MISO IMG LiDAL. Section 7.6 describes the simulation setup and the performance analyses of MISO IMG LiDAL systems. At the end of the chapter a summary is provided.

## 7.2 System Configurations

The MISO-IMG-LiDAL system consists of eight LiDAL transmitter units and one imaging receiver installed in the centre of room's ceiling (2m, 4m, 3m) as shown in Figure 7.1. The imaging receiver includes a number of pixels, where each pixel is a photodiode (PD) optical receiver. The advantage of the massive number of pixels is in providing spatial selection to separate the targets in the optical domain (i.e. more narrow optical footprints). This results in reduced targets ambiguity and increased resolution in the spatial domain. The imaging receiver lens forms an image of the floor on the receiver pixels thus dividing the floor into an optical grid as can be noted in Figure 7.1, where each sub-receiver has a narrow FOV and covers a given optical footprint.

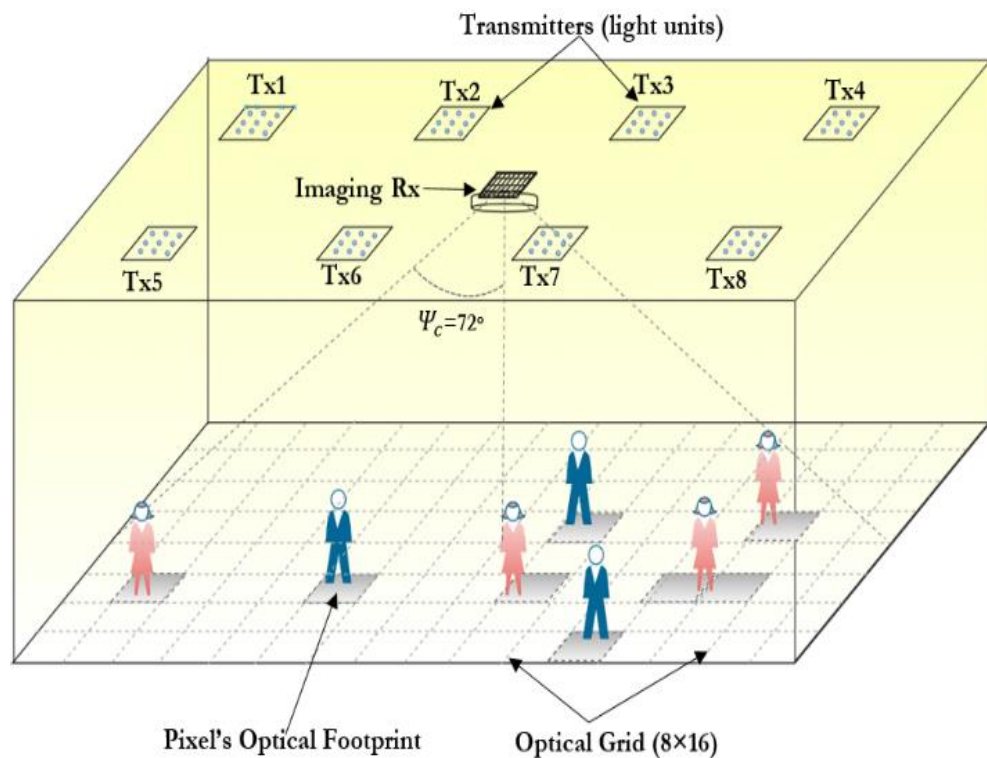


Figure 7.1: MISO-IMG-LiDAL system.

The configuration of the imaging receiver is defined by (i) the entrance area of imaging receiver lens where  $A = \frac{9\pi}{4} \text{ cm}^2$  [186]-[187], (ii) the semi-acceptance angle of the imaging lens with semi-angle FOV of  $\Psi_c=72^\circ$  in our system to enable the imaging receiver to cover the entire floor along room length of 8m, and (iii) the lens has an exit area as defined in [186]:

$$A' = \frac{A \sin^2(\Psi_c)}{N^2} \quad (7.1)$$

where  $N$  is the lens refractive index. The lens semi-angle FOV can be defined as (see Figure 7.2):

$$\Psi_c = \tan^{-1}\left(\frac{D}{2f}\right) \quad (7.2)$$

where,  $f$  is the lens focal length and  $D$  is the PD array length as can be seen in Figure 7.2.

The imaging receiver maximum range  $R_{Max}^{FOV}$  is related to the target as:

$$R_{Max}^{FOV} = \tan(\Psi_c) (d_o - h). \quad (7.3)$$

We define the imaging lens zooming ratio  $R_{zoom}$  as:

$$R_{zoom} = \frac{2R_{Max}^{FOV}}{D}. \quad (7.4)$$

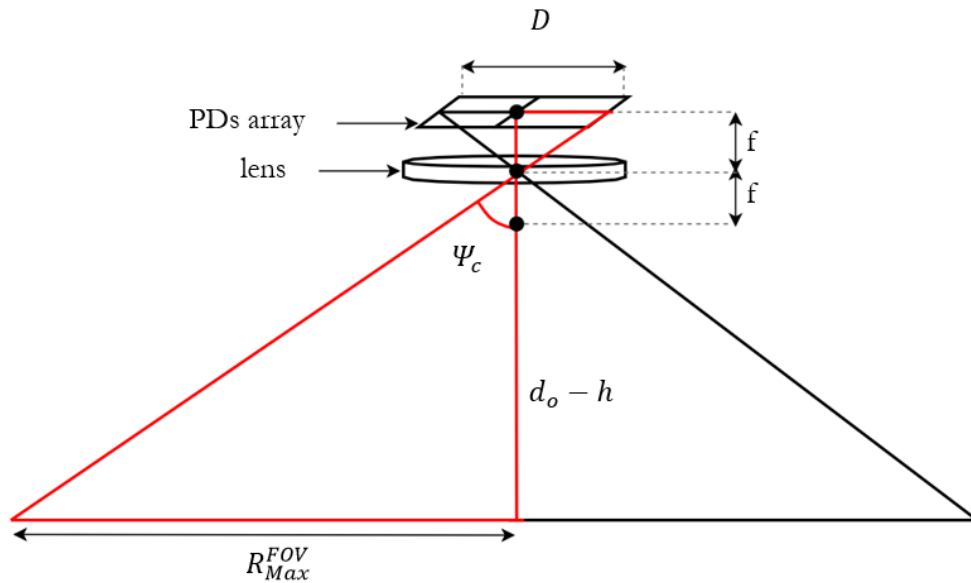


Figure 7.2: LiDAL imaging receiver design, lens FOV with  $R_{Max}^{FOV}$ .

To separate two targets at a distance of  $\Delta s$  from each other, as can be seen in Figure 7.3, the minimum distance between pixels  $\Delta d$  is given as:

$$\Delta d = \frac{\Delta s}{R_{zoom}}. \quad (7.5)$$

The imaging lens transmission factor  $T_f$  is defined as [186], [188] :

$$T_{f(img)}(\delta) = -0.198\delta^2 + 0.0425\delta + 0.8778 \quad (7.6)$$

where  $\delta$  is the incidence angle measured in radians.

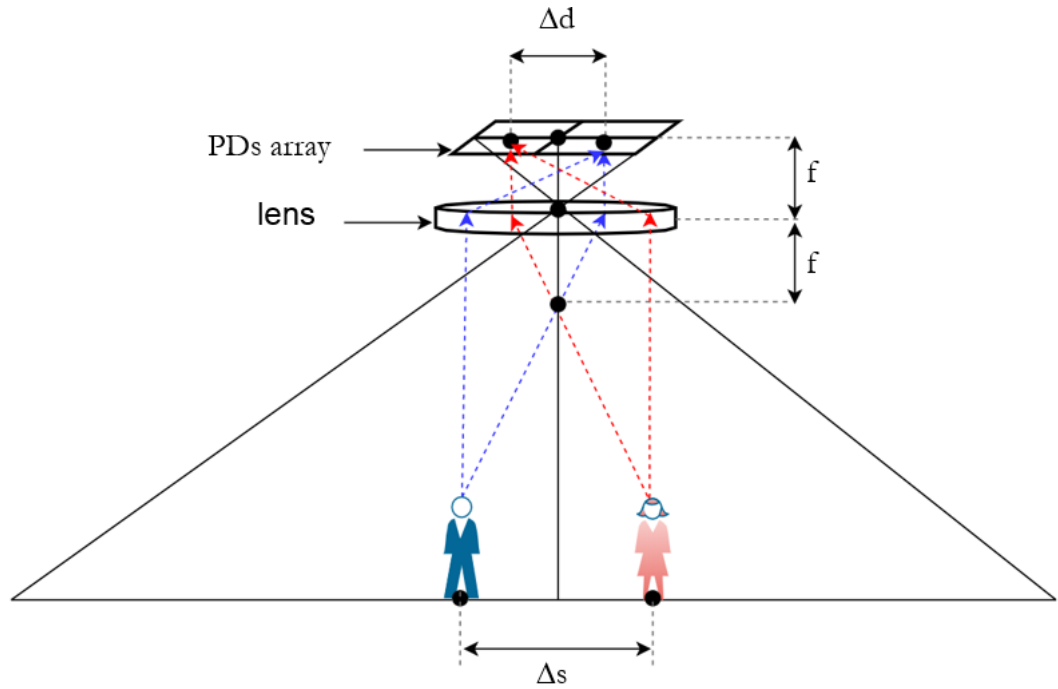


Figure 7.3: targets optical resolution in MISO IMG LiDAL system.

We selected an imaging receiver total photodetection area of  $2 \text{ cm}^2$  ( $2 \text{ cm}$  length  $\times$   $1 \text{ cm}$  width) which approximately fits into the exit area of the lens [186], [189]. The photodetector area is divided into an array of (8 columns  $\times$  16 rows) pixels to satisfy the design parameter  $\Delta s$  which is chosen as  $0.5 \text{ m}$ . We assumed there is no gap between the pixels. It is worth mentioning that, we change the LiDAL resolution from  $\Delta R$  of  $0.3 \text{ m}$  to  $\Delta s$  of  $0.5 \text{ m}$  to obtain an integer number of pixels. Each pixel has a square area of  $1.56 \text{ mm}^2$  ( $1.25 \text{ mm} \times 1.25 \text{ mm}$ ) and this corresponds to the area of a PD.



The pixel's optical detection area can be determined by calculating the viewing angles (azimuth and elevation) corresponding to the receiver location as can be seen in Figure 7.4. The azimuth ( $A_z$ ) and elevation ( $E_L$ ) angles of the imaging receiver pixels can be written as [187] [190] :

$$E_{Lj} = \tan^{-1} \left( \frac{\sqrt{d_{xj}^2 + d_{yj}^2}}{d_o - h} \right) \quad (7.7)$$

$$A_{zj} = \tan^{-1} \left( \frac{d_{yj}}{d_o - h} \right) \quad (7.8)$$

where  $d_x$  and  $d_y$  are the horizontal separation distances along the  $x$  and  $y$  axes as can be seen in Figure 7.4 and  $j$  is the pixels number.

According to the design parameters of the imaging receiver, each pixel is treated as a PD that covers a typical square optical footprint area of 0.25 m<sup>2</sup> (pixel's range  $P_R=0.5$ m i.e. pixel's FOV = 11°) on the floor. The optical grid which covers the total detection floor is divided into 128 optical footprints (8×16). We assumed that the imaging lens has no reception distortion with ideally square optical FOV for all pixels. The proposed MISO-IMG-LiDAL can be used for detection, counting, and localisation of multiple targets within the optical grid. In MISO-IMG-LiDAL, the transmitter unit and the imaging (pixel) receiver are separated and therefore work as bistatic LiDAL. We have calculated the maximum channel bandwidth for MISO-IMG-LiDAL using the approach described Chapter 3 for the bistatic LiDAL. The maximum channel bandwidth for a single pixel receiver is  $Bw_{ch(img)}=480$ MHz. We also employed the TIA in [153] for each pixel receiver with input noise current  $\sigma_{thermal(img)}$  of 2.6 pA/√Hz.

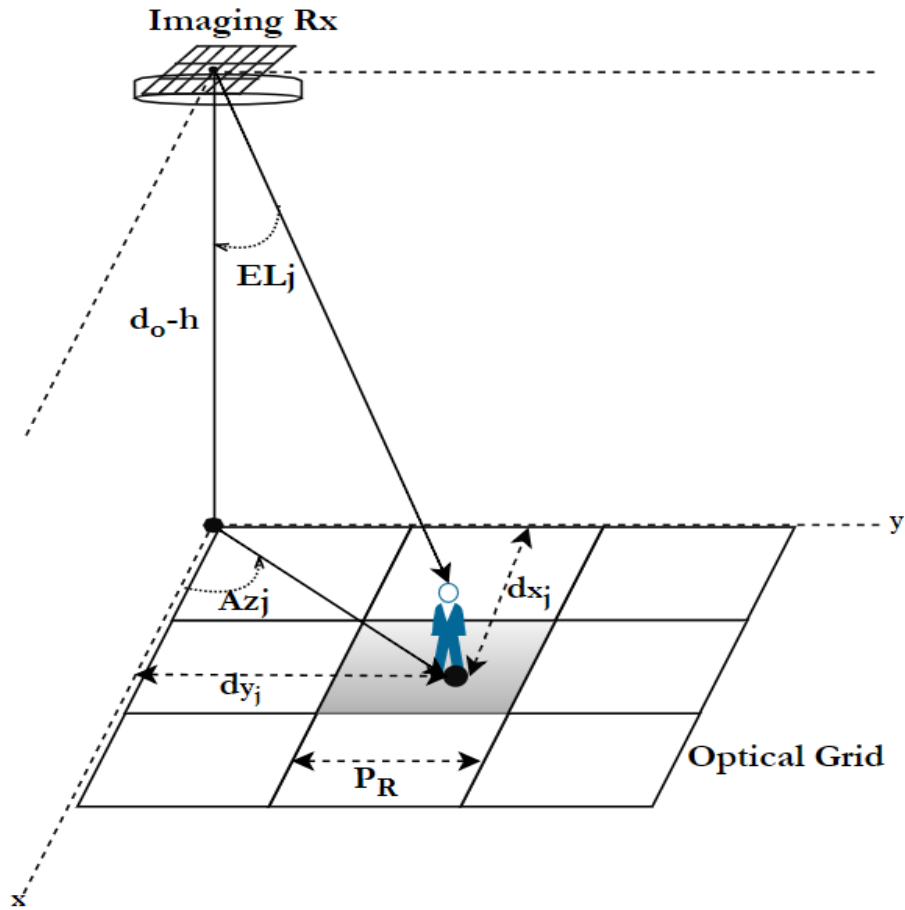


Figure 7.4: Pixel's angles of IMG LiDAL system.

### 7.2.1 MISO-IMG-LiDAL Receiver Operating Characteristics

In a Bistatic IMG-MISO LiDAL system, ie  $T_{x1}$  working with the imaging  $R_x$ .

The received reflected signal ( $P_{R_{FOV_{Max}}}^{B(img)}$ ) from the target is located on the edge of the optical footprint grid as can be seen in Figure 7.5 of bistatic IMG-MISO LiDAL can be given as:

$$\begin{aligned}
 & P_{R_{FOV_{Max}}}^{B(img)} \\
 &= \frac{(n+1)(n_{ele}+1)}{4\pi^2 R_1^2 R_2^2} T_{f(img)}(\Psi_c) G_c(\Psi_c) P_t \bar{d}_A \rho A \cos^n(\theta) \cos(\varphi) \cos^{n_{ele}}(\varphi_1) \cos(\delta)
 \end{aligned}
 \tag{7.9}$$

Due to the narrow detection of the pixel, the value of target cross section area  $d_A$  within a FOV of a single pixel was  $0.14\text{m}^2$ . It can be noted from bistatic IMG-MISO LiDAL in Figure 7.5, that the  $R_1 \neq R_2$ ,  $\theta \neq \varphi$ , and  $\delta = \varphi_1$ , where:

$$R_1 = \sqrt{(2\sqrt{2} P_R)^2 + (d_o - h)^2} \quad (7.10)$$

and:

$$R_2 = \sqrt{R_{\text{Max}}^{\text{FOV}^2} + (d_o - h)^2} \quad (7.11)$$

The mean received reflected signal ( $\bar{P}_{R_{\text{Max}}}^{\text{Bimg}}$ ) from a target located at the edge of the optical footprint (grid), as can be seen in Figure 7.5, is:

$$\bar{P}_{R_{\text{Max}}}^{\text{Bimg}} = \frac{C_{\text{img}} \mu_\rho (d_o - h)^{n+3}}{4\pi^2 \left( (2\sqrt{2} P_R)^2 + (d_o - h)^2 \right)^{\frac{n+3}{2}} \left( R_{\text{Max}}^{\text{FOV}^2} + (d_o - h)^2 \right)^2} \quad (7.12)$$

where:  $C_{\text{img}} = (n + 1)(n_{\text{ele}} + 1)P_t d_A A T_{f(\text{img})}(\Psi_c)G_c(\Psi_c)$ .

The standard deviation of the received signal  $\hat{P}_{R_{\text{Max}}}^{\text{Bimg}}$  is given as:

$$\hat{P}_{R_{\text{Max}}}^{\text{Bimg}} = \frac{C_{\text{img}} \sigma_\rho (d_o - h)^{n+3}}{4\pi^2 \left( (2\sqrt{2} P_R)^2 + (d_o - h)^2 \right)^{\frac{n+3}{2}} \left( R_{\text{Max}}^{\text{FOV}^2} + (d_o - h)^2 \right)^2} \quad (7.13)$$

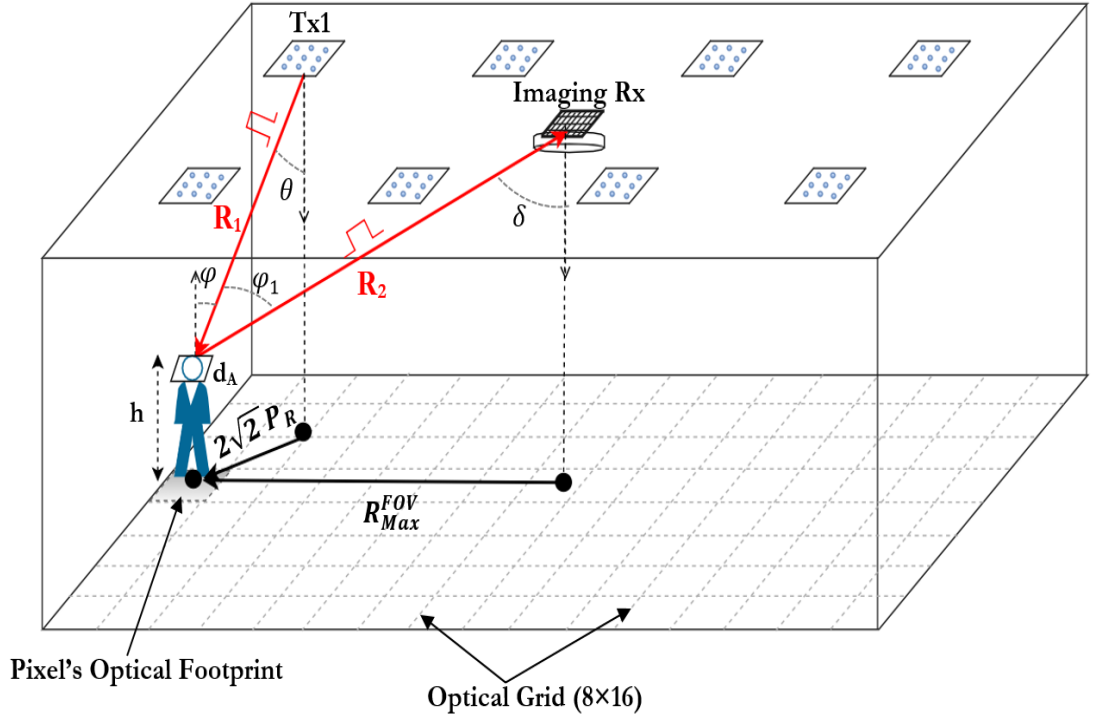


Figure 7.5: Bistatic MISO-IMG-LiDAL system.

Figure 7.6, presents the ROC depicting the trade-off between  $P_D^{B(img)}$  and  $P_{FD}^{B(img)}$  of the bistatic MISO-IMG-LiDAL system for a target located at a range of  $R_{Max}^{FOV}$ . The impact of selecting the detection threshold  $D_{th}^{B(img)}$  on the target false detection can be seen in Figure 7.7. In this work, we consider MISO-IMG-LiDAL for people counting and localisation applications. Thus, we selected the detection threshold  $D_{th}^{B(img)}$  to maximise the value of  $P_D^{B(img)}$ . We accept  $P_{FD}^{B(img)}=0.1$ , thus giving  $P_D^{B(img)}=0.9$  and giving an optimum detection threshold  $D_{th}^{B(img)} = 0.39 \bar{P}_r^{B(img)} r_{R_{Max}^{FOV}}$  in this case.

The maximum number of targets  $C_M$  that can be counted in MISO-IMG-LiDAL system is:

$$C_{M(MISO_{img})} = \frac{T_w(img)}{\tau} O_{GS} \quad (7.14)$$

where  $O_{GS}$  is the optical grid size (128 optical footprints) and  $T_w(img)$  is the channel time window of the imaging receiver's pixel ( $j$ ) which corresponds to the difference in trip times of a target placed at the edge of a pixel's optical

footprint  $P_R$  (see target location in Figure 7.5) and a target placed underneath the transceiver. Thus  $T_{w(img)}$  is given as:

$$T_{w(img)} = \frac{\left(\sqrt{P_R^2 + (d_o - h)^2}\right) - (d_o - h)}{c} \quad (7.15)$$

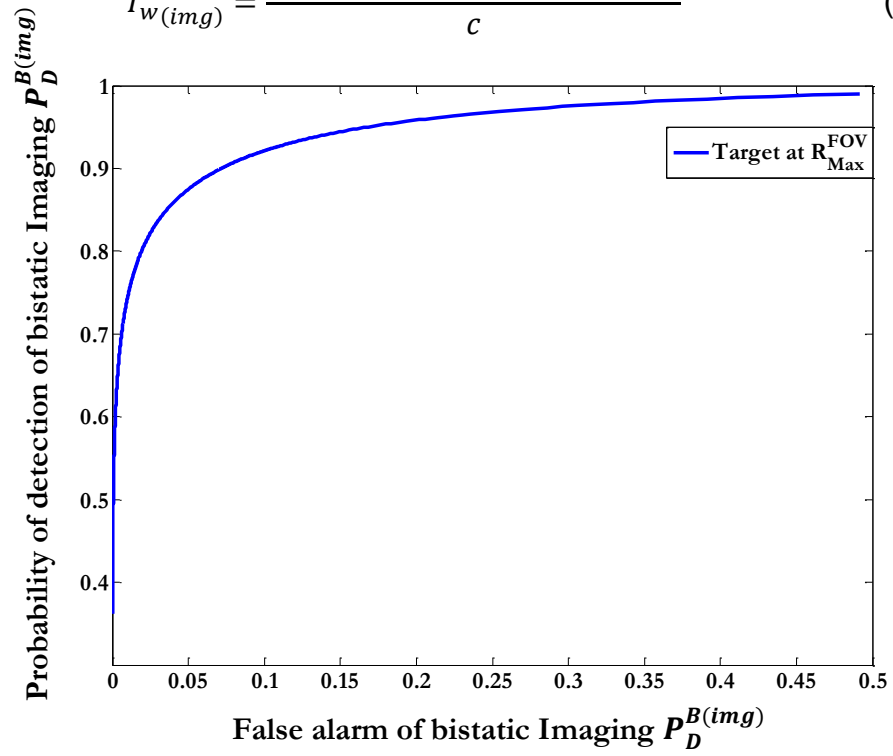


Figure 7.6: ROC of Bistatic MISO-IMG-LiDAL system.

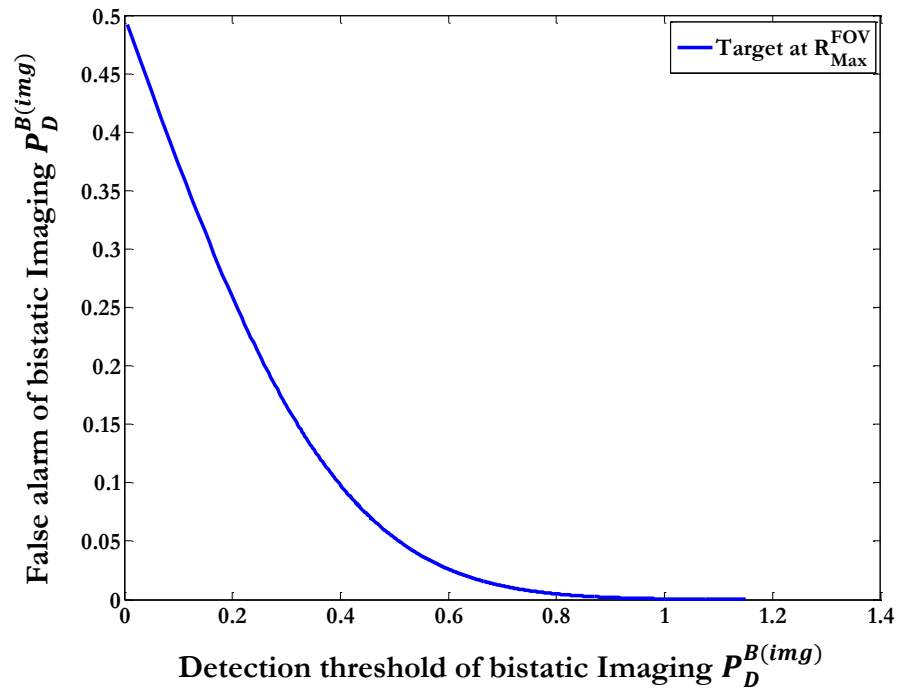


Figure 7.7: Bistatic MISO-IMG-LiDAL false detection with optimum  $D_{th}^{B(img)}$ .

### 7.3 Target localisation

Target localisation in MISO-IMG-LiDAL relies on the calculation of the direction of arrival (DOA) of the reflected signal arriving at the pixel's centre. The elevation and azimuth angles of the pixels are determined based on the design specifications of the imaging receiver with respect to the receiver's coordinates. However, the values of these angles are recalculated whenever the location of the receiver is changed (note that the receiver in our system is fixed in one location for a given room). The target position can be found by calculating the distance between the imaging receiver location  $(x_r, y_r, z_r)$  and the centre of the target's pixel as shown in Figure 7.8. The (range) distance  $R_j$  between the ground reference point and the pixel's centre is given as:

$$R_j = \sqrt{\left(\frac{d_o - h}{\cos(E_{Lj})}\right)^2 - (d_o - h)^2} \quad (7.16)$$

and the pixel  $(x_j, y_j)$  coordinates are defined by:

$$x_j = R_j \cos(A_{zj}) \quad (7.17)$$

$$y_j = R_j \sin(A_{zj}). \quad (7.18)$$

The coordinates of target  $k$ ,  $P_k(x, y)$ , are calculated with respect to the receiver ground reference centre point  $L_o(x_o, y_o)$  (see Figure 7.8):

$$P_k(x, y) = (x_o + x_j), (y_o + y_j) \quad (7.19)$$

The probability of localizing a target located at  $R_{\text{Max}}^{\text{FOV}}$  ( see target in see Figure 7.8) in the MISO IMG LiDAL system,  $P_{L(\text{img})}^{R_{\text{Max}}^{\text{FOV}}}$ , can be written as:

$$P_{L(\text{img})}^{R_{\text{Max}}^{\text{FOV}}} = \text{erfc} \left( \frac{D_{th}^{B(\text{img})} - \bar{P}_r^{B_{\text{img}}}}{\hat{P}_r^{B(\text{img})} \sqrt{2}} \right) \quad (7.20)$$

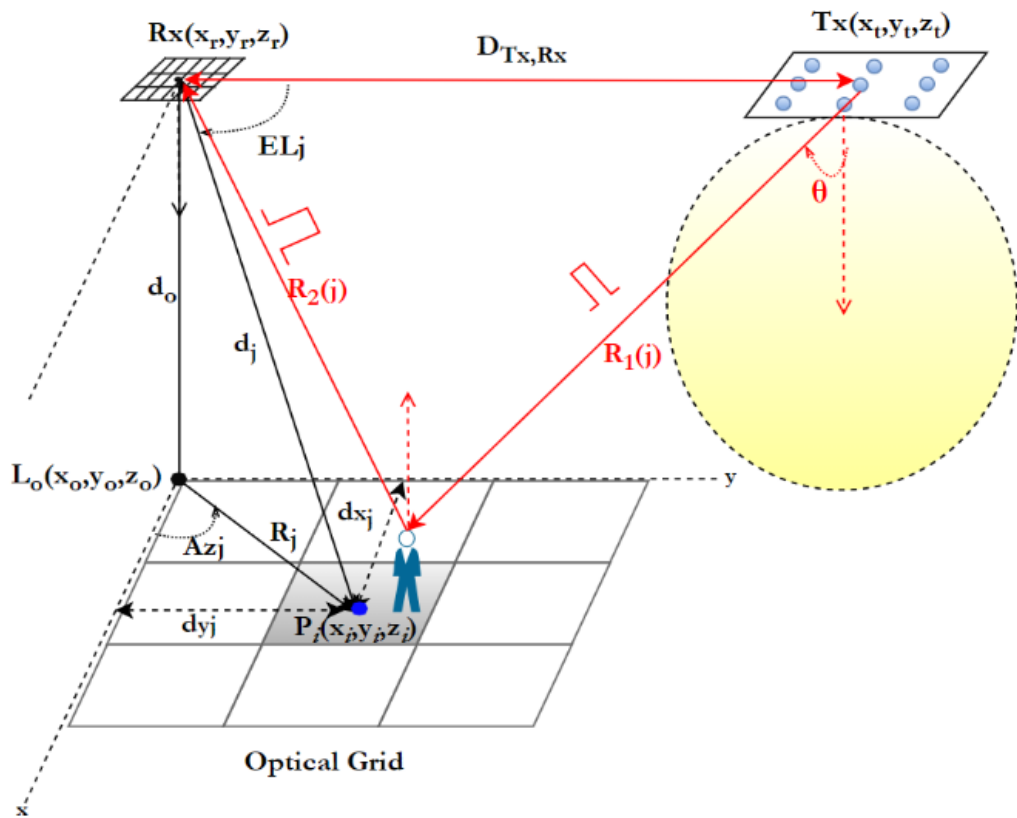


Figure 7.8: Target localisation in MISO IMG-LiDAL.

## 7.4 Multiple Target Detection in MISO-IMG-LiDAL

The MISO-IMG-LiDAL system (which has many small optical detection footprints) has the ability to detect targets under different mobility schemes by tracking and marking the target in the imaging optical detection grid, see Figure 7.9. In MISO-IMG-LiDAL, detection is accomplished using snapshot measurements, considering the change in the received reflected signals observed by the pixels due to target motion. When the target moves a distance more than the spatial distance of the imaging receiver  $\Delta s$ , the target is distinguished by monitoring the change that occurs in the pixels in at least two IMG LIDAL scans (snapshots). We identify the change between pixel snapshot measurements using a pixels cross-correlation method (PCCM) and pixels subtractions method (PSM). PCCM is similar to the slow cross-correlation we discussed in Chapter 5, however in IMG LiDAL we employ the correlation between the pixel snapshots instead of the time slots snapshots. Thus, the cross-correlation  $\left(\mathcal{R}_{p_{r_k} p_{r_{k+1}}}\right)$  between the  $k^{th}$  received pixels snapshot and  $S$  consecutive received pixel snapshots is given as:

$$\mathcal{R}_{p_{r_k} p_{r_{k+1}}}(\tau_p | N_p) \triangleq \int_{-N_p}^{N_p} p_{r_{k+1}}(x_n - \tau_p) \sum_{k=1}^S p_{r_k}(x_n) dx_n \quad (7.21)$$

and:

$$p_{r_k}(x_n) = \sum_{i=1}^{I_p} \sum_{j=1}^{J_p} \int_0^T (p_{r_k}^{(i,j)}(t) + n(t)) dt \quad (7.22)$$

where,  $N_p$  is the total number of pixel receivers ( $N_p = I_p \times J_p$ ),  $i$  is number of pixels in row  $i$ ,  $i \in [1, \dots, I_p]$ ,  $j$  is number of pixels in column  $j$ ,  $j \in [1, \dots, J_p]$ ,  $x_n$  is the pixel number,  $x_n \in [1, \dots, N_p]$  and  $p_{r_k}(t)$  is the received reflected signal power in each pixel receiver. The pixel displacement factor ( $\hat{X}_n^s$ ) can be defined as:

$$\hat{X}_n^s = \arg \max_{\tau_p} \left( \mathcal{R}_{p_{r_k} p_{r_{k+1}}}(\tau_p | N_p) \right) \quad \hat{X}_n^s \in [1, \dots, N_p - 1]. \quad (7.23)$$



When  $\hat{X}_n^s$  is zero, this indicates no change between the received reflected pulses in the  $x_n^{th}$  pixel. When  $\hat{X}_n^s \neq 0$ , target motion is observed from the  $x_n^{th}$  pixel with a displacement number of  $\hat{X}_n^s$  pixels. Similar to the CCM with time slots receiver, we define a weight  $w_{x_n}^s$  for each pixel receiver to be employed with the pixel sub-optimum receiver. Thus  $w_{x_n}^s$  is defined as:

$$w_{x_n}^s = \begin{cases} 0 & \text{if } \hat{X}_n^s = 0 \\ 1 & \text{otherwise} \end{cases}. \quad (7.24)$$

For PSM, the subtraction of the  $k^{th}$  received pixel snapshot from  $S$  consecutive received pixel snapshots can be written as:

$$p_{r_{S(k,k+1)}}^{x_n} = p_{r_{k+1}}(x_n) - \sum_{k=1}^S p_{r_k}(x_n). \quad (7.25)$$

The computed value  $p_{r_{S(k,k+1)}}^{x_n}$  is used in the sub-optimum receiver to decide the presence or absence of the target.

Figure 7.9 shows an example of pedestrian targets where the targets move on the detection floor of the MISO-IMG-LiDAL system with different mobility schemes. Targets 1, 2 and 3 are nomadic, pedestrian and 'power walking' (ie fast) targets respectively. As can be seen in Figure 7.9, the motion of target 1 is distinguished through snapshots measurements of  $k=1$  and  $k=2$  where target 1 has moved from pixel (1,1) to pixel (1,3). While observing snapshots  $k=2$  and  $k=3$ , target 2 is detected and marked in pixel (1, 1) and no change occurs in pixel (1,3), the nomadic target. Thus the total number of marked pixels is two (counter value) indicating the presence of two targets and their locations. In snapshot  $k=4$ , target 2 moves to the location of target 1 (at the same narrow optical zone). In this case, a counting error occurs as the distance between targets becomes less than the radar resolution, as pixel (1, 3) now contains both targets. In snapshot  $k=4$ , target 3 enters the environment at (3, 7). In the next snapshots, comparing snapshot  $k=4$  and  $k=5$ , the counter value is updated where the detection error that occurred at  $k=4$  is now resolved due to the movement of target 2 away from target 1. Note that the nomadic target 1 has not moved at  $k=4$  and at  $k=5$ , and is still at pixel (1, 3). The pedestrian target 2 has moved from (1, 3) at  $k=4$  to (1, 4) at  $k=5$ . The

power walking target 3 has moved from (3, 7) at  $k=4$  to (3, 2) at  $k=5$ . A similar pattern continues, comparing  $k=6$  and  $k=7$ .

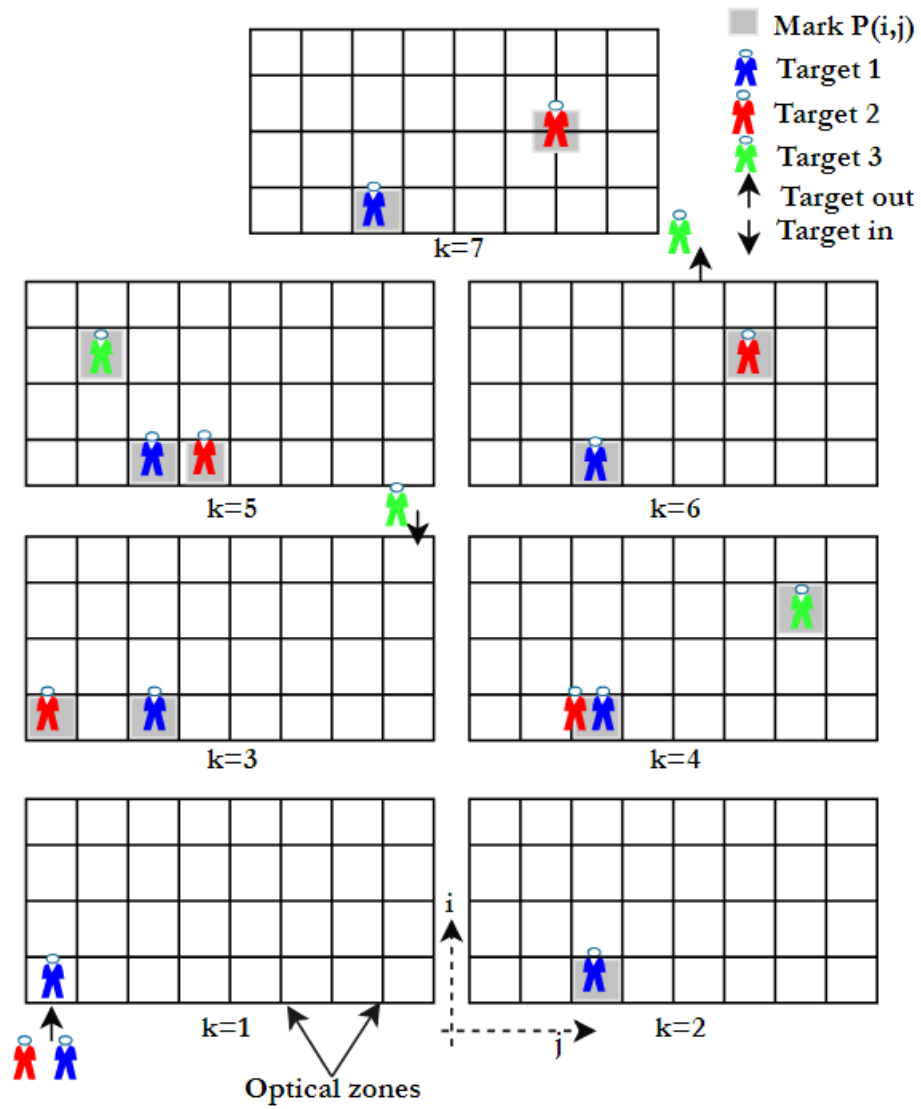


Figure 7.9: A top view of three targets movement on the detection floor of MISO-IMG- LiDAL system during  $S$  snapshots measurements.

### 7.4.1 Challenges of Target Detection in MISO-IMG-LiDAL

The main challenges of target detection in MISO-IMG-LiDAL are; (i) the transmitters have limited optical footprints and for coverage, these transmitter optical footprints overlap on the floor. Therefore, for target localisation, the transmitters have to be turned on in turn to scan the entire room. A target located in the region where the optical footprints overlap, can be counted more than a single time when it is reported by the scans associated with each transmitter. Such duplicate counting has to be removed; (ii) the receiver pixels cover finite regions on the floor. A target may be located at the intersection of up to four pixels, see target 2, at  $k=7$  in Figure 7.9. In this case, the issue is resolved by setting up a low and a high threshold as was done in Chapter 4, where we dealt there with target overlap over multiple time slots and here we deal with target overlap in multiple pixels. A pixel reporting an output above the threshold contains a target, a target is absent if the signal is below the threshold and the pixel with the highest output energy is selected when multiple pixels have outputs between the thresholds.

Thus, in relation to challenge (i), and in order to eliminate multiple counting of a single target due to  $L_{tx}$  active transmitters, we activate each transmitter individually and listen to reflections from the targets using the imaging receiver. To simplify the process, we note that each transmitter covers a finite optical footprint on the floor. Therefore, the only pixels that can possibly report a reflection are a group of pixels that cover the transmitter optical footprint on the floor. As such we divided our imaging receiver 128 pixels into 8 groups with 16 pixels per group. Here each group of receiver pixels (GRP), as can be seen in Figure 7.10, covers one transmitter optical footprint, with 8 transmitter in our setup, see Figure 7.1.

In relation to challenge (ii), the solution was described at top level above. Note that the signal at the output of each pixel is processed using an orthonormal expansion shown in Figure 7.11 which is an approach that follows our work in Chapter 4 translated from a time domain approach to a spatial approach at the pixel level in this chapter.

Note that, the sub-optimum imaging receiver in Figure 7.11 collects signals from  $N_p$  pixels. In terms of listening time, we considered one time slot ( $T_s = T$ ) for each pixel receiver. Figure 7.11 shows the sub-optimum imaging receiver (SOIMR) for the MISO-IMG-LiDAL system. The SOIMR has  $N_p$  orthonormal functions  $\phi_p(x_n)$  with integrators and comparators. The decision circuit decides as follows:

1. If the observed received signal  $z_{x_n}$  is below the lower threshold,  $D_{th_L}$ , then the target is absent in pixel  $(i, j)$ , denoted here as pixel  $x_n$ .
2. If the observed received signal  $z_{x_n}$  is above the higher threshold,  $D_{th_H}$ , then the target is present in pixel  $(i, j)$ , denoted here also as pixel  $x_n$ . Note that, both detection thresholds  $D_{th_L}$  and  $D_{th_H}$  have been optimised for the MISO-IMG LiDAL system in this section following an approach similar to that discussed in Chapter 4.
3. If the observed received signal  $z_{x_n}$  is above  $D_{th_L}$  and below  $D_{th_H}$ , then it is a received reflected pulse from a target located within the FOVs of multiple neighbouring pixels. Thus the decision circuit compares  $z_{x_n}$  with all possible neighbouring pixels and selects the pixel that has the largest  $z_{x_n}$  as the pixel that contains the target. We considered a worst case scenario of three neighbour pixels as shown in Figure 7.11, where the decision circuit compares  $z_1$  with its three neighbouring pixels  $z_2, z_3$  and  $z_4$  and chooses the largest.

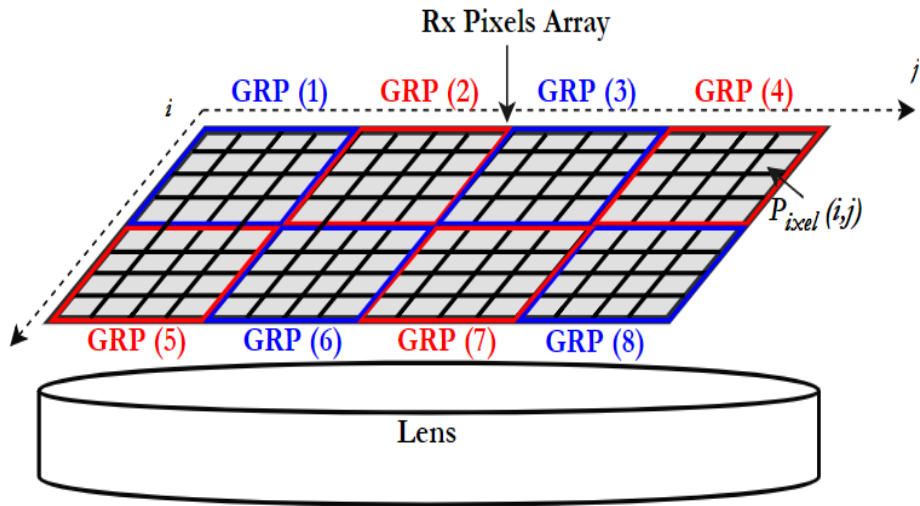


Figure 7.10: Eight GRPs of the imaging receiver.

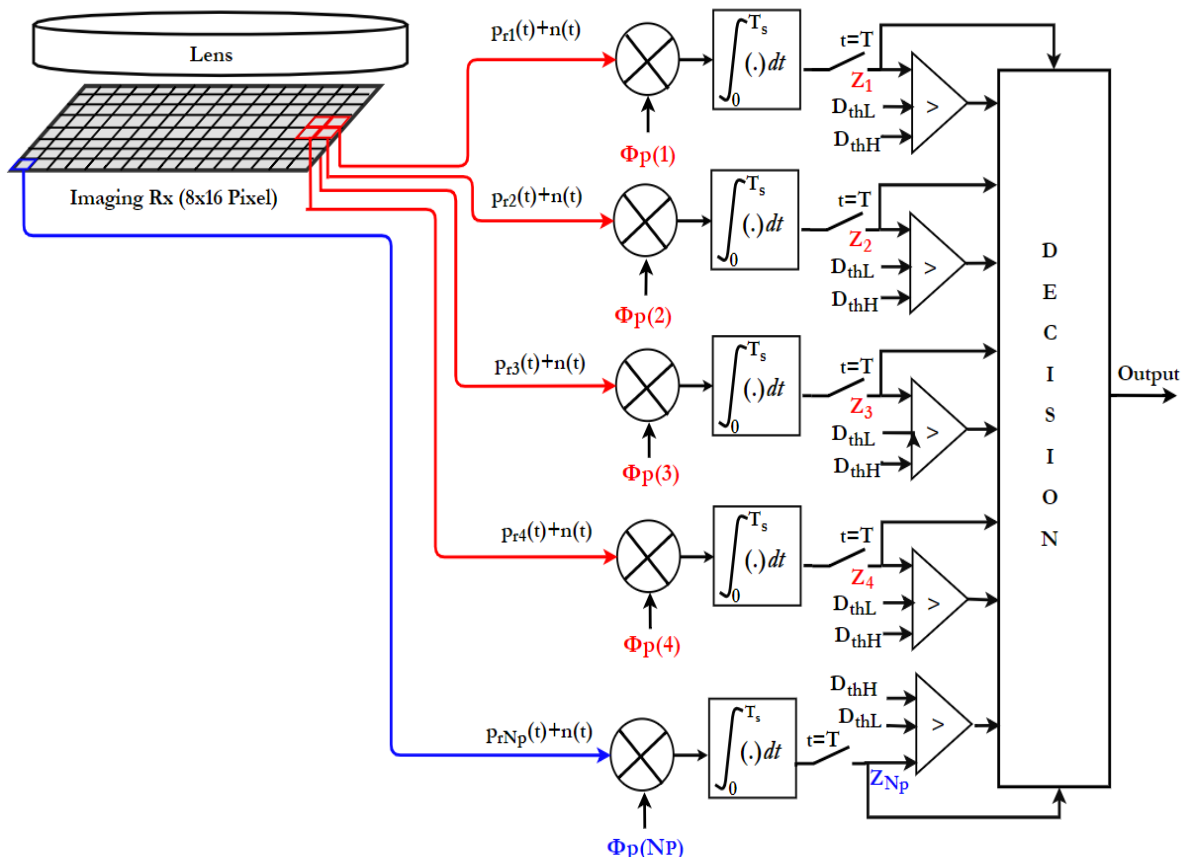


Figure 7.11: The proposed sub-optimum imaging receiver (SOIMR) for IMG LiDAL system.

## 7.5 MISO-IMG-LiDAL System Operating Algorithm

Figure 7.12 shows the schematic receiver diagram of the MISO-IMG-LiDAL system. The controller coordinates the detection, counting and localisation processes as detailed below:

- 1) The controller activates transmitter  $T_x(n)$  which sends an optical pulse, and also initialises the group receiver's pixels  $GRP(n)$  to collect the reflected signals. We divided the imaging receiver pixels into  $n = 8$   $GRPs$  (see Figure 7.10).
- 2) The controller then updates the value of  $n$ , and if  $L_{tx} > n$  step (1) is repeated, where  $L_{tx}$  is the number of active transmitter units ( $L_{tx}=8$ ) of the MISO-IMG-LiDAL system.
- 3) A distinguishing method (PSM or PCCM) is applied with the SOIMR to process the received reflected signals from all pixel receivers to detect and count the targets.
- 4) Finally, pixel identification is carried out to estimate the target location.

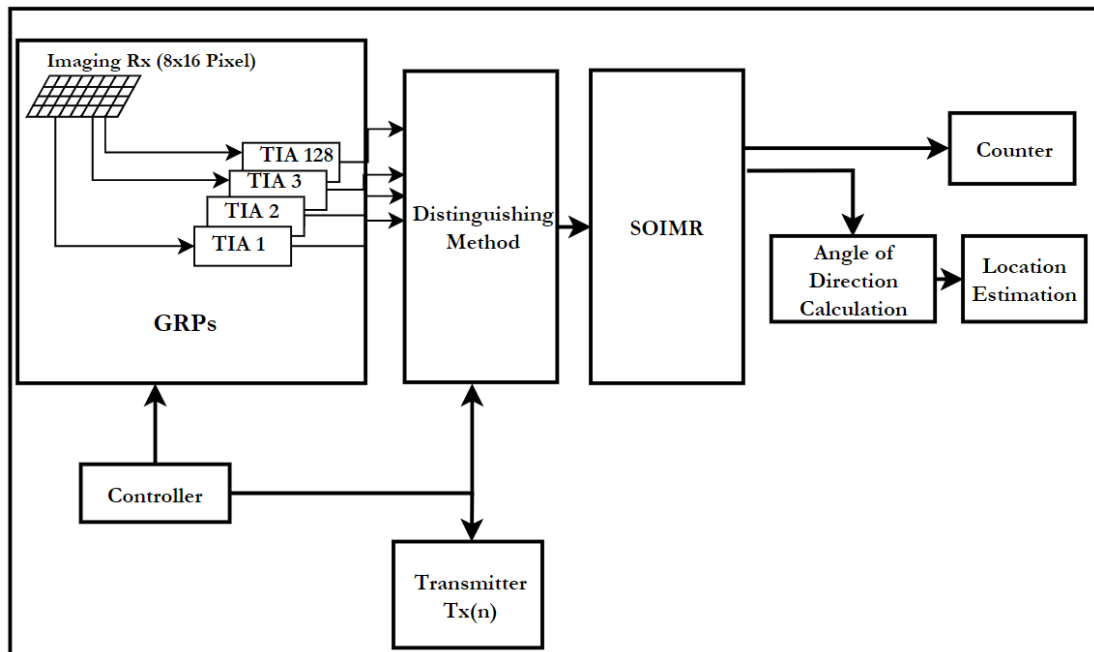


Figure 7.12: the receiver block diagram of MISO-IMG-LiDAL.

### 7.5.1 MISO-IMG LiDAL Overhead

For the MISO-IMG-LiDAL, the number of frames  $M$  required to detect and localise targets is equals to 8. Therefore, the overhead occupied in the VLC system MAC frame can be calculated using (6.29) as discussed Chapter 6. Note that, the MISO-IMG-LiDAL system requires 8 observation frames to complete one monitoring cycle of the room, compared to 24 observation frames for the MIMO-LiDAL system. The reduction in complexity is always a factor of 3 regardless of the number of transmitters (optical footprints) used and regardless of the number of receiver pixels. This factor relates to the need for 3 anchors in the MIMO-LiDAL system.

Note that parallels can be drawn between our MISO-IMG-LiDAL system and camera imaging sensors in the sense that an image sensor mounted on the ceiling can also localise a target. The main differences between our MISO-IMG-LiDAL system and traditional image sensors are: (i) with reduced number of pixels, high speed photodetectors and wideband optical receivers can be used leading to a localisation system that can detect fast moving targets, which become increasingly important in applications such as robotics, (ii) our space-based MISO-IMG-LiDAL system is combined with our time domain approach of Section V, then the pixels determine the target location in two dimensions (ie on the floor) while the time delay between the transmitted pulse and the pulse received by the pixel determines the distance of the target. Thus this combined system can localise the target in three dimensions while image sensors localise targets in two dimensions.

## 7.6 Simulation Setup and Results Discussion

In this section, The MISO IMG LiDAL system is examined considering the three scenarios described in Chapter 6. In addition a performance comparison showed between the proposed LiDAL system namely; MIMO LiDAL and MISO IMG LiDAL. The three scenarios were; (i) the first scenario establishes *the baseline*, ie the best performance expected in our LiDAL systems. It evaluates the performance of our LiDAL systems in an ideal environment where obstacles are absent (Room A) with considering continuous motion, where pedestrians move continuously. (ii) the second scenario represents a *challenging localisation* setting, this scenario considers a realistic room with furniture (realistic environment of Room B). (iii) the third scenario represents a *harsh localisation* environment as adds nomadic motion to the second scenario.

### 7.6.1 Systems Setup

In this section we introduce the systems setup and the parameters used. The LiDAL systems were evaluated in two types of environments; Room A and Room B. For MISO IMG LiDAL, Room A is an empty environment as shown Figure 7.13 and Room B is a realistic environment as shown Figure 7.14. For MIMO LiDAL, Room A and Room are shown in Figure 6.11 and Figure 6.12. Table 7.1 illustrates the simulation parameters used in both LiDAL systems. Note that for MISO IMG LiDAL, we considered the simulation flow, key parameters (MAPE and DRMSE) and setup of three scenarios (1, 2, 3) as discussed in Chapter 6 to establish a fair comparison between the MIMO LiDAL and MISO IMG LiDAL systems.



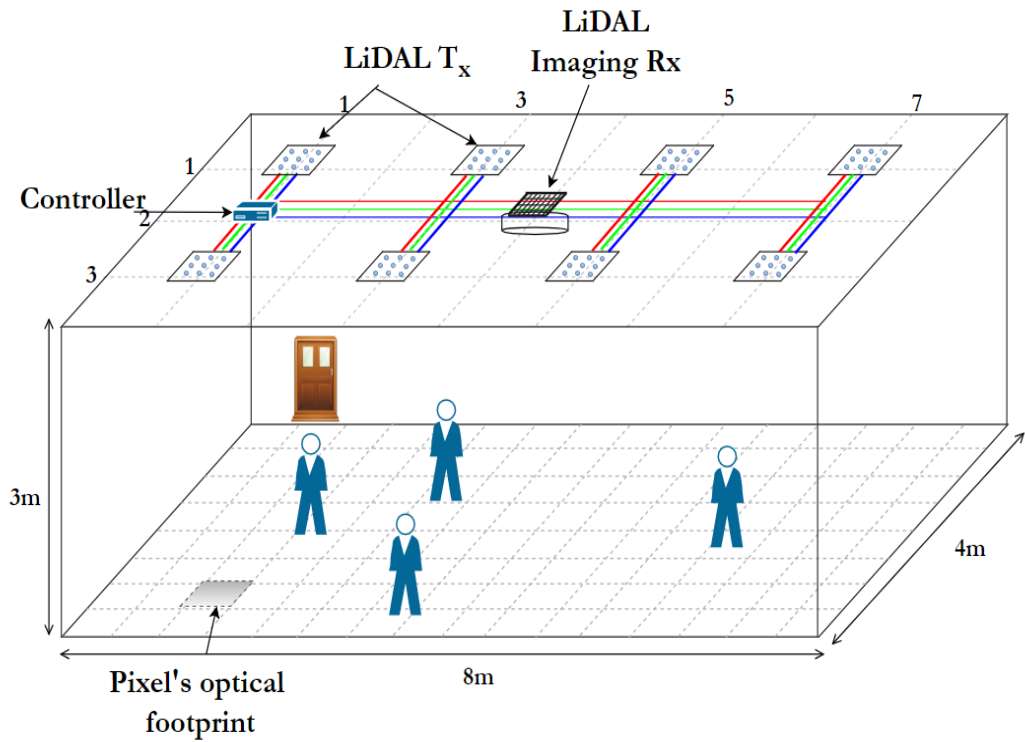


Figure 7.13: MISO IMG LiDAL Room A setup in scenario 1.

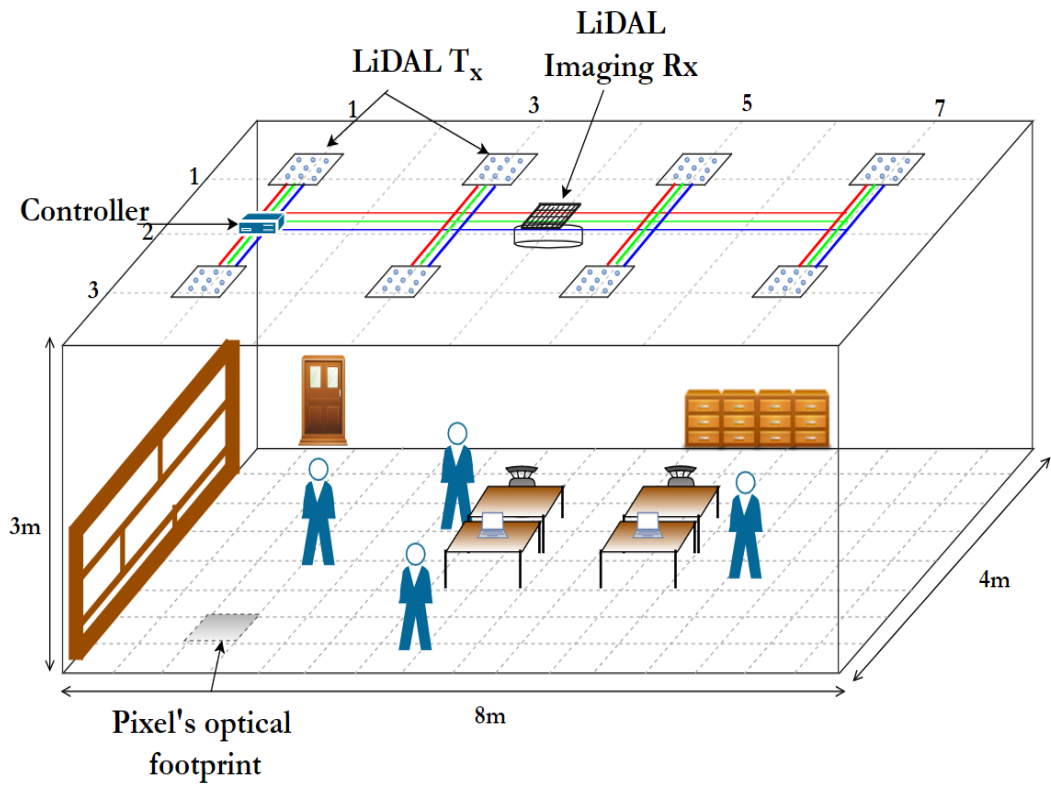


Figure 7.14: MISO IMG LiDAL Room A setup in scenario 2.

Table 7.1: Simulation parameters of LiDAL systems

| Parameters  | Configurations  |
|---|---|
| Room A and B  |   |
| Length  | 8m  |
| Width   | 4m  |
| Height  | 3m  |
| $\rho$ - ceiling                                      | 0.8   |
| $\rho$ - floor  | 0.3   |
| $\rho$ - walls  | 0.8   |
| LiDAL Transmitter Units                               |   |
| locations (x , y, z)                                  | (1,1,3), (1,3,3), (1,5,3), (1,7,3)<br>(3,1,3), (3,3,3), (3,5,3), (3,7,3)m |
| Elevation   | 90°   |
| Azimuth   | 0°  |
| RGB-LDs in each unit                                  | 9 (3×3)   |
| Transmitted optical power per unit                    | 18 W  |
| Transmitted Pulse width $\tau$                        | 2ns   |
| RGB-LD semi-angle at half power beam width ( $\Phi$ ) | 75°   |
| MIMO LiDAL Receiver                                   |   |
| Photodetector Area                                    | 20 mm <sup>2</sup>  |
| Receivers locations                                   | Attached with Tx units  |
| Photodetector Responsivity                            | 0.4 A/W   |
| Receiver Acceptance Semi-angle                        | 43.8°   |
| CPC Reflective Index ( $N$ )                          | 1.7   |
| TIA Noise Current                                     | 2.5 pA/ $\sqrt{\text{Hz}}$  |
| MISO IMG LiDAL Receiver                               |   |
| Photodetector Area                                    | 2cm <sup>2</sup>  |
| Receiver location (x , y, z)                          | (2,4,3)m  |
| Number of pixels                                      | 128   |
| Pixel's area  | 1.56 mm <sup>2</sup>  |
| TIA Pixel Receiver Noise Current                      | 2.6 pA/ $\sqrt{\text{Hz}}$  |
| Lens FOV  | 72°   |
| Time Bin Duration                                     | 0.01 ns   |
| Sampling Time $T_{sa}$                                | 0.1ns   |
| Time Slot Width $T_s$                                 | 2ns   |
| Listening Time $T$                                    | 1ms   |

### 7.6.2 Scenario 1: The Baseline

Figure 7.15. depicts the counting error, MAPE, of the LiDAL systems tested in scenario 1. The best detection results are due to our MISO-IMG-LiDAL configuration as can be seen in Figure 7.15. The MAPE associated with MISO-IMG-LiDAL with BSM for single target detection is about 0.8% which comparable to  $P_M^{B(img)} = 0.1$  (see Figure 7.6 with  $P_M^{B(img)} = 1 - P_D^{B(img)}$ ). The MAPE range of MISO-IMG-LiDAL is from 0.8% to 3.5% with BSM, and 0.6% to 3% with CCM as seen in Figure 7.15. Compared to the MIMO-LiDAL system, the MISO-IMG-LiDAL has better performance due to the ability of the latter to use the spatial dimension to resolve the ambiguity of targets (i.e. separate the targets using multiple pixels that have distinct narrow optical footprints). Due to the spatial resolution of targets, the MISO-IMG-LiDAL system has comparable performance under the BSM and the CCM, with a slight difference of 0.5% in MAPE where the CCM performs better. This increases the probability of error in counting the targets; (ii) with a larger number of targets, there is a higher potential for targets to occur either at the optical footprint overlap zones of MIMO LiDAL or between up to four pixels in the MISO-IMG-LiDAL (see Figure 7.1). These locations are the most challenging for the LiDAL localisation systems.

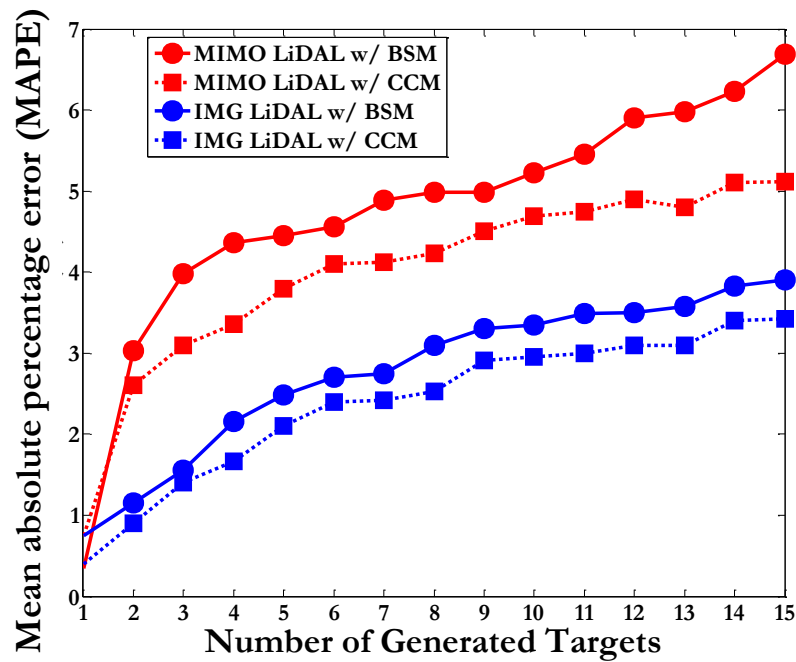


Figure 7.15: MAPE of LiDAL systems with BSM and CCM in empty environment of scenario 1.

### 7.6.3 Scenario 2: Challenging Localisation Environment

Figure 7.16 presents the MAPE associated with the LiDAL systems for targets in scenario 2. One can observe that the MAPE increased significantly for MIMO-LiDAL with BSM from its range of 0.5% to 7% in scenario 1 to a new range of 6% to 35% in scenario 2. Similarly under MISO-IMG-LiDAL with BSM, the MAPE increased from its previous range of 0.3% to 5% in scenario 1, to a new range of 5.5% to 22%. The best system in both scenarios is the MISO-IMG-LiDAL with CCM. This system saw its MAPE increase from a “0.5% to 3.5%” in scenario 1 to “2% to 12%” in scenario 2 due to the presence of obstacles and their associated reflections and due to the reduced residual space available for human motion. It is worth noting that the other general trends are comparable in the two scenarios, with the MAPE performance deteriorating with increase in the number of targets, and improving with the use of the imaging system and the CCM.

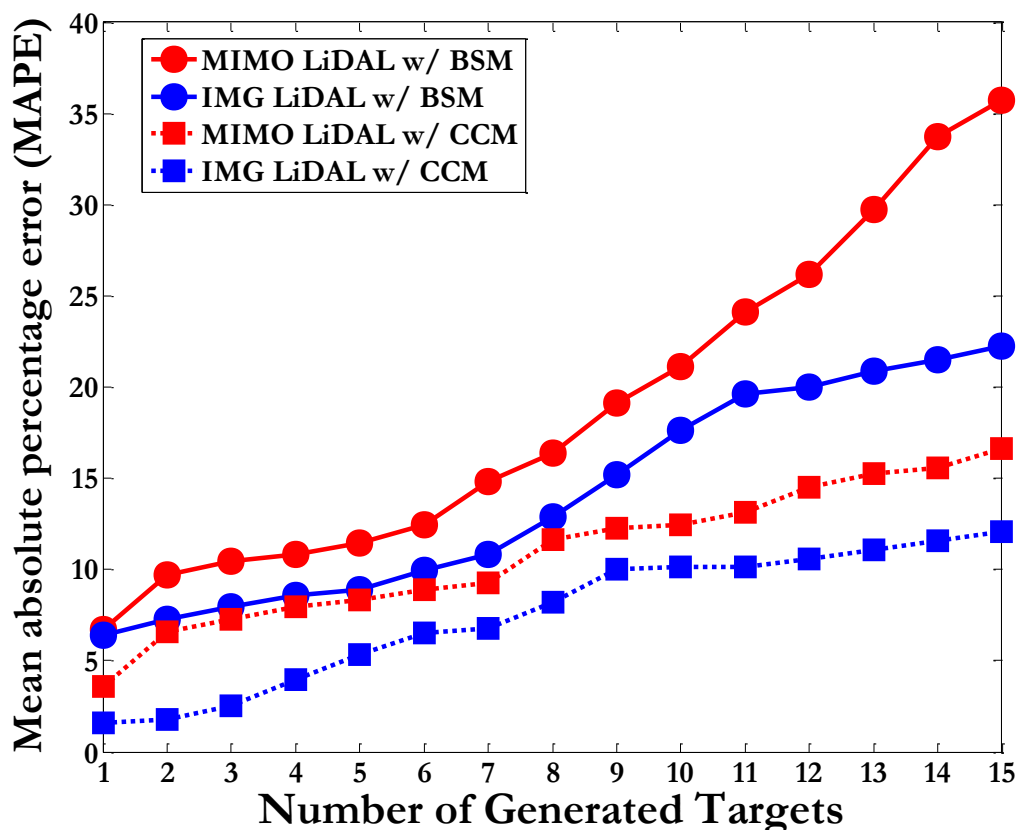


Figure 7.16: MAPE of LiDAL systems with BSM and CCM in realistic environment of scenario 2.

The DRMSE CDF results associated with MISO-IMG-LIDAL and MIMO LiDAL in scenarios 1 and 2 are shown in Figure 7.17. It should be observed that overall, the DRMSE values in MISO-IMG-LIDAL are smaller than the corresponding values in MIMO-LiDAL due to the enhanced resolution of the imaging receiver which resolves the target locations spatially into pixels, whereas the MIMO-LiDAL system relies on three ranges that have to be determined accurately, with the potential for wrong slot errors in the three ranges. In the MISO-IMG-LiDAL system, at the 95% confidence interval, Figure 7.17, the DRMSE are 0.21m and 0.23m for scenarios 1 and 2 respectively, whereas the average values of DRMSE are 0.16m and 0.19m for scenarios 1 and 2 respectively. The sources of error in MISO-IMG-LiDAL are attributed to noise, reflections, and targets random reflection coefficients. These sources of error can translate in the worst case into targets appearing at the intersection of up to four pixels, or targets assumed to be located at the centre of the coverage area of each pixel on the floor when the target may be at the edge of the pixel coverage area.

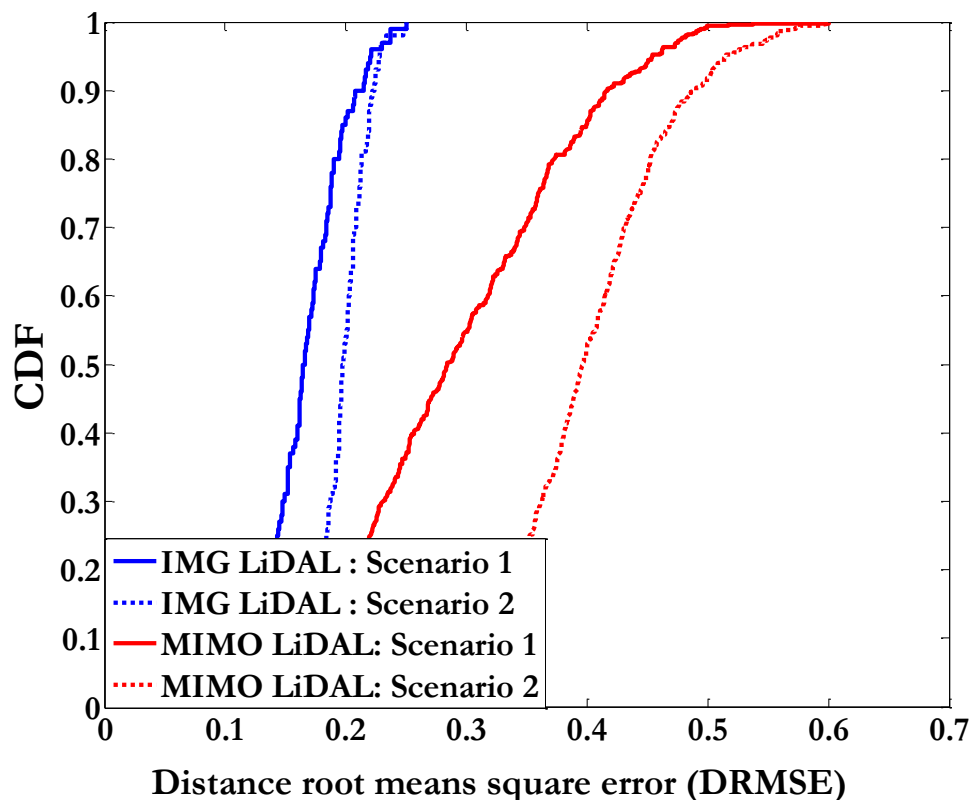


Figure 7.17: CDFs of DRMSE of the proposed LiDAL systems.

### 7.6.4 Scenario 3: Harsh Localisation Environment

Figure 7.18 and Figure 7.19 shows the MAPE CDF for MISO IMG LiDAL and MIMO LiDAL respectively where nomadic behaviour is now considered. The MAPE decreases with increase in mobility, ie increase in the MF and also decreases with decrease in the number of targets that can cause clutter. The most important observation however, is that the MAPE in the MISO IMG LiDAL system is much lower than that of the MIMO-LiDAL system. This is attributed mainly to the improved ability of the imaging receiver to resolve targets in space and subsequently track these targets as the targets move from pixel to pixel. This also means that a stationary target that was mobile at a previous point in time, continues to be marked as a target in a new pixel. This reduces the MAPE by correctly identifying targets from obstacles. For example, for MAPE of 20% or less a MF of 0.5 or higher is sufficient.

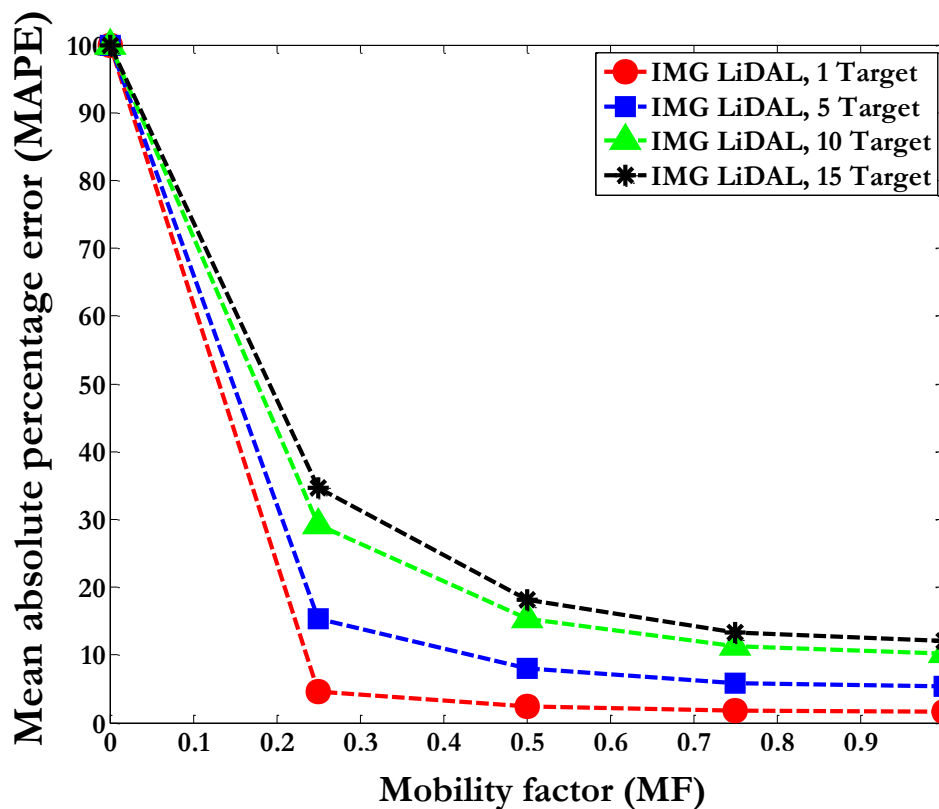


Figure 7.18: MISO-IMG LiDAL system MAPE CDF for the nomadic targets with different MF.

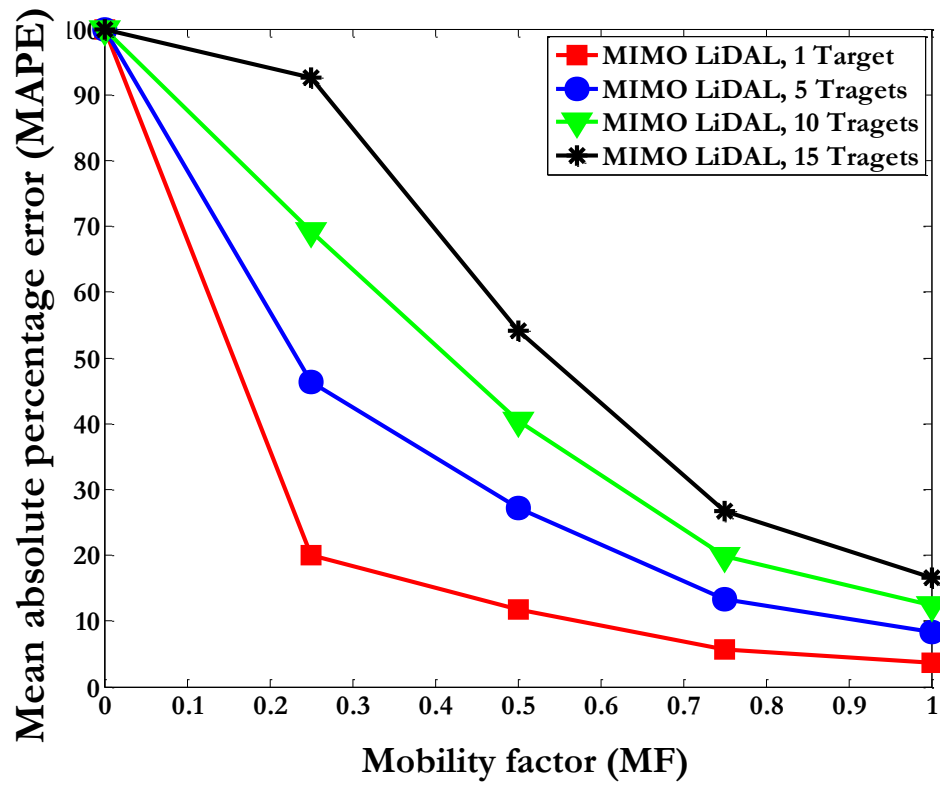


Figure 7.19: CDF of counting MAPE in the MIMO LiDAL system for nomadic targets with different MF.

## 7.7 Case Study Setup and Results Discussion

In this section, we consider a case study where a realistic office environment is considered (see Figure 7.14) with pedestrian arrivals, departures, nomadic behaviour, pathway mobility and a finite evaluation window of one hour when the office is evaluated. In this case we use the better target distinguishing method, namely CCM and evaluate both systems: MIMO-LiDAL and MISO-IMG-LiDAL.

### 7.7.1 Case Study Setup

In this case study, we extend the cases we considered in the three scenarios. We build on scenario 3, namely, the case study considers obstacles and nomadic behaviour. The case study however extends scenario 3 in a number of ways. In particular, we consider (i) arrival and departure processes for human targets into and out of the office environment (not considered in scenario 3); (ii) obstacles (furniture as in scenario 3); (iii) challenging nomadic mobility behaviour, (nomadic pathway mobility (not considered in scenario 3) and random walk with nomadic behaviour (this was considered in scenario 3)); (iv) one hour evaluation period (new in the case study); (v) both MIMO-LiDAL and MISO-IMG-LiDAL systems with the better CCM for mobile target distinguishing.

The parameters used in the case study are shown in Table 7.2. The arrival and departure rates into and out of the office environment are 12 arrivals per hour and 14 departures per hour following a Poisson distribution as outlined in Chapter 5 (Section 5.4). This leads to an average of 30 minutes spent in the environment, with an average of 6 targets present in the environment as shown in Chapter 5 (Section 5.4) and in Table 7.2.

The case study considers both pedestrian targets who move at 1m/s and nomadic targets who move at 0.5 m/s – 2 m/s when moving between locations of interest as shown in Table 7.2 and in Chapter 5 (Section 5.4). We considered 9 locations of interest in the room where the nomadic user spends random and uniformly distributed times.



Table 7.2: Mobility simulation parameters of the case study

| Parameters                                 | Configurations           |
|--|--------------------------|
| Simulation time $T_{ob}$                   | 60 min                   |
| LiDAL frame time $T$                       | 1ms                      |
| Snapshots per second                       | 5                        |
| Total number of snapshots $n$ per $T_{ob}$ | 18000                    |
| Target destinations of interest $L_D$      | 9                        |
| Buffering window                           | 1000 snapshots           |
| Targets mobility behaviour                 | random walk and pathways |
| Nomadic target range speed                 | 0.5-2 m/s                |
| Pedestrian target speed                    | 1 m/s                    |
| Targets arrival rate $\lambda$             | 12 arrivals per hour     |
| Targets departure rate $\gamma$            | 14 departures per hour   |
| Expected no. of target per $T_{ob}$        | 6                        |

The simulation time was  $T_{ob}$  equal to one hour. The LiDAL frame duration is 1ms where at the start of the frame the LiDAL system, carries out its transmissions and measurements as discussed to determine the targets locations. LiDAL localisation measurements are not carried out in each LiDAL frame, instead in this case study a LiDAL set of measurements is carried out every 200 frames, ie every 200ms, leading to 5 snapshot location measurements per second as shown in Table 7.2. This leads to a total of 18000 snapshot measurements in the one hour duration of the case study.

The nomadic targets have 9 locations of interest in the room and spend 30 minutes on average in this office environment. The localisation measurements are aggregated for the duration of a buffering window (see Table 7.2) and are processed in batch mode. This batch processing mode allows the localisation process to consider a time span long enough for the nomadic user to start moving again. With 30 minutes on average in the office environment, 9 locations of interest, equally popular with random stay duration per location, and with 5 snapshot measurements per second, we considered a buffering window of duration equal to 1000 frames to capture the nomadic motion after stationary periods as shown in Table 7.2.

### 7.7.2 Targets Following a Pathway Model

Figure 7.20 presents the CDF of the MAPE associated with counting targets for the proposed LiDAL systems when the targets are either pedestrians or nomadic targets. Both types of targets move in Figure 7.20 following a pathway model as described in Chapter 5. Three key observations can be made on the results in Figure 7.20. Firstly, nomadic target behaviour leads to higher MAPE when counting the number of targets regardless of type of LiDAL type of system used. Secondly, the IMG-LiDAL system performs better than the MIMO-LiDAL system due to its improved spatial resolution. Finally, the difference in counting MAPE between cases when the targets are pedestrian and when they are mobile is smaller when the IMG-LiDAL system is considered compared to the MIMO-LiDAL system. This is due to the ability of the tracking algorithms to identify targets in pixels and track these targets, labelling them as targets even when they become stationary during their nomadic motion.

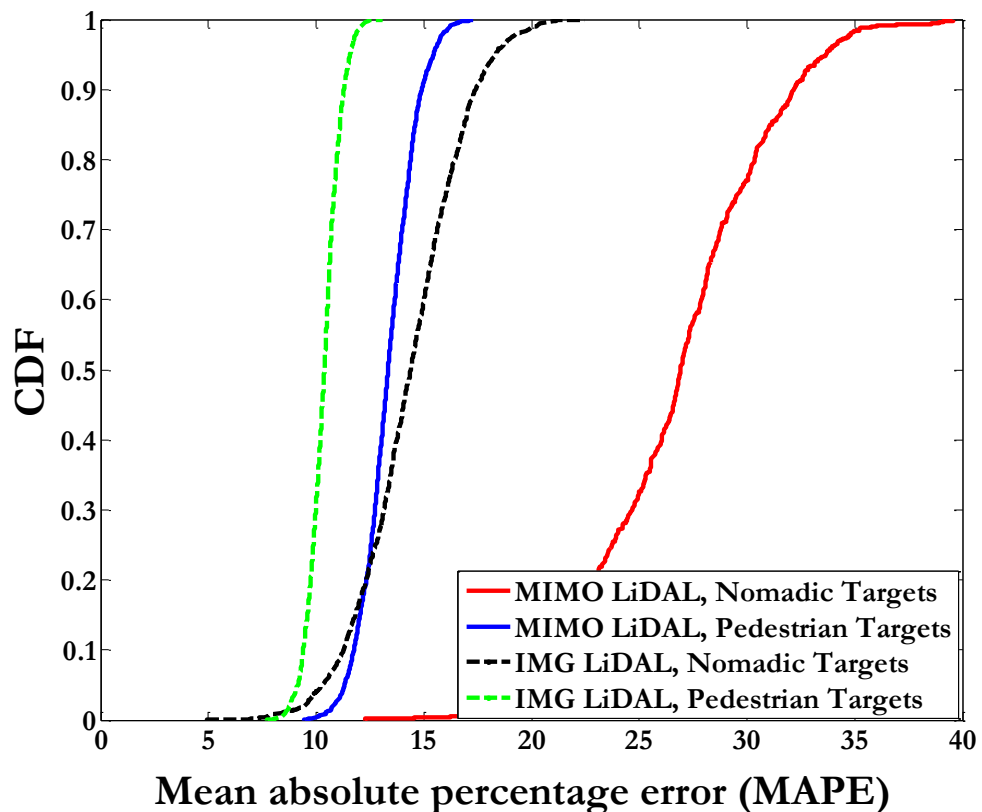


Figure 7.20: CDF of counting MAPE of the targets, when the targets move along fixed pathways.

In Figure 7.20, the counting error of targets with nomadic behaviour is more than the counting errors associated with pedestrian targets with an average (at CDF=0.5) MAPE of 28% and 15% for MIMO-LiDAL and MISO-IMG-LiDAL systems respectively under nomadic mobility. The average MAPE of pedestrian targets in MISO-IMG-LiDAL is 10% while for MIMO-LiDAL is 15%. For the 0.9 CDF interval, the MAPE of pedestrian targets is 14% and 11% for MIMO-LiDAL and MISO-IMG-LiDAL systems respectively. For nomadic targets, the MAPE is 33% and 18% for MIMO-LiDAL and MISO-IMG-LiDAL for the 0.9 CDF interval.

### 7.7.3 Targets Following a Random Walk Model

As can be seen in Figure 7.21, the MAPE associated with the number of targets with nomadic behaviour detected by the MIMO-LiDAL system increased significantly in Figure 7.21 (random walk) with average error of 38%, compared to 28% in Figure 7.20 (pathway mobility pattern). The increase in MAPE under random walk compared to pathway mobility is attributed to the nature of the random walk, where the random walk can result in (almost locked) mobility in a small geographic region, whereas the pathway mobility results in targets covering larger spans in the room and hence the detection of such “very” mobile targets improves.

For the MISO-IMG-LiDAL system with nomadic targets, the average MAPE in counting targets is 15% and 16% for pathway mobility and random walk mobility respectively. It should be noted that the increase in MAPE in the MISO-IMG-LiDAL system when mobility becomes a random walk rather than pathway based, is smaller compared to the corresponding increase in MAPE when the mobility pattern changes in the MIMO-LiDAL system. This is attributed to the ability of the imaging system to detect small movements on the detection floor, where each pixel corresponds to 0.5m x 0.5m whereas the MIMO-LiDAL coverage is within a circle of radius 1.25m.

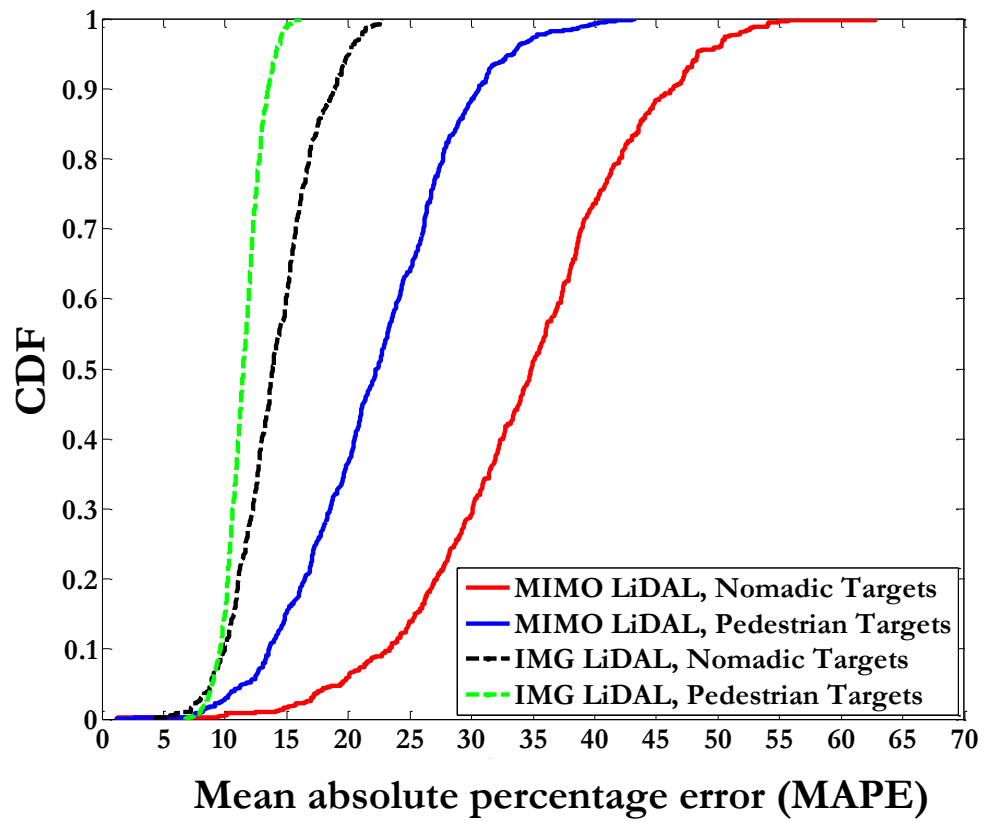


Figure 7.21: CDF of counting MAPE of the targets, when the targets move following a random walk model.

## 7.8 Summary

In this chapter, we introduced an imaging LiDAL (MISO-IMG-LiDAL) system for target localisation. The MISO-IMG-LiDAL system employs an imaging detection receiver with multiple VLC transmitters. The MISO-IMG-LiDAL is an alternative system design to the MIMO LiDAL which has better performance compared to the latter. It makes use of the spatial resolution afforded by the multiple pixels of an imaging receiver. We studied and compared the performance of our systems (MISO-IMG-LiDAL and MIMO LiDAL) in three scenarios and in a case study which progressively test our LiDAL systems.

In the first scenario, the better target distinguishing method, ie CCM is used. The maximum target counting MAPE was reduced from 5.5% to 3.5% when the MISO-IMG-LiDAL system is used instead of the MIMO LiDAL system. In the second scenario, the maximum target counting MAPE was 16% and 12% for the two systems respectively. In terms of localisation errors, in scenario 1, the average DRMSE was 0.28m and 0.16m for the MIMO LiDAL system and the MISO-IMG-LiDAL system respectively, while or scenario 2 the corresponding values were 0.38m and 0.19m respectively. In the third scenario, for a MAPE of 20% or less, a MF of 0.5 or higher is sufficient in MISO-IMG-LiDAL compared to about MF=0.9 for MIMO LiDAL. Thus the latter system needs significantly more mobility to distinguish targets.

The case study added a number of additional realistic features to the environment including arrival rates and departure rates of targets. In the case study, the worst performance was obtained by the MIMO LiDAL system with nomadic random walk for the targets where the average MAPE associated with counting was 38%. In contrast the best system evaluated in this case study, ie the MISO-IMG-LiDAL system, when considered with nomadic random walk for the targets, reduced the counting MAPE from 38% to 16%. The best result for the MISO-IMG-LiDAL system was when the targets were pedestrian (continuous motion) pathway targets, and here the counting MAPE was 10%.

# Chapter 8

## Conclusions and Future Work

This thesis presented the first study, to the best of our knowledge, of light used in a 'radar' fashion for people localisation in indoor environments where visible light communication (VLC) and optical wireless communication may be present and in use. Our LiDAL systems can be used to count and localise people in indoor environments, and as such the LiDAL systems introduced can find application in a wide range of areas from security and safety to crowd management and marketing.

We introduced models for the indoor environment and for the human body, the materials used indoor and their reflection coefficients as well as the reflection coefficients of different forms of clothing taking into account colours and textures of clothing.

We introduced for the first time monostatic and bistatic optical indoor 'radar' configurations. Our resulting LiDAL systems provide coverage of the indoor environment through the use of multiple transmitters. The transmitters have broad beams for illumination, however we use relatively narrow FOV receivers to define optical target detection zones on the floor. This is very compatible with VLC systems where multiple light engines are used to illuminate the indoor environment. These light VLC sources can also act as our LiDAL transmitters. Humans located in the optical zones reflect the incident optical pulses, thus allowing optical receivers collocated with the transmitters in bistatic or monostatic configurations to detect the reflected pulses. Each optical zone is defined by the receiver FOV. We therefore developed models for the LiDAL systems range, namely the horizontal distance covered by each receiver / optical zone. We modelled the optical channel and estimated the receiver bandwidth needed and developed models for the spatial resolution that can be achieved with a given optical pulse duration. Based on indoor

human occupancy, we concluded that the minimum human to human separation is typically more than 30cm even in meeting rooms and thus determined the LiDAL pulse duration needed as 2ns.

We identified the forms of target ambiguity that can occur in our LiDAL systems given that the target (human) has to be on the detection floor of the room and hence determined the number of anchors (light sources / light engines) needed concluding that three such anchors are needed for three dimensional localisation.

We developed models for the sources of randomness in our LiDAL environment considering randomness due to the random nature of the reflection factor of humans (random colour and texture of clothing), the variable cross section of the target (human) which depends on human orientation with respect to the light source; and finally randomness due to receiver noise and background noise.

We derived optimum Bayes receiver structures based on the signal and noise models, considering and interpreting the priors associated with target presence and absence and the costs associated with correct decisions and the costs associated with wrong decisions together with the forms of decision errors. To simplify the receiver design, we derived a sub-optimum receiver structure that uses two thresholds for detection thus eliminating the need for exhaustive search and quantified the complexity reduction and the sacrifice in performance.

To distinguish reflections due to furniture from reflections attributed to the human targets, we used human mobility as the discriminator. We introduced two methods that use human motion to distinguish human targets from furniture; namely the background subtraction method (BSM) and the cross correlation method (CCM). We integrated both methods in the receiver designs developed.

To enable the evaluation of our LiDAL systems in a realistic environment, we furthermore developed models for human motion in the indoor environment of interest. In particular, we developed a directed random walk with obstacle

avoidance mobility model and a pathway mobility model. Both models are based on Markov chains.

We introduced two LiDAL system configurations for target localisation, a MIMO LiDAL system which has multiple transmitters (can be the same transmitters as the VLC transmitters, with MAC which we outlined) and multiple collocated receivers, with each receiver having a single photodiode. An improved alternative system design, MISO-IMG-LiDAL, was introduced making use of the spatial resolution afforded by the multiple pixels of an imaging receiver.

We studied the performance of our systems in three scenarios and in a case study which progressively test our LiDAL systems. The first scenario is a baseline system that produces the best performance possible. This scenario has an empty room with no obstacles (furniture) which reduces the localisation errors and has continuous human (pedestrian) motion which helps distinguish humans. When the better target distinguishing method, ie CCM, is used the maximum target counting MAPE was reduced from 5.5% to 3.5% when the MISO-IMG-LiDAL system is used instead of the MIMO LiDAL system. The maximum MAPE occurs at maximum number of targets, which was 15 human targets in our 8m×4m×3m room.

In the second scenario, obstacles (furniture) are introduced, however the environment has continuous pedestrian motion. Here the maximum target counting MAPE was reduced from 16% to 12% for the two systems respectively.

In terms of localisation errors, in scenario 1, the average DRMSE was 0.28m and 0.16m for the MIMO LiDAL system and the MISO-IMG-LiDAL system respectively, while for scenario 2 the corresponding values were 0.38m and 0.19m respectively.

The third scenario is more challenging, with obstacles (furniture) present in the room and with targets moving in a nomadic fashion rendering the target distinguishing task harder. We defined a target mobility factor (MF), with MF=1 representing a fully mobile target and MF=0 being the extreme end of nomadic behaviour (fully stationary target). It is worth observing that a MPAGE of 20%



or less is only achieved in the MIMO LiDAL system for mobility levels that correspond to MF approaching one. The MISO-IMG-LiDAL system offered improved performance in scenario 3 compared to the MIMO LiDAL system due to the ability of the imaging receiver to track a human target that then becomes stationary, but is still marked as a human target. For example, for MAPE of 20% or less a MF of 0.5 or higher is sufficient in MISO-IMG-LiDAL.

The case study added a number of additional realistic features to the environment including arrival rates and departure rates of targets (humans) and hence finite time spent per target in the environment, as well as more realistic directed pathways mobility with nomadic motion or pedestrian motion (continuous motion). This more challenging environment resulted in increased localisation and counting errors. For example, the worst performance was observed in the MIMO LiDAL system with nomadic random walk for the targets where the average MAPE associated with counting was 38%. In contrast the best system evaluated in this case study, ie the MISO-IMG-LiDAL system with nomadic random walk, reduced the counting MAPE from 38% to 16%. The best result for the MISO-IMG-LiDAL system was when the targets were pedestrian (continuous motion) pathway targets, and here the counting MAPE was 10%. In all three scenarios and case study, the presence of additional targets in the room increases the amount of reflections, hence the LiDAL clutter and hence leads to worse MAPE and DRMSE performance.

The best performance for our LiDAL systems was obtained when an ANN with forward backward propagation was used for target detection. The MIMO-LiDAL system with ANN in scenario 2 reduced the counting MAPE to 2% from the 16% associated with the MIMO-LiDAL system. In the MISO-IMG-LiDAL system the use of the ANN reduced the counting MAPE from 12% to approximately 1%. Furthermore, we studied the impact of training the ANN on a given room, and subsequently changing the furniture locations in the room. In a monostatic configuration with a single target, the counting MAPE was below 11% for up to 40% change in the room furniture locations showing high ANN robustness. For furniture location changes beyond 40%, the CCM performs better than ANN as it is able to adapt to the new furniture locations, unlike the ANN which is pre-trained. It is highly likely though that typical

changes in room furniture locations will be below 40%, and if above this level, the ANN can include new self-training routines.

We can draw a conclusion that the LiDAL system is suitable for people counting applications more than security application due to a high false alarm and misdetection probabilities which require a highly reliable and complicated detection systems such as an IR laser beam and video cameras. In addition, the LiDAL system does not support people tracking and identification as the reflected light signals from multiple targets are similar in nature.

The LiDAL system may suffer from a high path loss attenuation due to the weak received reflected signal from the target. For instance, the results show a significant path loss attenuation of 82.5 dB for a target located with a 1.25m range from the bistatic LiDAL system. Also, the best LiDAL system, the imaging LiDAL system, the configuration of the imaging receiver with a few numbers of pixels is complicated and costly to be implemented practically. Furthermore, the VLC transmitter (used for illumination, communication then for LiDAL) doesn't support very narrow optical beam width to improve the detection as compared to RF radar detection systems.

In particular dense target wise indoor environments similar to scenario 2 and 3, the performance of proposed target distinguishing methods may be degraded due to limited space available for targets to move, hence the probability target detection will decrease which can significantly impact the performance of the MIMO LiDAL system. However, for MISO-IMG- LiDAL this issue can have less impact on the system performance due to the advantage of target marking and tracking inside the detection floor in the MISO-IMG- LiDAL system.

**Future areas of work can include:**

(i) Consideration of MIMO-IMG-LiDAL where an imaging receiver is used with each light source instead of our MISO-IMG-LiDAL which uses a single imaging receiver in the entire room. This can lead to improved performance in terms of people detection and localization which enable the MIMO-IMG-LiDAL to separate the target in the space domain with range resolution. Also, MIMO-IMG-LiDAL will minimise the interference results from reflections from the

background obstacles) which can lead to improvement in the performance of the distinguishing methods such as the BSM.

(ii) The ANN can be trained as an additional/alternative mobility distinguishing method instead of our BSM and CCM. Based on our observations in the LiDAL systems in Chapters 6 and 7, the received reflected signals in the time domain have different patterns corresponding to the number of targets and their locations in an indoor environment. The indoor environment with obstacles (furniture) appears as a set of patterns in the time domain when the transmitted optical signals are reflected from objects in MIMO LiDAL systems. The patterns appear in the spatial domain in the imaging receiver pixels in MISO IMG LiDAL systems. When targets enter the environment, they add/change the time and space patterns in the room. Therefore, a trained neural network that has the ability to classify and recognise the received signal patterns can distinguish the targets from the background obstacles in a realistic environment. Training the neural network to recognize a target from any other obstacle based on the target reflection response by decomposing the reflected received signal to identify the target's reflection signature. This method can be more reliable to detect targets at any dynamic environment without retraining the neural network.

(iii) The time domain can be introduced through pulses and snapshots and used with the spatial domain in the imaging receiver to determine the target location in the third dimension, ie not only the pixel or two-dimensional location of the target on the floor, but also the height of the target. Where The performance of the continuous snapshots measurements to detect the presence of the target (with MISO and MIMO imaging LiDAL) can also be enhanced using a neural network. A trained neural network compares the snapshots to identify the targets by monitoring the change inside the environment in the space domain.

(iv) Passive LiDAL structures can be designed where the visible light *communication* signals reflected from targets (humans) are observed and measured to determine the target locations. In this system, the target detection relies on the observed changes in the received signal from the VLC

system. In other words, passive LiDAL makes use of the transmitted VLC signals for data communication in order to detect and distinguish the target presence.

(v) The LiDAL localisation information can be used to aid the VLC system, for example in terms of improved handovers through mobility direction and speed prediction.

(vi) The LiDAL can be used for improved resource allocation in VLC systems by knowing the locations of users hence steering beams or allocating resources (wavelengths, time slots, transmitters etc) to reduce interference.

## References

- [1] P. H. Pathak, X. Feng, P. Hu, and P. Mohapatra, *Visible light communication, networking, and sensing: A survey, potential and challenges*. IEEE, 2015, pp. 2047-2077.
- [2] H. Burchardt, N. Serafimovski, D. Tsonev, S. Videv, and H. Haas, "VLC: Beyond point-to-point communication," *IEEE Communications Magazine*, vol. 52, no. 7, pp. 98-105, 2014.
- [3] T.-H. Do and M. Yoo, "An in-depth survey of visible light communication based positioning systems," *Sensors*, vol. 16, no. 5, p. 678, 2016.
- [4] H. Haas, L. Yin, Y. Wang, and C. Chen, "What is lifi?," *Journal of Lightwave Technology*, vol. 34, no. 6, pp. 1533-1544, 2016.
- [5] D. Karunatilaka, F. Zafar, V. Kalavally, and R. Parthiban, "LED based indoor visible light communications: State of the art," *IEEE Communications Surveys & Tutorials*, vol. 17, no. 3, pp. 1649-1678, 2015.
- [6] C. Wang, H.-Y. Yu, and Y.-J. Zhu, "A long distance underwater visible light communication system with single photon avalanche diode," *IEEE Photonics Journal*, vol. 8, no. 5, pp. 1-11, 2016.
- [7] S. Schmid, G. Corbellini, S. Mangold, and T. R. Gross, "LED-to-LED visible light communication networks," in *Proceedings of the fourteenth ACM international symposium on Mobile ad hoc networking and computing*, 2013, pp. 1-10: ACM.
- [8] S. Schmid, G. Corbellini, S. Mangold, and T. R. Gross, "An LED-to-LED Visible Light Communication system with software-based synchronization," in *2012 IEEE Globecom Workshops*, 2012, pp. 1264-1268: IEEE.
- [9] Z. Zhou, M. Kavehrad, and P. Deng, "Indoor positioning algorithm using light-emitting diode visible light communications," *Optical engineering*, vol. 51, no. 8, p. 085009, 2012.
- [10] W. Zhang, M. S. Chowdhury, and M. Kavehrad, "Asynchronous indoor positioning system based on visible light communications," *Optical Engineering*, vol. 53, no. 4, p. 045105, 2014.

- [11] T. Li, C. An, Z. Tian, A. T. Campbell, and X. Zhou, "Human sensing using visible light communication," in *Proceedings of the 21st Annual International Conference on Mobile Computing and Networking*, 2015, pp. 331-344: ACM.
- [12] A. J. Suzuki and K. Mizui, "Laser radar and visible light in a bidirectional V2V communication and ranging system," in *2015 IEEE International Conference on Vehicular Electronics and Safety (ICVES)*, 2015, pp. 19-24: IEEE.
- [13] Y.-L. Hou and G. K. Pang, "People counting and human detection in a challenging situation," *IEEE transactions on systems, man, and cybernetics-part a: systems and humans*, vol. 41, no. 1, pp. 24-33, 2011.
- [14] J. García, A. Gardel, I. Bravo, J. L. Lázaro, M. Martínez, and D. Rodríguez, "Directional people counter based on head tracking," *IEEE Transactions on Industrial Electronics*, vol. 60, no. 9, pp. 3991-4000, 2013.
- [15] J. Liu, J. Liu, and M. Zhang, "A detection and tracking based method for real-time people counting," in *2013 Chinese Automation Congress*, 2013, pp. 470-473: IEEE.
- [16] T. Teixeira, G. Dublon, and A. Savvides, "A survey of human-sensing: Methods for detecting presence, count, location, track, and identity," *ACM Computing Surveys*, vol. 5, no. 1, pp. 59-69, 2010.
- [17] S. Chang, R. Sharan, M. Wolf, N. Mitsumoto, and J. W. Burdick, "UWB radar-based human target tracking," in *2009 IEEE Radar Conference*, 2009, pp. 1-6: IEEE.
- [18] H. Zhao and R. Shibasaki, "A novel system for tracking pedestrians using multiple single-row laser-range scanners," *IEEE Transactions on systems, man, and cybernetics-Part A: systems and humans*, vol. 35, no. 2, pp. 283-291, 2005.
- [19] H. Liu, S. Chen, and N. Kubota, "Intelligent video systems and analytics: A survey," *IEEE Transactions on Industrial Informatics*, vol. 9, no. 3, pp. 1222-1233, 2013.
- [20] Y. Xu, J. Dong, B. Zhang, and D. Xu, "Background modeling methods in video analysis: A review and comparative evaluation," *CAA/ Transactions on Intelligence Technology*, vol. 1, no. 1, pp. 43-60, 2016.
- [21] A. Jovicic, J. Li, and T. Richardson, "Visible light communication: opportunities, challenges and the path to market," *IEEE Communications Magazine*, vol. 51, no. 12, pp. 26-32, 2013.
- [22] M. Nakajima and S. Haruyama, "New indoor navigation system for visually impaired people using visible light communication," *EURASIP Journal on Wireless Communications and Networking*, vol. 2013, no. 1, p. 37, 2013.
- [23] J. Luo, L. Fan, and H. Li, "Indoor positioning systems based on visible light communication: State of the art," *IEEE Communications Surveys & Tutorials*, vol. 19, no. 4, pp. 2871-2893, 2017.
- [24] J. Luo, J. Wang, H. Xu, and H. Lu, "Real-time people counting for indoor scenes," *Signal Processing*, vol. 124, pp. 27-35, 2016.
- [25] S. Khan, G. Vizzari, S. Bandini, and S. Basalamah, "Detecting dominant motion flows and people counting in high density crowds," 2014.

- [26] J. W. Choi, D. H. Yim, and S. H. Cho, "People counting based on an IR-UWB radar sensor," *IEEE Sensors Journal*, vol. 17, no. 17, pp. 5717-5727, 2017.
- [27] J. W. Choi, S. H. Cho, Y. S. Kim, N. J. Kim, S. S. Kwon, and J. S. Shim, "A counting sensor for inbound and outbound people using IR-UWB radar sensors," in *2016 IEEE Sensors Applications Symposium (SAS)*, 2016, pp. 1-5: IEEE.
- [28] Y. Zhuang *et al.*, "A survey of positioning systems using visible LED lights," *IEEE Communications Surveys & Tutorials*, vol. 20, no. 3, pp. 1963-1988, 2018.
- [29] P. Luo, Z. Ghassemlooy, H. Le Minh, E. Bentley, A. Burton, and X. Tang, "Fundamental analysis of a car to car visible light communication system," in *2014 9th International Symposium on Communication Systems, Networks & Digital Sign (CSNDSP)*, 2014, pp. 1011-1016: IEEE.
- [30] H. Elgala, R. Mesleh, and H. Haas, "Indoor optical wireless communication: potential and state-of-the-art," *IEEE Communications Magazine*, vol. 49, no. 9, pp. 56-62, 2011.
- [31] J. Grubor, S. Randel, K.-D. Langer, and J. Walewski, "Bandwidth-efficient indoor optical wireless communications with white light-emitting diodes," in *2008 6th International Symposium on Communication Systems, Networks and Digital Signal Processing*, 2008, pp. 165-169: IEEE.
- [32] H. Le Minh *et al.*, "High-speed visible light communications using multiple-resonant equalization," *IEEE Photonics Technology Letters*, vol. 20, no. 14, pp. 1243-1245, 2008.
- [33] T. Komine and M. Nakagawa, "Fundamental analysis for visible-light communication system using LED lights," *IEEE transactions on Consumer Electronics*, vol. 50, no. 1, pp. 100-107, 2004.
- [34] H. Le Minh *et al.*, "80 Mbit/s visible light communications using pre-equalized white LED," in *2008 34th European Conference on Optical Communication*, 2008, pp. 1-2: IEEE.
- [35] L. Zeng *et al.*, "Equalisation for high-speed visible light communications using white-leds," in *2008 6th International Symposium on Communication Systems, Networks and Digital Signal Processing*, 2008, pp. 170-173: IEEE.
- [36] A. T. Hussein and J. M. Elmirghani, "Mobile multi-gigabit visible light communication system in realistic indoor environment," *Journal of Lightwave Technology*, vol. 33, no. 15, pp. 3293-3307, 2015.
- [37] J. Vučić, C. Kottke, S. Nerreter, K.-D. Langer, and J. W. Walewski, "513 Mbit/s visible light communications link based on DMT-modulation of a white LED," *Journal of lightwave technology*, vol. 28, no. 24, pp. 3512-3518, 2010.
- [38] M. Biagi, T. Borogovac, and T. D. Little, "Adaptive receiver for indoor visible light communications," *Journal of Lightwave Technology*, vol. 31, no. 23, pp. 3676-3686, 2013.
- [39] T. Komine, J. H. Lee, S. Haruyama, and M. Nakagawa, "Adaptive equalization system for visible light wireless communication utilizing multiple white LED lighting equipment," *IEEE Transactions on Wireless Communications*, vol. 8, no. 6, pp. 2892-2900, 2009.

- [40] G. Cossu, A. Khalid, P. Choudhury, R. Corsini, and E. Ciaramella, "3.4 Gbit/s visible optical wireless transmission based on RGB LED," *Optics express*, vol. 20, no. 26, pp. B501-B506, 2012.
- [41] C. Lee *et al.*, "4 Gbps direct modulation of 450 nm GaN laser for high-speed visible light communication," *Optics express*, vol. 23, no. 12, pp. 16232-16237, 2015.
- [42] H. Chun, S. Rajbhandari, D. Tsonev, G. Faulkner, H. Haas, and D. O'Brien, "Visible light communication using laser diode based remote phosphor technique," in *2015 IEEE International Conference on Communication Workshop (ICCW)*, 2015, pp. 1392-1397: IEEE.
- [43] D. Tsonev, S. Videv, and H. Haas, "Towards a 100 Gb/s visible light wireless access network," *Optics express*, vol. 23, no. 2, pp. 1627-1637, 2015.
- [44] J. B. Carruthers and J. M. Kahn, "Angle diversity for nondirected wireless infrared communication," in *ICC'98. 1998 IEEE International Conference on Communications. Conference Record. Affiliated with SUPERCOMM'98 (Cat. No. 98CH36220)*, 1998, vol. 3, pp. 1665-1670: IEEE.
- [45] K. L. Sterckx, J. M. Elmirghani, and R. A. Cryan, "Pyramidal fly-eye detection antenna for optical wireless systems," 1999.
- [46] A. G. Al-Ghamdi and J. M. Elmirghani, "Performance evaluation of a triangular pyramidal fly-eye diversity detector for optical wireless communications," *IEEE Communications magazine*, vol. 41, no. 3, pp. 80-86, 2003.
- [47] J. M. Kahn, R. You, P. Djahani, A. G. Weisbin, B. K. Teik, and A. Tang, "Imaging diversity receivers for high-speed infrared wireless communication," *IEEE Communications Magazine*, vol. 36, no. 12, pp. 88-94, 1998.
- [48] J. M. Kahn and J. R. Barry, "Wireless infrared communications," *Proceedings of the IEEE*, vol. 85, no. 2, pp. 265-298, 1997.
- [49] A. T. Hussein, M. T. Alresheedi, and J. M. Elmirghani, "20 Gb/s mobile indoor visible light communication system employing beam steering and computer generated holograms," *Journal of lightwave technology*, vol. 33, no. 24, pp. 5242-5260, 2015.
- [50] S. Arnon, *Visible light communication*. Cambridge University Press, 2015.
- [51] S.-H. Yang, E.-M. Jung, and S.-K. Han, "Indoor location estimation based on LED visible light communication using multiple optical receivers," *IEEE Communications Letters*, vol. 17, no. 9, pp. 1834-1837, 2013.
- [52] K. Asatani and T. Kimura, "Analyses of LED nonlinear distortions," *IEEE Journal of Solid-State Circuits*, vol. 13, no. 1, pp. 125-133, 1978.
- [53] X. Ning, R. Winston, and J. O'Gallagher, "Dielectric totally internally reflecting concentrators," *Applied optics*, vol. 26, no. 2, pp. 300-305, 1987.
- [54] J. Fadlullah and M. Kavehrad, "Indoor high-bandwidth optical wireless links for sensor networks," *Journal of lightwave technology*, vol. 28, no. 21, pp. 3086-3094, 2010.

- [55] A. J. Moreira, R. T. Valadas, and A. de Oliveira Duarte, "Optical interference produced by artificial light," *Wireless Networks*, vol. 3, no. 2, pp. 131-140, 1997.
- [56] D. C. O'Brien, L. Zeng, H. Le-Minh, G. Faulkner, J. W. Walewski, and S. Randel, "Visible light communications: Challenges and possibilities," in *2008 IEEE 19th International Symposium on Personal, Indoor and Mobile Radio Communications*, 2008, pp. 1-5: IEEE.
- [57] S. Dimitrov and H. Haas, *Principles of LED light communications: towards networked Li-Fi*. Cambridge University Press, 2015.
- [58] T. Komine, S. Haruyama, and M. Nakagawa, "A study of shadowing on indoor visible-light wireless communication utilizing plural white LED lightings," *Wireless Personal Communications*, vol. 34, no. 1-2, pp. 211-225, 2005.
- [59] L. Zeng *et al.*, "High data rate multiple input multiple output (MIMO) optical wireless communications using white LED lighting," *IEEE Journal on Selected Areas in Communications*, vol. 27, no. 9, pp. 1654-1662, 2009.
- [60] C. Singh, J. John, Y. Singh, and K. Tripathi, "A review of indoor optical wireless systems," *IETE Technical review*, vol. 19, no. 1-2, pp. 3-17, 2002.
- [61] D. O'Brien *et al.*, "High data-rate infra-red optical wireless communications: implementation challenges," in *2010 IEEE Globecom Workshops*, 2010, pp. 1047-1051: IEEE.
- [62] H. Le Minh *et al.*, "A 1.25-Gb/s indoor cellular optical wireless communications demonstrator," *IEEE Photonics Technology Letters*, vol. 22, no. 21, pp. 1598-1600, 2010.
- [63] M. Khatib, *Advanced trends in wireless communications*. 2011.
- [64] J. M. Senior and M. Y. Jamro, *Optical fiber communications: principles and practice*. Pearson Education, 2009.
- [65] P. Haigh, T. Son, E. Bentley, Z. Ghassemlooy, H. Le Minh, and L. Chao, "Development of a visible light communications system for optical wireless local area networks," in *2012 Computing, Communications and Applications Conference*, 2012, pp. 351-355: IEEE.
- [66] J.-Y. Sung, C.-W. Chow, and C.-H. Yeh, "Is blue optical filter necessary in high speed phosphor-based white light LED visible light communications?," *Optics express*, vol. 22, no. 17, pp. 20646-20651, 2014.
- [67] B. G. Streetman and S. Banerjee, *Solid state electronic devices*. Prentice Hall Englewood Cliffs, NJ, 1995.
- [68] S. Hranilovic, *Wireless optical communication systems*. Springer Science & Business Media, 2006.
- [69] Y.-G. Wey *et al.*, "108-GHz GaInAs/InP pin photodiodes with integrated bias tees and matched resistors," *IEEE photonics technology letters*, vol. 5, no. 11, pp. 1310-1312, 1993.
- [70] J. R. Barry, J. M. Kahn, E. A. Lee, and D. G. Messerschmitt, "High-speed nondirective optical communication for wireless networks," *IEEE Network*, vol. 5, no. 6, pp. 44-54, 1991.
- [71] H. Le Minh, Z. Ghassemlooy, D. O'Brien, and G. Faulkner, "Indoor gigabit optical wireless communications: challenges and possibilities,"



- in *2010 12th International Conference on Transparent Optical Networks*, 2010, pp. 1-6: IEEE.
- [72] A. Street, P. Stavrinou, D. Edwards, and G. Parry, "Optical preamplifier designs for IR-LAN applications," in *IEE Colloquium on Optical Free Space Communication Links*, 1996, pp. 8/1-8/6: IET.
- [73] J. Elmirghani, H. Chan, and R. Cryan, "Sensitivity evaluation of optical wireless PPM systems utilising PIN-BJT receivers," *IEE Proceedings-Optoelectronics*, vol. 143, no. 6, pp. 355-359, 1996.
- [74] S. Arnon, J. Barry, G. Karagiannidis, R. Schober, and M. Uysal, *Advanced optical wireless communication systems*. Cambridge university press, 2012.
- [75] A. T. Hussein and J. M. Elmirghani, "High-speed indoor visible light communication system employing laser diodes and angle diversity receivers," in *2015 17th International Conference on Transparent Optical Networks (ICTON)*, 2015, pp. 1-6: IEEE.
- [76] A. G. Al-Ghamdi and J. M. Elmirghani, "Analysis of diffuse optical wireless channels employing spot-diffusing techniques, diversity receivers, and combining schemes," *IEEE Transactions on Communications*, vol. 52, no. 10, pp. 1622-1631, 2004.
- [77] A. G. Al-Ghamdi and J. M. Elmirghani, "Line strip spot-diffusing transmitter configuration for optical wireless systems influenced by background noise and multipath dispersion," *IEEE Transactions on Communications*, vol. 52, no. 1, pp. 37-45, 2004.
- [78] A. A. Al-Hameed, A. T. Hussein, M. T. Alresheedi, and J. M. Elmirghani, "Adaptive receiver for visible light communication system," in *2016 18th International Conference on Transparent Optical Networks (ICTON)*, 2016, pp. 1-6: IEEE.
- [79] A. A. Al-Hameed, A. T. Hussein, M. T. Alresheedi, S. H. Younus, and J. M. Elmirghani, "Transmitters mapping of visible light communication system," in *2017 19th International Conference on Transparent Optical Networks (ICTON)*, 2017, pp. 1-6: IEEE.
- [80] F. R. Gfeller and U. Bapst, "Wireless in-house data communication via diffuse infrared radiation," *Proceedings of the IEEE*, vol. 67, no. 11, pp. 1474-1486, 1979.
- [81] J. R. Barry, J. M. Kahn, W. J. Krause, E. A. Lee, and D. G. Messerschmitt, "Simulation of multipath impulse response for indoor wireless optical channels," *IEEE journal on selected areas in communications*, vol. 11, no. 3, pp. 367-379, 1993.
- [82] F. E. S. Alsaadi, *MIMO MC-CDMA Systems over indoor optical wireless communication channels*. University of Leeds, 2011.
- [83] A. T. Hussein, "Visible light communication system," University of Leeds, 2016.
- [84] J. R. Barry and J. M. Kahn, "Link design for nondirected wireless infrared communications," *Applied optics*, vol. 34, no. 19, pp. 3764-3776, 1995.
- [85] A. Al-Ghamdi and J. M. Elmirghani, "Optimization of a triangular PFDR antenna in a fully diffuse OW system influenced by background noise and multipath propagation," *IEEE transactions on communications*, vol. 51, no. 12, pp. 2103-2114, 2003.

- [86] J. B. Carruthers and J. M. Kahn, "Modeling of nondirected wireless infrared channels," *IEEE transactions on communications*, vol. 45, no. 10, pp. 1260-1268, 1997.
- [87] S. Jivkova and M. Kavehrad, "Indoor wireless infrared local access, multi-spot diffusing with computer generated holographic beam-splitters," in *1999 IEEE International Conference on Communications (Cat. No. 99CH36311)*, 1999, vol. 1, pp. 604-608: IEEE.
- [88] S. Jovkova and M. Kavehard, "Multispot diffusing configuration for wireless infrared access," *IEEE Transactions on Communications*, vol. 48, no. 6, pp. 970-978, 2000.
- [89] M. I. Skolnik, "Radar handbook," 1970.
- [90] M. A. Richards, J. Scheer, W. A. Holm, and W. L. Melvin, *Principles of modern radar*. Citeseer, 2010.
- [91] V. N. Bringi and V. Chandrasekar, *Polarimetric Doppler weather radar: principles and applications*. Cambridge university press, 2001.
- [92] M. I. Skolnik, "Introduction to radar systems," *New York, McGraw Hill Book Co., 1980. 590 p.*, 1980.
- [93] R. J. Doviak, *Doppler radar and weather observations*. Courier Corporation, 2006.
- [94] D. K. Barton, "Modern radar system analysis," *Norwood, MA, Artech House, 1988, 607 p.*, 1988.
- [95] S. A. Hovanessian, "Radar system design and analysis," *Dedham, MA, Artech House, Inc., 1984, 394 p.*, 1984.
- [96] J. Li and P. Stoica, "MIMO radar with colocated antennas," *IEEE Signal Processing Magazine*, vol. 24, no. 5, pp. 106-114, 2007.
- [97] M. Jackson, "The geometry of bistatic radar systems," in *IEE proceedings F (communications, radar and signal processing)*, 1986, vol. 133, no. 7, pp. 604-612: IET.
- [98] N. J. Willis, *Bistatic radar*. SciTech Publishing, 2005.
- [99] K. Gage and J. Green, "Evidence for specular reflection from monostatic VHF radar observations of the stratosphere," *Radio Science*, vol. 13, no. 6, pp. 991-1001, 1978.
- [100] U. Spagnolini and V. Rampa, "Multitarget detection/tracking for monostatic ground penetrating radar: Application to pavement profiling," *IEEE Transactions on Geoscience and Remote sensing*, vol. 37, no. 1, pp. 383-394, 1999.
- [101] G. T. Ruck, D. E. Barrick, W. D. Stuart, and C. K. Krichbaum, *Radar cross section handbook*. Plenum press New York, 1970.
- [102] H. Rohling and C. Moller, "Radar waveform for automotive radar systems and applications," in *2008 IEEE Radar Conference*, 2008, pp. 1-4: IEEE.
- [103] D. Atlas, R. Srivastava, and R. S. Sekhon, "Doppler radar characteristics of precipitation at vertical incidence," *Reviews of Geophysics*, vol. 11, no. 1, pp. 1-35, 1973.
- [104] J. Marcum, "A statistical theory of target detection by pulsed radar," *IRE Transactions on Information Theory*, vol. 6, no. 2, pp. 59-267, 1960.
- [105] K. i. Nishiguchi and M. Kobayashi, "Improved algorithm for estimating pulse repetition intervals," *IEEE transactions on Aerospace and Electronic Systems*, vol. 36, no. 2, pp. 407-421, 2000.

- [106] J. Houston and A. Carswell, "Four-component polarization measurement of lidar atmospheric scattering," *Applied optics*, vol. 17, no. 4, pp. 614-620, 1978.
- [107] G. L. Heritage and A. R. Large, "Principles of 3D laser scanning," *Laser scanning for the environmental sciences*, vol. 1, pp. 21-34, 2009.
- [108] K. Lim, P. Treitz, M. Wulder, B. St-Onge, and M. Flood, "LiDAR remote sensing of forest structure," *Progress in physical geography*, vol. 27, no. 1, pp. 88-106, 2003.
- [109] G. P. Agrawal, *Fiber-optic communication systems*. John Wiley & Sons, 2012.
- [110] G. R. Osche, "Optical detection theory for laser applications," *Optical Detection Theory for Laser Applications*, by Gregory R. Osche, pp. 424. ISBN 0-471-22411-1. Wiley-VCH, July 2002., p. 424, 2002.
- [111] R. M. Gagliardi and S. Karp, "Optical communications," *New York, Wiley-Interscience, 1976. 445 p.*, 1976.
- [112] E. Ip, A. P. T. Lau, D. J. Barros, and J. M. Kahn, "Coherent detection in optical fiber systems," *Optics express*, vol. 16, no. 2, pp. 753-791, 2008.
- [113] E. Chuvieco, *Fundamentals of satellite remote sensing*. CRC press, 2009.
- [114] C. Weitkamp, *Lidar: range-resolved optical remote sensing of the atmosphere*. Springer Science & Business, 2006.
- [115] P. Dong and Q. Chen, *LiDAR remote sensing and applications*. CRC Press, 2017.
- [116] T. Labeodan, W. Zeiler, G. Boxem, and Y. Zhao, "Occupancy measurement in commercial office buildings for demand-driven control applications—A survey and detection system evaluation," *Energy and Buildings*, vol. 93, pp. 303-314, 2015.
- [117] A. B. Watson and A. J. Ahumada, "Model of human visual-motion sensing," *JOSA A*, vol. 2, no. 2, pp. 322-342, 1985.
- [118] A. Droitcour, V. Lubecke, J. Lin, and O. Boric-Lubecke, "A microwave radio for Doppler radar sensing of vital signs," in *2001 IEEE MTT-S International Microwave Symposium Digest (Cat. No. 01CH37157)*, 2001, vol. 1, pp. 175-178: IEEE.
- [119] C. Li, J. Cummings, J. Lam, E. Graves, and W. Wu, "Radar remote monitoring of vital signs," *IEEE Microwave Magazine*, vol. 10, no. 1, pp. 47-56, 2009.
- [120] J. A. Nanzer and R. L. Rogers, "Human presence detection using millimeter-wave radiometry," *IEEE Transactions on Microwave Theory and Techniques*, vol. 55, no. 12, pp. 2727-2733, 2007.
- [121] F. Liang *et al.*, "Detection of multiple stationary humans using UWB MIMO radar," *Sensors*, vol. 16, no. 11, p. 1922, 2016.
- [122] A. Yarovoy, L. Ligthart, J. Matuzas, and B. Levitas, "UWB radar for human being detection," *IEEE Aerospace and Electronic Systems Magazine*, vol. 21, no. 3, pp. 10-14, 2006.
- [123] S. Singh, Q. Liang, D. Chen, and L. Sheng, "Sense through wall human detection using UWB radar," *EURASIP Journal on Wireless Communications and Networking*, vol. 2011, no. 1, p. 20, 2011.
- [124] M. Leib, W. Menzel, B. Schleicher, and H. Schumacher, "Vital signs monitoring with a UWB radar based on a correlation receiver," in

*Proceedings of the Fourth European Conference on Antennas and Propagation*, 2010, pp. 1-5: IEEE.

- [125] C. G. Bilich, "Bio-medical sensing using ultra wideband communications and radar technology: A feasibility study," in *2006 Pervasive Health Conference and Workshops*, 2006, pp. 1-9: IEEE.
- [126] I. I. Immoreev and P. D. V. Fedotov, "Ultra wideband radar systems: advantages and disadvantages," in *2002 IEEE Conference on Ultra Wideband Systems and Technologies (IEEE Cat. No. 02EX580)*, 2002, pp. 201-205: IEEE.
- [127] Q. Hao, F. Hu, and J. Lu, "Distributed multiple human tracking with wireless binary pyroelectric infrared (PIR) sensor networks," in *SENSORS, 2010 IEEE*, 2010, pp. 946-950: IEEE.
- [128] J. Singh, U. Madhow, R. Kumar, S. Suri, and R. Cagley, "Tracking multiple targets using binary proximity sensors," in *Proceedings of the 6th international conference on Information processing in sensor networks*, 2007, pp. 529-538: ACM.
- [129] S. Z. Gürbüz, W. L. Melvin, and D. B. Williams, "Detection and identification of human targets in radar data," in *Signal Processing, Sensor Fusion, and Target Recognition XVI*, 2007, vol. 6567, p. 65670I: International Society for Optics and Photonics.
- [130] L. E. Navarro-Serment, C. Mertz, N. Vandapel, and M. Hebert, "LADAR-based pedestrian detection and tracking," 2008.
- [131] T. Taipalus and J. Ahtiainen, "Human detection and tracking with knee-high mobile 2D LIDAR," in *2011 IEEE International Conference on Robotics and Biomimetics*, 2011, pp. 1672-1677: IEEE.
- [132] J. Shackleton, B. VanVoorst, and J. Hesch, "Tracking people with a 360-degree lidar," in *2010 7th IEEE International Conference on Advanced Video and Signal Based Surveillance*, 2010, pp. 420-426: IEEE.
- [133] L. Snidaro, C. Micheloni, C. J. I. T. o. S. Chiavedale, Man,, C.-P. A. Systems, and Humans, "Video security for ambient intelligence," vol. 35, no. 1, pp. 133-144, 2004.
- [134] C.-F. Shu *et al.*, "Ibm smart surveillance system (s3): a open and extensible framework for event based surveillance," in *IEEE Conference on Advanced Video and Signal Based Surveillance, 2005.*, 2005, pp. 318-323: IEEE.
- [135] C. Rother, V. Kolmogorov, and A. J. A. T. o. G. Blake, "Interactive foreground extraction using iterated graph cuts," no. 23, p. 3, 2012.
- [136] S. Se, D. G. Lowe, and J. J. J. I. T. o. r. Little, "Vision-based global localization and mapping for mobile robots," vol. 21, no. 3, pp. 364-375, 2005.
- [137] M. Bertozzi *et al.*, "Pedestrian detection by means of far-infrared stereo vision," vol. 106, no. 2-3, pp. 194-204, 2007.
- [138] W. Wang, A. X. Liu, M. Shahzad, K. Ling, and S. Lu, "Understanding and modeling of wifi signal based human activity recognition," in *Proceedings of the 21st annual international conference on mobile computing and networking*, 2015, pp. 65-76: ACM.
- [139] L. Gong, W. Yang, D. Man, G. Dong, M. Yu, and J. J. S. Lv, "WiFi-based real-time calibration-free passive human motion detection," vol. 15, no. 12, pp. 32213-32229, 2015.

- [140] C. Wu, Z. Yang, Z. Zhou, X. Liu, Y. Liu, and J. J. I. J. o. S. A. i. C. Cao, "Non-invasive detection of moving and stationary human with wifi," vol. 33, no. 11, pp. 2329-2342, 2015.
- [141] A. E. Kosba, A. Saeed, and M. Youssef, "Rasid: A robust wlan device-free passive motion detection system," in *2012 IEEE International Conference on Pervasive Computing and Communications*, 2012, pp. 180-189: IEEE.
- [142] J. R. Smith *et al.*, "RFID-based techniques for human-activity detection," vol. 48, no. 9, pp. 39-44, 2005.
- [143] H. Li, C. Ye, and A. P. Sample, "IDSense: A human object interaction detection system based on passive UHF RFID," in *Proceedings of the 33rd Annual ACM Conference on Human Factors in Computing Systems*, 2015, pp. 2555-2564: ACM.
- [144] A. T. Hussein and J. M. Elmirghani, "10 Gbps mobile visible light communication system employing angle diversity, imaging receivers, and relay nodes," *Journal of Optical Communications and Networking*, vol. 7, no. 8, pp. 718-735, 2015.
- [145] A. T. Hussein, M. T. Alresheedi, and J. M. Elmirghani, "25 Gbps mobile visible light communication system employing fast adaptation techniques," in *2016 18th International Conference on Transparent Optical Networks (ICTON)*, 2016, pp. 1-7: IEEE.
- [146] P. Buxton, *Metric handbook: planning and design data*. Routledge, 2015.
- [147] T. Yasuda, S. Yokoi, and J.-i. Toriwaki, "A shading model for cloth objects," *IEEE Computer Graphics and Applications*, no. 6, pp. 15-24, 1992.
- [148] M. Akgun, B. Becerir, and H. R. Alpay, "Reflectance prediction of colored polyester fabrics by a novel formula," *Fibers and Polymers*, vol. 15, no. 1, pp. 126-137, 2014.
- [149] C. Le Bas, S. Sahuguede, A. Julien-Vergonjanne, A. Behloul, P. Combeau, and L. Aveneau, "Human body impact on mobile visible light communication link," in *2016 10th International Symposium on Communication Systems, Networks and Digital Signal Processing (CSNDSP)*, 2016, pp. 1-6: IEEE.
- [150] S. R. Marschner, S. H. Westin, A. Arbree, and J. T. Moon, "Measuring and modeling the appearance of finished wood," in *ACM Transactions on Graphics (TOG)*, 2005, vol. 24, no. 3, pp. 727-734: ACM.
- [151] V. Jungnickel, A. Forck, T. Haustein, U. Kruger, V. Pohl, and C. Von Helholt, "Electronic tracking for wireless infrared communications," *IEEE Transactions on Wireless Communications*, vol. 2, no. 5, pp. 989-999, 2003.
- [152] M. Nakamura, Y. Imai, Y. Umeda, J. Endo, and Y. Akatsu, "1.25-Gb/s burst-mode receiver ICs with quick response for PON systems," *IEEE journal of solid-state circuits*, vol. 40, no. 12, pp. 2680-2688, 2005.
- [153] T. INSTRUMENTS, "Ultra-Low Noise, High-Speed Operational Amplifier'," no. Available: <http://www.ti.com/lit/ds/symlink/lmh6629.pdf>, 2018.
- [154] C. Cisco, "Cisco TelePresence System TX1310 65 Room Recommendations," [https://www.cisco.com/c/en/us/td/docs/telepresence/cts\\_1300/cts\\_13](https://www.cisco.com/c/en/us/td/docs/telepresence/cts_1300/cts_13)

10/assembly/guide/1310\_assembly\_guide/1310\_room\_recommendations.html, 2018.

- [155] P. Downs, "Conference Table Size from Room," *www.custom-conference-tables.com*, 2018.
- [156] J. Hallock, "Preferences Favorite Color Survey," <http://www.joehallock.com/edu/COM498/index.html>, 2018.
- [157] I. Mironova, "Reflectance analysis and thermochromicity of fabrics dyed with indigo, 6 bromoindigo, 6, 6'-dibromoindigo," 2013.
- [158] H. L. Van Trees, *Detection, estimation, and modulation theory, part I: detection, estimation, and linear modulation theory*. John Wiley & Sons, 2004.
  
- [159] R. Zeimer and W. Tranter, "Principles of communications," ed: Houghton Mifflin Company, 1990.
- [160] J. R. Barry, "Sequence detection and equalization for pulse-position modulation," in *Proceedings of ICC/SUPERCOMM'94-1994 International Conference on Communications*, 1994, pp. 1561-1565: IEEE.
- [161] J. G. Proakis and M. Salehi, *Digital communications*. McGraw-hill New York, 2001.
- [162] V.-H. Nguyen and J.-Y. Pyun, "Location detection and tracking of moving targets by a 2D IR-UWB radar system," *Sensors*, vol. 15, no. 3, pp. 6740-6762, 2015.
- [163] M. Piccardi, "Background subtraction techniques: a review," in *2004 IEEE International Conference on Systems, Man and Cybernetics (IEEE Cat. No. 04CH37583)*, 2004, vol. 4, pp. 3099-3104: IEEE.
- [164] R. Zetik, S. Crabbe, J. Krajnak, P. Peyerl, J. Sachs, and R. Thomä, "Detection and localization of persons behind obstacles using M-sequence through-the-wall radar," in *Sensors, and Command, Control, Communications, and Intelligence (C3I) Technologies for Homeland Security and Homeland Defense V*, 2006, vol. 6201, p. 62010I: International Society for Optics and Photonics.
- [165] A. Mclvor, Q. Zang, and R. Klette, "The background subtraction problem for video surveillance systems," in *International Workshop on Robot Vision*, 2001, pp. 176-183: Springer.
- [166] A. P. Hoeks, T. G. Arts, P. J. Brands, and R. S. Reneman, "Comparison of the performance of the RF cross correlation and Doppler autocorrelation technique to estimate the mean velocity of simulated ultrasound signals," *Ultrasound in medicine & biology*, vol. 19, no. 9, pp. 727-740, 1993.
- [167] Y. W. Lee, T. Cheatham, and J. B. Wiesner, "The application of correlation functions in the detection of small signals in noise," 1949.
- [168] M. Azaria and D. Hertz, "Time delay estimation by generalized cross correlation methods," *IEEE Transactions on Acoustics, Speech, and Signal Processing*, vol. 32, no. 2, pp. 280-285, 1984.
- [169] H.-M. Sun, R.-S. Jia, Q.-Q. Du, and Y. Fu, "Cross-correlation analysis and time delay estimation of a homologous micro-seismic signal based on the Hilbert–Huang transform," *Computers & geosciences*, vol. 91, pp. 98-104, 2016.

- [170] D. L. Isaacson and R. W. Madsen, *Markov chains theory and applications*. 1976.
- [171] M. Frydenberg, "The chain graph Markov property," *Scandinavian Journal of Statistics*, pp. 333-353, 1990.
- [172] F. A. Haight, "Handbook of the Poisson distribution," 1967.
- [173] A.-L. Barabasi, "The origin of bursts and heavy tails in human dynamics," *Nature*, vol. 435, no. 7039, p. 207, 2005.
- [174] H. R. Anderson, *Fixed broadband wireless system design*. John Wiley & Sons, 2003.
- [175] B. Tang, C. Jiang, H. He, and Y. Guo, "Probabilistic human mobility model in indoor environment," in *2016 International Joint Conference on Neural Networks (IJCNN)*, 2016, pp. 1601-1608: IEEE.
- [176] H. G. Britain, "Workplace Health, Safety and Welfare: Workplace (Health, Safety and Welfare) Regulations 1992 (as Amended by the Quarries Miscellaneous Health and Safety Provisions Regulations 1995): Approved Code of Practice and Guidelines,," *London, United Kingdom: HMSO*, 1996.
- [177] Y. Gu, A. Lo, and I. Niemegeers, "A survey of indoor positioning systems for wireless personal networks," *IEEE Communications Surveys & Tutorials*, 11 (1), 2009, 2009.
- [178] H. Liu, H. Darabi, P. Banerjee, and J. Liu, "Survey of wireless indoor positioning techniques and systems," *IEEE Transactions on Systems, Man, and Cybernetics, Part C (Applications and Reviews)*, vol. 37, no. 6, pp. 1067-1080, 2007.
- [179] A. Küpper, *Location-based services: fundamentals and operation*. John Wiley & Sons, 2005.
- [180] A. Kushki, K. N. Plataniotis, and A. N. Venetsanopoulos, *WLAN positioning systems: principles and applications in location-based services*. Cambridge University Press, 2012.
- [181] W. Gu, M. Aminikashani, P. Deng, and M. Kavehrad, "Impact of multipath reflections on the performance of indoor visible light positioning systems," *Journal of Lightwave Technology*, vol. 34, no. 10, pp. 2578-2587, 2016.
- [182] S. Makridakis, "Accuracy measures: theoretical and practical concerns," *International Journal of Forecasting*, vol. 9, no. 4, pp. 527-529, 1993.
- [183] C. J. Willmott and K. Matsuura, "Advantages of the mean absolute error (MAE) over the root mean square error (RMSE) in assessing average model performance," *Climate research*, vol. 30, no. 1, pp. 79-82, 2005.
- [184] T. S. Rappaport, J. H. Reed, and B. D. Woerner, "Position location using wireless communications on highways of the future," *IEEE communications Magazine*, vol. 34, no. 10, pp. 33-41, 1996.
- [185] S. M. Ross, *Introduction to probability and statistics for engineers and scientists*. Academic Press, 2014.
- [186] P. Djahani and J. M. Kahn, "Analysis of infrared wireless links employing multibeam transmitters and imaging diversity receivers," *IEEE Transactions on Communications*, vol. 48, no. 12, pp. 2077-2088, 2000.

- [187] F. E. Alsaadi and J. M. Elmirghani, "High-speed spot diffusing mobile optical wireless system employing beam angle and power adaptation and imaging receivers," *Journal of Lightwave Technology*, vol. 28, no. 16, pp. 2191-2206, 2010.
- [188] A. T. Hussein, M. T. Alresheedi, and J. M. Elmirghani, "Fast and efficient adaptation techniques for visible light communication systems," *IEEE/OSA Journal of Optical Communications and Networking*, vol. 8, no. 6, pp. 382-397, 2016.
- [189] S. H. Younus, A. T. Hussein, Aubida Al-Hameed, M. T. Alresheedi and J. M. Elmirghani, "Subcarrier Multiplexing for Parallel Data Transmission in Indoor Visible Light Communication Systems," *IEEE Access*, 2019.
- [190] F. Alsaadi and J. Elmirghani, "Mobile multigigabit indoor optical wireless systems employing multibeam power adaptation and imaging diversity receivers," *IEEE/OSA Journal of Optical Communications and Networking*, vol. 3, no. 1, pp. 27-39, 2011.



# Appendix A

## A.1 Simulation results of VLC system originally reported in [A1]

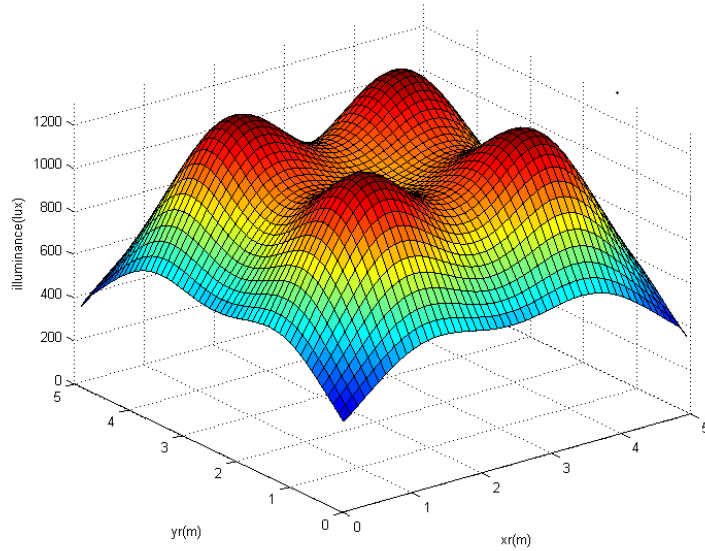


Figure A1.1: Distribution of horizontal illumination at the communication plane

(0.85m) in room with dimensions of 5 m × 5 m × 3 m.

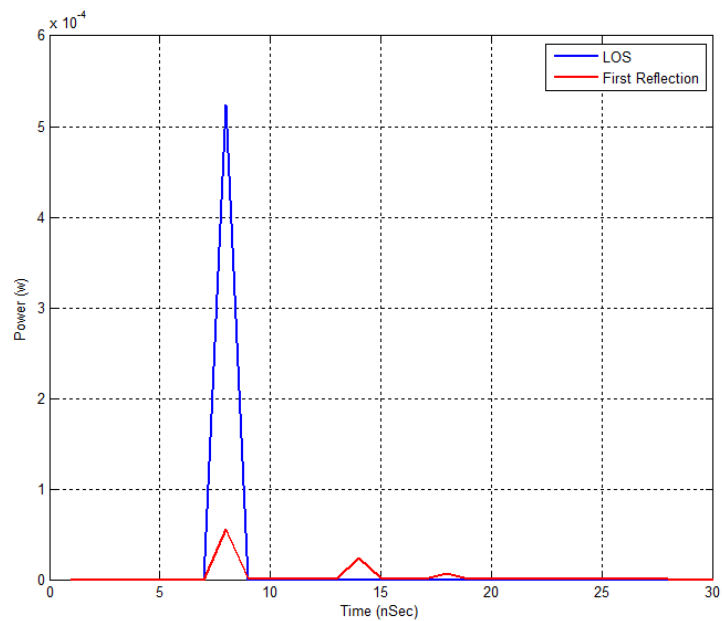


Figure A1.2: Impulse response at 0.01m, 0.01m, 0.85m in room with dimensions of 5 m × 5 m × 3 m.

## References

[A1] T. Komine and M. Nakagawa, "*Fundamental analysis for visible-light communication system using LED lights*," IEEE transactions on Consumer Electronics, vol. 50, no. 1, pp. 100-107, 2004

### A.2 Simulation results of VLC system originally reported in [A2]

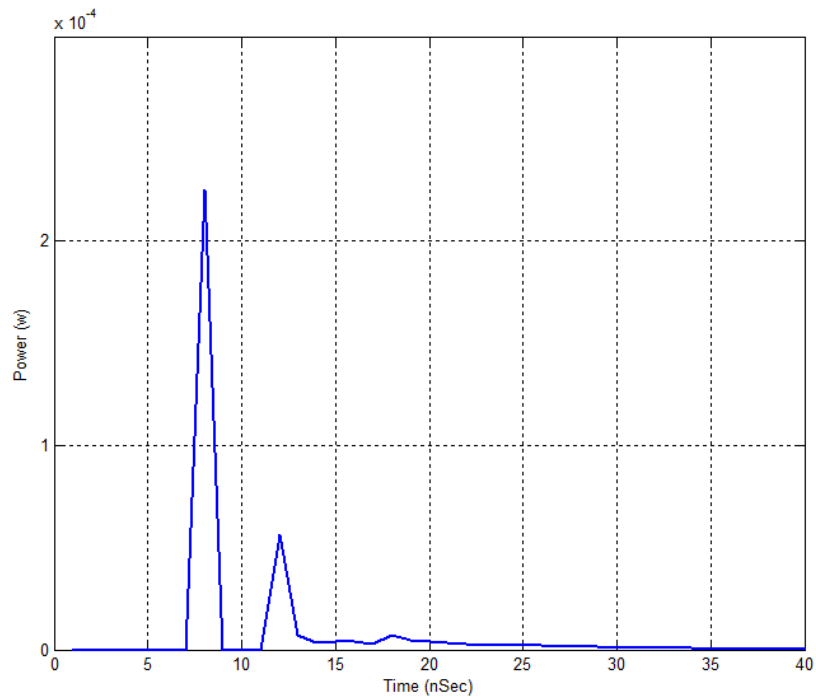


Figure A 2.1: Impulse response of wide FOV receiver at x=2m, y=4m, z =1m

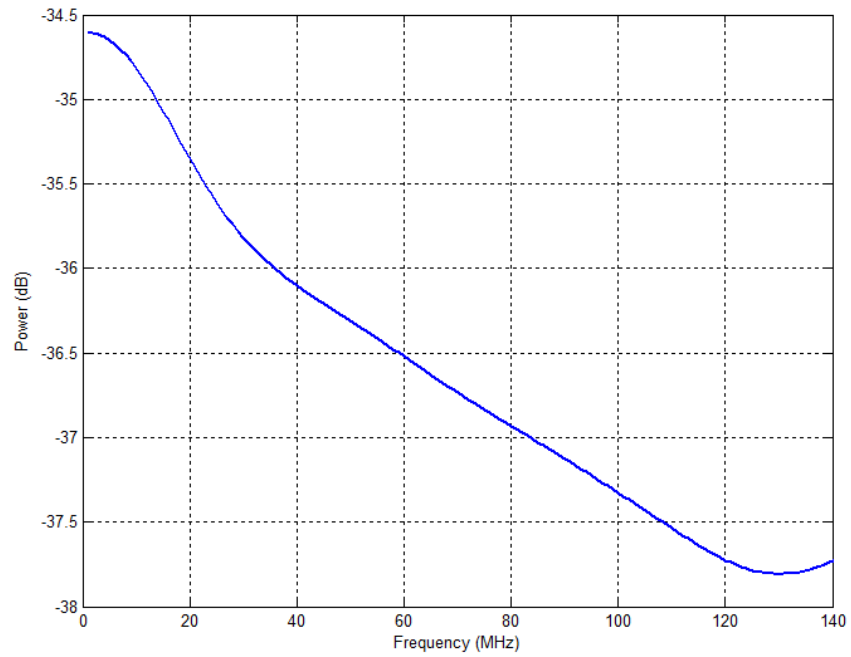


Figure A 2.2: frequency response of wide FOV receiver at  $x=2\text{m}$ ,  $y=4\text{m}$ ,  $z=1\text{m}$

## References

- [A2] A. T. Hussein and J. M. Elmirghani, "*High-speed indoor visible light communication system employing laser diodes and angle diversity receivers*," in *2015 17th International Conference on Transparent Optical Networks (ICTON)*, 2015: IEEE, pp. 1-6.

### A.3 Simulation results of OW system originally reported in [A3]

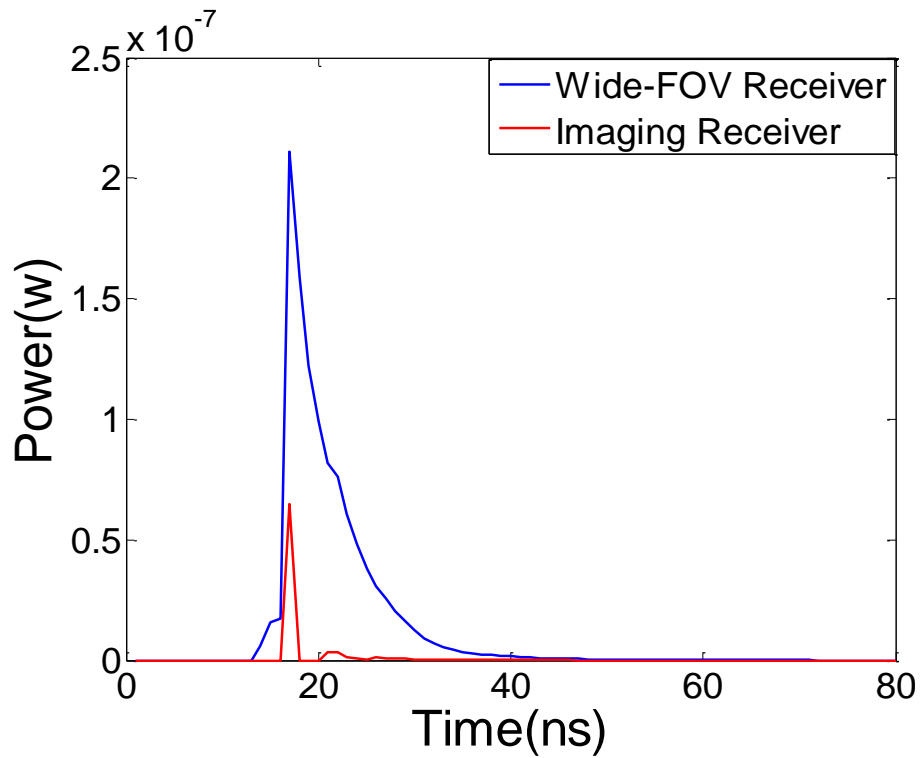


Figure A 3.1: Impulse response of of CDS system with receiver at  $x=1\text{m}$ ,  $y=1\text{m}$ ,  $z=1\text{m}$

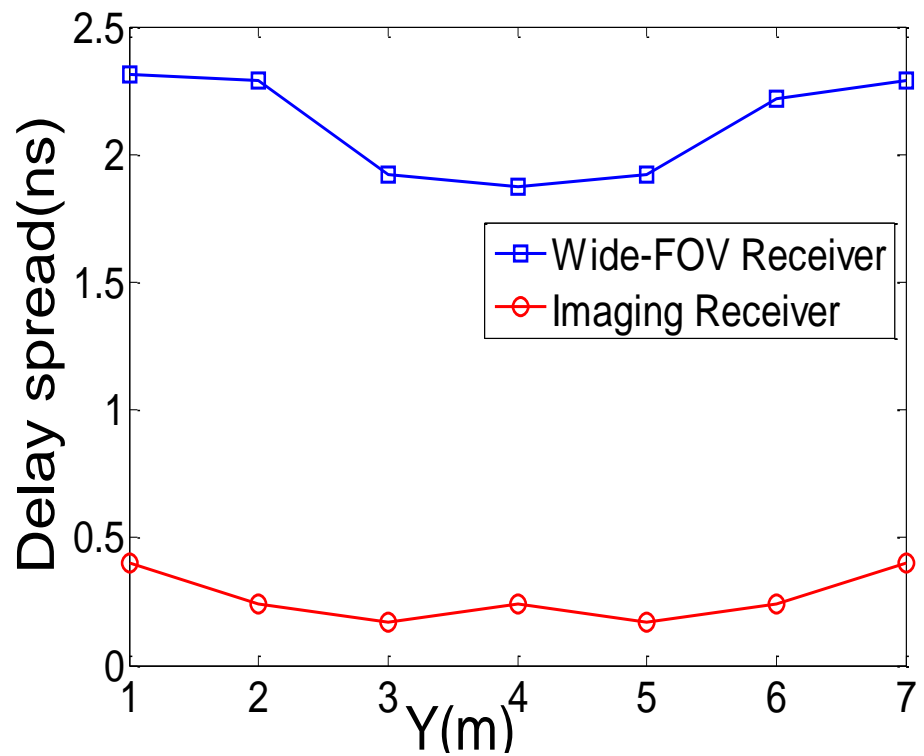


Figure A 3.2: Delay spread of CDS system with receiver at  $x=1\text{m}$

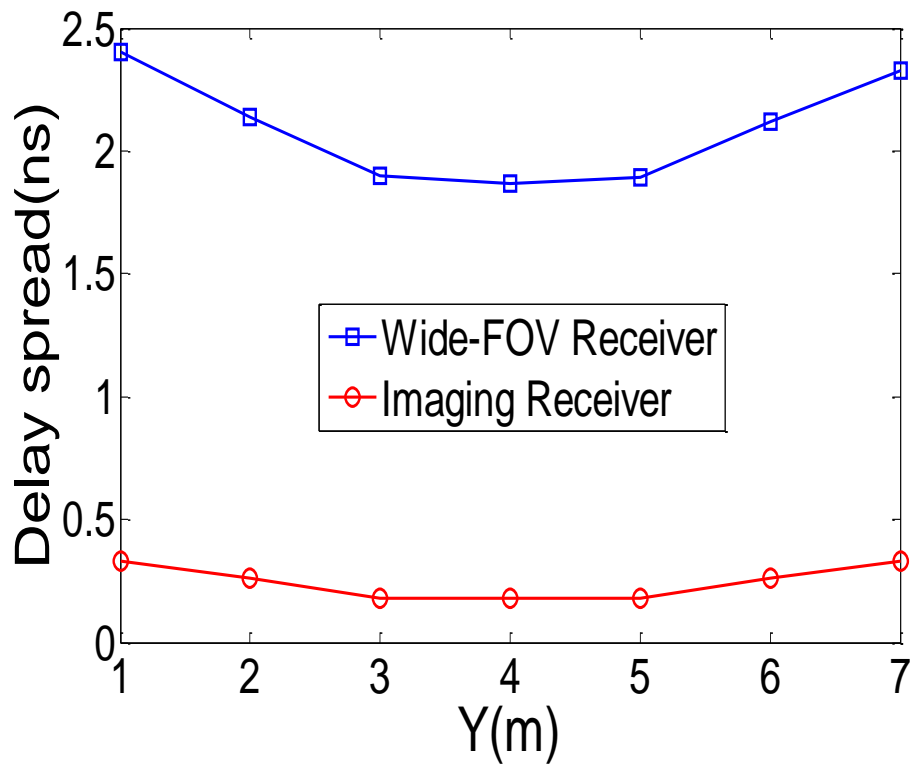


Figure A 3.3: Delay spread of CDS system with receiver at x=2m

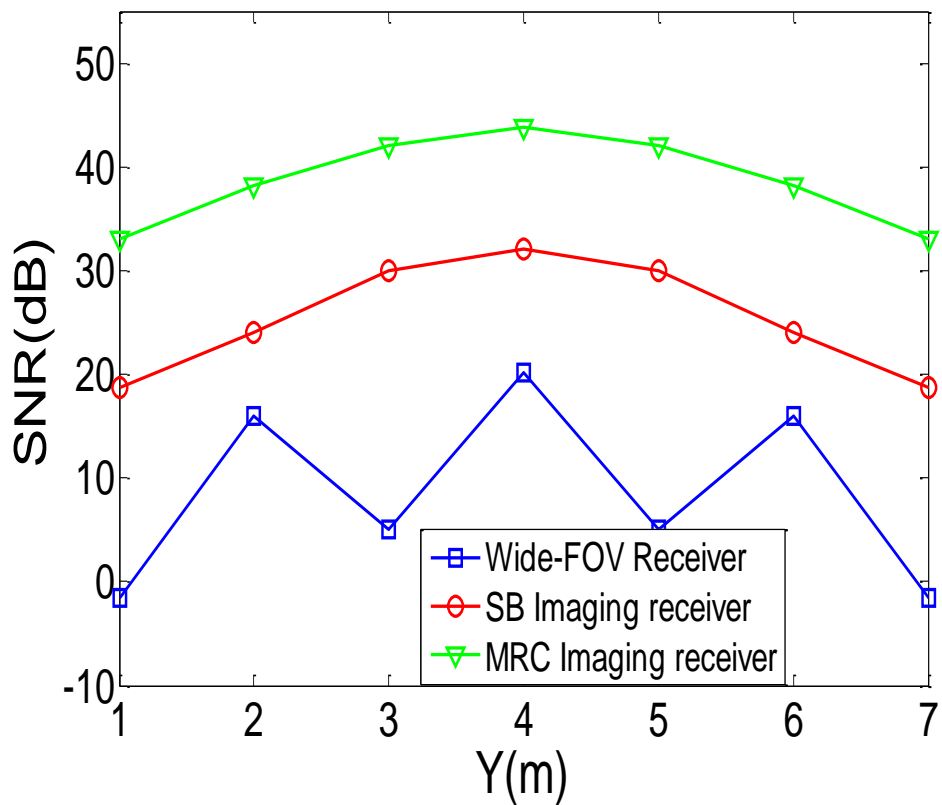


Figure A 3.4: SNR of CDS system with receiver at x=1m.

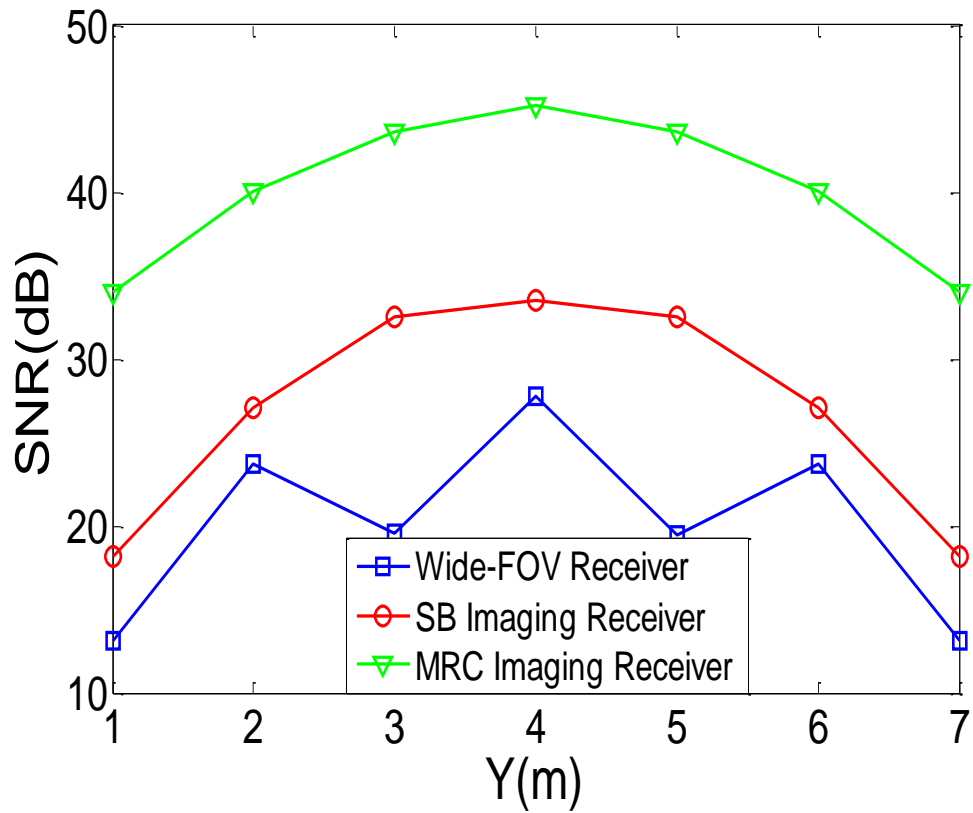


Figure A 3.5: SNR of CDS system with receiver at  $x=2m$ .

## References

- [A3] A. G. Al-Ghamdi and J. M. Elmirghani, "Analysis of diffuse optical wireless channels employing spot-diffusing techniques, diversity receivers, and combining schemes," *IEEE Transactions on*

#### A.4 Simulation results of OW system originally reported in [A4]

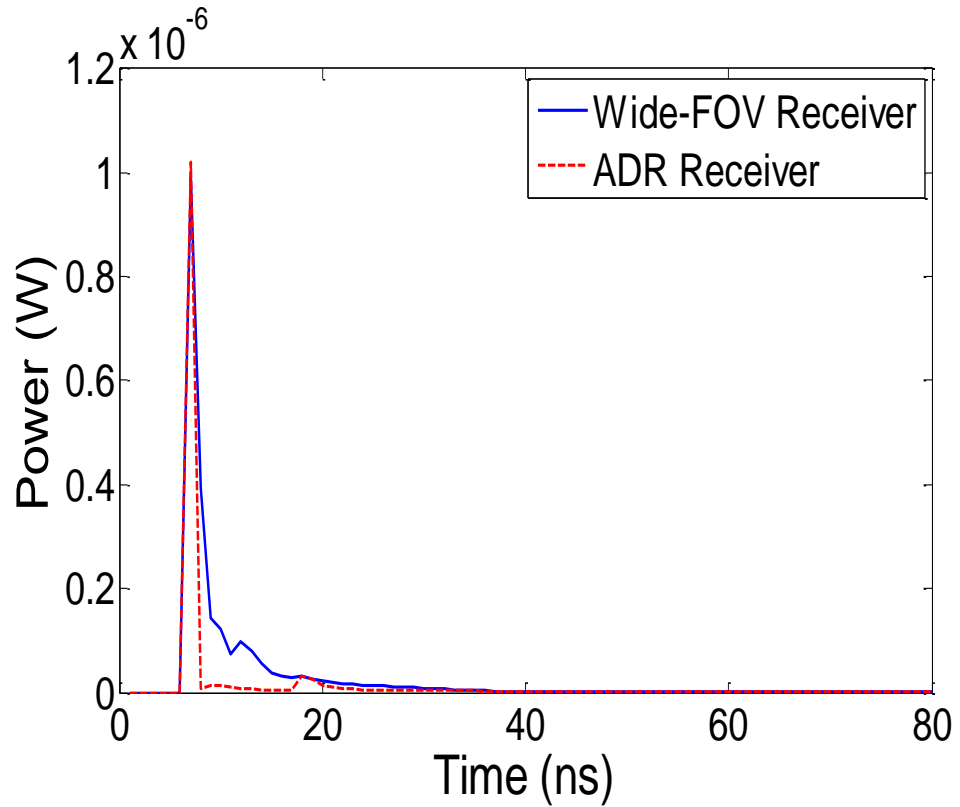


Figure A 4.1: Impulse response of of LSMS system with receiver at  $x=1\text{m}$ ,  $y=1\text{m}$ ,  $z=1\text{m}$

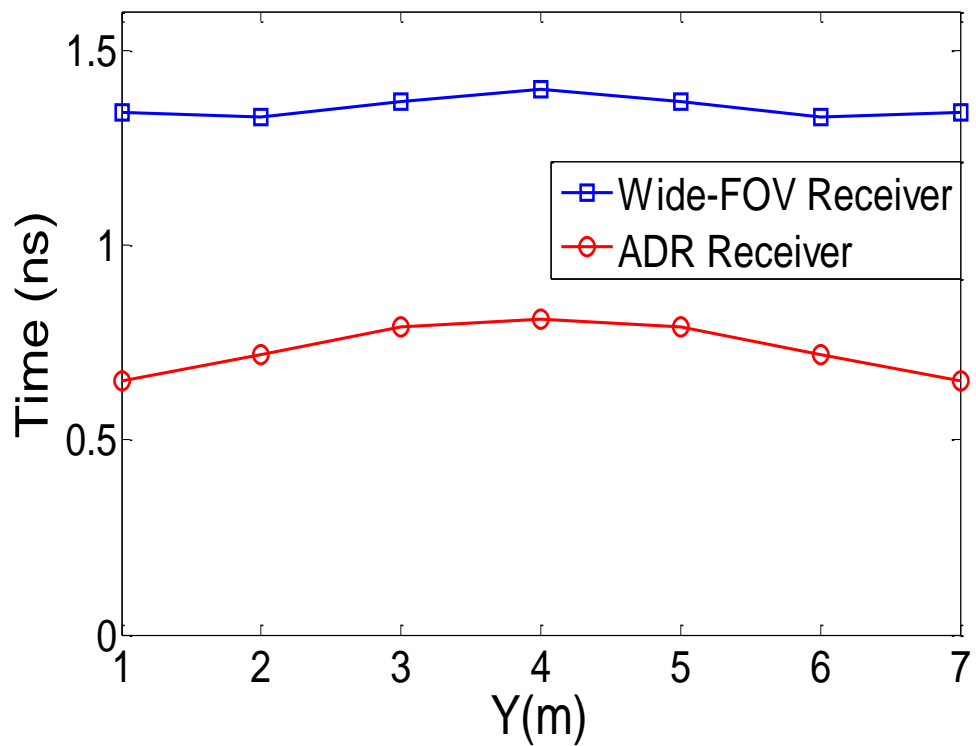


Figure A 4.2: Delay spread of LSMS system with receiver at  $x=1\text{m}$

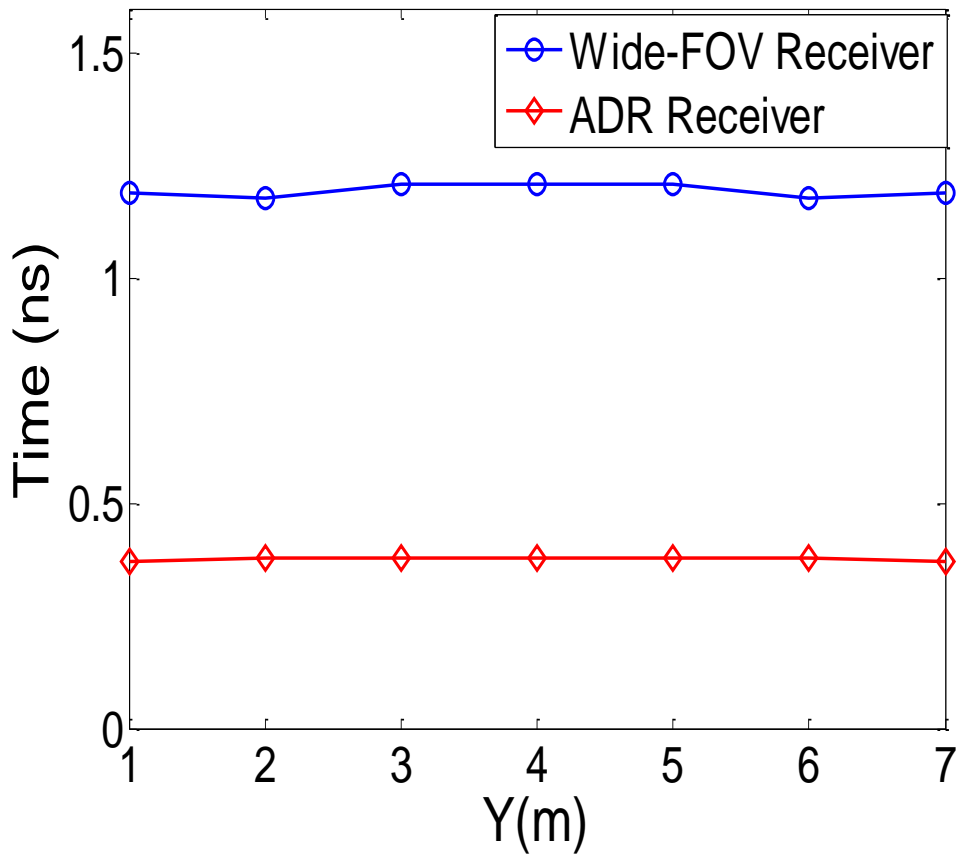


Figure A 4.3: Delay spread of LSMS system with receiver at x=2m

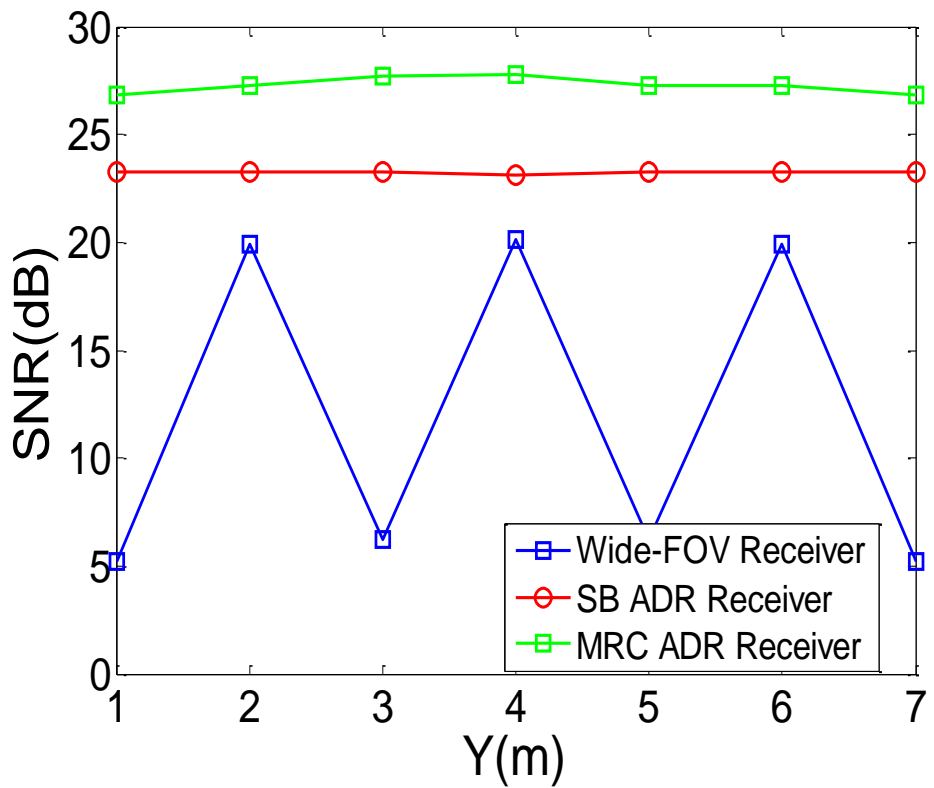


Figure A 4.4: SNR of LSMS system with receiver at x=1m



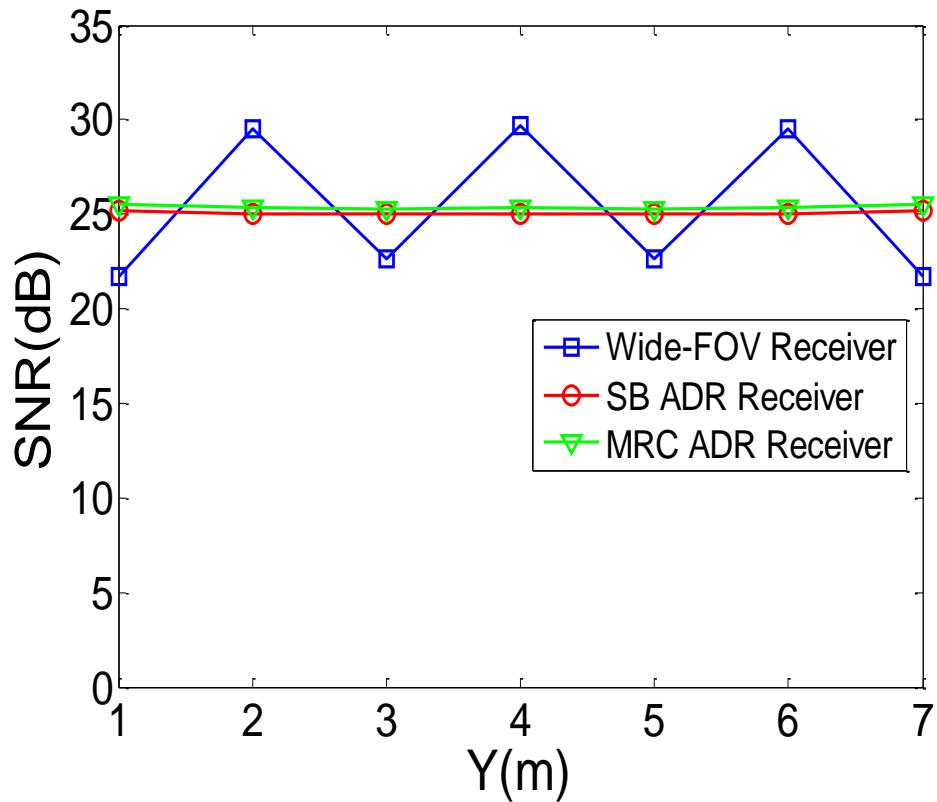


Figure A 4.5: SNR of LSMS system with receiver at x=2m

## References

- [A4] A. G. Al-Ghamdi and J. M. Elmirghani, "*Line strip spot-diffusing transmitter configuration for optical wireless systems influenced by background noise and multipath dispersion*," *IEEE Transactions on Communications*, vol. 52, no. 1, pp. 37-45, 2004.

# Appendix B

## Convolution of Gaussian Random Variables

Let:  $\sigma_1 = \sigma_n$  and  $\sigma_2 = \sigma_s$

$$f(x) = \frac{1}{\sqrt{2\pi}\sigma_1} e^{-\left(\frac{x^2}{2\sigma_1^2}\right)} \quad (\text{A.1})$$

And:

$$g(x) = \frac{1}{\sqrt{2\pi}\sigma_2} e^{-\left(\frac{(x-\mu)^2}{2\sigma_2^2}\right)} \quad (\text{A.2})$$

$$F(x) = f(x) \otimes g(x) = \int_{-\infty}^{\infty} f(x-z)g(z) dz \quad (\text{A.3})$$

Substituting (A.1) and (A.2) into (A.3), we get:

$$F(x) = \frac{1}{2\pi\sigma_1\sigma_2} \int_{-\infty}^{\infty} e^{-\frac{(\sigma_2^2(x-z)^2 + \sigma_1^2(z-\mu)^2)}{2\sigma_1^2\sigma_2^2}} dz \quad (\text{A.4})$$

$$F(x) = \frac{1}{2\pi\sigma_1\sigma_2} \int_{-\infty}^{\infty} e^{-\frac{(\sigma_2^2(x^2 - 2xz + z^2) + \sigma_1^2(z^2 - 2\mu z + \mu^2))}{2\sigma_1^2\sigma_2^2}} dz \quad (\text{A.5})$$

$F(x)$

$$= \frac{1}{2\pi\sigma_1\sigma_2} \int_{-\infty}^{\infty} e^{-\frac{(z^2(\sigma_2^2 + \sigma_1^2) - 2z(\sigma_2^2 x + \sigma_1^2 \mu) + \sigma_2^2 x^2 + \sigma_1^2 \mu^2)}{2\sigma_1^2\sigma_2^2}} dz \quad (\text{A.6})$$

Let  $\sigma^2 = \sigma_2^2 + \sigma_1^2$  and dividing (A.6) by  $\sigma^2$ , we get:

$$F(x) = \frac{1}{2\pi\sigma_1\sigma_2} \int_{-\infty}^{\infty} e^{-\frac{\left(z^2 - \left(2z\frac{(\sigma_2^2 x + \sigma_1^2 \mu)}{\sigma^2}\right) + \frac{(\sigma_2^2 x^2 + \sigma_1^2 \mu^2)}{\sigma^2}\right)}{\frac{2\sigma_1^2 \sigma_2^2}{\sigma^2}}} dz \quad (\text{A.7})$$

Adding and subtracting  $\left(\frac{(\sigma_2^2 x + \sigma_1^2 \mu)}{\sigma^2}\right)^2$  to the numerator of (A.7), we

get:

$$F(x) = \frac{1}{2\pi\sigma_1\sigma_2} \int_{-\infty}^{\infty} e^{-\frac{\left(z^2 - \left(2z\frac{(\sigma_2^2 x + \sigma_1^2 \mu)}{\sigma^2}\right) - \left(\frac{(\sigma_2^2 x + \sigma_1^2 \mu)}{\sigma^2}\right)^2 + \left(\frac{(\sigma_2^2 x + \sigma_1^2 \mu)}{\sigma^2}\right)^2 + \frac{(\sigma_2^2 x^2 + \sigma_1^2 \mu^2)}{\sigma^2}\right)}{\frac{2\sigma_1^2 \sigma_2^2}{\sigma^2}}} dz \quad (\text{A.8})$$

$F(x)$

$$= \frac{1}{2\pi\sigma_1\sigma_2} \int_{-\infty}^{\infty} e^{-\frac{\left(\left(z - \frac{(\sigma_2^2 x + \sigma_1^2 \mu)}{\sigma^2}\right)^2 - \left(\frac{(\sigma_2^2 x + \sigma_1^2 \mu)}{\sigma^2}\right)^2 + \frac{(\sigma_2^2 x^2 + \sigma_1^2 \mu^2)}{\sigma^2}\right)}{\frac{2\sigma_1^2 \sigma_2^2}{\sigma^2}}} dz \quad (\text{A.9})$$

$F(x)$

$$= \left( \frac{e^{-\left(\frac{(\sigma_2^2 x^2 + \sigma_1^2 \mu^2)}{\sigma^2} - \left(\frac{(\sigma_2^2 x + \sigma_1^2 \mu)}{\sigma^2}\right)^2\right)}}{2\pi\sigma_1\sigma_2} \right) \left( \int_{-\infty}^{\infty} e^{-\frac{\left(\left(z - \frac{(\sigma_2^2 x + \sigma_1^2 \mu)}{\sigma^2}\right)^2\right)}{\frac{2\sigma_1^2 \sigma_2^2}{\sigma^2}}} dz \right) \quad (\text{A.9})$$

Let  $\sigma_z = \left(\frac{\sigma_1\sigma_2}{\sigma}\right)$  and  $\mu_z = \left(\frac{(\sigma_2^2x+\sigma_1^2\mu)}{\sigma^2}\right)$  and multiplying (A.9) by  $\frac{\sigma_z}{\sigma_z}$ , we

get :

$$= \left( \frac{e^{-\left(\frac{(\sigma_2^2x^2+\sigma_1^2\mu^2)-\left(\frac{(\sigma_2^2x+\sigma_1^2\mu)}{\sigma^2}\right)^2}{\frac{2\sigma_1^2\sigma_2^2}{\sigma^2}}\right)}}{\sqrt{2\pi}\sigma_1\sigma_2} \right) \left( \frac{1}{\sqrt{2\pi}\sigma_z} \int_{-\infty}^{\infty} e^{-\frac{(z-\mu_z)^2}{2\sigma_z^2}} dz \right) \quad (\text{A.10})$$

The integral of term  $\frac{1}{\sqrt{2\pi}\sigma_z} \int_{-\infty}^{\infty} e^{-\frac{(z-\mu_z)^2}{2\sigma_z^2}} dz = 1$ . Thus (A.10) can be

written as:

$$= \frac{1}{\sqrt{2\pi}\sigma} \left( e^{-\left(\frac{(\sigma_2^2x^2+\sigma_1^2\mu^2)-\left(\frac{(\sigma_2^2x+\sigma_1^2\mu)}{\sigma^2}\right)^2}{\frac{2\sigma_1^2\sigma_2^2}{\sigma^2}}\right)} \right) \quad (\text{A.11})$$

Dividing the numerator and denominator of the exponential term of (A.11) by  $\sigma^4$ , we get:

$$F(x) = \frac{1}{\sqrt{2\pi}\sigma} \left( e^{-\left(\frac{\sigma^2(\sigma_2^2x^2+\sigma_1^2\mu^2)-(\sigma_2^2x+\sigma_1^2\mu)^2}{2\sigma^2\sigma_2^2\sigma_1^2}\right)} \right) \quad (\text{A.11})$$

Simplifying (A.11) and substituting  $\sigma^2 = \sigma_2^2 + \sigma_1^2$  resulting in:

$$F(x) = \frac{1}{\sqrt{2\pi}\sqrt{\sigma_2^2 + \sigma_1^2}} \left( e^{-\left(\frac{x^2-2\mu+\mu^2}{2(\sigma_2^2+\sigma_1^2)}\right)} \right) \quad (\text{A.12})$$

$$F(x) = \frac{1}{\sqrt{2\pi}\sqrt{\sigma_2^2 + \sigma_1^2}} \left( e^{-\left(\frac{(x-\mu)^2}{2(\sigma_2^2+\sigma_1^2)}\right)} \right) \quad (\text{A.13})$$